Analysis of the Anomalous Spin Precession of the Muon for the Fermilab Muon $g-2$ Experiment

Joshua LaBounty

A dissertation
submitted in partial fulfillment of the
requirements for the degree of

Doctor of Philosophy

University of Washington
2024

Reading Committee:
David Hertzog, Chair
Jason Detwiler
Quentin Buat

Program Authorized to Offer Degree:
Physics

University of Washington

Abstract

Analysis of the Anomalous Spin Precession of the Muon for the Fermilab Muon $g-2$ Experiment

Joshua LaBounty

Chair of the Supervisory Committee:

David Hertzog
Physics

The E989 Muon $g-2$ Experiment at Fermilab searches for signals of physics beyond the standard model by precisely measuring the anomalous magnetic moment of the muon (a_μ) and comparing the result to the standard model prediction. The measurement of a_μ can be broken into three components: measurement of the anomalous spin precession frequency of the muon (ω_a), measurement of the magnetic field of the $g-2$ storage ring using proton NMR, and characterization of the dynamic motion of the muon beam. Recently published results from Runs 2 and 3 of the experiment have increased the precision on the world average value of a_μ by a factor of two to 0.19 parts-per-million (ppm). These results are in strong tension with a 2020 evaluation of a_μ in the standard model. This thesis describes the work to analyze the remaining data (Runs 4-6) of the Muon $g-2$ experiment. These datasets represent 73% of the total data collected and are expected to bring the final experimental uncertainty to ≤ 0.14 ppm. An overview of the $g-2$ experiment is presented, with special attention paid to the precession frequency measurement hardware and the analysis chain through which the ω_a data is processed and collated into 'physics-quality' datasets. A preliminary analysis of the Run-4 ω_a data follows, which yields by itself a statistical precision of 0.19 ppm. Finally, selected systematic studies and remaining analysis work are presented and discussed.

Acknowledgements

I'd first like to thank my advisor, David Hertzog. Without our whiteboard conversations and 'wack-a-duck' ideas I wouldn't be half the physicist I am today. From your endless wisdom on $g-2$, to our shared confusion about PIONEER, it's been an absolute pleasure. And a special thanks of course for allowing me to commandeer the group espresso machine ('g minus brew') during lockdown.

More broadly, I'd like to thank all of the members of the $g-2$ and PIONEER groups at UW, past and present: Omar Beesley, Quentin Buat, Christine Claessens, Erik Swanson, Peter Kammel, Zach Hodge, Aaron Fienberg, Jason Hempstead, Martin Fertl, Nathan Froemming, and Rachel Osofsky. Many thanks especially go to Brynn MacCoy and Hannah Binney for being 2 out of the 3 detector ops musketeers and the best officemates one could ask for. Thank you to Kim Siang Khaw and Jarek Kaspar for their mentorship as I first joined the group. Thanks also to Svende Braun, I couldn't have asked for a better partner in the Run-4+ analysis. Finally, thank you to Patrick Schwendimann, for showing me around PSI and for all of your chocolate and cheese recommendations while we were there.

Thanks as well to the members of the $g-2$ and PIONEER collaborations at large. The perspectives of each person I've spoken with have been invaluable towards shaping how I think about the problems we've come together to tackle. Thanks in particular to Lawrence Gibbons, Sean Foster, James Mott, Chris Polly, David Tarazona, Simon Corrodi, Matt Bressler, Zepyoor Khechadoorian, Tyler Barrett, Tim Gorringe, Elia Bottalico, and so many others for all of their help over the years. Thanks as well to all the members of the $g-2$ data production team: Tammy Walton, Liang Li, Paolo Girotti, Irwin Gaines, Andy Edmonds, Fred Gray, Lorenzo Cotrozzi, Gavin Hesketh, Adam Lyon, Leah Welty-Rieger, Lisa Goodenough, and Yuri Oksuzian. Without your hard work none of this would have been possible. Thanks to all of the run coordinators, operations managers, engineers, technicians, accelerator physicists, and others at Fermilab for making the experiment possible. Thanks to all of the ω_a analyzers, who have provided me with many fruitful discussions over the years. And a special thanks to everyone at Fermilab who was willing to pick up a screwdriver and disassemble a calorimeter at a moments notice.

Thanks to each of the members of my committee: Miguel Morales, Sarah Tuttle, Jason Detwiler, Jerry Miller, and Quentin Buat (double thanks!).

Many thanks to those who helped me through my undergraduate studies as well. Thank you to Abhay Deshpande and Nils Feege, who taught me that research wasn't nearly as intimidating as I thought (and trusted me to be 'in charge' enough to figure that out). To Page and Tom, I can't imagine having gotten through Stony Brook without the two of you.

Thanks to all of the friends I've made in Seattle. Especially to all of the members of 'My Long Lost Appendix,' a trivia group with middling success but a lot of heart, and to the D&D group that puts up with my shenanigans. And special thanks to the group who were there for the weird times: Audrey, Kato, Dan, Anna, and Anthony. I look back on the things we did to keep ourselves sane as a beacon of light in an otherwise dismal era.

Finally, I'd like to thank all my family. To My Grandpa John, who taught me that I could do anything under the sun (and showed me how to do half of it himself). To Mom, Dad, Jacob, Grandma, Meme, Kris, Mike, Carlin, Papa, and Sam — thank you for your continual support and encouragement. And the family I'm joining: Carol, Zac, Jacob, Valleta (Granny). Thank you for welcoming me into your lives. And to Dahli, for appreciating a well cooked steak.

And of course my thanks go out to my loving partner, Jared, without the support of whom none of this would be possible. Thank you for being the bright light in every cloudy Seattle day. Thank you for always being willing to say 'yes, and' to my crazy ideas, and for dragging me to the things that I enjoy but wouldn't do without someone to share in them. You make everything better and every day worth living.

DEDICATION

To my parents, whose unconditional love and support has buoyed me through.

And to Jared, without whom I would be lost.

Contents

Glossary

Δ__ Used in the text to mean 'difference in.' For instance, $\Delta x = x_1 - x_2$.

δ__ Used in the text to mean 'uncertainty on.' For instance, the 1σ uncertainty on x arising from a fit could be written as $x \pm \delta x$. Sometimes used interchangeably with σ.

$\tilde{\omega}_p$ Muon weighted proton precession frequency, proportional to the magnetic field of the storage ring.

ω_a Anomalous precession frequency of the muon.

ω_p Proton precession frequency, proportional to the magnetic field of the storage ring.

f_i Frequency i. In the text $f_i \equiv \omega_i / 2\pi$.

$\mathcal{R}$ The ratio ω_a/ω_p.

$R(\omega_a)$ The blinded proxy for ω_a. A shift in $R(\omega_a)$ by one unit corresponds to a change in ω_a by 1 ppm.

$\mathcal{O}$(__) Order of magnitude of the quantity in parentheses.

BSM Beyond the Standard Model.

c.t. 1 'clock tick' of the 800 MS/s digitizer. ≈ 1.25 ns.

calo Calorimeter.

CBO Coherent Betatron Oscillation.

CTAG Literally ‘calorimeter tag’. Defined as a positron detected in the calorimeters with $E >$ 1700 MeV and $30 < t\ [\mu s] < 650$. CTAG/Fill is used as a measure of the rate of data acquisition.

DQC Data Quality Control (or alternatively Data Quality Cuts) applied to filter the ‘physics-quality’ data from the ‘raw’ data.

ESQ Electrostatic quadrupole magnet.

Nearline An intermediate analysis chain used in the Muon $g-2$ experiment with a turnaround time of 1-2 hours.

ppb Parts per billion.

ppm Parts per million.

SM The Standard Model of particle physics.

TDR Technical Design Report.

WP The 2020 White Paper published by the Muon $g-2$ Theory Initiative. This contains the SM prediction for a_μ [1].

xtal Crystal.

Chapter 1

Introduction

The standard model (SM) of particle physics is the most successful theoretical framework in existence. Since its conception in the early 20^{th} century, it has made countless successful predictions and become the underpinning of the modern description of the physics of fundamental particles. However despite its many successful predictions, there remain a number of areas where the SM falls short. For example, it fails to explain the existence of the dark matter, nor why the universe consists of an abundance of matter and not antimatter. Precision tests of the SM provide footholds to explore physics beyond the standard model (BSM) through examination of tiny perturbations on existing SM quantities. Any tensions between measured values and those calculated using the standard model can be used to guide theoretical developments and test predictions from specific models of BSM physics. The anomalous magnetic moment of the muon — a_μ — provides one such test: as it can be predicted to high precision in the SM, can be measured to high precision, and is potentially quite sensitive to the effects of beyond the standard model physics.

This thesis describes the author's contributions to the Muon $g-2$ experiment at Fermilab. This chapter gives a brief introduction to magnetic moments, as well as the general principles underpinning storage ring measurements of Muon $g-2$. Chapter 2 describes the current status of the theoretical prediction of the anomalous magnetic moment in the SM, including the current tensions present therein. Chapter 3 details how this particular experiment is performed, from the production of muons to the detection of the positron energy signals from which a_μ is extracted.

This chapter also describes the calculation of various necessary correction factors. Chapters 4 and 5 describe the processing of the raw data through the nominal UW analysis chain. In those chapters, Run-4 of the experiment (data taken from December 2020 – July 2021) is treated as the 'nominal' set of running conditions. Chapter 6 presents some systematic evaluations by the author, as well as a summary of the current status of the overall systematics of the Run-4+ analysis. Ongoing studies, as well as major differences between Run-4 and other running periods, are described in Chapter 7. Finally, some brief closing thoughts are presented in Chapter 8.

Over the past several years, the author participated in a wide assortment of investigations related to the extraction of the anomalous precession frequency of the muon (ω_a) and the behavior of the muon beam ('beam dynamics'). Throughout this work a holistic picture of the experiment is presented at a high level, while special attention is paid to those aspects of the experiment where the author has made significant contributions[1]. A condensed description of specific contributions by the author are presented in Appendix A.

1.1 Background

Classically, an electric charge with angular momentum $\vec{L}$ will generate a magnetic moment $\vec{\mu}$ [2]:

$$\vec{\mu} = \frac{q}{2m}\vec{L}, \tag{1.1}$$

where q and m are the charge and mass[2] of the particle respectively. When an external magnetic field $\vec{B}$ is applied, such an object will experience a torque:

$$\vec{N} = \vec{\mu} \times \vec{B}, \tag{1.2}$$

and associated potential energy:

$$U = -\vec{\mu} \cdot \vec{B}. \tag{1.3}$$

---

[1] Or, barring significant contributions, has great fondness for nonetheless.

[2] It is assumed here the charge and mass distributions are the same.

This set of equations works well to describe macroscopic objects, but (like many aspects of classical physics) they begin to fail at quantum scales. In particular, this classical description of magnetic moments was found to be lacking when it came to describing the behavior of subatomic particles with an internal angular momentum. Starting from the 1920's, many measurements of such particles found deviations from the magnetic moment predicted by a classical approximation of spherical charges. This led to the modification of Equation (1.1), adding the 'gyromagnetic ratio' g to account for the discrepancy between theory and experiment:

$$\vec{\mu} = g\frac{q}{2m}\vec{s}, \tag{1.4}$$

where $g \equiv 1$ for classical systems, $g \equiv 2$ for the electron, and g for composite particles like the proton and neutron being determined experimentally. The angular momentum $\vec{L}$ is replaced by the spin vector of the particle $\vec{s}$, to better differentiate between internal and orbital angular momentum. This allowed calculations to be done, but was an ad-hoc solution to what was quickly becoming a glaringly obvious problem: quantum systems are fundamentally different from classical ones.

1.1.1 Quantum Moments and the Dirac Equation

A solution to the ad-hoc nature of this addition soon presented itself. When Dirac formulated his eponymous equation[3]:

$$\left[(i\partial_\mu - eA_\mu)^2 - \frac{e}{2}F_{\mu\nu}\sigma^{\mu\nu} - m^2\right]\psi = 0, \tag{1.5}$$

in 1928 it was noted that it implicitly predicted $g = 2$ for a spin-$^1/_2$ particle like an electron. This can be seen more clearly when this equation is taken to its non-relativistic limit. This yields the Hamiltonian:

$$H = \frac{\vec{p}^2}{2m} + V(\vec{r}) + \frac{e}{2m}\vec{B}\cdot\left(\vec{L} + 2\vec{S}\right). \tag{1.6}$$

---

[3] Following the notation from [3].

In this form, $g = 2$ can be read off (as highlighted in red). The 'anomalous' portion of the magnetic moment is defined as the difference from g to the pure Dirac prediction, divided by 2:

$$a \equiv \frac{g-2}{2}. \tag{1.7}$$

The value of a is non-zero due to loop corrections from virtual particles in the vacuum. The various contributions to the muon anomaly are given in detail in Chapter 2.

It should be noted that an analogous electric dipole moment (EDM) can also be constructed:

$$\vec{d} = \eta \frac{e}{2m} \vec{s}, \tag{1.8}$$

where η is the electric equivalent of g. In the calculations which follow it is assumed that such an EDM is zero, which is consistent with the best measurements at this time[4].

1.2 The Foundation of the Muon $g-2$ Experiment

The Muon $g-2$ experiment extracts the value a_μ from the energy spectrum of positrons produced from the decay of muons held in a magnetic storage ring. Measurements of a_μ have a history stretching back almost 70 years, and in that time a number of key refinements of the technique have been made. While the specific details of the current experiment are described in Chapter 3, the measurement technique can be distilled into the following pillars which underpin the experiment today.

1.2.1 Parity Violation in the Weak Decay

The parity violating nature of weak decay is foundational to the Muon $g-2$ experiment, first in the decay of pions (π^+) into muons (μ^+), and then in the decay of those μ^+ to positrons (e^+). The

---

[4] A measurement of this quantity is possible from the Muon $g-2$ data, and a publication is forthcoming with results from the first years of data taking. Such a measurement was performed as part of the previous generation $g-2$ experiment [4], which yielded:

$$|d_\mu| < 1.9 \times 10^{-19} e * \text{cm [95\% c.l.]} \tag{1.9}$$

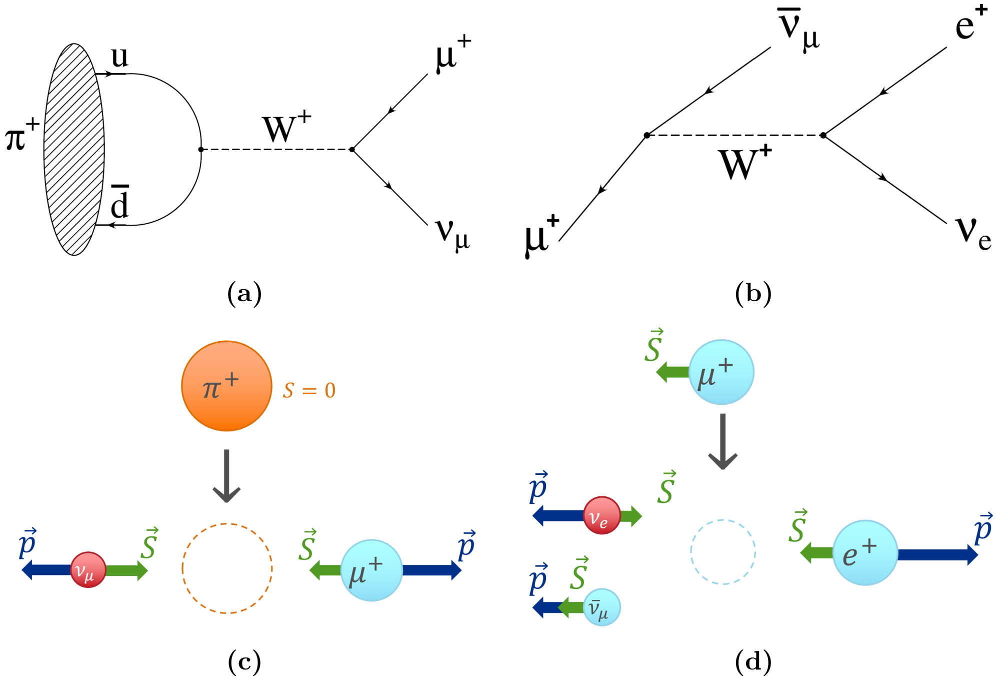

(a) (b) (c) (d)

Figure 1.1: Feynman diagrams showing the positive pion and muon decay channels, as well as the analysis of the momentum and spin of the initial/final states for each in the rest frame of the decaying particle.

π^+ is a spin-0 pseudoscalar meson. When it decays, the final state must also be spin-0. The π^+ decays through the weak interaction (Figure 1.1a) primarily[5] to a muon and a neutrino:

$$\pi^+ \to \mu^+ + \nu_\mu. \tag{1.10}$$

The two body nature of the decay means that the muon must be emitted back to back with the neutrino. Each will have an energy in the pion rest frame of $m_\pi/2$. All neutrinos in the standard model are left handed, which means that the muon must be born with a definite helicity state as well in order to to conserve angular momentum. The muons produced in positive (negative) pion decays are therefore entirely polarized against (along) their direction of motion. A polarized beam of muons can be created by selecting from a mono-energetic π^+ beam either the highest (lowest) energy decay muons, which will have been emitted in (opposite to) the direction of the pion's momentum vector in the lab frame.

---

[5] With a branching ratio of 99.987% [5].

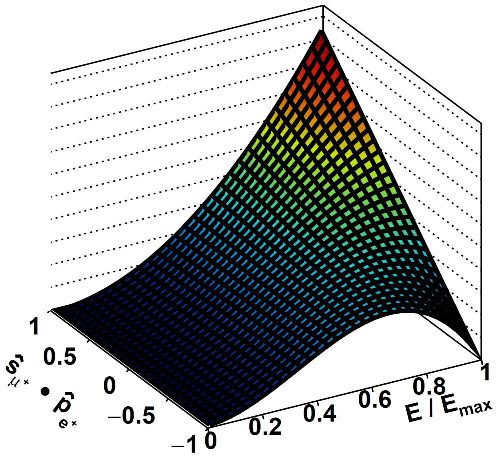

Figure 1.2: The correlation between the normalized energy of the positron and the spin direction of the parent muon. The highest energy decay positrons are produced when the positron is emitted in the direction of the muon spin vector ($\hat{s}_\mu \cdot \hat{p}_e = 1$). The color scale and z-axis are normalized from 0 to 1. Reproduced from [6].

The decay of the muon to an electron also proceeds through the weak decay (Figure 1.1b). Conservation of lepton number requires a three body decay:

$$\mu^+ \to e^+ + \nu_e + \bar{\nu}_\mu. \tag{1.11}$$

The highest energy decay positrons will be created when the two neutrinos are emitted parallel to one another and opposite in direction to the positron. This can be seen pictorially in Figure 1.1d. In this case, the angular momentum of the neutrino and anti-neutrino cancel and the positron necessarily carries the same spin as the parent muon. The correlation between positron momentum and muon spin decreases as the positron energy decreases, as shown in Figure 1.2. The muon decay is often referred to as ‘self-analyzing’, as the direction of the spin vector of the muon at the time of the decay can be inferred from the energy of the decay positron.

1.2.2 Muons in Motion: Direct Sensitivity to the Anomaly

Shortly after the concept of parity violation in the weak decay was proposed [7], measurements of the g-factor of the muon (g_μ) were performed. Early measurements, such as those conducted at the Nevis synchrocyclotron, utilized polarized muons which were brought to rest in a fixed target [8–10]. The spins of the muons would then precess in a magnetic field applied to this target. Variation of the magnitude of this field caused a modulation in the number of high energy positrons measured by a fixed counter after a set time. Measurements performed using this technique were critical to confirming the Dirac nature of the muon[6]. However, these techniques were sensitive to g_μ directly and were therefore limited in their ability to measure the anomalous portion of the magnetic moment (even to 1st order).

A leap forward for measurements of the anomaly came from considering muons which were undergoing relativistic cyclotron motion in a magnetic field. Considering only motion perpendicular to the field:

$$\left|\frac{d\vec{p}}{dt}\right| \equiv \omega_c = \frac{eB}{m\gamma}. \tag{1.12}$$

The torque such a field provides to a point-like particle manifests in the form of a Larmor precession of the spin vector:

$$\frac{d\vec{s}}{dt} = \vec{\mu} \times \vec{B} \rightarrow \left|\frac{d\vec{s}}{dt}\right| = \omega_s = g\frac{eB}{2m}. \tag{1.13}$$

In this accelerating, relativistic reference frame, Equation (1.13) is modified to include the effects of Thomas precession [2]:

$$\omega_s = g\frac{eB}{2m} + (1-\gamma)\frac{eB}{m\gamma}. \tag{1.14}$$

Taking the difference of these frequencies yields:

$$\begin{aligned} \omega_s - \omega_c &= \frac{g-2}{2}\frac{eB}{m} \\ &= a\frac{eB}{m} \equiv \omega_a \end{aligned} \tag{1.15}$$

where it can be seen that the difference between these two frequencies (the ‘anomalous precession

---

[6] It was still unclear whether the muon (or ‘mu meson’) had any substructure, like the ‘other’ mesons of the time such as the π^+.

frequency' ω_a) is directly proportional to the anomalous portion of the magnetic moment:

$$a_\mu = \frac{\omega_a m_\mu}{eB} \tag{1.16}$$

For a pure Dirac particle, $g = 2$ and $\omega_a = 0$. A measurement of ω_a, as opposed to ω_s, is directly sensitive to the anomalous portion of the magnetic moment. Since $g_\mu - 2 \approx {}^{g_\mu}/_{850}$, any relative uncertainties on the measurement are correspondingly reduced by a factor of 850. From this fact, three orders of magnitude in experimental precision are gained entirely for free.

In the previous section, it was stated that the highest energy decay positrons are emitted preferentially in the direction of the muon's spin vector $\vec{s}$. The angle of the spin vector with the momentum vector ($\vec{p}$) of the μ^+ will precess with frequency ω_a. Likewise, the shape of the observed (Lorentz boosted) positron energy spectrum will also oscillate with ω_a. An illustration of this can be seen in Figure 1.3.

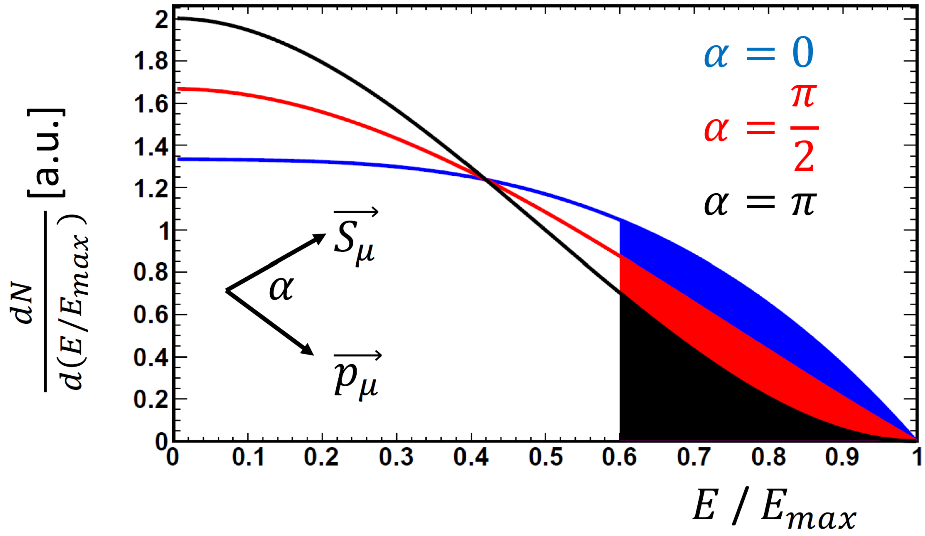

Figure 1.3: The energy spectrum of the decay positrons in the lab frame is distorted by the oscillation of the muon spin vector ($\vec{s}_\mu$) relative to the momentum vector ($\vec{p}_\mu$) with frequency ω_a. Here, the energy spectrum corresponding to three different phases of the ω_a oscillation are shown. Counting the positrons above some energy threshold (shown pictorially by the shaded region) yields a quantity which is $\propto \omega_a$. Reproduced from [6].

1.2.2.1 Boosted Muons: Fit Function and Associated Error

The ultimate statistical precision of a measurement of the anomalous magnetic moment can be calculated by examining the fitting procedure used to analyze the data. The positrons measured from such boosted muon decays are described by the following functional form:

$$N(t) = N_0 e^{-t/\tau_a} \left[1 + A\cos\left(\omega_a t + \phi_a\right)\right] \tag{1.17}$$

where N_0 is an overall normalization factor, τ_a is the effective muon lifetime[7], A is the $g-2$ asymmetry[8], ϕ_a is the $g-2$ phase, and ω_a is the anomalous precession frequency. Following the argument in reference [11][9], in a general storage ring experiment the observed positron counts can be histogrammed vs. time ($N_{\mathrm{obs}}(t)$) and fit to Equation (1.17). This is done by minimizing the χ^2 for the function:

$$\chi^2 = \sum_{i=1}^{n} \left[\frac{N_{th}(\vec{\alpha}, t_i) - N_{obs}(ti)}{\sigma(t_i)}\right]^2 \tag{1.18}$$

for a histogram with n bins (each centered at t_i) and fit parameters $\vec{\alpha} = \{\alpha_0,\ \alpha_1,\ ...\}$. Here, $N_{th}(\vec{\alpha}, t_i)$ represents the form given in Equation (1.17) evaluated with a given set of parameters. Many algorithms have been developed to vary the parameters $\vec{\alpha}$ in order to arrive at the minimum value of the χ^2 (the so-called 'best' fit). Poisson statistics where $\sigma(t_i) \approx \sqrt{N_{\mathrm{obs}}(t_i)}$ are assumed. The general form of the variance is:

$$\langle \alpha_i \alpha_j \rangle = \mathbf{S}_{ij}^{-1}, \tag{1.19}$$

$$\tag{1.20}$$

---

[7] This 'lifetime' also incorporates any non-physics effects which might cause the muons to 'disappear' from the measurement. For instance, scattering off of physical material might cause τ_a to not be exactly consistent with $\gamma\tau_\mu$ (see Section 5.3.8)

[8] The asymmetry encodes the degree of correlation between the muon spin and its momentum. Its value is influenced by many factors (the initial beam polarization, detector acceptance effects, energy thresholds, etc.).

[9] This reference refers the reader to 'any decent book on error analysis', for which the author suggests [12].

where:

$$S = \frac{1}{2}\frac{\partial^2 \chi^2}{\partial \alpha_i \partial \alpha_j} \tag{1.21}$$

is evaluated at the $\vec{\alpha}$ that minimizes χ^2. For Equation (1.17):

$$\frac{1}{2}\frac{\partial^2 \chi^2}{\partial \alpha_i \partial \alpha_j} \approx \sum_{i=1}^{n} \frac{1}{\sigma^2}\frac{\partial N_{th}}{\partial \alpha_j}\frac{\partial N_{th}}{\partial \alpha_k}.$$

In the $g-2$ fitting procedure the only parameter that is significantly correlated with ω_a is ϕ_a, and so the error on ω_a can be effectively evaluated by examining the two-parameter minimization:

$$S^{-1}_{\text{2-Param}} = \begin{bmatrix} \langle \delta\omega_a \rangle^2 & \langle \delta\omega_a \phi_a \rangle \\ \langle \delta\omega_a \phi_a \rangle & \langle \delta\phi_a \rangle^2 \end{bmatrix} = \begin{bmatrix} \frac{1}{2}\frac{\partial^2\chi^2}{\partial\omega_a^2} & \frac{1}{2}\frac{\partial^2\chi^2}{\partial\omega_a\partial\phi_a} \\ \frac{1}{2}\frac{\partial^2\chi^2}{\partial\omega_a\partial\phi_a} & \frac{1}{2}\frac{\partial^2\chi^2}{\partial\phi_a^2} \end{bmatrix}^{-1} \tag{1.22}$$

Evaluating these partial derivatives and solving for $\delta\omega_a$, the fractional error on ω_a is:

$$\frac{\delta\omega_a}{\omega_a} = \frac{1}{\omega_a}\left[\frac{\frac{\partial^2\chi^2}{\partial\phi_a^2}}{\frac{1}{2}\frac{\partial^2\chi^2}{\partial\omega_a^2}\frac{1}{2}\frac{\partial^2\chi^2}{\partial\phi_a^2} - \frac{1}{2}\frac{\partial^2\chi^2}{\partial\omega_a\partial\phi_a}\frac{1}{2}\frac{\partial^2\chi^2}{\partial\omega_a\partial\phi_a}}\right]^{1/2} \tag{1.23}$$

$$\approx \frac{1}{\omega_a}\frac{\sqrt{2}}{A\tau\sqrt{N}}, \tag{1.24}$$

where $N \equiv \int_0^\infty N_0 e^{-t/\tau} dt = N_0\tau$. The uncertainty on the extraction of ω_a can thus be minimized by increasing any of the parameters in the denominator. This relation relation shows that (to first order) storing as many muons as possible ($N \uparrow$), with as high a momentum as possible ($\tau = \gamma\tau_\mu \uparrow$), and with as high a degree of polarization as possible ($A \uparrow$) will yield the most precise measurement of ω_a.

If one were to integrate over all decay positron energies, the $g-2$ signal would vanish. This motivates putting an energy threshold on any analysis, and from inspection of Equation (1.23) it can be seen that the proper choice is the threshold at which the integrated NA^2 is maximized[10]. This is the 'figure of merit' for the $g-2$ experiment. This is discussed further in Section 5.2.4.

---

[10] For a fixed value of τ

Of some note is the fact that the factor of $\sqrt{2}$ in the numerator of Equation (1.24) is only present because ϕ_a is a free parameter in the fit. Were this quantity to be known a-priori, or be able to be measured independent of ω_a, then the runtime of the $g-2$ experiment could be reduced by a factor of two for the same precision [11, 13].

1.2.3 Precise Extraction of the Magnetic Field

Measuring ω_a alone is not enough for an accurate measurement of a_μ. From Equation (1.16), it can be seen that a measurement of the magnetic field to equal or better precision is also required. Proton Nuclear Magnetic Resonance (NMR) techniques allow for such a measurement to be performed with great precision. The value of the magnetic field in a proton NMR measurement given by:

$$B = \omega_p \frac{2m_p}{eg_p}, \tag{1.25}$$

where ω_p is the precession frequency of the proton in the external field, m_p/g_p are the mass and gyromagnetic ratio of the proton respectively. The application of this technique means that the $g-2$ experiment can be most accurately thought of as a co-magnetometer experiment, where two measurements of the magnetic field — one using protons and one using muons — are compared and the value of a_μ is extracted from that comparison. The results are therefore often expressed in terms of the ratio:

$$\mathcal{R} \equiv \frac{\omega_a}{\omega_p}, \tag{1.26}$$

which is related to a_μ through various constants:

$$\begin{aligned} a_\mu &= \frac{\omega_a m_\mu}{eB} \\ &= \frac{\omega_a m_\mu}{e}\left(\frac{eg_p}{2m_p\omega_p}\right) \\ &= \mathcal{R}\,\frac{m_\mu g_p}{2m_p}. \end{aligned} \tag{1.27}$$

The exact values of these constants used to extract a_μ are given in Section 3.7. Further details regarding the magnetic field measurements for the E989 $g-2$ experiment are given in Section 3.2.

1.2.4 Electric Focusing and the 'Magic' Momentum

Holding muons in a magnetic field for an extended period of time and allowing them to precess until they decay is crucial for a high statistics measurement of ω_a. Some early muon $g-2$ experiments at CERN (the so-called CERN-I and CERN-II experiments) were able to perform the experiment in a purely magnetic environment [14]. These experiments utilized a magnetic field gradient to confine muons vertically while they precessed in the horizontal plane. This technique by definition required that the magnetic field be non-uniform, and therefore the path that any individual muon took in such a field would alter its individual spin precession. Uncertainties on the knowledge of the field gradients and the paths that muons took through this distorted field dominated these experiments.

If instead, the magnetic field is made uniform and an electric quadrupole field is used to provide vertical focusing then this uncertainty disappears. However, the introduction of the electric field in the lab frame modifies the precession equations given in the previous sections:

$$\left|\frac{d\vec{p}}{dt}\right| \equiv \omega_c = \frac{e}{mc}\left(\frac{\vec{B}_{\text{lab}}}{\gamma} - \frac{\gamma}{\gamma^2+1}\vec{\beta}\times\frac{\vec{E}_{\text{lab}}}{c}\right), \tag{1.28}$$

and

$$\begin{aligned}\frac{d\vec{s}}{dt}_{\text{rest}} &= \vec{\mu}\times\vec{B}_{\text{rest}} \\ &= \vec{\mu}\times\left[\vec{B}_{\text{lab}} - \vec{\beta}\times\vec{E}_{\text{lab}} - \frac{\gamma}{\gamma+1}\vec{\beta}\left(\vec{\beta}\cdot\vec{B}_{\text{lab}}\right)\right].\end{aligned} \tag{1.29}$$

where the substitution on the second line is a Lorentz transform from the rest frame of the muon to the lab frame[11]. From here onward, it is assumed any $\vec{B}$ or $\vec{E}$ without a subscript refers to the fields in the lab frame. The Thomas precession is similarly altered by the electric field:

$$\frac{d\vec{s}}{dt}_{\text{lab}} = \frac{d\vec{s}}{dt}_{\text{rest}} + \vec{\omega}_T\times\vec{s} \tag{1.30}$$

---

[11] Jackson 11.149 [2]

$$\vec{\omega}_T = \left(\frac{\gamma^2}{1+\gamma}\right)\frac{d\vec{\beta}}{dt}\times\vec{\beta} \tag{1.31}$$

$$\frac{d\vec{\beta}}{dt} = \frac{e}{\gamma mc}\left(\vec{E}+\vec{\beta}\times\vec{B}-(\vec{\beta}\cdot\vec{E})\vec{\beta}\right). \tag{1.32}$$

Substituting[12] Equations (1.31) and (1.32) into Equation (1.30) and rearranging:

$$\begin{aligned}\frac{d\vec{s}}{dt} &= \frac{e}{mc}\vec{s}\times\left[\left(\frac{g-2}{2}+\frac{1}{\gamma}\right)\vec{B}-\frac{g-2}{2}\frac{\gamma}{\gamma+1}(\vec{\beta}\cdot\vec{B})\vec{\beta}-\left(\frac{g-2}{2}+\frac{1}{\gamma+1}\right)\vec{\beta}\times\vec{E}\right]\\ &= \frac{e}{mc}\vec{s}\times\left[\left(a_\mu+\frac{1}{\gamma}\right)\vec{B}-a_\mu\frac{\gamma}{\gamma+1}(\vec{\beta}\cdot\vec{B})\vec{\beta}-\left(a_\mu+\frac{1}{\gamma+1}\right)\vec{\beta}\times\vec{E}\right], \end{aligned}\tag{1.33}$$

Taking the difference between the forms of the spin precession and cyclotron frequencies in Equations (1.28) and (1.33) yields[13]:

$$\begin{aligned}\omega_a \equiv \omega_s-\omega_c &= \left|\frac{d\vec{s}}{dt}\right|-\left|\frac{d\vec{p}}{dt}\right|\\ &= \frac{e}{mc}\left[a_\mu\vec{B}-a_\mu\frac{\gamma}{\gamma+1}(\vec{\beta}\cdot\vec{B})\vec{\beta}-\left(a_\mu-\frac{1}{\gamma^2+1}\right)(\vec{\beta}\times\vec{E})\right]. \end{aligned}\tag{1.34}$$

The first term remains the same as it was in the magnetic-field-only formalism. However, in this case the factors of γ have not yet entirely disappeared. The first term can be accounted for by designing an experiment which minimizes any motion of the muons parallel to the magnetic field ($\vec{\beta}\cdot\vec{B}\to 0$). The second term can be cancelled with a particular choice of momentum such that:

$$\gamma = \sqrt{\frac{1}{a_\mu}-1} \equiv \gamma_0 \approx 29.3. \tag{1.35}$$

At this 'magic γ', the prefactor of the $\vec{\beta}\times\vec{E}$ term goes to zero. The corresponding 'magic momentum' (p_0) is $3.094\,\mathrm{GeV}/c$. Operating at this momentum yields a time dilated muon lifetime of $\gamma_0\tau_\mu = 64.4\,\mu\mathrm{s}$, which also benefits the extraction of ω_a (as seen from Equation (1.24)). Small corrections are required to account for the residual effects of these terms, as detailed in Section 3.6.3, but to

---

[12] See Jackson 1.143 to 1.170 for a more thorough derivation [2].

[13] In this substitution the identity:

$$\frac{1}{\gamma+1}-\frac{\gamma}{\gamma^2+1}=\frac{-1}{\gamma^2-1}$$

is used [2].

first order all of the factors of γ can once again be neglected.

1.2.5 Summary

To reiterate, in order for a high precision measurement of a_μ to be successful, it is required that:

- Pions, decaying via the weak interaction, yield a source of polarized muons;
- Parity violation imprints the direction of the muon spin vector onto the decay positron energy, thus making the decay of the muon 'self-analyzing';
- Storage ring measurements be sensitive to '$g-2$' and not 'g';
- The magnetic field of such a storage ring be able to be measured precisely using NMR; and
- Operating at the 'magic γ' cancels the $E \times B$ terms in Equation (1.34).

These have been colloquially referred to as the 'miracles' of $g-2$ (with only a small degree of hyperbole).

In order for this measurement to be *useful* as a test of the standard model, one additional 'miracle' is required: the value of a_μ must be able to be predicted to high precision. This is indeed the case and, as will be shown in Chapter 2, the theoretical value can be predicted in the standard model to the same order of precision as the experimental results.

1.3 Current Status of Experimental Results

The Fermilab Muon $g-2$ experiment has published the results from the Run-1 [16] and the Run-2/3 [15, 17] datasets (see Figure 1.4b). This has reduced the uncertainty on the world average measurement of the anomalous magnetic moment of the muon to 190 parts-per-billion (ppb). The current world average evaluation of a_μ is:

$$a_\mu = 116,592,059(22) \times 10^{-11} \tag{1.36}$$

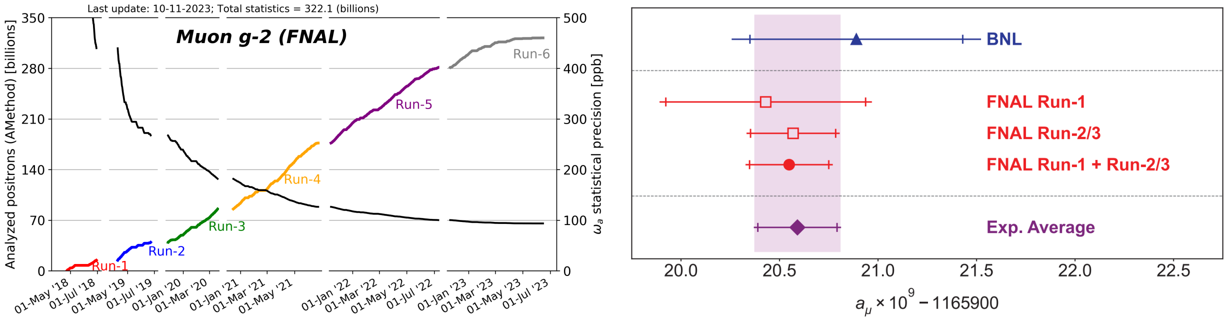

(a) Image credit P. Girotti.

(b) Reproduced from [15].

Figure 1.4: (a) Accumulated statistics and corresponding estimate of the final uncertainty. (b) Current status of a_μ^{exp}. The values on this plot include only ≈ 27% of the total accumulated statistics at FNAL.

When compared to the 2020 theoretical evaluation of a_μ [1, 18–37]:

$$\Delta a_\mu = -249(48) \times 10^{-11} > 5\sigma. \tag{1.37}$$

While this may be an exciting[14] threshold to meet, any celebrations or conclusions are on hold while the updated evaluation of the theoretical calculation is in progress (see Section 2.2).

1.4 Outlook

1.4.1 J-PARC E34

Hearkening back to an earlier era of $g-2$ experiments, the E34 experiment at J-PARC aims to measure the value of a_μ in a purely magnetic environment by using an ultra cool muon beam. This beam is formed by first creating muonium atoms, which are then re-ionized and the muons accelerated to 300 MeV/c. This produces a pencil-like beam with very little need for vertical focusing, and so trapping muons with only weak magnetic focusing is achievable. The experiment seeks to begin taking data by 2028 and publish an evaluation of a_μ with similar precision to the FNAL Run-1 results after two years of data taking. This independent measurement of a_μ using a novel method, while not competitive with the latest Fermilab results in terms of statistical power,

---

[14] 🍾

will yield increased confidence in the experimental result. A recent summary can be found in [38].

1.4.2 Fermilab E989

The datasets published by the Fermilab Muon $g-2$ Experiment thus far amount to only $\approx 27\%$ of the total data taken. Analysis of the remaining data (Runs 4-6) is in progress and results from these datasets are expected to be published by early 2025. Portions of this analysis are presented in Chapters 5 to 7. The addition of this data is expected to bring the statistical uncertainty on a_μ below 100 ppb for the first time (see Figure 1.4a). Based on the collaborations current understanding of the data and the associated systematic uncertainties, it is likely that the experiment will achieve or better its proposed goal of 140 ppb total uncertainty on a_μ.

Chapter 2

Muon $g - 2$ in the Standard Model

As the E989 Muon $g - 2$ collaboration was being formed, the 'Muon $g - 2$ Theory Initiative'[1] (TI) was also convened. The goal of the Theory Initiative is to achieve a theoretical prediction for the value of a_μ with an uncertainty on the same order as the projected experimental precision. Only through the combination of both efforts is a precision test of the standard model possible. This chapter describes the latest official status of the theoretical prediction from the Theory Initiative, some of the updates since the publication of that result in 2020, and the expectations for the theory going forward.

The matrix element for the generic interaction between a lepton and a photon (representing an external magnetic field) shown in Figure 2.1 is [3]:

$$i\mathcal{M}^\mu = (-ie)\bar{u}(q_2)\left[F_1\left(\frac{p^2}{m^2}\right)\gamma^\mu + \frac{i\sigma^{\mu\nu}}{2m}p_\nu F_2\left(\frac{p^2}{m^2}\right)\right]u(q_1), \tag{2.1}$$

where F_1 and F_2 are independent form factors which describe the interaction, $\bar{u}(q_2)$ and $u(q_1)$ are Dirac spinors, $\sigma^{\mu\nu} \equiv \frac{i}{2}\left[\gamma^\mu, \gamma^\nu\right]$, γ^μ are the Dirac matrices, $p^\mu \equiv q_2^\mu - q_1^\mu$ is the momentum exchange with the external field, and m is the mass of the particle (in this case the muon). Inspection of this relation shows that only the second term has any dependence on the particles spin. It is therefore this second term which produces the magnetic moment. From this relation, and taking

---

[1] `https://muon-gm2-theory.illinois.edu/`

the non-relativistic limit where ${}^{p^2}\!/\!{}_{m^2} \to 0$, it can be derived[2] [3]:

$$g = 2 + 2F_2(0), \tag{2.2}$$

and therefore:

$$a = F_2(0). \tag{2.3}$$

The interaction involving F_2 has the structure of a dimension-5 operator, and thus must be 0 at tree level. The anomalous portion of the magnetic moment therefore can only arise from loop corrections to the bare vertex in Figure 2.1. The value of a_μ in the standard model (a_μ^{SM}) can be calculated by summing the contributions to $F_2(0)$ from different loop diagrams.

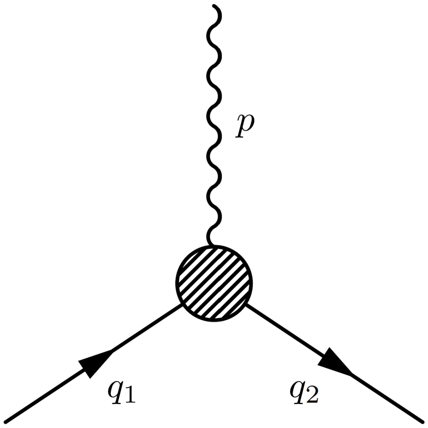

Figure 2.1: A Feynman diagram representing a generic interaction between a fermion and an external photon.

2.1 Latest Muon $g - 2$ Theory Initiative Consensus

In 2020, the Theory Initiative released a white paper which detailed their most up to date evaluation of the theoretical prediction of a_μ [1]. This white paper (WP) collated results from many different sources, and the initiative worked diligently to combine each of them in a way which took into

---

[2] This derivation can be found in most (if not all) introductory QFT textbooks. For instance, see Section 17.1 (pg. 315-318) of reference [3].

account all correlated and uncorrelated uncertainties. A summary of the results of this white paper can be seen in Table 2.1. By convention, the calculation is broken up into four parts which are evaluated separately: quantum electrodynamics diagrams (QED), electroweak interactions (EW), and two terms involving hadronic contributions. These are the hadronic vacuum polarization (HVP) and the hadronic light-by-light sets of diagrams (HLbL). As of the publication of the white paper, the Theory Initiative evaluation of a_μ^{SM} was [1, 18–37]:

$$\begin{aligned} a_\mu^{\mathrm{SM}} &= a_\mu^{\mathrm{QED}} + a_\mu^{\mathrm{EW}} + a_\mu^{\mathrm{HVP}} + a_\mu^{\mathrm{HLbL}} \\ &= 116\,591\,810(43) \times 10^{-11}\,. \end{aligned} \tag{2.4}$$

Each of these contributions, as given in the 2020 white paper, is described shortly below.

Contribution	Order	Value ($\times 10^{-11}$)	Uncertainty ($\times 10^{-11}$)	Uncertainty (ppb)	Method of Calculation	Status
QED	5 loops α^5	116,584,718.93	0.1	0.9	Perturbation Theory	✅
EW	2 loops	153.6	1	8.6	Perturbation Theory Effective Field Theory	✅
HVP	NNLO α^2	6,845	40	343	Dispersive Methods Lattice QCD	🚩
HLbL	NLO α^3	92	18	154	Dispersive Methods Lattice QCD	📝
Total	—	**116,591,810**	**43**	**368**	—	—

Table 2.1: Latest evaluation by the Theory Initiative of the individual contributions to a_μ, from 2020 [1], with added commentary from the author on developments since then: The EW and QED contributions are stable, updates to the HLbL contributions are in progress (with no major changes to the white paper value expected), and updates to the HVP are in progress (with the potential for a major change in the value from white paper). The total is calculated by the Theory Initiative, taking into account some correlation between values.

2.1.1 QED

The largest contribution to the anomalous magnetic moment of the muon in the standard model comes from quantum electrodynamics (QED) loops involving only photons and leptons: a_μ^{QED}. This contribution can be further divided up into a mass-dependant and a mass-independent terms. The former is identical for all leptons, while the latter is specific to the muon. Following the notation

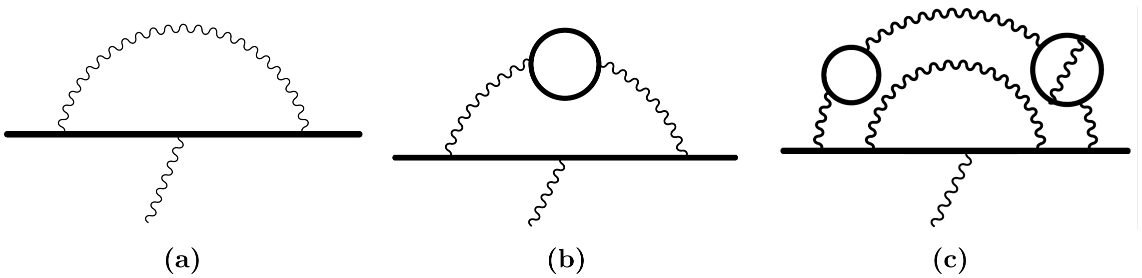

Figure 2.2: Example diagrams contributing to the QED portion of a_μ^{SM} (a_μ^{QED}) at (a) 1st, (b) 4th, and (c) 10th order. Solid lines in these diagrams represent leptons. Reproduced from [1].

in [1]:

$$a_\mu^{\mathrm{QED}} = A_1 + A_2\left(\frac{m_\mu}{m_e}\right) + A_2\left(\frac{m_\mu}{m_\tau}\right) + A_3\left(\frac{m_\mu}{m_e}, \frac{m_\mu}{m_\tau}\right), \tag{2.5}$$

where each of the A_i can be expanded using perturbation theory:

$$A_i = \sum_{n=0}^{\infty} \left(\frac{\alpha}{\pi}\right)^n A_i^{(2n)}. \tag{2.6}$$

A_1 is mass independent, A_2 depends only on the ratio of masses of two generations of leptons, and A_3 depends on all three generations. QED is fully renormalizable ($\alpha \approx 1/137 \ll 1$) and therefore each of these $A_i^{(2n)}$ can be calculated using Feynman techniques.

The first calculations of lepton anomalous magnetic moments were motivated by measurements of Zeeman splitting in atomic spectra [39, 40], which continually yielded results that were inconsistent with a pure Dirac electron ($g_e = 2$). The first order QED correction was calculated by Julian Schwinger in 1947. By analyzing the 1st order radiative correction[3] shown in Figure 2.2a, Schwinger found [41]:

$$g = 2\left(1 + \frac{\alpha}{\pi} + \mathcal{O}(\alpha^2)\right). \tag{2.7}$$

This correction factor matched results from the atomic experiments, proving to be an early success of QED. In 1959, measurements of g_μ at Nevis (described in Section 1.2.2) yielded a result consistent with Schwinger's prediction for the muon as well [9].

---

[3] Again, this derivation is present in most QFT textbooks. See Section 17.2 of reference [3].

In the notation of Equation (2.6), the Schwinger calculation is equivalent to $A_1^{(2)} = 1/2$. The mass independent portion of a_μ^{QED} has been calculated up to 6th order completely analytically and 8th order semi-analytically [41–45]. The 10th order contribution, involving 12,672 Feynman diagrams, has been calculated numerically [19].

The mass dependent portion of a_μ^{QED} involves diagrams with closed fermion loops (for instance, Figure 2.2b). Lepton loops exclusively are evaluated here; hadronic contributions are considered later as part of a_μ^{HVP} (see Section 2.1.3). Mass dependent terms appear at 4th order in the perturbation theory expansion. These have been fully calculated out to 10th order, and leading 12th order terms have been checked to ensure that any contribution would be below the target uncertainty goal for the Theory Initiative [1, 18]. An example 10th order diagram can be seen in Figure 2.2c.

All of the calculations above are expressed in terms of the fine structure constant α. It should be noted that there are two independent evaluations of the value of α which are considered in the white paper, one taken from atom interferometry experiments involving Cs or Rb atoms [46, 47] and the other extracted from measurements of g_e [48]. These can differ by 3.9σ [48], but the differences between a_μ^{QED} evaluated from each of these α values is $\mathcal{O}\left(0.1 \times 10^{-11}\right)$. Taking the value of α from the Cs experiments yields a QED contribution of [18, 19]:

$$a_\mu^{\mathrm{QED}}\left(\alpha_{\mathrm{Cs}}\right) = 116584718.931(104) \times 10^{-11}. \tag{2.8}$$

2.1.2 EW

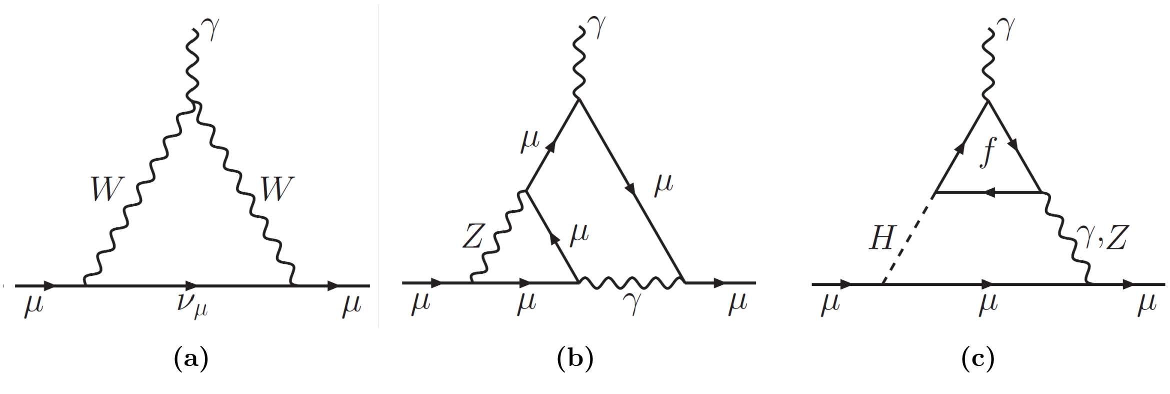

(a) **(b)** **(c)**

Figure 2.3: Example diagrams contributing to the electroweak portion of a_μ^{SM}: a_μ^{EW}. Reproduced from [1].

It is a natural extension from QED to next evaluate electroweak contributions. These bear great similarity to the QED results, with the addition of loops involving one or more $W^{\pm}$, Z, or H bosons (see Figure 2.3). These contributions are in general quite small, being suppressed by powers of $m_{\mu}/m_{\mathrm{W,Z,H}}$. This contribution also serves as the 'catch-all' term for those diagrams which do not neatly fall into any of the other categories. For instance, quark loops can enter diagrams like Figure 2.3c.

Contributions of this form have been calculated fully using an effective field theory approach for 1 and 2-loop diagrams, and leading order contributions from 3-loop diagrams have been included. These calculations yield [20, 21]:

$$a_{\mu}^{\mathrm{EW}} = 153.6(1.0) \times 10^{-11}. \tag{2.9}$$

2.1.3 Hadronic Vacuum Polarization (HVP)

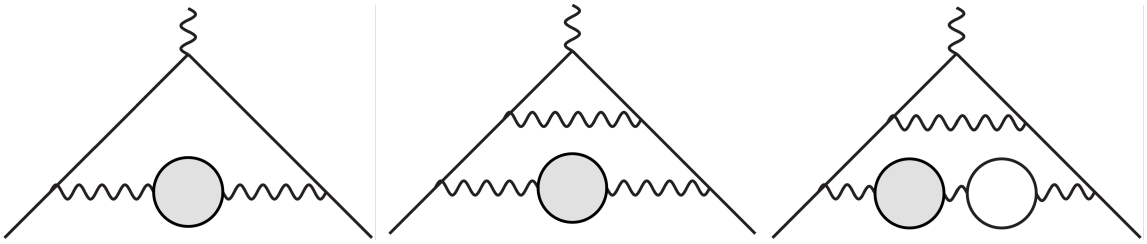

(a) LO **(b)** NLO **(c)** NNLO

Figure 2.4: Example diagrams contributing to the HVP portion of a_{μ}^{SM} (a_{μ}^{HVP}) at the three orders considered as part of the white paper. Adapted from [1]. The filled bubbles indicate hadronic loops while the unfilled bubbles indicate lepton loops.

The hadronic vacuum polarization (HVP) contribution to a_{μ} is given by diagrams such as those shown in Figure 2.4, involving hadronic pair production in the vacuum. This is the largest hadronic modification of a_{μ}^{SM}, and also the source of the largest uncertainty in the final evaluation of the total standard model prediction. Because of the hadronic physics involved, perturbation theory can no longer be employed to calculate the HVP contribution. Instead, this contribution has been calculated in two ways:

- A data-driven approach relating measured scattering cross-sections in $e^{+}e^{-}$ collisions to a_{μ}^{HVP}.

- Evaluating QCD numerically on a lattice.

The latter approach is extremely computationally intensive, and only in the past few years have lattice evaluations of the HVP contributions with comparable uncertainties to the data-driven approaches become available. No lattice evaluations of a_μ^{HVP} were available with sub-percent precision by the deadline established by the Theory Initiative for inclusion of results in the white paper, and thus the white paper estimate includes only the former technique.

The principle behind data-driven method for the evaluation of a_μ^{HVP}, also called the 'Dispersive' or 'R-Ratio' method, is shown schematically in Figure 2.5. Utilizing principles of analyticity and unitarity, the insertion of an HVP loop in a photon propagator can be related to the cross section of a virtual photon decaying into hadrons [1, 49, 50]. Following the notation from [1], the leading/lowest order (LO) contribution is:

$$a_\mu^{\mathrm{HVP,\ LO}} = \frac{\alpha^2}{3\pi^2}\int_{M_\mu^2}^{\infty}\frac{K(s)}{s}R(s)ds. \tag{2.10}$$

$K(s)$ is a kernel function, which goes roughly as m_μ/s at low energies and varies from ≈ 0.63 to 1 in the integral region. $R(s)$ is the hadronic 'R-Ratio' defined as:

$$R(s) = \frac{\sigma^0(e^+e^- \to \mathrm{hadrons})}{\sigma_{pt}}, \tag{2.11}$$

where $\sigma_{pt} = {}^{4\pi\alpha^2}/_{3s}$, s is the center of mass energy of the system, and the bare cross section σ^0 is the result of the careful combination of many collider measurements. A detailed review of how this combination is done can be found in reference [1]. The results of one such combination of cross section data (dubbed 'KNT19' [23, 51]) can be seen in Figure 2.6.

Because of the factor $K(s)/s$ in the integral, the lowest energy portion of the cross section is weighted most heavily: the low energy $e^+e^- \to \pi^+\pi^-$ cross section therefore contributes $\approx 72\%$ of the magnitude of the total value of $a_\mu^{\mathrm{HVP,\ LO}}$. Unfortunately, this is also where the largest tensions lie in the data. The two most precise measurements of this cross section, coming from the BABAR [1, 52] and KLOE [1, 53–55] experiments, disagree at the level of a few σ. This tension was incorporated as a systematic error in the white paper evaluation of a_μ^{HVP}.

Similar relations are constructed for NLO ('next-to-leading-order') and NNLO ('next-to-next-

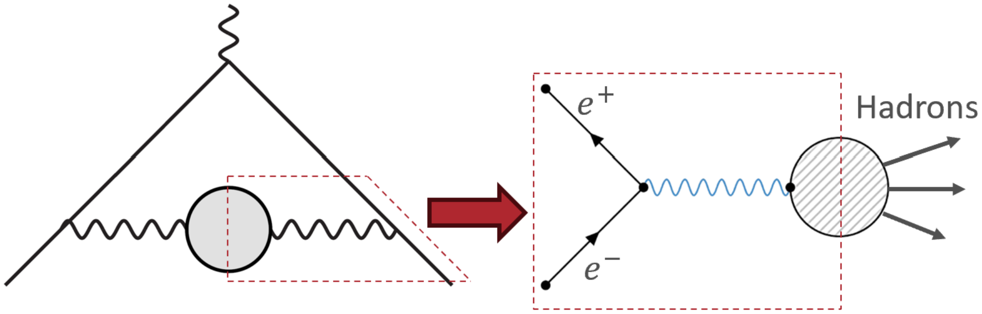

Figure 2.5: Schematic showing how the $a_\mu^{\text{HVP, LO}}$ can be related to scattering cross section measurements.

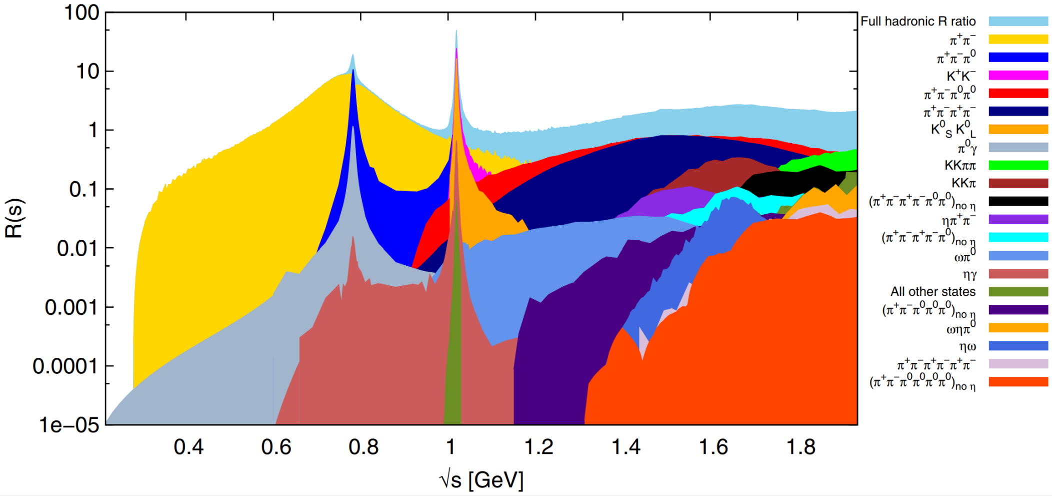

Figure 2.6: Contributions to $R(s)$ broken down by hadronic channel. The $\pi^+\pi^-$ contribution (yellow) is the single largest contribution to $a_\mu^{\text{HVP, LO}}$. Reproduced from [23].

to-leading-order') contributions to a_μ^{HVP} as well. Based on these dispersive inputs, the value of a_μ^{HVP} was determined to be [22–28]:

$$a_\mu^{\mathrm{HVP}}\big|_{\mathrm{WP}} = 6845(40) \times 10^{-11} \tag{2.12}$$

Since the publication of the white paper, new lattice results from the BMW collaboration have provided the first complete sub-percent evaluation of a_μ^{HVP} on the lattice [56]. Since then, many other groups have presented intermediate lattice calculations which agree with the BMW result[4]. These are in significant tension with the data-driven evaluations. New cross section measurements from CMD-3 have also been released, which have raised questions about the inputs to the dispersive approach [57]. While no updated conclusions can yet be drawn, these developments are discussed in detail in Section 2.2. Alternative data-driven evaluations of a_μ^{HVP} are also being developed (see Section 2.3.4).

2.1.4 Hadronic Light by Light (HLBL)

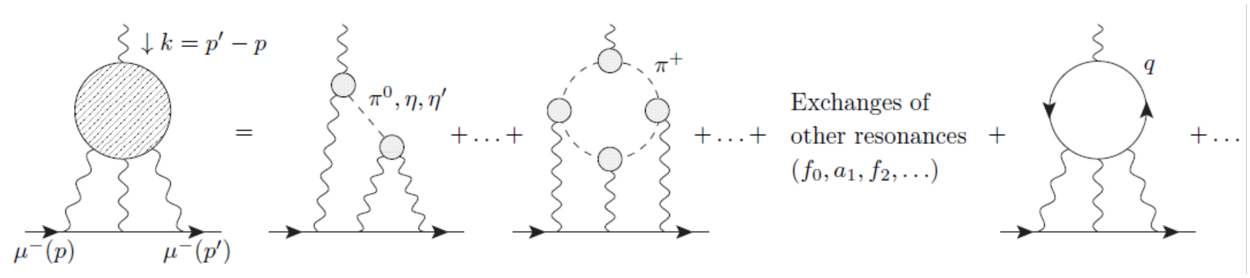

Figure 2.7: Example diagrams contributing to the HLbL portion of a_μ^{SM}: a_μ^{HLbL}. Reproduced from [1].

The final contribution to a_μ^{SM}, the smaller of the two hadronic contributions, is the 'hadronic light by light' (HLBL) set of diagrams. These are the diagrams which follow the general form represented in Figure 2.7, where 3 photons coming off of a hadronic 'blob' mediate the interaction between the muon and the external field. This term was a large source of uncertainty in the theoretical predictions at the time of the BNL experiment. Since that time, new techniques pioneered by the Theory Initiative allowed for the first ever dispersive and high-precision lattice based calcu-

---

[4] Many such results were presented at the Lattice 2023 conference

lations of the HLBL. The data-driven and computational techniques agree nicely in this case[5], and are combined to yield a final result [29–37, 58–63]:

$$a_\mu^{\text{HLbL}} = 92(18) \times 10^{-11} \tag{2.13}$$

This term contributes the second largest contribution to the uncertainty on a_μ^{SM}, about half that of a_μ^{HVP}. Updates to this result are in progress and are discussed briefly in Section 2.3.1.

2.2 Open Questions

A great deal of the work in the Theory Initiative is currently oriented towards understanding the discrepancies in a_μ^{HVP} which have arisen when considering two new results: The publication of the first sub-percent lattice calculation of $a_\mu^{\text{HVP, LO}}$ and the results of new $\pi^+\pi^-$ cross section measurements by the CMD-3 collaboration.

2.2.1 Lattice Calculations of a_μ^{HVP}

Lattice QCD, briefly, involves discretizing spacetime onto a finite grid and evaluating the QCD lagrangian numerically at each point. A basic primer on lattice QCD can be found in reference [64], and a description of the specific techniques used by those evaluating a_μ^{HVP} can be found in reference [1]. The first sub-percent evaluation of $a_\mu^{\text{HVP, LO}}$ using lattice techniques was published in April of 2021, concurrent with the release of the Run-1 Fermilab data [56]. This value is in significant tension with the data-driven evaluations of the same quantity and, if taken in place of the R-Ratio evaluation of $a_\mu^{\text{HVP, LO}}$, reduces the tension between theory and experiment to $< 2\sigma$ (see Figure 2.10).

Lattice calculation uncertainties are dominated by two types of extrapolations: extrapolating from a finite calculation volume to free space (long distance), and extrapolating from a finite lattice spacing to the continuum (short distance). Each of these extrapolations requires a large number of samples with different lattice spacings to be generated, which each in turn require a great deal

---

[5] It should be noted that the lattice uncertainties are approximately twice the size of the data-driven uncertainties in the white paper.

of computation time and resources to complete. To allow for intermediate comparisons while those calculations are in progress, a system was devised to divide the lattice results into three ‘euclidean time windows’: short distance, intermediate distance, and long distance. The windows are shown schematically in Figure 2.8a. The intermediate window (black) is the most isolated from either of those sources of uncertainty, and many independent groups have been able to make complete calculations of the contribution to a_μ^{HVP} in this window. One comparison of these calculations, considering only contributions from the light quarks in the intermediate window, is reproduced in in Figure 2.8b. The independent calculations agree well in this region and show a significant tension with the same quantity calculated using data-driven techniques [65]. These initial comparisons are promising, and more updates are expected throughout this coming year.

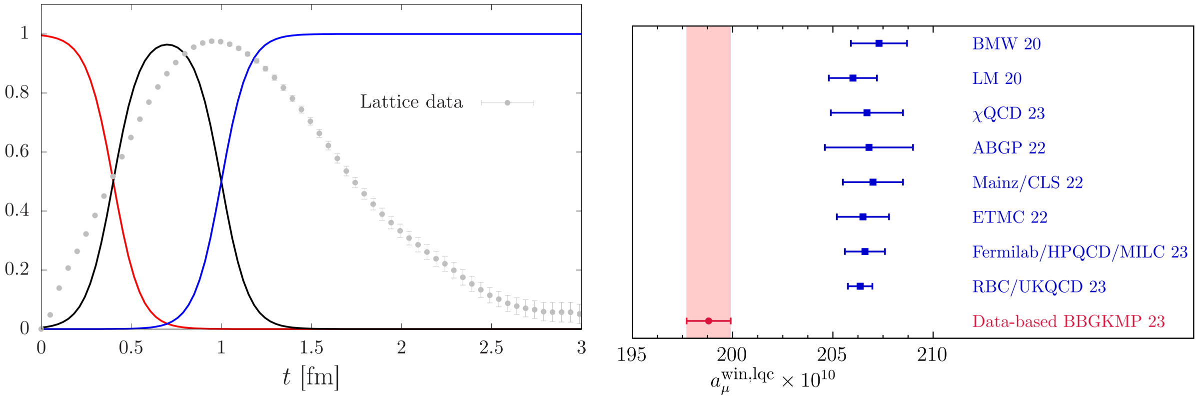

(a) Reproduced from [66].

(b) Reproduced from [65].

Figure 2.8: (a) The three euclidean time windows used in lattice comparisons. (b) Light quark connected contribution to the intermediate window for various lattice groups and the R-ratio. Significant tensions can be seen in this region between lattice (blue) and data-driven (red) evaluations of a_μ^{HVP} in this window.

2.2.2 CMD-3 Results and Their Implications

Before the publication of the 2020 White Paper, the main area of tension in the HVP R-Ratio data was between the KLOE and BABAR determinations of the $\pi^+\pi^-$ cross section. The discrepancies between these two experiments were incorporated as a systematic error in the overall value of a_μ^{HVP}, but the cause remains unknown. This tension can be seen in Figure 2.9a and is described in detail in reference [1].

In February 2023, new results from the CMD-3 experiment at Novosibirsk were released which also disagreed with previous cross section measurements [57]. These results, while still in pre-print form as of the writing of this thesis, have undergone much scrutiny. The Theory Initiative alone has held two seminar sessions dedicated to understanding where the discrepancies between this updated result and previous results may have arisen from[6]. As yet, no 'smoking guns' have been found.

Regardless of the cause, the a preliminary evaluation of the effect of the CMD-3 results on a_μ^{HVP} can be seen in Figures 2.9 and 2.10. The CMD-3 cross sections, if taken by themselves, push the value of a_μ^{HVP} much closer to the experimental value and the one predicted by the lattice calculations. These preliminary results illustrate the scale of the shift between this single measurement and the average of all others.

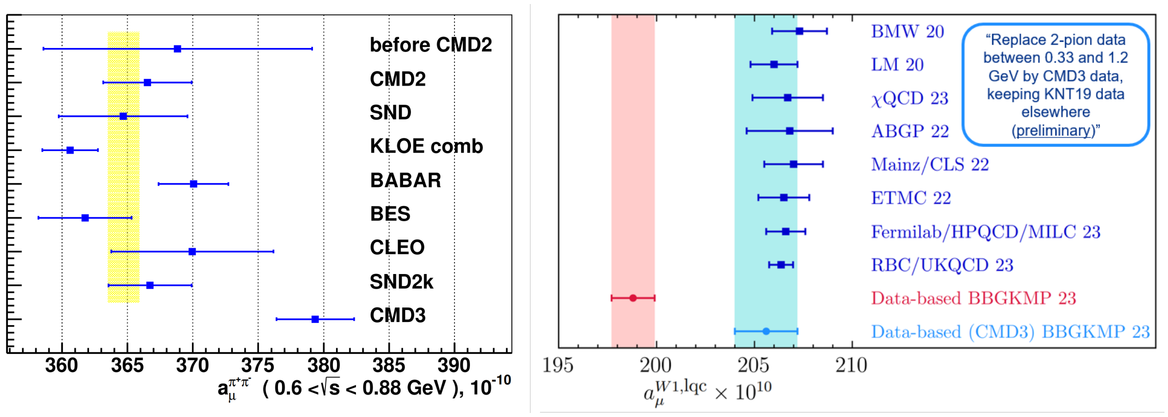

"Replace 2-pion data between 0.33 and 1.2 GeV by CMD3 data, keeping KNT19 data elsewhere (preliminary)"

(a) Reproduced from [57].

(b) Reproduced from [67].

Figure 2.9: (a) The contribution to $a_\mu^{\pi^+\pi^-}$ in the limited energy range $0.6 < \sqrt{s} < 0.88$ GeV. The tension between CMD-3 and all other measurements can clearly be seen. (b) A (*very preliminary*) estimate of the effect of the CMD-3 data on the comparison in Figure 2.8b. The data from CMD-3 seems to better agree with the lattice calculation results.

---

[6] The agendas of these sessions can be found here and here. Discussions also took place at the 6th Annual Theory Initiative Workshop.

2.3 Theoretical Outlook

The Muon $g-2$ Theory Initiative plans to publish an updated value of a_μ^{SM} in late 2024. No significant changes[7] are expected in the values of a_μ^{QED} nor a_μ^{EW}. This evaluation will be the first to include lattice results in a_μ^{HVP}, which have the potential to greatly alter the value of a_μ^{SM} and decrease the tension with a_μ^{exp}. The scale of the potential effect can be seen in Figure 2.10, where two different *preliminary* evaluations for $a_\mu^{\mathrm{HVP,\ LO}}$ are substituted into the white paper result. This evaluation will also include new lattice evaluations of a_μ^{HLbL} (with uncertainties on par with the data driven evaluations).

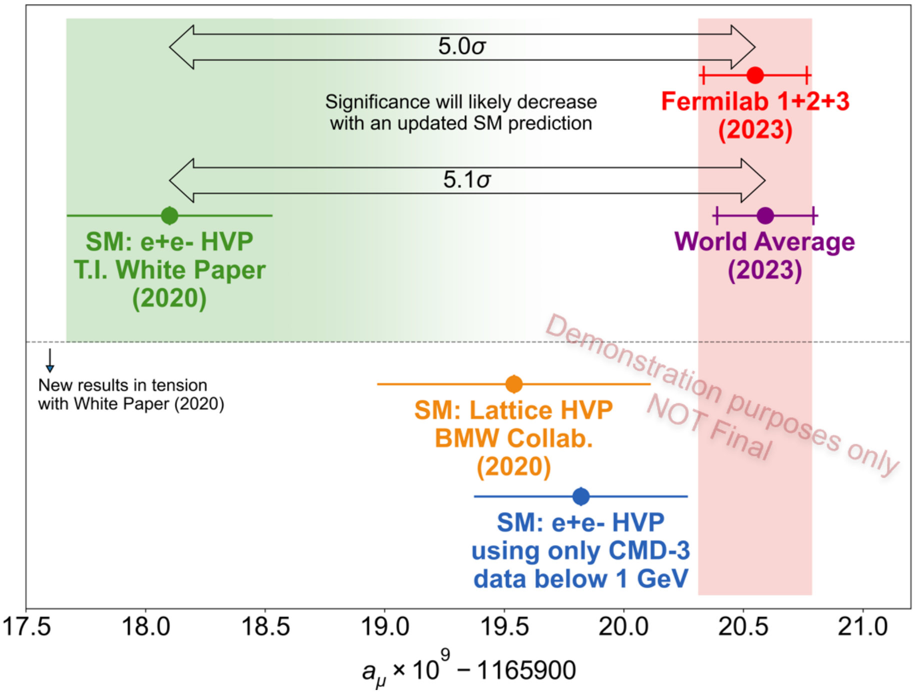

Figure 2.10: Comparison of the experimental value of a_μ (purple, red) vs. a_μ^{SM} for three evaluations of the $a_\mu^{\mathrm{HVP,\ LO}}$ contribution: the 2020 white paper consensus (green), substituting the BMW Lattice QCD evaluation of the HVP (orange), and substituting the CMD-3 $\pi-\pi$ cross section data into the R-Ratio HVP evaluation (blue). The latter two theoretical values should be taken as initial estimates only to show the scale of the effect. Full evaluation of systematic errors has not yet been done. Image credit: A. Keshavarzi.

---

[7] New measurements of α have been published since the 2020 white paper [48], and so the value of α used to evaluated these calculations may slightly change. This will not impact the result appreciably.

2.3.1 HLbL Updates

The uncertainty on the white paper evaluation of a_μ^{HLbL} alone is approximately the same as the total uncertainty on the current experimental value. It is therefore the goal of the Theory Initiative to reduce the uncertainty on this term by a factor of two or more [68, 69]. At the time of the white paper, the lattice uncertainties were about double the uncertainties from the data driven evaluation of a_μ^{HLbL} [1]. Work performed since the publication of the white paper has brought HLbL lattice uncertainties to a level competitive with the data driven evaluations. Two recent lattice evaluations:

$$a_\mu^{\mathrm{HLbL}}\Big|_{\mathrm{Lattice}} = 109.6(15.9) \times 10^{-11} \text{ [70, 71]} \tag{2.14}$$

$$a_\mu^{\mathrm{HLbL}}\Big|_{\mathrm{Lattice}} = 124.7(14.9) \times 10^{-11} \text{ [72]} \tag{2.15}$$

have yielded values which are compatible with the white paper results, albeit with a slightly larger central value. Improvements to these results are underway, and an uncertainty of $\leq 10\%$ on a_μ^{HVP} from both the lattice results and data-driven results is possible on the timescale of a few years [69].

2.3.2 Additional HVP Lattice Results

At the recent Muon $g-2$ Theory Initiative Workshop in September 2023, updates from six or more independent groups were presented (for instance, see the result in Figure 2.8b). Each of these groups is on track to produce an evaluation of $a_\mu^{\mathrm{HVP,\ LO}}$ to be included in the next white paper average. Importantly, mirroring the experiment, these groups have pioneered blinded analysis techniques. This reduces the potential for any bias when performing these calculations and corrections, either towards or away from the experimental results.

2.3.3 Updates to HVP Dispersive Inputs

The white paper dispersive calculations of $a_\mu^{\mathrm{HVP,\ LO}}$ are based on only part of the full dataset measured by KLOE and BABAR. Given the recent interest in these cross sections, renewed efforts have been launched by those respective collaborations to process these datasets to completion. Both collaborations presented updates on ongoing analyses at the 2023 Theory Initiative workshop.

Updates to the various cross sections from other collaborations, such as Belle-II and BES-III, are also planned. For a brief overview, see the official outlook statement on the Theory Initiative website. A 2022 review of the prospects for the prediction of a_μ in the SM can also be found in reference [73].

2.3.4 Additional Data-Driven HVP Evaluations: MUonE, τ Decays

A novel method for a data driven evaluation of a_μ^{HVP} has been proposed by the MUonE collaboration [74]. This method uses a data driven approach to measure $a_\mu^{\text{HVP, LO}}$ in the space-like regime by measuring the $\mu{+}e$ scattering cross section. The timeline of the experimental development currently projects that a 0.3% measurement of $a_\mu^{\text{HVP, LO}}$ is achievable by 2030.

It is also possible to extract a_μ^{HVP} from measurements of semileptonic τ decay at colliders. In the past, large isospin breaking corrections needed to properly interpret the data were not well understood, and so this data was not incorporated into any Theory Initiative evaluations [1]. However, much work has been done to rectify this and the status of such contributions will be re-evaluated as part of the Theory Initiative updated prediction. A recent summary of τ developments can be found in [75].

Chapter 3

The E989 Experiment at Fermilab

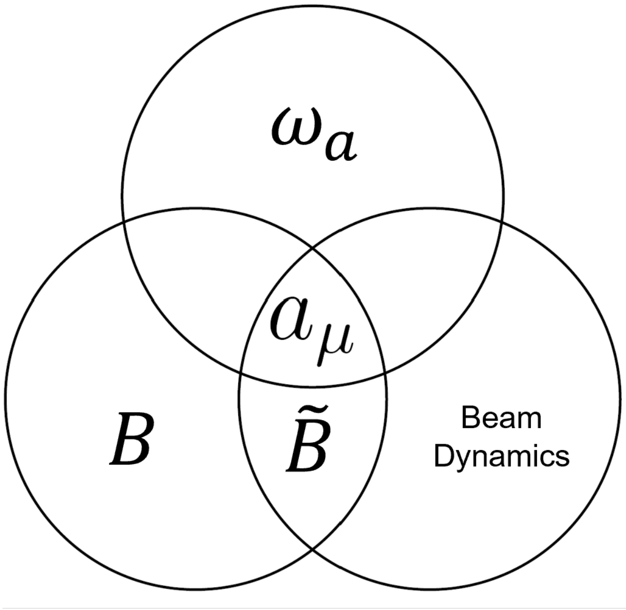

Figure 3.1: The three factors which go into a successful measurement of a_μ: The extraction of ω_a, the precision measurement of the magnetic field B, and the understanding of the dynamical motion of the beam (BD) within the storage ring.

As stated in Chapter 1, a_μ is extracted from the relation:

$$a_\mu = \frac{\omega_a}{B}\frac{m_\mu}{e}. \tag{1.16}$$

The E989 Muon $g-2$ experiment can be divided into three interrelated but distinct sets of measurements (Figure 3.1): the extraction of the anomalous precession frequency of the muon ω_a, the measurements of the magnetic field B, and the reconstruction of the dynamic motion of the stored muon beam (so-called 'beam dynamics' or 'BD'). This last term is not immediately obvious in Equation (1.16), but enters through two categories of effect:

- The muons do not evenly explore the magnetic field of the storage ring, and therefore knowing their average position allows for the proper weighting of the magnetic field. This is described in Section 3.6.2.
- The dynamic motion and momentum content of the beam couples to a number of correction factors to ω_a (Section 3.6.3) and systematic effects (Section 6.4).

The author was involved most heavily in the extraction of ω_a and in the evaluation of some BD related corrections. In this chapter, the apparatus and techniques that go into the measurements of these three quantities are described.

3.1 From Protons to Muons

3.1.1 Muon Production Chain

Figure 3.2 shows the layout of the portion of the Fermilab accelerator complex that creates the polarized muon beam for the $g-2$ experiment. The process begins with a bottle of hydrogen gas. This gas is ionized and p^+ are accelerated to 400 MeV through the Fermilab LINAC, and then up to 8 GeV in the Booster Ring. The high energy proton beam, with a temporal extent of $\approx 1600\,\mathrm{ns}$, is then injected into the recycler ring. This process repeats twice to fill the ring. The stored proton beam is re-shaped into $8 \approx 120\,\mathrm{ns}$ long 'bunches' using 2.5 MHz RF cavities (Figure 3.3a). Each bunch contains $\approx 10^{12}$ p^+. This process reduces the width of each bunch to below the cyclotron period of the $g-2$ storage ring ($T_c = 149\,\mathrm{ns}$), and is therefore critical for creating muon bunches compatible with eventual injection. RF shaping has the side effect of imparting each of the bunches with a characteristic 'W' shape. This shape is propagated through the beamline to the injected muon bunch[1]. Each bunch is extracted one-by-one at a time-averaged rate of $\approx$ 11.4 Hz (see

---

[1] This can be seen when comparing the protons in Figure 3.3b and in the muons later in Figure 3.6b

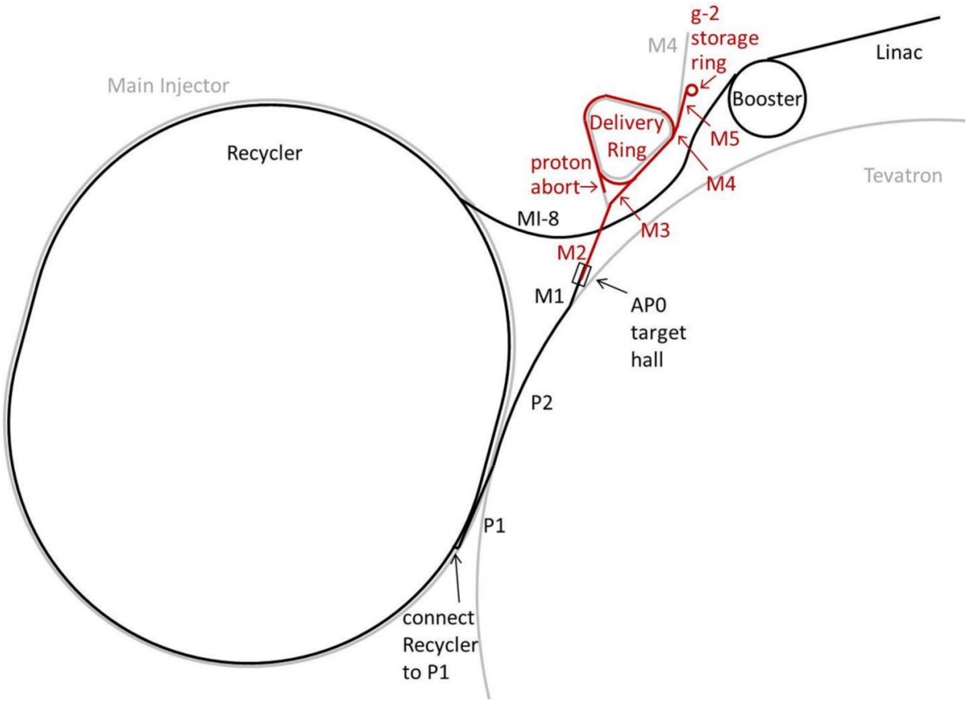

Figure 3.2: Layout of the beamlines at the Fermilab accelerator complex which are relevent for the Muon $g-2$ Experiment. Reproduced from [76].

Figure 3.3c) from the recycler ring along the M1 beamline to the AP0 target hall.

In the target hall, the protons impact an Iconel[2] target and create a shower of secondary particles. Forward going particles are collected as a secondary beam using a lithium lens, and these are then momentum selected using bending magnets at the entrance to the M2/M3 beamline [76]. The momentum of the secondary beam is $3.11\,\mathrm{GeV/c} \pm 10\%$. Accounting for their relativistic motion along the beamline, with a $\gamma \approx 21.9$ and thus a decay length of $\approx 170\,\mathrm{m}$, 80% of pions in this beam will decay by the time they reach the end of the 280 m beamline segment. The majority of the muons that reach the $g-2$ storage ring are born at this stage [79].

As stated in Section 1.2.1, the weak decay of the pion creates a correlation between the muon spin and its momentum. Selecting the highest momentum decay muons[3], which have (through random chance) been boosted in the pions direction of motion, yields a muon beam with a net polarization of 94%. The M2/M3 beamline (see Figure 3.2) consists of a series of ‘Focusing-defocusing’ quadrupole

---

[2] Iconel is a nickel-chromium ‘superalloy’ which is capable of withstanding high temperatures and stresses associated with being a beam target.

[3] The muons acquire a kinetic energy of $\approx 4\,\mathrm{MeV}$ in the π^+ rest frame from the decay.

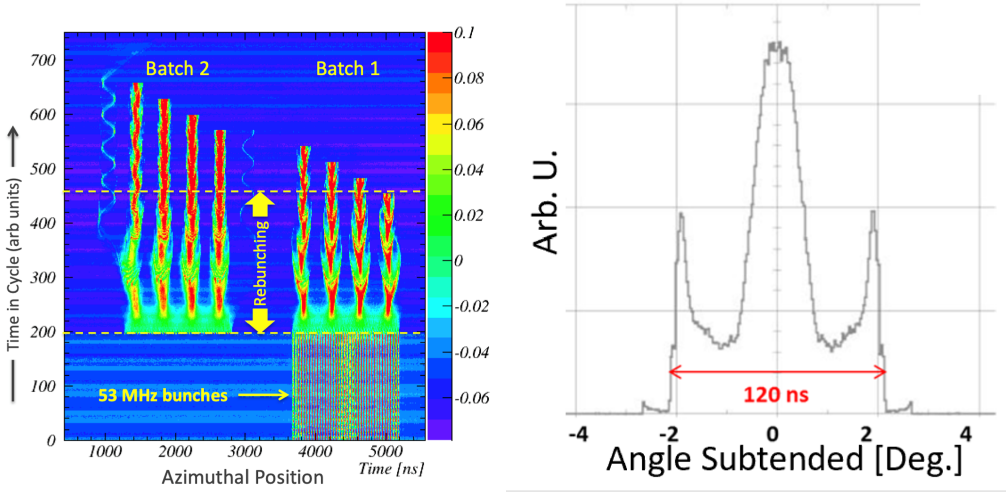

(a) Reproduced from [77]. **(b)** Reproduced from [78].

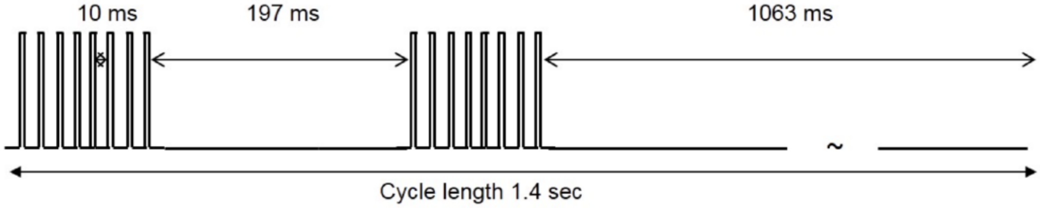

(c) Reproduced from [78].

Figure 3.3: RF Re-bunching of the proton beam in the recycler ring creates a characteristic 'W' shape in the proton bunch. This shape carries through to the injected muons. (a) Two batches of protons are injected into the recycler ring $\approx 200\,\mu$s apart before being reshaped into 8 proton bunches. (b) The shape of an individual proton bunch, from simulation. The RF re-bunching imparts this characteristic 'W' shape. The x-axis measurement of angle subtended refers to the portion of the recycler ring that the bunch occupies, which is proportional to its width in time. (c) The time structure with which bunches are extracted from the recycler ring towards the $g-2$ storage ring. This yields an average beam injection rate to the $g-2$ storage ring of $\approx 11.4\,$Hz.

elements which select precisely these decay muons for further transport along the beamline [76]. Muons with spins that are not aligned with the π^+ momentum are largely lost at this point, due to the transverse momentum they acquire from the decay. At the end of the M3 beamline, the beam still contains significant contamination from other particle species such as e^+, π^+, protons, and deuterons.

3.1.2 Delivery Ring: Proton Separation

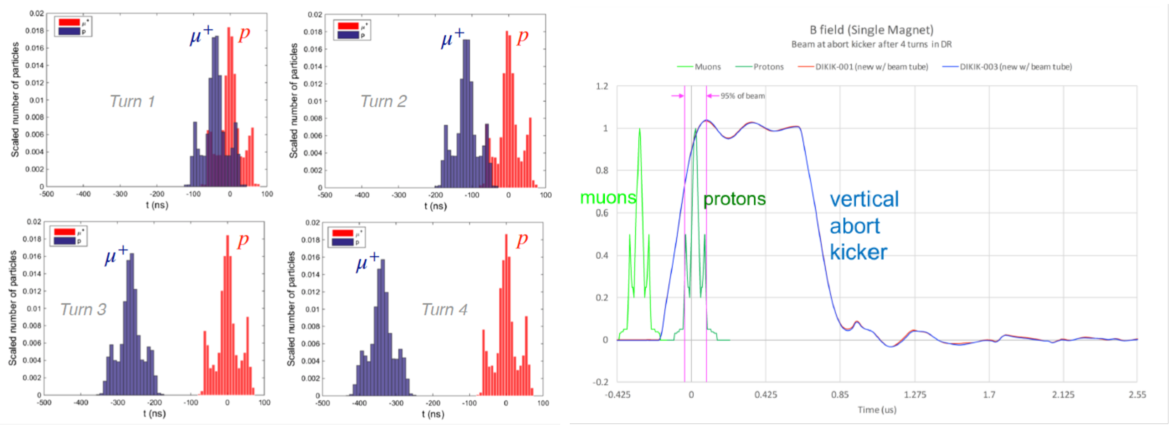

(a) Reproduced from [80].

(b) Reproduced from [81].

Figure 3.4: (a) The proton bunch separates from the muon bunch after four revolutions around the DR. (b) The proton abort kicker removes the proton contamination before the extraction of muons to the $g-2$ storage ring.

Muons are next injected into the 'Delivery Ring' (DR)[4]. The purpose of the DR is to yield as pure of a muon beam as possible by separating the species of particles by their velocity. The particles that enter the DR all have a momentum of around 3.1 GeV/c. Their different masses, however, yield a substantial spread in velocities (ranging from $0.86 - 0.999c$, shown later in Table 6.3). After travelling the 280 m of the M2/M3 beamlines, the particle species are not very well separated. However, the DR can circulate these particles around its 580 m circumference as many times as is necessary to obtain clean separation. This increases the effective length of the beamline to where pion contamination is not a significant concern, as $> 99\%$ of them will have decayed. Residual protons are cleanly separated from the muons after four turns in the DR (see Figure 3.4). After

---

[4] In a previous life, this was the anti-proton accumulator ring for the Tevatron.

four turns, an electromagnetic 'abort kicker' removes the protons and a septum magnet opens, which allows the muon bunch to exit the DR and propagate along the M4/M5 beamlines. At the exit of the DR, the beam consists primarily of $\approx 57\%$ μ^+ and $\approx 43\%$ e^+, with some remaining contamination from other particle species. Particles which are not removed by the abort kicker or selected by the septum magnet can persist in the DR for up to 45 minutes [82].

In the previous generation experiment at BNL, no analogue to the DR was present and the experiment was severely impacted by a 'flash' of non-muon particles at each injection (primarily pions). In fact, the flash was so disruptive that the photomultiplier tubes in each calorimeter were powered down for the first $\approx 10\mu s$ after injection and then rapidly ramped up to their operational voltage. Long-lived thermal neutrons, created by the impact of the pion flash on the iron of the beam yoke, were also a concern [83].

3.1.2.1 Initial Phase-Momentum Relationship

Since the majority of the muons which are stored in the $g-2$ experiment are born upstream of the DR, their spins will begin to precess as they undergo these four revolutions in the DR. Momentum dependent path lengths lead to an initial phase-momentum relationship being imparted onto the muon bunch. From 'back of the envelope' calculations (supported by sophisticated beamline simulation programs) the expected phase-momentum relationship is:

$$\frac{d\phi}{dp} \approx 9.54 \, \frac{\text{mrad}}{\% \Delta p / p_0} \tag{3.1}$$

A measurement of this quantity was performed for the Run-1 publication and found to agree well with this prediction [84]. However, a campaign by the author to re-measure this relationship in Run-6 found a 35% increase in this correlation. This campaign and the impacts of this increase are detailed further in Section 6.1.

3.1.3 M4/M5 Beamline to Injection

Once outside the DR, the muon bunch travels down the M4/M5 beamline towards the entrance to the $g-2$ storage ring. This beamline was optimized for muon transmission using a series of wire chambers situated along its length.

During Run-2, a momentum cooling wedge was inserted in this section of the $g-2$ beamline (see Figure 3.5), at a location where the momentum dispersion of the beam was maximal [85]. The purpose of this wedge was to increase the fraction of muons from the overall distribution ($\Delta p/p_0 \approx \pm 2.5\%$) which could be accepted by the $g-2$ storage ring ($\Delta p/p_0 \approx \pm 0.15\%$) by degrading high momentum muons to be within the momentum acceptance of the storage ring. Simulations suggested that this should yield up to a 7% increase in the number of stored muons [85], although an increase of this magnitude was never observed. This momentum degradation is suspected to be responsible for the observed 35% increase in the phase-momentum correlation. This is elaborated upon in Section 6.1. Beamline simulations are ongoing to confirm or deny this hypothesis.

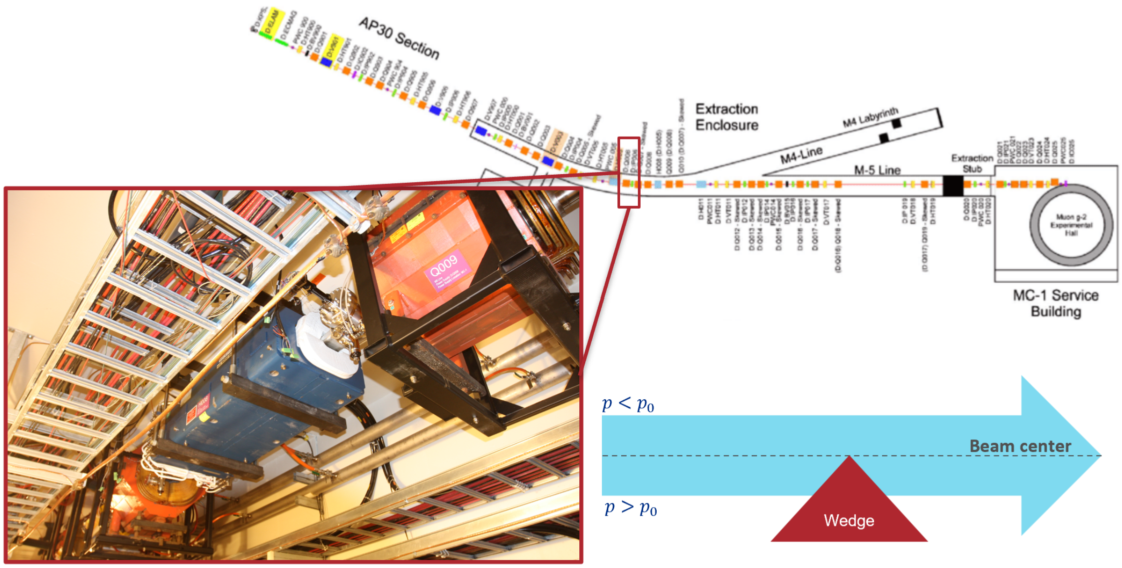

Figure 3.5: Location of the beam cooling wedge in the M4/M5 Beamline.

3.1.4 Injection

At the end of the M5 beamline, the muon bunch contains $\mathcal{O}(10^5)$ μ^+. The final focus beamline is highly optimized for maximum transmission of particles into the storage ring. Even with this optimization, only $2-4\%$ of μ^+ are able to be stored (primarily due to the large momentum spread). Fewer μ^+ still persist to the start of the ω_a measurement period at $t = 30\,\mu\text{s}$. The process of injecting this beam into the storage ring is described in the following sections.

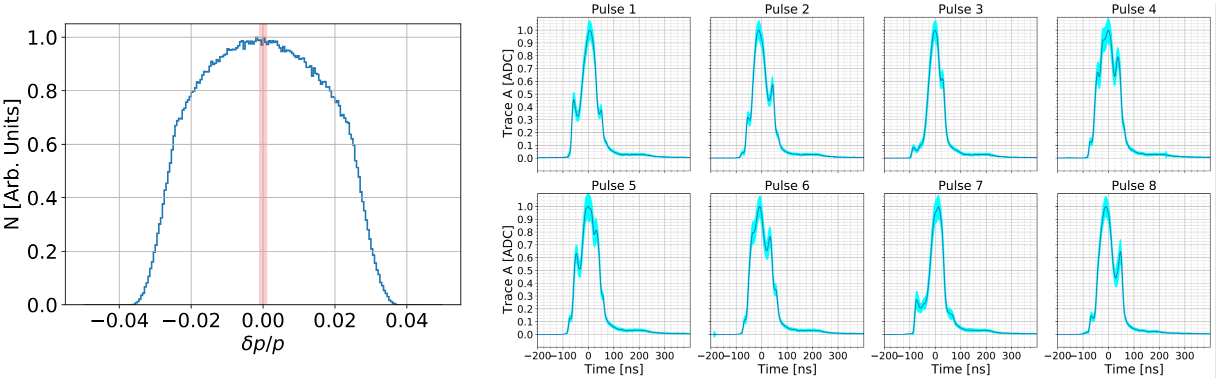

(a) Data courtesy of E. Valetov, R. Fatemi.

(b) Reproduced from [86].

Figure 3.6: (a) The momentum distribution of the beam at injection. The momentum acceptance of the $g-2$ storage ring is only $\pm 0.15\%$, indicated by the red band. (b) The average T0 pulse shape for dataset 4A (the first portion of Run-4). Each bunch has its own distinct shape, which can also vary between datasets. The distinct 'W' structure remains from the proton bunch formation in the recycler ring.

3.1.4.1 The T0 Detector

At the end of M5, just before injection into the storage ring, the muon bunch passes through the 'T0' detector, which consists of a scintillator paddle read out by two PMTs. Like its name suggests, this detector is responsible for setting the start time (t_0) for each muon fill. This is taken to be the intensity weighted average time of the injected distribution as seen by the primary PMT. The eight bunches of protons created in the recycler ring (Figure 3.3a) yield eight distinct muon bunch shapes, as shown in Figure 3.6b. There is a significant variation bunch-to-bunch in the average shape of the pulse. This results in an $\mathcal{O}(20\,\mathrm{ns})$ difference in the value of t_0 bunch-to-bunch. While this variation does not cause significant effects on the scale of the ω_a analysis[5], it can have significant implications for any systematics where the exact knowledge of t_0 is important (such as C_{dd}, as discussed in Section 3.6.3.4).

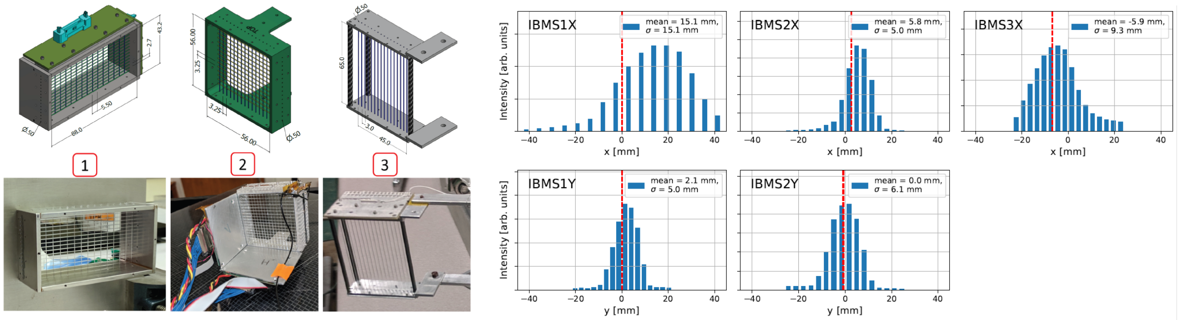

(a) Reproduced from [81].

(b) Reproduced from [81].

Figure 3.7: (a) The IBMS system, which provides a view of the beam before (IBMS 1/2) and immediately after (IBMS3) injection. Locations of the three detectors can be seen in Figure 3.9. (b) Example beam profiles measured by the three IBMS detectors. The change in the radial shape of the beam to pass through the inflector aperture can be seen in the sequence IBMS $1X \rightarrow 2X \rightarrow 3X$.

3.1.4.2 Inflector Beam Monitoring System (IBMS)

The three Inflector Beam Monitoring System (IBMS) detectors are critical to tuning the beam for maximal transmission and determining the angle of injection of the beam into the storage ring. Each of the IBMS detectors, shown in Figure 3.7, consist of a grid of 0.5 mm diameter scintillating fibers. IBMS1 and 2 consist of fibers oriented both horizontally and vertically, while IBMS3 consists only of vertical fibers. Each of these fibers are read out by individual silicon photomultipliers (SiPMs). The IBMS system was designed and built at CENPA primarily by B. MacCoy and P. Kammel [81].

IBMS1 and IBMS2 are inserted in the beamline at all times, 196 mm and 49 mm upstream of the inflector entrance respectively. IBMS3 is 274 mm downstream of the inflector inside the storage ring, and can be inserted for special systematic runs. These detectors monitor the x/y-profile of the beam at injection, and were used by the Fermilab accelerator division when tuning the upstream beamline. They also provide a crucial input to beamline simulations [81].

The three IBMS detectors together provide an excellent measurement of the injection angle of the beam through the inflector channel. Carefully controlling this angle is crucial for achieving a high storage fraction, as this angle can couple to various systematics. For instance, some simulations suggest that tiny variations in the injection angle can radically change the phase-momentum

---

[5] The period of the ω_a oscillation is $\approx 4.4\,\mu$s, and so this would amount to a 0.4% change in the phase. This only minutely dilute the oscillation signal. Bunch-by-bunch analyses are still performed as a cross-check, however.

correlation ($^{d\phi}/_{dp}$) of the stored beam [87, 88]. These simulations are still in progress, but the IBMS measurements of the injection angle of the beam will be crucial to interpreting such results.

3.1.4.3 Inflector

The muon bunch is injected through a hole in the iron yoke and into the storage region (see Figure 3.9). To counteract any effects from the fringe field of the magnet and allow the muons to be injected (relatively) unperturbed, a field free region is created in the portion of this entrance tunnel nearest the storage region by a superconducting 'inflector' magnet (Figure 3.8). The inflector consists of a double cosine theta winding of superconducting coils [89, 90]. This design is able to cancel out the main field of the magnet in a 1.7 m long 18 × 56 mm aperture while creating a minimal distortion of the field within the storage region.

The tuning required to pass the beam efficiently through the inflector aperture (vertically tall and horizontally narrow, as shown in Figure 3.8b), as well as going from a straight beamline with zero dispersion to the storage ring, creates a phase space mismatch between the injected beam and the ring [81]. Significant beam tuning is therefore required to optimize the parameters of the beam at injection for transmission through the inflector while not compromising storage efficiency [80, 81, 90].

The muon bunch that exits the inflector immediately begins to precess in the uniform field of storage ring magnet. Each injection of a muon bunch is referred to as a 'fill'.

3.2 The $g-2$ Storage Ring

Now that the muons have reached the storage ring, it seems appropriate to zoom in and examine the details of the ring itself. Up to this point, the exact details of the magnetic field experienced by the muons have been unimportant. Any phase advance of the initial polarization upstream of the ring is 'locked-in' as an initial condition of the ω_a measurement. Once in the storage ring, however, precise knowledge of the magnetic field becomes crucial to the extraction of a_μ.

The $g-2$ storage ring, the same one used in the BNL experiment, consists of inner and outer superconducting coils surrounded by a C-shaped iron yoke [92, 93]. At the time of its construction it

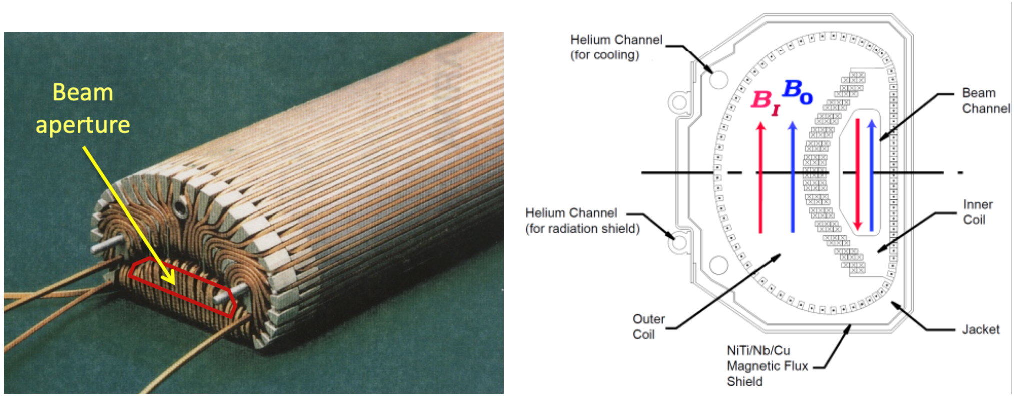

(a) Reproduced from [77] **(b)** Reproduced from [81]

Figure 3.8: (a) An image of the inflector magnet showing the magnet coils the muons must pass through at the entrance and exit of the inflector. (b) A cross section of the inflector showing the field generated.

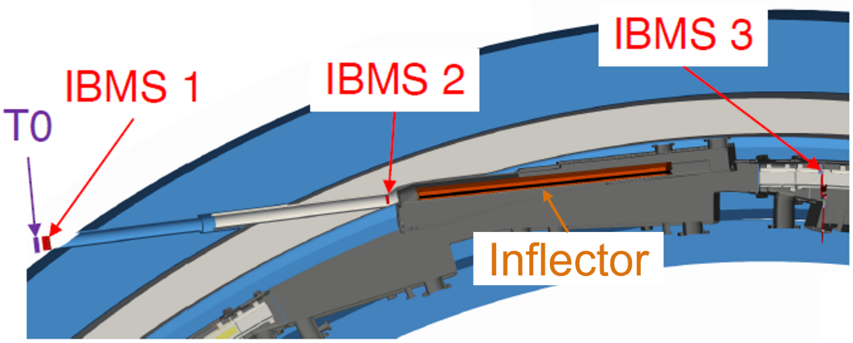

Figure 3.9: Diagram of the injection region of the $g-2$ storage ring, showing the T0 (Section 3.1.4.1) and IBMS (Section 3.1.4.2) detectors relative to the inflector. Modified from [91].

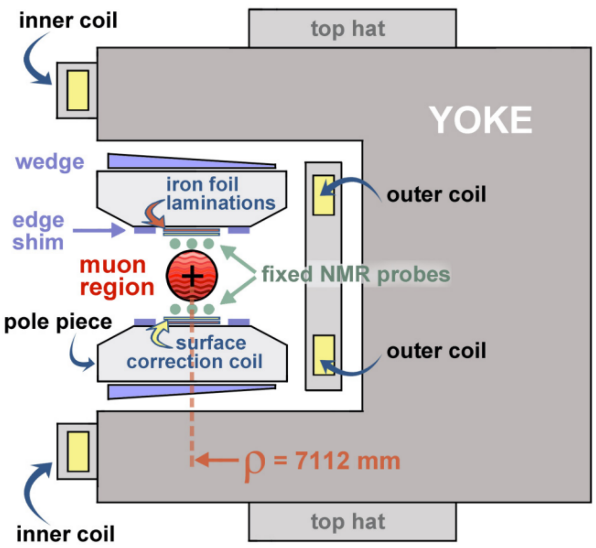

Figure 3.10: A cross section of the $g-2$ storage ring, showing the major components of the field system. Reproduced from [92].

was the largest diameter superconducting magnet in the world, measuring 14 m across. The magnet is designed to produce a highly uniform 1.45 T vertical B field in a 45 mm diameter muon storage region while keeping the inner radius relatively unobstructed to be able to detect inwardly spiraling decay positrons. A cross-sectional diagram of the storage ring, with the muon storage region shown in red, can be seen in Figure 3.10. During commissioning of the experiment, the storage ring field was made uniform using $> 10,000$ pieces of ferrous and non-ferrous metal 'shims'. This resulted in an azimuthal uniformity of < 14 ppm RMS — a threefold improvement over the field uniformity achieved at BNL [92, 94] — as can be seen in Figure 3.12c. A set of 'surface correction coils' are installed between these passive shims and the muon storage region. These provide an active feedback system which is able to continuously correct for any drift in the magnetic field of the ring.

3.2.1 NMR Probes

As stated in Section 1.2.3, the magnetic field is measured continuously using proton NMR magnetometer probes [92]. This technique has been used since the 1950's for precise measurement of magnetic fields, including in several previous generation $g-2$ experiments [10, 14, 96, 97]. These particular probes (shown in Figure 3.11a) contain a sample of petroleum jelly surrounded by an

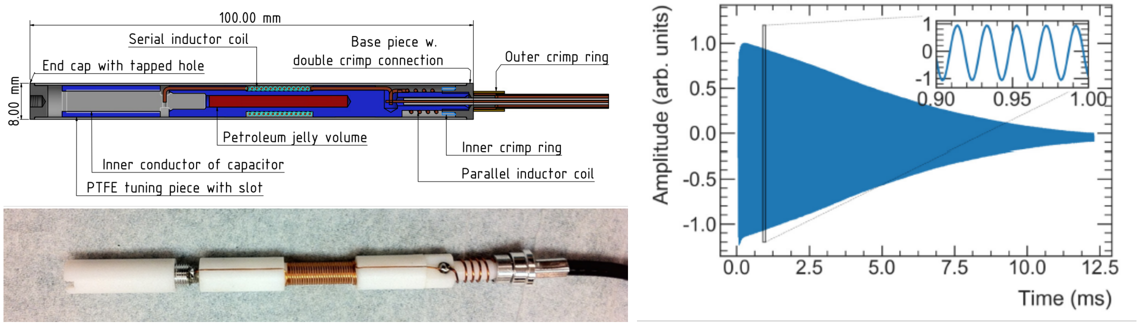

(a) Reproduced from [95]. **(b)** Reproduced from [92]

Figure 3.11: (a) A single proton NMR probe used in the $g-2$ experiment. (b) An example NMR free induction decay waveform, showing the ω_p oscillation.

RF coil. A subset of the protons in the sample will be magnetized by the field of the storage ring. To measure the field, an RF pulse (a so-called '$\pi/2$ pulse') is applied to the sample to flip the spins of these protons perpendicular to the field. As the spins re-align with the field, they precess in what is known as a free induction decay (FID). This FID signal is picked up by the RF coil and the frequency at which the protons precess — ω_p — is extracted (Figure 3.11b). This oscillation is related to the magnetic field via:

$$\omega_p = g_p \frac{e}{2m_p} B, \tag{3.2}$$

where g_p and m_p are the gyromagnetic ratio and mass of the proton respectively. A series of small corrections are required to transform the measured ω_p to the frequency which would be measured by a free proton, denoted ω_p'. These include corrections from the shape of the container, ambient temperature, and others. A summary of all of the corrections applied can be found in references [17, 92].

Each NMR probe measures the absolute value of the magnetic field at its position. This scalar information is transformed into a map of the field by combining measurements from various probes using a 2D multipole expansion:

$$f_i(r,\theta) = \begin{cases} 1 & i = 1 \\ \left(\frac{r}{r_0}\right)^{i/2} \cos\left(\frac{i}{2}\theta\right) & i > 1,\ \text{Even} \\ \left(\frac{r}{r_0}\right)^{(i-1)/2} \sin\left(\frac{i-1}{2}\theta\right) & i > 1,\ \text{Odd} \end{cases} \tag{3.3}$$

where r is the radius with respect to the center of the storage region, $r_0 \equiv 45\,\text{mm}$, and θ is the angle from the vertical. This expansion is motivated by the fact that these multipoles form a solution to the 2D Laplace equation. There are two sets of NMR probes used in the experiment: fixed probes (for continuous measurement of the field while muons are in the ring) and trolley probes (for precise measurement of the field in the storage region, but without muons). The fixed probes can measure up to $f_4\,(f_5)$ at stations with $4\,(6)$ probes while the trolley is sensitive up to f_{12} [98].

3.2.2 NMR Trolley

The value of the magnetic field in the storage region is measured by inserting a trolley with 17 NMR probes into the ring. The trolley runs along a rail system, mapping the magnetic field at 400 points around the full circumference of the ring. The trolley mapping process (a 'trolley run') takes ≈ 2 hours. An example of an azimuthal map for the dipole (f_1) field can be seen in Figure 3.12c. Such a map is created for each multipole. These are combined and averaged azimuthally to create the final field map as shown in Figure 3.12b. The azimuthally averaged field uniformity is better than 1 ppm in the region where muons orbit.

Because the trolley is able to measure the field of the muon storage region directly, the trolley measurements are treated as fixed 'truth' values while the fixed NMR probes interpolate between them. Because of this, the uncertainty on the current value of the magnetic field increases the longer it has been since a trolley run has been performed [17, 92]. But while the trolley is present in the ring no muon data can be taken for several hours. This is an optimization problem central to minimizing the overall uncertainty on a_μ. The ideal spacing between trolley runs for normal production running has been found to be ≈ 3 days [92]. Great care is taken to obtain trolley runs evenly spread throughout the day-night cycle to ensure proper tracking of any diurnal oscillations.

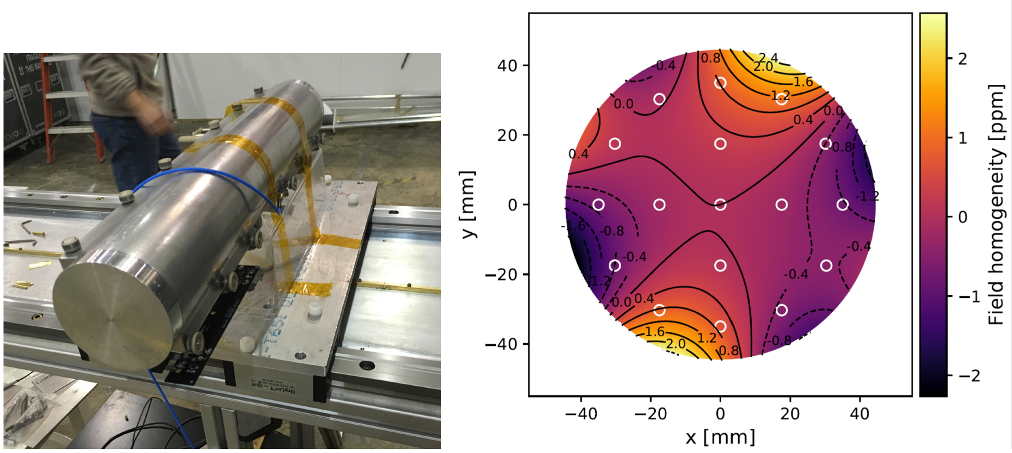

(a) **(b)** Reproduced from [81].

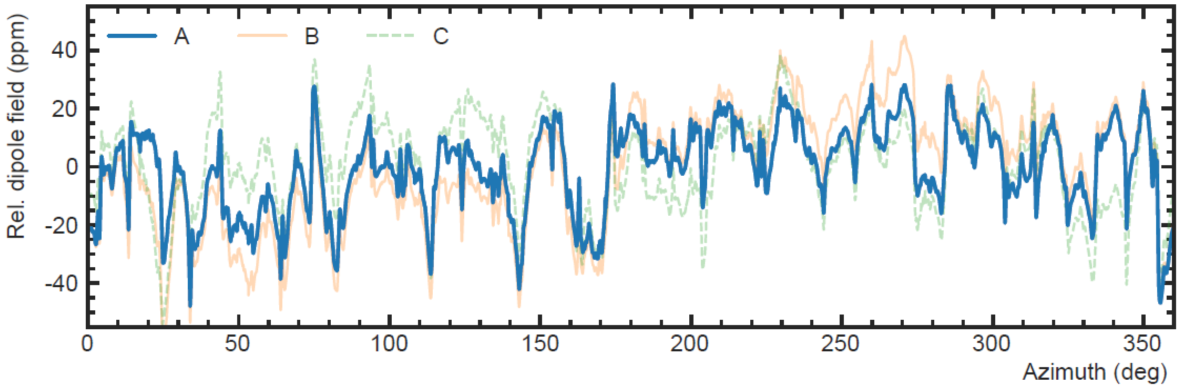

(c) Reproduced from [17].

Figure 3.12: (a) Image of the NMR trolley that measures the magnetic field azumuthally around the ring. (b) Layout of the fixed probes in the trolley, overlaid with the azimuthally averaged field map. (c) Three magnetic field maps obtained by the trolley from (blue) the start of Run-2, (orange) the end of Run-2, and (green) the end of Run-3.

Special trolley run arrangements (back-to-back runs, daily runs, etc.) are taken during beam-off periods to quantify systematic effects [92, 99].

Various corrections are also required to account for the differences in ring conditions from when the muons are present: namely the retraction of various aperture defining collimators, and the powering off of the Kicker and ESQ systems. These corrections are described in detail in [17, 92]. Each of the 17 NMR probes of the trolley have undergone an absolute calibration procedure in-situ using a reference probe calibrated at Argonne National Lab [92, 100].

3.2.3 Fixed NMR Probes and Field Interpolation

In order to track the field in-between trolley runs, an array of 378 'fixed' NMR probes are situated around the ring. These probes are arranged into 4-probe and 6-probe stations[6] which are each separated by $\approx 5^\circ$ of the storage ring azimuth. These probes constantly read out the magnetic field above and below the storage region at a rate of $\approx 0.5\,\mathrm{Hz}$. The location of these stations around the ring and relative to the storage region can be seen in Figures 3.13a and 3.13b.

The continuous measurements of the magnetic field from the fixed probes are used to interpolate between trolley runs. This tracking is not perfect[7], as can be seen in Figure 3.13d. In this figure, the difference in the relative dipole moment extracted from the fixed probes with and without an anchoring trolley run at the end can be seen. This tracking uncertainty is incorporated into the overall error on ω_p, and is $\mathcal{O}(10\,\mathrm{ppb})$.

The overall goal for the uncertainty on the determination of the muon-weighted magnetic field is 70 ppb. For the tracking of the non-transient field this target has been reached: $\delta\tilde{\omega}'_p\big|_{\text{Run-2/3}} = 46\,\mathrm{ppb}$ [15, 17]. Transient magnetic fields (see Section 3.6.1) add some additional uncertainties, but the quadrature sum remains $< 55\,\mathrm{ppb}$. Post Run-6, a series of systematic field measurement have been performed which are expected reduce these uncertainties further.

---

[6] Each station consists of 2(3) probes above and below the muon storage region.

[7] In part, because of the limited subset of multipoles to which these probes sensitive to compared to the trolley.

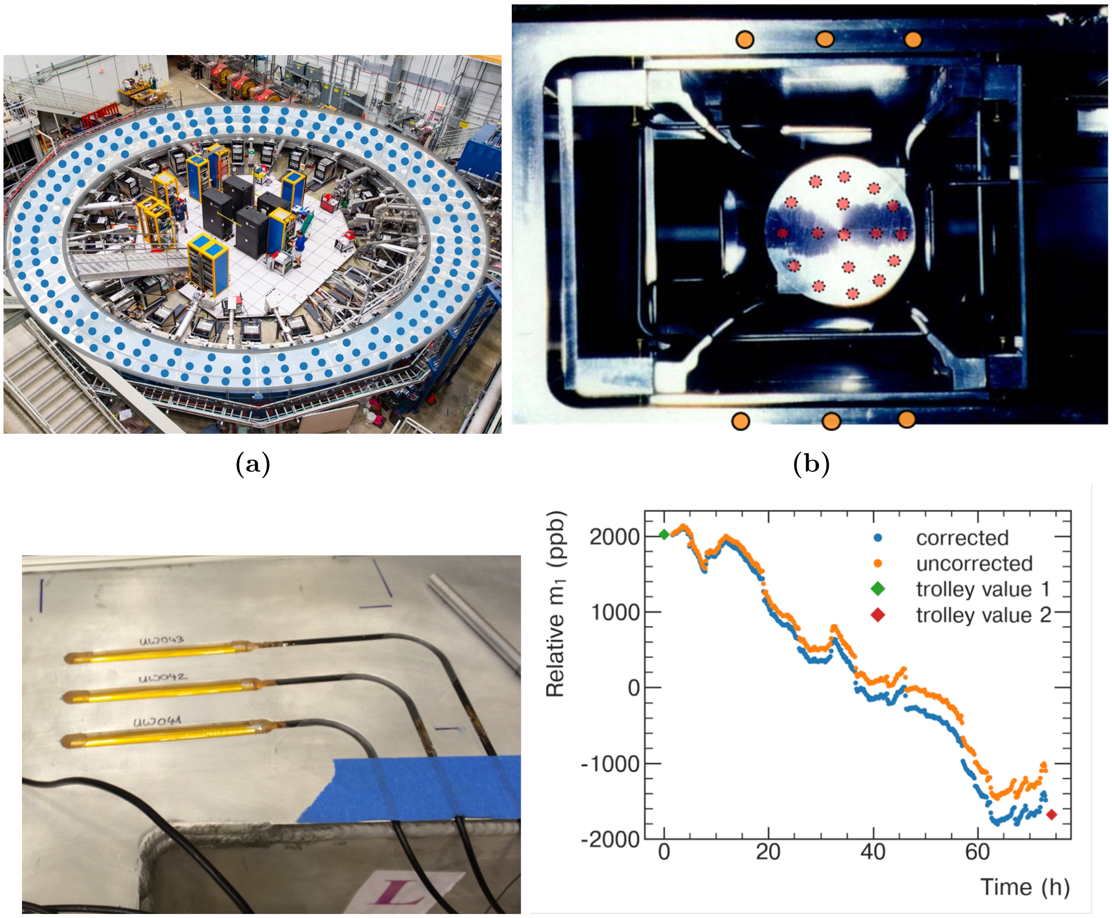

(a)

(b)

(c) Reproduced from [101]

(d) Reproduced from [92]

Figure 3.13: (a) Locations of 4 and 6-probe arrangements of fixed NMR probes around the ring. (b) Image of the relative positions of the trolley and the fixed probes during a trolley run. (c) Installation of 3 fixed probes within specialized cutouts below the storage region. (d) Interpolation of the magnetic field at a single fixed probe station a Run-1 dataset, with and without an anchoring trolley run at the end of the interpolation period. The temperature control in Run-1 was quiet poor, which exacerbated these tracking uncertainties.

3.3 Creating Stable Orbits

Having established the mechanism for creating a uniform magnetic field, let us return to the injected muon bunch. These muons, having just exited the inflector, are not yet on stable orbits. The inflector channel is angled 1.25° from tangent to the nominal orbit, and the exit is offset from the nominal storage orbit by 77 mm [81]. Two additional pieces of equipment are required to place the muons on stable orbits: an electromagnetic kicker and a series of electrostatic quadrupoles.

3.3.1 The $g-2$ Electromagnetic Kicker

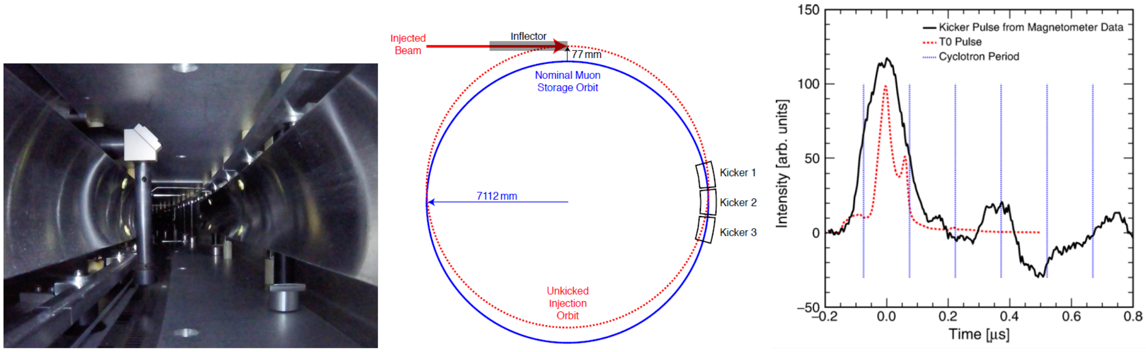

(a) Reproduced from [102]. **(b)** Reproduced from [80]. **(c)** Reproduced from [103].

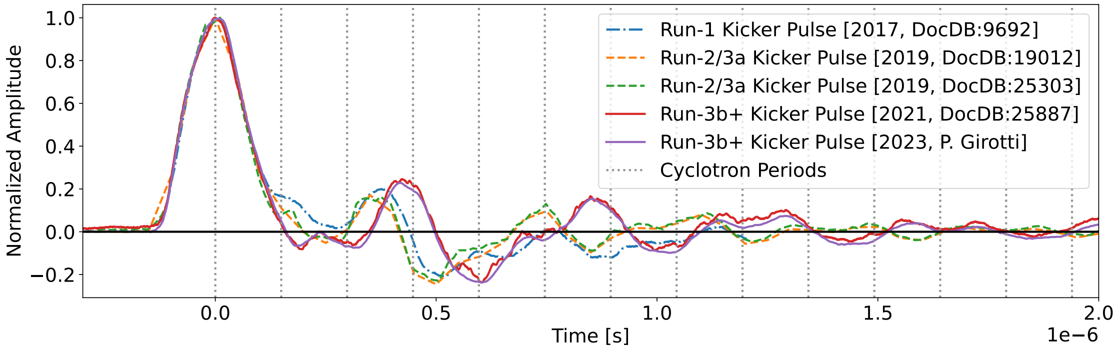

(d)

Figure 3.14: The $g-2$ electromagnetic kicker system creates a brief magnetic field in time with the beam entrance to deflect muons onto stable orbits as they are injected. (a) An image of the kicker plates with an early magnetometer to measure the pulse shape. (b) A diagram showing how the beam is deflected radially by the kicker to avoid impacting the inflector. (c) The kicker pulse shape overlaid with the average T0 pulse in Run-1. (d) Overlay of the kicker pulse as measured in Run-1, Run-2/3a, and Run-3b+ conditions. The pulse amplitudes have been normalized to the same value for comparison. The behavior in the tail is quite different in Run-3b due to the changes in the kicker electronics.

Without any additional intervention the injected muons would make only a single turn in the ring before impacting the back side of the inflector magnet and scattering out of the ring (as illustrated in Figure 3.14b). To prevent this, an electromagnetic kicker magnet is installed 90° downstream from the inflector. The kicker consists of three plates which are independently pulsed and in total occupy $\approx 13\%$ of the rings circumference.

The kicker creates a brief electromagnetic pulse ($\approx$ 220 Gauss) in time with muon injection (as shown in Figure 3.14c). This magnetic field compensates for the radial offset of the muon bunch and places the muons onto the design orbit. The kicker electronics were designed such that the field pulse would be as close to a square pulse as possible — providing the muons with a uniform kick for $< 150\,\mathrm{ns}$ before turning off completely [104]. The non-uniformity in the kicker pulse over the course of the injected bunch creates a time-momentum correlation which couples to later systematic effects (such as C_{dd}, see Section 3.6.3.4).

It wasn't until Run-3b that the kicker reached its design strength. Before this, the equilibrium radius (x_e) for muons in the ring was $\approx 6\,\mathrm{mm}$ above the design orbit ($R_0 = 7112\,\mathrm{mm}$) [105]. This under-kicking caused large oscillations around x_e, which couple to the measurement of ω_a (see Section 5.3.4). After hardware upgrades in the middle of Run-3, the equilibrium radius for the stored muons was lowered to $\approx 1\,\mathrm{mm}$ above the design radius. This update significantly altered the behavior of the beam dynamics oscillations around the ring (see Section 5.3.4 as well as references [17, 84]). The ringing tail of the kicker pulse creates a transient magnetic field while the muons are stored, which is discussed in detail in Section 3.6.1.1.

3.3.2 Electrostatic Quadrupoles

Electrostatic quadrupoles (ESQ) cover $\approx 43\%$ of the interior of the ring and provide vertical focusing of the muon beam at the expense of slight radial defocusing. There are four sets of quadrupoles, each of which consists of four plates which surround the storage region (see Figure 3.15b). High voltage held across those plates creates the quadrupole field. These essentially transform the $g-2$ storage ring into a large Penning trap.

The focusing of the ESQ system creates oscillations in the stored beam. In the approximation

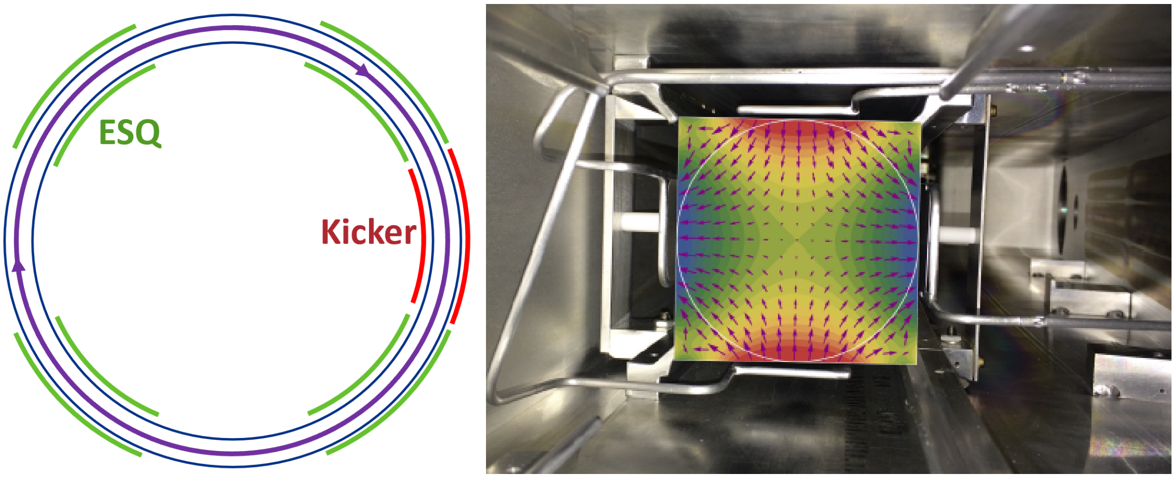

(a) **(b)** Reproduced from [91].

Figure 3.15: (a) Diagram showing the locations of the kicker and ESQ plates around the ring. The ESQ covers ≈ 43% of the ring azimuth. (b) An image of the ESQ system in the ring with the electrostatic potential field lines overlaid. This field provides vertical focusing of the stored muon beam.

of a continuous uniform electric field[8], the fields experienced by the muons can be expressed as:

$$\vec{B} = (0, B_0, 0), \tag{3.4}$$

$$\vec{E} = \kappa(x, -y, 0). \tag{3.5}$$

where κ is the magnitude of the electric field and B_0 is value of the dipole field (nominally 1.45 T, as stated above). The equations of motion for non-equilibrium muons in these fields are (to 1^{st} order):

$$\ddot{x} = -(1-n)\omega_c^2 x \tag{3.6}$$

$$\ddot{y} = -n\omega_c^2 y, \tag{3.7}$$

---

[8] This approximation is good to first order, allowing us to predict the oscillation frequencies of the beam to within ≈ 2%. The exact expressions describing the dynamic motion of the stored muon beam can be found in [81, 105].

where x is the radial coordinate and y is the vertical. The field index n is given by:

$$n \equiv \frac{\kappa R_0}{v B_0}. \tag{3.8}$$

where v is the velocity of the muon bunch. The stored muons oscillate radially and vertically around their equilibrium radii with frequencies $\omega_x = \sqrt{1-n}\omega_c$, $\omega_y = \sqrt{n}\omega_c$ respectively. The beam is in a stable configuration when $0 < n < 1$. In Run-2, the nominal operating voltage for the ESQ system was 18.3 kV ($n = 0.108$), while in Run-3+ it was reduced slightly to 18.2 kV ($n = 0.107$) to move further from a betatron resonance condition[9].

During the first few μs of a fill, the ESQ plates are not all immediately brought up to the full operating voltage. Instead, two of the 4 plates in each ESQ station are first brought up to an intermediate 13 kV, before being raised up to full voltage. This procedure is known as 'scraping'. By displacing the muon beam radially and vertically, muons with large betatron amplitudes (and thus a high probability of being scattered and lost later in the fill) impact aperture defining collimators[10] and are scattered. This reduces a potential systematic effect (C_{ml}, see Section 3.6.3.3). After operating for 7 μs at this reduced voltage, the remaining ESQ plates are brought up to the normal operating point with a time constant of 6 μs. Driven by this recovery time, the ω_a measurement period begins at $t \approx 30\,\mu$s to ensure stable beam conditions over the entirety of the fit[11]. At the end of the fill, the ESQ system discharges and any remaining particles are ejected from the storage ring (see Section 6.2). Pulsing of the ESQ system causes a slight perturbation to the magnetic field (see Section 3.6.1.2).

In an effort to reduce the beam dynamics oscillations, an RF phase-space matching system was integrated into the ESQ system in Run-5 [107]. Rather than just scraping in the first few μs of the fill, the ESQ system would also apply an RF modulation which would damp the oscillations of the stored muon beam. This process was successful, and was operated in two modes: damping

---

[9] Due to an enhancement of muon losses, the storage efficiency is low near betatron resonances, where

$$i\omega_x + j\omega_y = k\omega_c \tag{3.9}$$

for integer i, j, k.

[10] Five such collimators are situated around the ring.

[11] Some residual effects from scraping are still observed during the measurement period. These are described in Section 5.3.7.3.

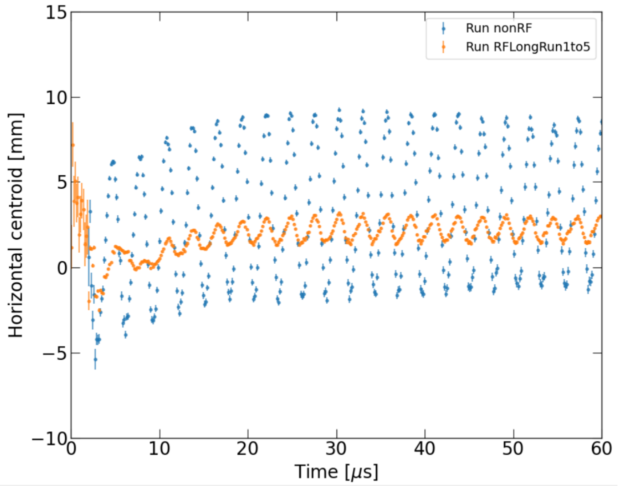

Figure 3.16: Amplitude of the horizontal oscillations of the beam centroid (CBO) as seen by the trackers with and without the RF. Reproduced from [106].

only the horizontal beam centroid oscillations in the first portion of Run-5 (DS-5A→M[12]), and damping both the horizontal and vertical oscillations in the latter half of Run-5 and all of Run-6 (DS-5L→6N). An example of the effect of the RF system on the horizontal centroid of the beam can be seen in Figure 3.16. The effects of the ESQ RF system on ω_a in Run-5 are discussed in Section 7.3.2.

3.4 ω_a: Precession Frequency

3.4.1 Muons to Positrons

After the application of the kicker pulse and the ESQ field, the muons are now on stable orbits. Muons that remain stored $30\,\mu$s after injection are likely to be stored until they decay into positrons[13]. At a momentum of $3.094\,\mathrm{GeV}/c$, muons in the $g-2$ storage ring have a time-dilated, lifetime of $\gamma\tau_\mu \approx 64.4\,\mu$s. When a muon decays, the resulting positron spirals inwards towards the center of the ring. There it will encounter the main measurement system for the $g-2$ experiment: the electromagnetic calorimeters.

---

[12] The definition of these DS-___ ‘datasets’ is given later in Chapter 4.

[13] Some muons still have the chance to hit an aperture defining collimator or other material and scatter out of the storage region. This process is described in detail in Section 5.3.8, and these lost muons amount to $< 0.1\%$ of all muons stored after $30\,\mu$s.

3.4.2 Calorimeters

The Muon $g-2$ calorimetry system consists of 24 detectors equally spaced around the inner edge of the storage ring. Each calorimeter consists of a 9×6 array of lead fluoride (PbF_4) Cerenkov crystals (Figure 3.17c), measuring $(25 \times 25)\,\mathrm{mm}^2$ on the front face and with a length of 140 mm (≈ 15 radiation lengths[14]). Each crystal is optically isolated from its neighbors by a single layer of $50\,\mu$m thick black[15] Tedlar$^{\mathrm{TM}}$. Each crystal is read out by a SiPM[16] with a $(12 \times 12)\,\mathrm{mm}^2$ active area ($\approx 25\%$ of the back area of the crystal). Each SiPM consists of $57,344$ avalanche photodiode 'pixels' [6]. When a photon of Cerenkov light strikes one of the pixels it causes it to discharge. The current from this discharge is collected, integrated, amplified on the board, and sent as a differential signal to the WFD5[17] digitizers located in each calorimeter crate (Figure 3.17e). Each of the SiPM signals is read out individually, and the processing of the data is described in Chapter 4. Once discharged, a single pixel takes $\mathcal{O}(10\mathrm{ns})$ to recharge and re-enter Geiger mode. The pixel cannot re-fire during this time, and the recharging therefore has some effect on the short-term gain stability of the system (see Section 4.1.5). Typically $\approx 2,000$ pixels fire for a high energy positron hit [6].

The bias voltages and on-board amplification for each of the 1296 SiPMs are optimized at the beginning of each Run year to ensure the detector is operating in a linear regime, where the amplitude of the signal increases linearly with respect to the light hitting the sensor. During this process the response of the SiPMs are roughly equalized, to ensure that the energy calibration constants (Section 4.1.4) do not differ too wildly and that the DAQ does not need to consider differences in detector response when triggering.

A prototype calorimeter system was tested extensively in a high-energy electron testbeam at SLAC to ensure excellent timing ($\approx 40\,\mathrm{ps}$ at $3\,\mathrm{GeV}$) and energy resolution (3.1% at $2\,\mathrm{GeV}$) [108]. Excellent linearity over the $g-2$ energy range was also observed. The Moliere radius for PbF_4 is

---

[14] The radiation length of a material is defined as the mean length after which the energy of a particle passing through will by reduced by a factor of $1/e$.

[15] The choice of a black wrapping reduces the overall light output compared to a reflective or white material, slightly worsening the energy resolution but sharpening the peak of the signal in time [108, 109]. Between this choice and the inherently fast nature of Cerenkov light production, it was found that all of the light produced from a charged particle hitting a crystal would be collected in $< 10\,\mathrm{ns}$ [6]. This contributed to the excellent time resolution of the calorimeter system.

[16] Hamamatsu "Multi-Pixel Photon Counter" model number: S12642-4040PA-50 [108].

[17] A board developed by Cornell University for use in the $g-2$ experiment, so called because each one consisted of five waveform digitizers (WFDs).

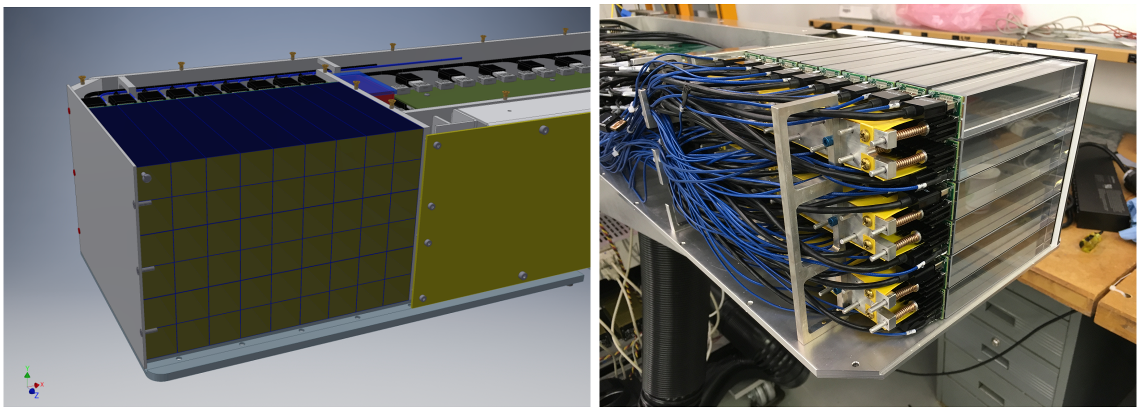

(a) Image of the $g-2$ calorimeter from simulation, showing the 9×6 crystal array structure.

(b) An image of the $g-2$ calorimeter, showing the crystals and electronics.

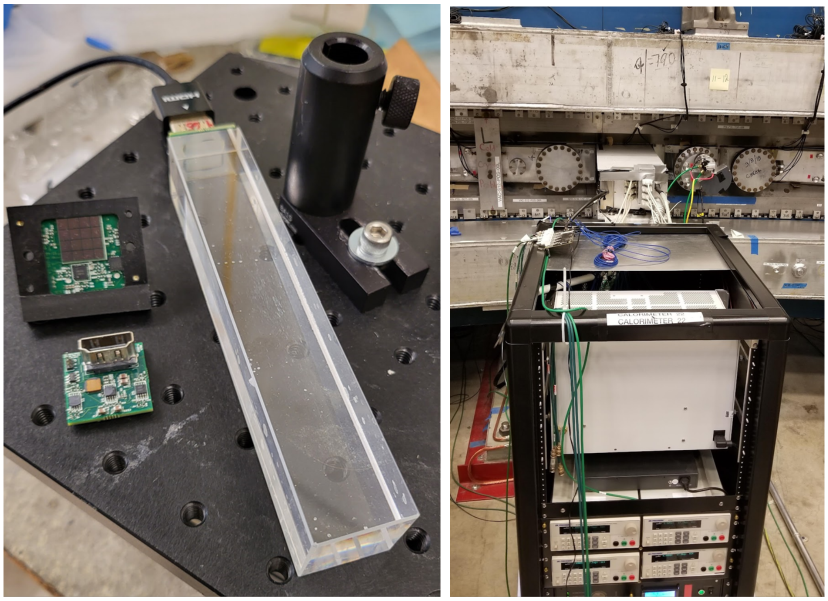

(c) Calorimeter crystal and SiPM.

(d) A calorimeter crate in-situ

(e) Digitizer crate for a calorimeter.

Figure 3.17: Images of the $g-2$ calorimetry system.

22 mm, therefore the majority of positron showers will deposit energy in 3+ crystals. Energy sharing means that a position resolution of ≈ 5 mm is achieved [108]. The inherent spatial separation of the calorimeters can help to reduce the effect of pileup in the detector (see Section 4.1.6.1). A dedicated publication detailing the calorimeter systems performance over the lifetime of the experiment is forthcoming. Additional details of the design, commissioning, and operation of the calorimeters can be found in [6, 91].

The calorimeters are inserted into specialized indentations (‘scallops’) in the vacuum chamber (see Figure 3.17a), designed such that as little material as possible is present between the storage region and the calorimeter active volume. The space constraints severely restrict the dimensions of the calorimeters, which amplifies acceptance[18] differences across their face. Where the calorimeter is located in the ring (behind a kicker plate, ESQ plate, etc.) can alter its acceptance. The acceptance of the calorimeters comes into play in the ω_a analysis, where it (along with other detector effects) distorts the observed positron spectrum (see Section 5.2.4). Acceptance also enters into the various BD corrections (Section 3.6.3), where it can couple to beam motion to produce biases to the measurement of ω_a.

3.4.3 Laser Calibration System

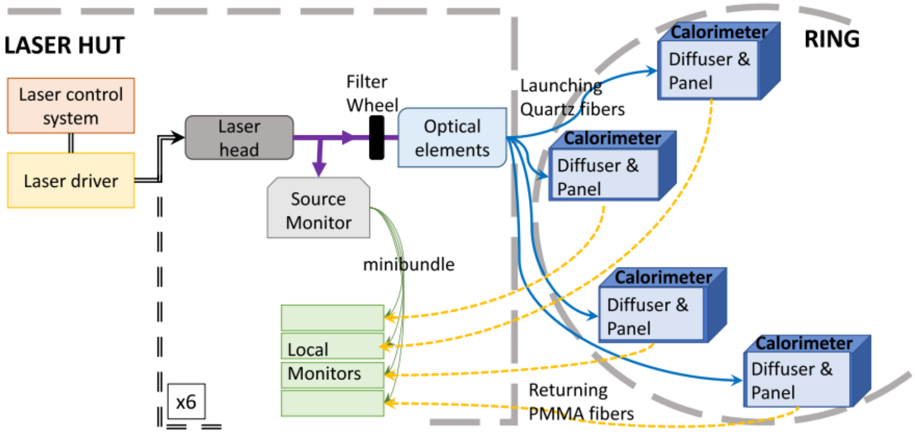

Figure 3.18: Diagram showing one of the six laser heads for the $g-2$ calibration system. Reproduced from [110].

---

[18] The probability that a muon which decays with a given set of conditions ($\vec{p}$, $\vec{x}$, etc.) will yield a detected positron.

Each of the detectors in the experiment are synchronized in time using a laser-based calibration system [110, 111]. This system consists of six individual laser heads, each responsible for feeding 405 nm laser pulses to four of the calorimeter stations (as well as some other auxiliary systems or detectors). A diagram of a single laser head is shown in Figure 3.18. These laser pulses are sent out through a network of optical fibers arranged throughout the experimental hall. The front face of each of the of the $g-2$ calorimeters contains a laser light diffuser and distribution panel. Laser light from a single large fiber enters this system, which distributes it to 54 individual strands. Each one of these strands illuminates the front face of a single crystal with an amount of light roughly equivalent to that produced by an 2 GeV positron energy deposit.

At the start and end of each muon fill, the laser sends a single pulse to synchronize all of the detectors in time. In between muon fills, the laser system pulses to monitor the long term gain stability of the detector systems. The short term stability of the calorimeter systems is measured and corrected for using a series of special laser runs, as well as in-fill laser pulses (i.e. laser pulses while muons are present in the ring). For some of these specialized runs, the light path of the laser heads can be altered with a series of mirrors, allowing the lasers from the even laser heads to illuminate the calorimeters normally served by the odd laser heads (and vice versa). These 'crossed' laser pulses are useful when illuminating the calorimeters with two laser pulses in quick succession, or a burst of laser light followed by a single precise pulse, is required. This calibration system is able to monitor the stability of the detectors to a relative precision of better than 0.1% over the course of the fill. These gain corrections are described in more detail in Section 4.1.5.

To minimize any changes in the performance over the course of the Run, the laser system is kept in a highly temperature controlled room separate from the rest of the experimental hall. A series of calibrated monitors track the light output of the laser in order to correct for any slight drift of the source over time. Any changes in the lasers output are able to be tracked and corrected for at the 0.01% level [111].

3.4.4 End of Fill

The measurement period extends for $\approx 700\,\mu$s (> 10 muon lifetimes) after injection, allowing most of the muons to decay away. In a typical fill, the calorimeters will detect ≈ 5000 positrons within the ω_a measurement period of $30 < t\ [\mu\text{s}] < 700$. The ESQ system turns off $850\,\mu$s after injection, which clears any remaining muons (or other long lived particles) from the storage ring before the arrival of the next bunch. The ESQ and kicker systems then reset and prepare for the next bunch.

3.5 Beam Dynamics

Were all of the muons stored on the design orbit, the story of the experiment would largely end here. However, the varied trajectories of the muons through the storage ring create a number of effects which have the potential to bias the extraction of ω_a. To combat these effects, detailed studies of the dynamic motion of the beam throughout the fill are required.

3.5.1 Beam Dynamics Focused Detectors

The $g-2$ calorimeter system is only indirectly sensitive to the motion of the stored beam, and is overwhelmed by a positron flash during beam injection to the point where it is largely unable to reconstruct hits before $4\,\mu$s into the fill. A series of specialized detectors were utilized over the course of the experiment to fill these gaps and evaluate systematic effects.

3.5.1.1 Trackers

Two positron tracking detectors in the $g-2$ ring are located at $\approx 180°$ and $\approx 270°$ downstream from the inflector (directly in front of calorimeters 13 and 19) [113]. A tracking station consists of 8 modules, each consisting of two layers of aluminized Mylar straws oriented at a $\pm 7.5°$ angle from the vertical and filled with a mixture of Argon-Ethane gas [113]. As positrons spiral inward, they pass through the straws of the tracker stations and create an ionization signal in the gas. Tracking algorithms reconstruct these hits into tracks that the particles took through the detector. A diagram of such positron tracks is shown in Figure 3.19. These tracks can be extrapolated back

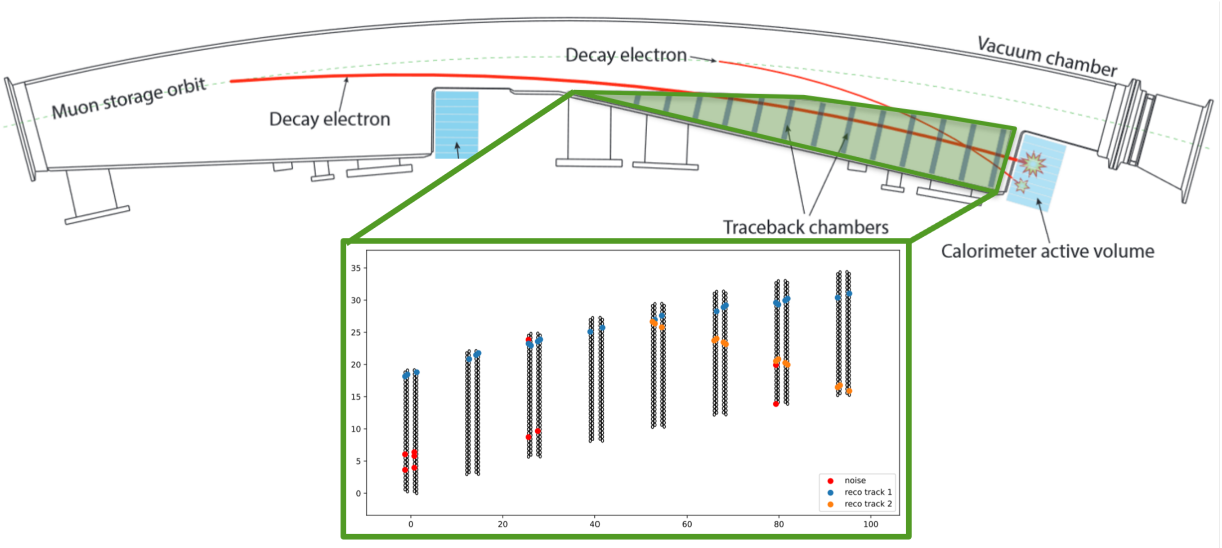

Figure 3.19: Reconstructed track(s) of positrons through a straw tracking station. Modified from [112].

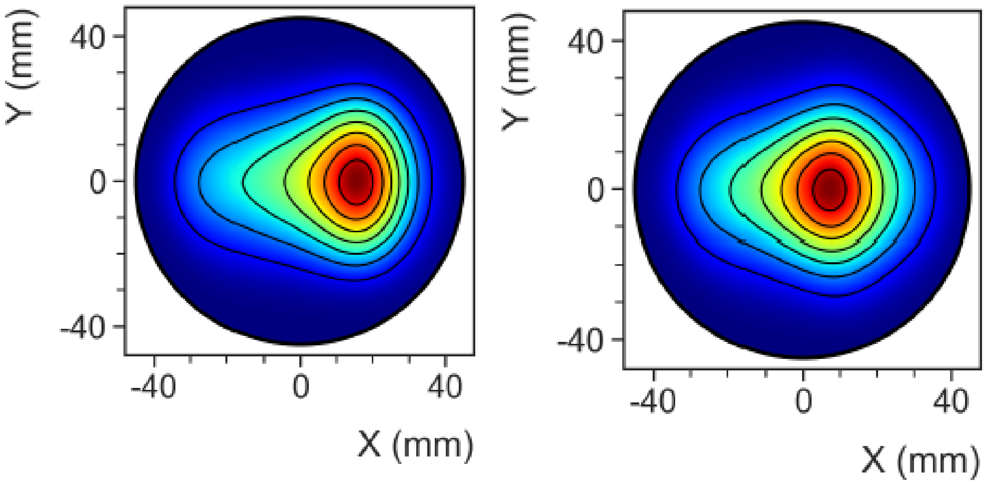

(a) Reproduced from [17].

(b) Reproduced from [17].

Figure 3.20: Example reconstructed beam profiles for a dataset in (a) Run-2 (DS-2B) and (b) Run-3b (DS-3O). The effect of the higher kick strength in Run-3b onward can be seen in the better centering of the beam.

to their point of radial tangency (with respect to the ideal orbit) to achieve an approximation of the decay location of that particular muon[19]. Performing this extrapolation for all positrons which pass through the tracker allows for monitoring of the dynamic evolution of the beam over the course of the fill. Since the trackers only sample positrons from a subset of the ring, some extrapolation is required to model the behavior of the beam at large[20]. These positron tracks are used to create a map of the beam: $M(x, y, \theta, t)$. Examples of such maps can be seen in Figure 3.20, where they have been averaged over time and azimuth. The knowledge of the beam motion from the trackers feeds into numerous systematic effects related to the extraction of ω_a (see Section 3.6.3). This also is crucial for the evaluation of the muon weighted magnetic field $\tilde{\omega}_p$ (see Section 3.6.2).

3.5.1.2 MiniSciFi

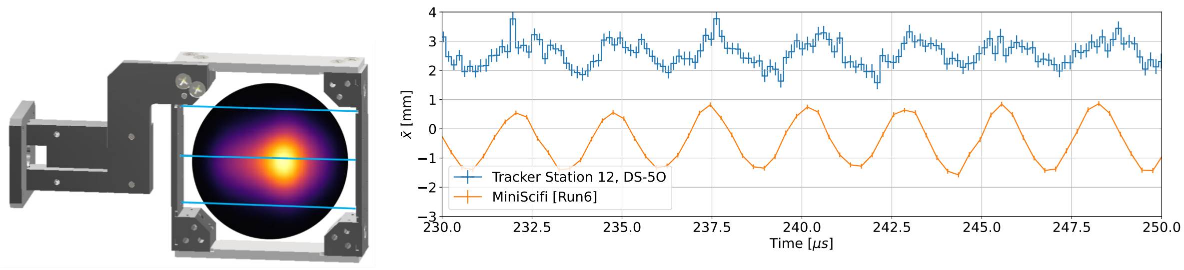

(a) Reproduced from [114]. **(b)** MiniSciFi data courtesy of C. Claessens.

Figure 3.21: (a) Engineering drawing of the horizontal MiniSciFi detector. (b) Comparison of the beam centroid from a few hours of Run-6 MiniSciFi data to the tracker profile from DS-5O (11 days). The difference in precision is striking. The large radial offset here can be ignored, it is due to a lack of absolute position calibration in this MiniSciFi data.

Thus far the only measurements of the stored muon beam have been indirect, obtained by measuring decay positrons. Acceptance effects, which require input from simulations to correct for, can thus complicate the interpretations of these measurements. To rectify this problem, a dedicated detector system was designed and constructed at CENPA by P. Kammel, B. MacCoy, and C. Claessens: the Minimally Intrusive Scintillating Fiber Detector (MiniSciFi). This detector system, first commissioned during Run-5, consists of three 250 μm diameter scintillating fibers

---

[19] This makes the assumption that the positrons have no initial lateral motion, which has been shown from simulation not to measurably alter the results of the reconstruction [113].

[20] This extrapolation is done using the beta functions of the ring. More details can be found in references [81, 105].

spaced 26 mm apart. Two separate versions were constructed, one with fibers oriented vertically and one with fibers oriented horizontally. The vertical MiniSciFi is optimized for a measurement of the radial profile of the beam, by stepping the three fibers through the storage region. The horizontal MiniSciFi is optimized for measurement of the 'fast rotation'[21] signal of the beam by being sensitive to particles at all radii at once.

The MiniSciFi detector can be inserted either 180° or 270° downstream of the beam injection point. When inserted, the effective muon lifetime is lowered by $\approx 1.5\%$ due to increased muon losses from scattering. The measurements of the beam from this detector system will provide new inputs to systematics for the Run-4+ data analysis. Many weeks of systematic measurements were taken in Run-6 to measure the dynamic motion of the beam under all permutations of the nominal experimental conditions (ESQ RF, ESQ scraping, kicker strength, etc.). These will all be used to benchmark simulation efforts. Comparison of tracker data with that from the MiniSciFi will also aid in disentangling the beam motion effects from the ESQ RF described in Section 7.3.2.

3.6 Correction Factors

A number of corrections are required for the measured values of ω_a and ω_p. The values (published and expected) of these corrections for all Runs of the experiment are discussed below and summarized in Table 3.1.

3.6.1 Corrections to ω_p

The main field of the storage ring (shown in Figures 3.12 and 3.13d) can change on the order of hours, but is nominally stable on the order of a single fill. However, the pulsed ring systems generate transient fields which vary rapidly and coherently over each fill. Any effects which occur on this timescale must be measured and taken as corrections to the nominal measurement. Two such effects have been identified in the running of the experiment.

---

[21] The term 'fast rotation' signal refers to modulation of positron hits vs. time arising from the debunching of the injected muon bunch and the spread in cyclotron frequencies in the ring. An analysis of this signal is described in Section 6.1.

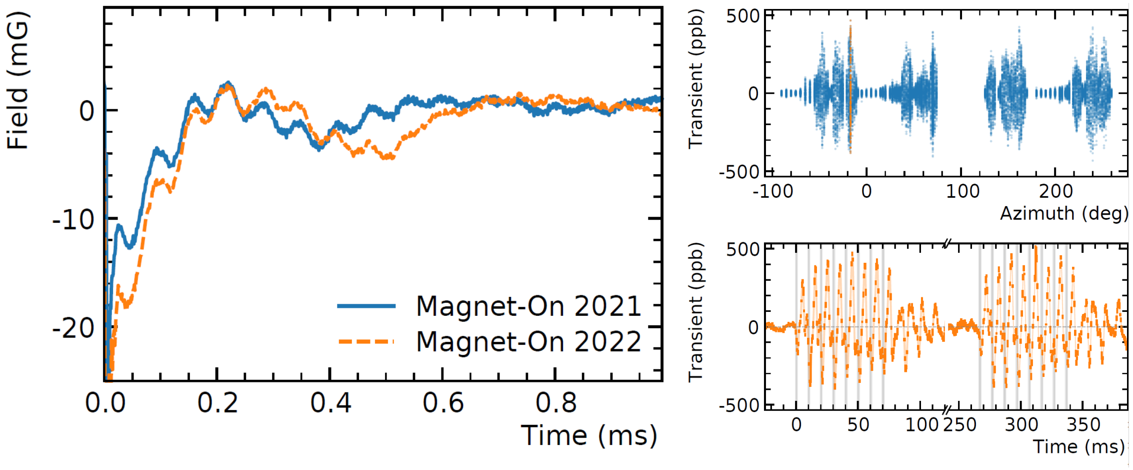

(a) **(b)**

Figure 3.22: The transient fields created by (a) the kicker and (b) the ESQ system. Reproduced from [17]. The transient field in (b) is given in terms of the perturbation of the main field of the $g-2$ storage ring.

3.6.1.1 B_k: Kicker Eddy Currents

The pulsing of the kicker magnet creates a residual, transient magnetic field through two mechanisms:

- An eddy current is produced in the metal of the vacuum chambers which persists throughout the muon storage period, well after the main kick has subsided.
- Ringing in the electronics chain creates a distinctive 'tail' of the kicker pulse

This transient magnetic field has been measured in-situ using two independent vibration-insulated magnetometers [92, 115]. The results of this measurement are shown in Figure 3.22a. The correction to ω_a is estimated by integrating the field over the muon storage period, and its value in Run-2/3 is given in Table 3.1.

The exact mechanism which creates the fast oscillatory patterns in the kicker transient field is not known. The frequency visible in Figure 3.22a does not perfectly align with what would be expected from the known degrees of freedom of the kicker system. An additional measurement campaign was conducted after the completion of Run-6 data taking in late-2023. From the results of this campaign, combined with additional modeling work to understand the vibrations in the system, it is likely that the uncertainty on this systematic will decrease in the Run-4+ publication.

3.6.1.2 B_q: Quad Transient Fields

The pulsing of the ESQ system creates mechanical vibrations which lead to a transient magnetic field while muons are present in the storage ring. A series of dedicated measurements were undertaken to map these transients in time and around the ring azimuth. Specially constructed NMR probes[22] were mounted on a trolley platform and driven around the ring. The ESQ system was pulsed continuously and the transient field was mapped out over many hours of asynchronous probe readouts. This field can be seen in Figure 3.22b around the ring (top) and vs. time (bottom). The 2×8 time structure of the injected bunches can clearly be seen in the latter (mirroring Figure 3.3c). Again, the integrated value of the measured transient field over the muon fill was used to set B_q (Table 3.1).

3.6.2 Weighting the Field: From ω_p' to $\tilde{\omega}_p'$

The magnetic field that each muon experiences is unique, determined by its individual trajectory through the storage ring. While a great deal of effort was undertaken to make the field as uniform as possible, a correction to account for any non-uniformity is required. This is distinct from a correction to ω_p', in the sense that there is no distortion of the field of the storage ring. The only change is in how the measured field is used in the final evaluation.

The azimuthally averaged magnetic field maps measured by the trolley and the average muon beam distribution measured by the trackers are broken into the multipole expansion given in Equation (3.3). The values of ω_p' and M can be expressed in this basis:

$$\omega_p' = \sum_{i=1}^{N_{\max}} m_i(\phi, t) f_i(r, \phi) \tag{3.10}$$

$$M = \sum_{i=1}^{N_{\max}} k_i(\phi, t) = \sum_{i=1}^{N_{\max}} \frac{\int M(x,t,\phi,t) f_i(x,y) dxdy}{\int M(x,t,\phi,t) dxdy} \tag{3.11}$$

---

[22] The probes, and the base upon which they are mounted needed to be as non-conductive as possible to avoid sparking in the ESQ HV.

where m_i is the magnitude of each of the multipoles in the field and k_i is the projection of the tracker map onto the i^{th} multipole moment. These expansions are used to weight ω'_p:

$$\tilde{\omega}'_p(\phi, t) = \sum_i m_i(\phi, t) k_i(\phi, t) \tag{3.12}$$

The effect of higher order multipoles on the beam weighting is reduced in Run-3b and beyond due to the improved kick. The improved temperature control in Run-3 also lessens the effect of higher order multipoles, as the work done to reduce any non-uniformities in the field at the beginning of each Run persists for a longer period of time. The difference in the field value with this weighting vs. approximating the field as a perfect uniform dipole is $\mathcal{O}(50\,\text{ppb})$ [81, 92].

3.6.3 Corrections to ω_a

There are a number of corrections which must be applied to the measured ω_a due to beam dynamics effects. These can be broadly divided up into two categories: those effects arising from corrections to the relationship of ω_a to a_μ, and those arising from a time dependent phase coupling to ω_a. Five such corrections (two of the former type and three of the latter) are taken into account in the E989 extraction of a_μ.

The argument for why a time changing phase is deleterious to the measurement is as follows. Imagine fitting a function of the form:

$$x(t) = \cos(\omega t + \phi)$$

Now, if $\phi \to \phi(t)$ and a simple Taylor expansion is performed:

$$\begin{aligned} x(t) &= \cos(\omega t + \phi(t)) \\ &= \cos\left(\omega t + \left(\phi_0 + \frac{d\phi}{dt} t + \frac{d^2\phi}{dt^2} t^2 ...\right)\right) \\ &= \cos\left(\left(\omega + \frac{d\phi}{dt}\right) t + \phi_0 + ...\right), \end{aligned} \tag{3.13}$$

it can be seen that the extraction of ω has been biased. A fit performed to such data will prefer a value of $\omega_{\text{measured}} = \omega + {}^{d\phi}/_{dt} \neq \omega_{\text{true}}$. Importantly, there is no way to determine from the fit itself that such a time shift has occurred[23]. It is only with outside knowledge that the correction factor can be established and the true $\omega = \omega_{\text{measured}}(1 + C)$ extracted.

3.6.3.1 The Electric Field Correction: C_e

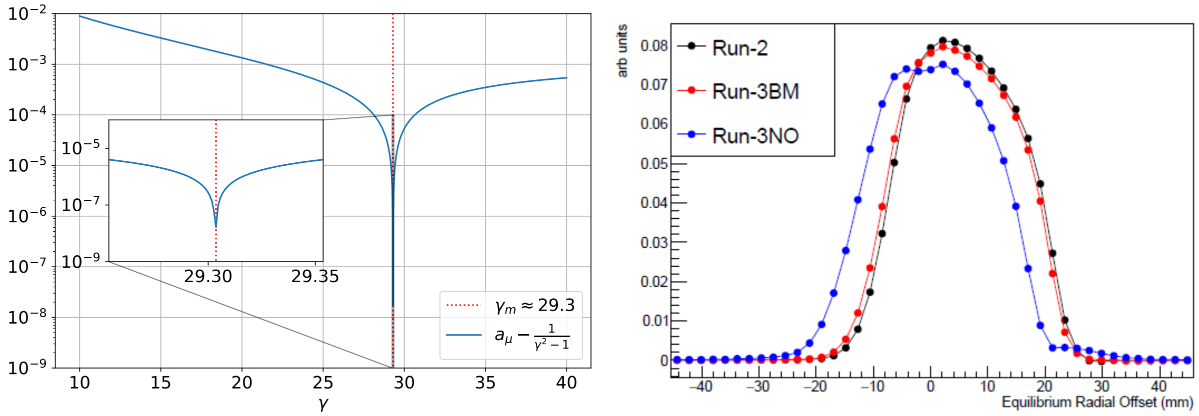

(a) **(b)** Reproduced from [84].

Figure 3.23: (a) The cancellation of the $\vec{\beta} \times \vec{E}$ term. (b) Reconstructed momentum distributions for Run-2, 3a, and 3b. The effect of the higher kick can clearly be seen.

The first such effect is caused by off-momentum muons in the field of the ESQ system. As shown in Equation (1.34), when the muons are at the magic momentum (with $\gamma_0 \approx 29.3$) the effect of the electric field cancels. This cancellation is shown in Figure 3.23a. The ideal momentum distribution for the $g-2$ experiment would be a delta-function at the magic momentum p_0. However, the momentum distribution in the $g-2$ storage ring ($\Delta p/p \approx 0.15\%$) means that some residual effect of the E field must be accounted for. This effect was exacerbated by the under-kicking of the beam before Run-3b, which resulted in a momentum distribution not centered around p_0 (and thus a large equilibrium radius x_e). The effect of the residual electric field is given by:

$$C_e = \left\langle \left(a_\mu - \frac{1}{\gamma + 1} \right) \vec{\beta} \times \vec{E} \right\rangle .$$

---

[23] Higher order terms, such as ${}^{d^2\phi}/_{dt^2}$, could in principle be detected and indicate the presence of such an effect. However, this would give no indication as to the magnitude nor sign of the bias to ω. In the data, ϕ_a is altered by various BD terms in a similar fashion (see Section 5.3.7).

For an individual muon with equilibrium radius x_e and momentum p, this can be expressed as an expansion of the $\vec{\beta} \times \vec{E}$ term in Equation (1.34) around $\beta = \beta_0$ [17, 116]:

$$\begin{aligned} \frac{\Delta\omega_a}{\omega_a} &= -2\frac{\beta_0}{B_0}\left(\frac{p - p_0}{p_0}\right) E_x \\ &\approx -2\frac{\beta_0}{B_0}\left(\frac{p - p_0}{p_0}\right)\left(n\frac{\beta_0 B_0}{R_0}x_e\right) \end{aligned} \tag{3.14}$$

where $R_0 = 7112\,\mathrm{mm}$ is the 'magic radius' and the electric field of the ESQ system is expressed in terms of the field index n (assuming a small displacement from R_0). Relating the momentum distribution to the equilibrium radius of the stored muons via the dispersion relation[24]:

$$\frac{\Delta p}{p_0} \approx \frac{1-n}{R_0}x_e,$$

and averaging over the stored muon distribution yields [105, 116]:

$$\begin{aligned} C_e &= -\left\langle \frac{\Delta\omega_a}{\omega_a} \right\rangle \\ &\approx 2n(1-n)\beta_0^2 \frac{\langle x_e^2 \rangle}{R_0^2}. \end{aligned} \tag{3.15}$$

The radial distribution of the stored muon beam is determined using two independent methods:

- Analysis of the spread of cyclotron frequencies present in the calorimeter data, which can be related to the spread in muon equilibrium radii. Two distinct procedures have been developed to perform this analysis: the so-called 'Fourier fast rotation' and 'CERN-III Extended' methods [116, 117]. The results from the Fourier fast rotation analysis of the Run-2/3 datasets are shown in Figure 3.23b.
- Analysis of the radial distribution directly measured by the trackers[25] [118].

All techniques yield good agreement for the reconstructed momentum spectrum of the stored beam. C_e is the largest correction applied to ω_a, with a magnitude of $\mathcal{O}(400\,\mathrm{ppb})$ [17, 105]. The

---

[24] A detailed derivation of this relation can be found in B. MacCoys recent thesis [81].

[25] This technique was not employed for the Run-1 analysis.

magnitude of this correction is larger than the total uncertainty on the measurement of a_μ. Thus obtaining the correct value for this correction is of paramount importance.

3.6.3.2 The Pitch Correction: C_p

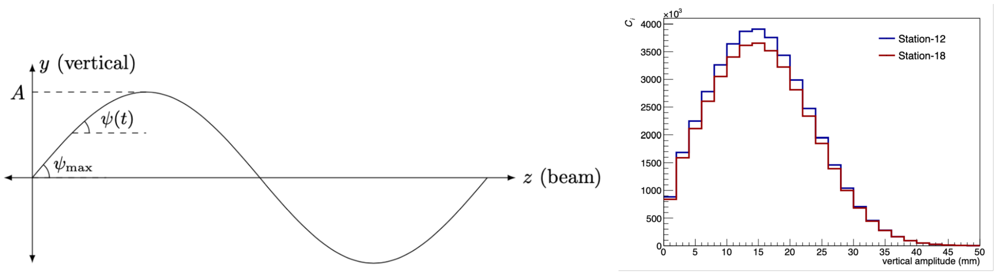

(a) **(b)** Reproduced from [119].

Figure 3.24: (a) Illustration of the vertical trajectory of a single muon. (b) The tracker reconstructed amplitude distribution from a single dataset in Run-2 (DS-2D). This is used to evaluate C_p using Equation (3.17).

The pitch correction C_p also arises primarily from the $\vec{\beta} \times \vec{E}$ term in Equation (1.34), with a small additional contribution from the $\vec{\beta} \cdot \vec{B}$ term [120]. The derivation of this correction is fairly involved, not least due to the unintuitive relative unimportance of the $\vec{\beta} \cdot \vec{B}$ term. A thorough derivation can be found in references [120, 121]. The resulting form of the correction (for a single muon) is:

$$C_p = -\frac{\psi_0^2}{4}\left(1 + \frac{\omega_a^2}{\gamma_0^2(\omega_y^2 - \omega_a^2)}\right), \tag{3.16}$$

where ψ_0 is the angle of the muon from the vertical (at $y = 0$), and ω_y is the vertical oscillation frequency of a particular muon. Averaging over the ensemble yields:

$$C_p = \frac{\langle \psi^2 \rangle}{2} = \frac{n}{4R_0^2}\langle A^2 \rangle, \tag{3.17}$$

where A is the average amplitude of the vertical beam oscillations as measured by the tracker stations (Figure 3.24b). Two independent analyzes of the data are compared to ensure accurate handling of all systematic effects.

3.6.3.3 The Muon Loss Correction: C_{ml}

Muons are 'lost' if they leave the storage region before they decay. This primarily happens when a muon impacts an aperture defining collimator and loses energy to the point where its orbit is no longer stable. Muon losses can couple to ω_a through the initial phase-momentum relationship created in the DR (as described in Section 3.1.2.1):

$$C_{ml} = \frac{1}{\omega_a}\frac{d\phi_a}{dt} = \frac{1}{\omega_a}\frac{d\phi_a}{dp}\left.\frac{dp}{dt}\right|_{lm}. \tag{3.18}$$

If the muons are lost in a momentum dependent fashion, i.e. ${}^{dp}/_{dt} \neq 0$, then a bias to ω_a is introduced. This effect was of great concern in Run-1, where it had the potential to be yield an uncertainty large as 125 ppb if unconstrained[26] [6, 122]. However, a series of dedicated measurement campaigns were performed to quantify this correction. These found $C_{ml} \leq 20\,\text{ppb}$ for the Run-1 datasets. Measurements of ${}^{dp}/_{dt}|_{lm}$ were taken by inserting momentum scraping wedges in the M4/M5 beamline to remove high/low momentum muons from the injected beam. The difference in loss rates, combined with the momentum distributions reconstructed from Fourier analysis, between these perturbed injected bunches allowed the momentum dependence of the muon losses to be extracted [84, 122].

Reductions in the overall loss rate[27] correspondingly reduced this systematic in Run-2/3 by a factor of ≈ 5. This reduction was so dramatic that the measurement technique used to quantify C_{ml} in Run-1 would have taken weeks of dedicated studies to be able to measure the effect. Since the effect was so small, only a subset of the measurements were performed to set an upper limit on ${}^{dp}/_{dt}|_{lm}$ in Run-2, Run-3/4, and Run-5/6 conditions. These confirmed that the correlation was no larger than it was for Run-1. From this, a scaling of the Run-1 value based on the loss rate was assigned as a residual uncertainty to cover any remaining effect in the Run-2/3 publication. It is expected that this effect will remain small in Run-4+. The author spent a great deal of time quantifying this correction (and the behavior of muon losses in general) for the Run-2/3 analysis.

---

[26] The unconstrained, 'worst-case' scenario assumes that all muons lost (the number of which can be extracted from the ω_a analysis) are from one side of the momentum distribution.

[27] Losses in Run-1 were inordinately high due to the damaged ESQ resistors causing the average position of the beam to move over the course of the fill.

3.6.3.4 The Differential Decay Correction: C_{dd}

The momentum spread in the $g-2$ storage ring, $\mathcal{D} \equiv {}^{\Delta p}/_{p_0} \approx 0.15\%$, leads to a change in the stored momentum over the course of the fill due to slight differences in the time-dilated muon lifetime [17]:

$$\begin{aligned} \frac{dp}{dt} &\propto e^{-t/\gamma\tau_\mu} \\ &\approx \frac{p_0}{\gamma_0 \tau_\mu} \sigma_{\mathcal{D}}^2, \end{aligned} \tag{3.19}$$

where $\sigma_{\mathcal{D}}$ is the width of the stored momentum distribution. The correction due to this effect is:

$$C_{dd} = -\frac{\Delta\omega_a}{\omega_a} = -\frac{1}{\omega_a}\frac{d\phi}{dp}\frac{dp}{dt}. \tag{3.20}$$

The phase of the muon ensemble can be described by an average over individual muons, each described by a set of spatial coordinates and injection time: $\phi_i(x_i, x'_i, y_i, y'_i, t_{0,i})$. Because the momentum dependence of the phase can come from any number of these terms, the differential decay correction is typically split into sub-effects:

$$\left.\frac{d\phi}{dp}\right|_{dd} = \underbrace{\frac{\partial\phi}{\partial p}}_{\text{'Beamline'}} + \underbrace{\frac{\partial\phi}{\partial t_0}\frac{\partial t_0}{\partial p}}_{\text{'Kicker'}} + \underbrace{\frac{\partial\phi}{\partial x}\frac{\partial x}{\partial p} + \frac{\partial\phi}{\partial x'}\frac{\partial x'}{\partial p}}_{\text{'Spin-orbit'}} + \underbrace{\frac{\partial\phi}{\cancel{\partial y}}\frac{\cancel{\partial y}}{\partial p} + \frac{\partial\phi}{\cancel{\partial y'}}\frac{\cancel{\partial y'}}{\partial p}}_{\text{N/A}}, \tag{3.21}$$

which are gathered into three contributions to C_{dd}:

$$C_{dd} = C_{dd}^{bl} + C_{dd}^{p-t_0} + C_{dd}^{p-x}. \tag{3.22}$$

To first order each of these contributions is independent of the others. The beamline contribution to C_{dd} is due to the initial phase-momentum dependence created in the DR (Section 3.1.2.1) [123]. The other two effects arise from the injection of the beam into the storage ring.

The 'kicker' ($p - t_0$) correlation is created from two effects. When the beam is injected into the storage ring, the head of the pulse begins to precess before the tail of the pulse enters the field. The non-uniformity of the kicker pulse over the muon bunch introduces a difference in spin phase over the length of the bunch. Studies have been performed using the MiniSciFi which have shown that the only source of an appreciable time-momentum correlation is the kicker, rather than any upstream beamline effect [124].

Similarly, the ‘spin-orbit’ ($p-x$, $p-x'$) correlation is created when the phase space of the beam is significantly perturbed during injection. Simulations indicate that both x and x' contribute in such a way [125]. Because the momentum of the beam does not vary with y, the y, y' coordinates do not contribute to this effect. The derivations of these parameters are beyond the scope of this work, but can be found in reference [17].

Both C_{dd}^{bl} and C_{dd}^{p-x} are expected to be stable over long timescales. However, $C_{dd}^{p-t_0}$ depends on the precise (ns-level) injection time of the muons relative to the kicker pulse. That quantity has been shown to wander (relative to the upstream accelerator signal which triggers the kicker pulse) on the order of $\mathcal{O}(10\,\text{ns})$ over the timescale of a few hours[28]. The effect of this wondering (Figure 3.25b) on the value of $C_{dd}^{p-t_0}$ is shown in Figure 3.25. It can therefore be important to analyze each dataset individually in order to ensure the correct average value for this correction for the entire Run is obtained.

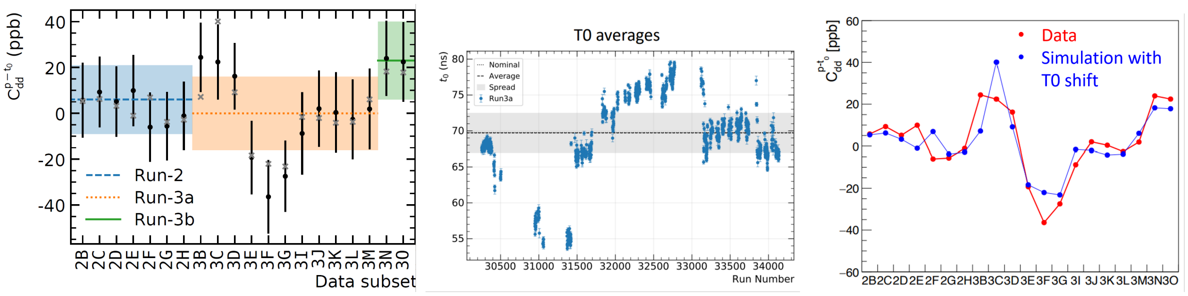

(a) Reproduced from [103]. **(b)** Reproduced from [116] **(c)** Reproduced from [126]

Figure 3.25: The ‘kicker’ portion of the differential decay correction, $C_{dd}^{p-t_0}$ can be influenced by minuscule changes in the incoming beam timing. (a) The value of $C_{dd}^{p-t_0}$ vs. dataset in Run-2 and Run-3. (b) The changes in T0 timing in Run-3a (corresponding to the orange region on the left). A similar oscillatory pattern is seen in (a). This correlation is still under active investigation. (c) Initial Monte Carlo simulations indicate that the shift in T0 is the cause of the ±20 ppb shift in C_{dd}.

In theory, the fit function for ω_a could be modified to include the momentum dependence of the lifetime and its evolution over the fill. The change in the momentum distribution from $30\mu s-650\mu s$

---

[28] This is also a confounding factor in analyses like those detailed in Section 6.1 where precise knowledge of t_0 is required.

results in a change in the average muon lifetime of

$$\Delta\tau_a = \tau_\mu(\gamma_0 - \gamma_1) \approx \tau_\mu(29.3233 - 29.32295) \approx 800\,\text{ps}. \tag{3.23}$$

Such effects are at the limit of the precision on the extraction of τ_a, and can safely be discounted.

3.6.3.5 The Phase-Acceptance Correction: C_{pa}

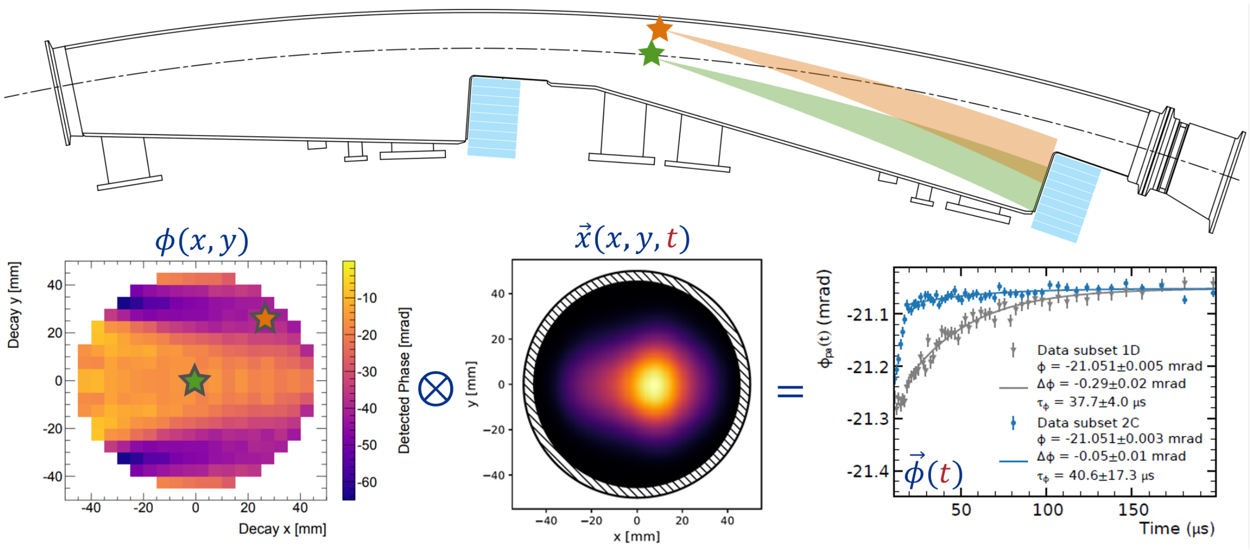

Figure 3.26: A schematic of the phase acceptance analysis. Positrons which are born in two different regions of the storage ring will have a different calorimeter acceptance and average detected phase. These factors, combined with a moving muon beam, lead to an average phase change over the course of the fill. Modified from [17].

The final, and largest, of the three phase related corrections is the phase-acceptance correction C_{pa}. This correction encapsulates the fact that the acceptance of the calorimeters is a decay position and momentum dependent effect. The implication being that if the beam moves over the course of the fill, the image of the beam as seen by the calorimeters is perturbed and a different average phase is observed at late vs. early times.

The procedure for the evaluation of C_{pa} is shown schematically in Figure 3.26. The phase $(\phi^c(x,y))$, asymmetry $(A^c(x,y))$ and acceptance $(\epsilon^c(x,y))$ map for each calorimeter c are computed using `gm2ringsim`, a `geant4` [127–129] based simulation of the storage ring. These maps are combined with the measured beam distribution from the trackers $(M(x,y,t))$ to create an average weighted phase as seen by the calorimeters over time [103]:

$$\phi_{pa}^{c}(t) = \arctan\left[\frac{\sum_{ij} M^{c}(x_i, y_i, t)\epsilon^{c}(x_i, y_i)A^{c}(x_i, y_i)\sin\left(\phi^{c}(x_i, y_i)\right)}{\sum_{ij} M^{c}(x_i, y_i, t)\epsilon^{c}(x_i, y_i)A^{c}(x_i, y_i)\cos\left(\phi^{c}(x_i, y_i)\right)}\right]. \tag{3.24}$$

The effect of this changing phase is evaluated using simulated data and a simplified ω_a fit model and from this the value of C_{pa} is extracted.

The size of the correction was reduced after a repair of the ESQ system between Run-1 and Run-2. A number of the resistors in the ESQ system were damaged throughout the course of Run-1, which meant that the scraping process did not complete before the fit start time. Instead, the beam continued to move vertically over the course of the fill. These resistors were replaced after Run-1, and the difference in the magnitude of ϕ_{pa} over the course of the fill can be seen in Figure 3.26.

3.6.4 Expectations for Corrections

A substantial amount of work is being performed across the collaboration to reduce the uncertainty on the various systematics. A visual summary of the current outlook for the various systematic effects is presented in Table 3.1. The value of most of the corrections is expected to stay approximately the same, except in two cases:

C_e: The increased kick strength in Run-3b onwards better centers the beam and will reduce the effect of the electric field.

C_{pa}: The reduction in the horizontal beam motion as an effect of the ESQ RF is expected to reduce the magnitude of the required phase-acceptance correction, as the position of the beam is more uniform over the course of the fill.

A number of better simulations, systematic measurements, and improved techniques will go towards decreasing the uncertainty associated with the various systematics nearly across the board.

One systematic is flagged as a potential cause for concern: C_{dd}. Towards the end of the Run-2/3 analysis, it was noted that the two simulation programs used to quantify this effect — `gm2ringsim` and `BMAD` — could disagree on the expected phase-momentum relationship of the stored beam by up to an order of magnitude [130]. The measurements of this quantity (Section 6.1) agreed well with `gm2ringsim` predictions, and the value of the `BMAD` prediction was found to vary dramatically with tiny changes in the injection angle of the beam. For these reasons, the discrepancy was discarded for the Run-2/3 publication. However, studies are still ongoing with `BMAD` to try and understand the source of this angular dependence and ensure that the correct injection parameters are used in all simulations. If the `BMAD` model proves correct, or if the true injection angle measured using the IBMS system proves to exacerbate the correlation, a re-evaluation of C_{dd} would be required — potentially changing the result by a significant amount.

Correction	Value [ppb]				Uncertainty [ppb]			
	Run 1	Run 2/3	Run-4	Run-5/6	Run-1	Run 2/3	Run-4	Run-5/6
C_e	489	451	⬇️	⬇️	53	32	⬇️	⬇️
C_p	180	170	∼	∼	13	10	∼	∼
C_{ml}	-11	0	∼	∼	5	3	∼	∼
C_{dd}	—	-15	∼🚩	∼🚩	—	17	∼🚩	∼🚩
C_{pa}	-158	-27	∼	⬇️	75	13	⬇️	⬇️
B_k	-27	-21	∼	∼	37	13	⬇️	⬇️
B_q	-17	-21	∼	∼	92	20	∼	∼

Table 3.1: Values of the various corrections in all runs of the Muon $g-2$ Experiment at Fermilab. Numbers for Runs 1-3 are finalized. Where numbers are not yet available the author has indicated whether the expectation is that the value will increase (⬆️), decrease (⬇️), or remain approximately the same (∼) compared to the Run-2/3 value. Areas where there is potential for a major difference, pending ongoing investigations, are indicated additionally with 🚩. These uncertainties are taken to be uncorrelated [17]. Estimates as of March 2024.

3.7 Putting it All Together

In summary, the simple relation which was introduced in Chapter 1:

$$\mathcal{R} = \frac{\omega_a}{\omega_p}, \tag{3.25}$$

is modified by all of the corrections and factors discussed in the previous sections[29] to the following [17]:

$$\mathcal{R} = \frac{f_{\text{clock}} \omega_a^{\text{meas}} \left[1 + C_e + C_p + C_{ml} + C_{pa} + C_{dd}\right]}{f_{\text{calib}} \langle \omega'_p(x, y, \phi) \times M(x, y, \phi) \rangle \left[1 + B_k + B_q\right]} \propto a_\mu \tag{3.26}$$

This quantity, however, is still only *proportional* to a_μ. As described in Chapter 1, the expression for a_μ is:

$$a_\mu = \frac{mc}{e\tilde{B}} \omega_a,$$

which can be expressed in terms of ω_p and external constants:

$$a_\mu = \mathcal{R} \frac{\mu'_p(T_r)}{\mu_e(H)} \frac{\mu_e(H)}{\mu_e} \frac{m_\mu}{m_e} \frac{g_e}{2}, \tag{3.27}$$

where g_e is the gyromagnetic ratio of the electron, ${}^{m_\mu}\!/_{m_e}$ is the mass ratio of the muon to the electron, and ${}^{\mu'_p(T_r)}\!/_{\mu_e(H)}$ is ratio of the magnetic moment of a proton in a spherical water sample at temperature T_r to the hydrogen atom, and ${}^{\mu_e(H)}\!/_{\mu_e}$ is the ratio between the magnetic moment of the hydrogen atom and the free electron. The values of these external constants, their uncertainties, and their sources are described in Table 3.2 (as of the Run-2/3 publication). In total, they contribute an additional 25 ppb uncertainty to a_μ in Run-2/3 [17].

External Input	**Uncertainty [ppb]**	**Source**
${}^{g_e}\!/_{2}$	< 1	[48]
${}^{m_\mu}\!/_{m_e}$	22	[131]
${}^{\mu'_p(T_r)}\!/_{\mu_e(H)}$	11	[132, 133]
${}^{\mu_e(H)}\!/_{\mu_e}$	Exact	[133]
Total	25	—

Table 3.2: External constants which are used in the evaluation of $a_\mu$in Run-2/3 [15]. These values can be updated as better experimental results become available.

---

[29] Two factors are present in this relation which have not been previously defined: f_{clock} and f_{calib}. These are the clock unblinding factor and the calibration constants for the NMR probes respectively. These are described in detail in reference [17, 103].

Chapter 4

Data Extraction: From Positrons to 'Wiggle Plots'

As stated in Section 3.1.4, a large number of muons are injected each fill, the majority of which are not stored. The muons which are stored yield $\approx$ 5000 positron hits in the calorimeters and $\approx$ 300 CTAGs/fill[1]. The output of the calorimeter SiPMs is continuously digitized at at a rate of 800 mega-samples per second (MS/s)[2]. This data stream, which if stored directly would yield $\approx$ 18 GB/s of data, is sent to a GPU farm to be chopped into different 'islands' of time around various pulses. The peak of each pulse is identified and then a configurable number of pre- and post-samples are saved around that peak. If a second peak is identified in an islands' time window (as would be the case for a second positron arriving in the calorimeter soon after an initial hit) the island can be automatically extended to encompass the second pulse with the appropriate number of post-samples as well. A schematic of this process is shown in Figure 4.1.

In Run-1, a trace from every one of the 54 crystals in a calorimeter was saved for each island. This yielded a data rate on the upper edge of what was achievable with the data writing capability at $g-2$ experimental hall (MC-1), and led to frequent DAQ crashes that lowered the overall efficiency of data taking. However, on average only 14/54 crystals were active in any given event (see Figure 4.2)

---

[1] 1 CTAG, or 'calorimeter tag' is denoted as 1 positron which deposits more that 1.7GeV in the calorimeter after $30\mu s$. CTAGs/fill is a standard metric for evaluating the intensity of the stored muon beam.

[2] Each 800 MS/s clock tick (c.t.) = 1.25 ns

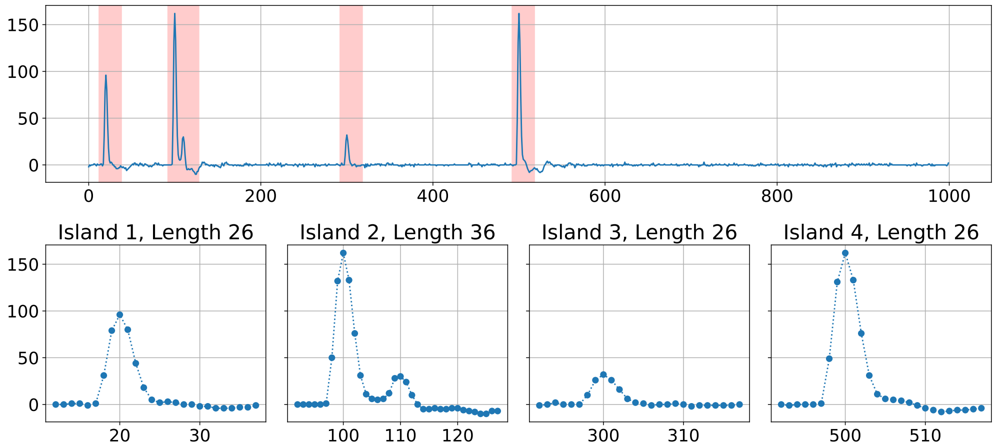

Figure 4.1: A schematic showing how individual islands are chosen from the raw SiPM datastream. Island 2 was automatically extended to include another pulse which occurred close in time. The boundaries of such islands are synchronized for every crystal in the given calorimeter.

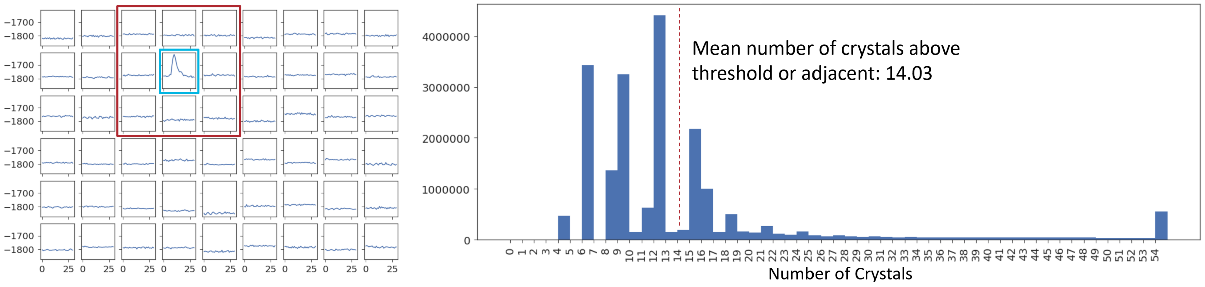

(a) **(b)**

Figure 4.2: (a) A Run-1 style island with only one crystal above threshold (blue) with an outline of the Run-2 style chopped boundary (red). (b) Average number of crystals above threshold, or adjacent to an above threshold crystal, in a given calorimeter island.

[134], and so a massive amount of this data did not contain any physics information. During the summer shutdown between Run-1 and Run-2, a new island chopping algorithm was developed and tested. This island chopping algorithm would discard data from any crystals that did not contain, or were not immediately adjacent to crystals that contained, pulses above the trigger threshold. For example: in a given island for which only one crystal was above threshold, only a 3x3 grid of crystals would be saved rather than all 54 (see Figure 4.2a). In practice, this amounted to a 75% reduction in calorimeter island data. Because of this and other improvements during the 2018 summer shutdown, the average uptime of the experiment rose from $\approx 75\%$ in Run-1 [135] to $> 90\%$ in Run-2 [136]. Tests were performed on Run-1 data by imposing this filter artificially and the shift in ω_a was determined to be negligible (< 3 ppb on a dataset with a statistical precision of ≈ 1 ppm).

As this change was made, special trigger modes were also implemented at various prescales. For instance, the Run-1 style full island readout was implemented with a prescale of 1/15 fills in Run-2+ and a ‘shadow trigger’ readout[3] was implemented at a prescale of 1/15 in Run-5+. Data from these special triggers are used for evaluation of systematics and were critical for ensuring that no data was lost or corrupted in the island chopping process.

The $g-2$ experiment uses MIDAS[4] as its data aquisition system (DAQ) [137]. As these islands are chopped, they are saved to MIDAS format binary data files. The file size recommended by Fermilab for large scale processing on its computing grid[5] is around 2GB, and so MIDAS was configured to save a new ‘subrun’ file once that amount of data was accumulated. Each subrun contained approximately 100 muon fills, which are stored as individual MIDAS ‘events’. Other event types are also read out: asynchronous events from slow control systems, laser fills in between muon bunches for tracking gain changes, kicker/ESQ monitoring data, etc. A run[6] consists of ≤ 496 subruns. When this count is reached, midas will automatically begin a run transition. When data

---

[3] In this mode, an island is triggered to be chopped out 1 cyclotron period after every real pulse, regardless of whether a positron hit was detected in that time range. This is useful for quantifying systematics due to ‘unseen’ pileup.

[4] Maximally Integrated Data Acquisition System

[5] Referred to throughout the text as ‘Fermigrid’ or simply ‘the grid’

[6] Somewhat unfortunately, for historical reasons only context and capitalization are used to distinguish between a ‘Run’ (a single years data taking) and ‘run’ (a single hours data taking).

was being taken in nominal conditions, this typically took between $1 - 1.5$ hours. This automatic transition ensures that a copy of the midas online database (ODB) is saved at least this often, which can be useful for tracking down any changes in experimental conditions during analysis.

4.1 A Single Fill Analysis: Fitting and Clustering

The $g-2$ reconstruction software is based on *art* [138], a package developed by Fermilab to provide a common framework for physics experiments. The *art* framework is designed to handle an analysis chain on an event-by-event basis, passing data between various analysis modules (for instance passing the results of a fitting algorithm to an energy calibration algorithm), and keeping track of the provenance of the data generated in the analysis chain. In this way, users of the software need only be concerned with writing their analysis code and allow *art* to handle low level details of memory management, file handling, etc.

The user interface to *art* consists mainly of three types of modules: producers, filters, and analyzers. Producers take in one or many inputs and create an art 'dataproduct'[7]. These inputs can be external objects (database entries, data read from input files, etc.) or the output from other producer modules. Filters are like producers, with the caveat that they produce only a boolean value and can control the flow of data through an analysis chain. The data quality control (DQC) modules (see Section 4.2.3.3) are implemented as such filters. Finally, analyzers take in one or more dataproducts and create an external output. In this analysis, these are typically ROOT [139] histograms or `TTrees`. The implementation of these modules is done in `C++`, and they are configured at runtime using a Fermilab Hierarchical Configuration Language (FHiCL or fcl) file.

The reconstruction chain used in this analysis (dubbed 'Recon West' or 'RW') was initially developed at the University of Washington by A. Fienberg in the lead up to the 2017 commissioning run of the experiment [6]. Since then, a number of improvements have been made to the reconstruction chain by J. Hempstead, H. Binney, and the author [84, 91]. The logical flow of the sections below follows from these references. Briefly, the steps required for the reconstruction of positron data in the UW analysis are:

---

[7] Essentially a C++ class, but with standard boilerplate which allows *art* to integrate them into its' event loop.

1. Correct for a known hardware jitter in the raw waveforms.
2. Fit the raw traces using a pulse template and extract the uncalibrated energy and time.
3. Align the fit results in time relative to the T0 trigger pulse.
4. Calibrate the energy of the fits.
5. Perform any needed corrections to the individual crystal fits (long term gain drift, in-fill gain sag, etc.).
6. Pass the energies through a clustering algorithm to extract the total energy deposited by the positron(s) in the entire calorimeter.

Each one of these is implemented as one or more *art* producer modules. Multiple independent evaluations and checks of each step in this process have been performed. In addition, multiple parallel efforts at reconstruction have been developed over the years. Comparisons to other reconstruction methods have been performed (see Section 4.1.6.1 and references [140, 141]).

4.1.1 Odd-Even Pedestal Correction

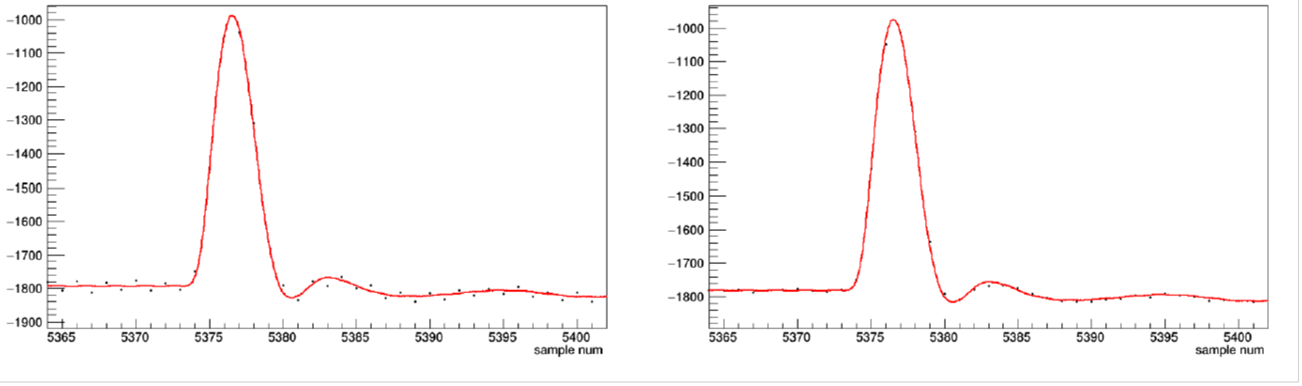

Figure 4.3: A single trace before and after the application of the odd-even pedestal correction. The y-axis represents uncalibrated ADC counts. Reproduced from [91].

The 800 MS/s digitization rate is achieved at a hardware level by utilizing two 400 MS/s digitizers which are offset from one another by 1/2 of a cycle. These two independent digitizers in general have slightly different pedestal levels. Thus the ‘raw’ trace which emerges from the digitizers has a jagged shape which must be corrected (see Figure 4.3). The shift varies between 0-10 ADC units (out of a total dynamic range of 4096 ADC units). Since each digitizer reads out 5 calorimeter channels, a total of 264 of these constants were calculated. This shift was recalculated at the start of each run, but was never found to change appreciably. This offset is calculated by taking the difference between odd and even samples of each waveform when a pulse is absent. This shift is applied before the trace is passed to the fitter.

4.1.2 Template Fitting

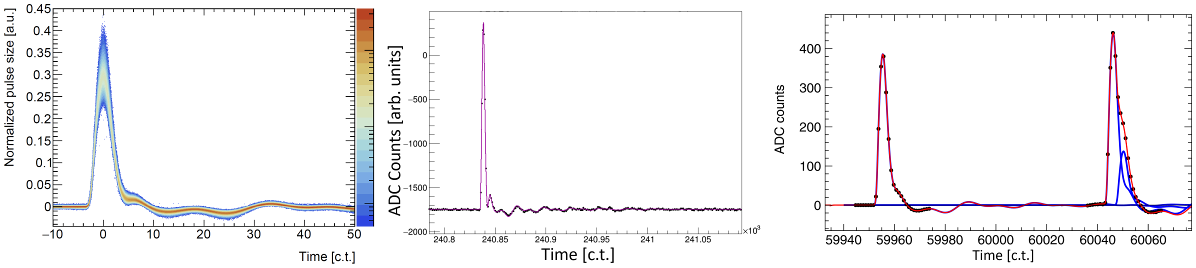

(a) Reproduced from [91] **(b)** Reproduced from [84] **(c)** Reproduced from [103].

Figure 4.4: (a) An example of a 'fuzzy' template created by overlaying many high-energy traces from a single crystal. (b) An example single pulse fit from the template building process. The extended island length shows the scale of the tail, and how well the template reproduces that behavior. (c) A chained island fit. The ringing tail of the first pulse impacts the second island and must be accounted for.

Because of the linearity of the $g-2$ calorimeter response to incident pulses over a wide range of energies, and due to the high likelihood of pileup occurring early in the fill, the most robust method found to reconstruct the positron energies and times was to fit each trace to a known template. This yields excellent timing resolution and robust behavior in the presence of many pileup pulses. The pulse fitting algorithm is able to distinguish positrons with 100% accuracy so long as they are separated by ≥ 2.5 ns[8]. A template fitter module was constructed which identifies pulses using two parameters per pulse: integral and peak time [6].

Specialized runs were taken at the start of each run to construct pulse templates from data. Normally, islands have a limited number of pre- and post-samples around the peak (8 and 18

---

[8] This is imposed as a hard threshold (known as the artificial dead time or ADT) in analysis. The fitter will not attempt to resolve two pulse which are closer than this in time.

respectively) but for this exercise that number was extended to 50/250. This was done to capture the ringing tail of the SiPM pulse and allow for ‘chaining’ islands together. This is required when a second pulse arrives before the effect of the first pulse has damped away completely. Data is taken for ≈ 6 hours in these conditions in order to accumulate enough statistics ($\approx 50,000$ unique high-energy positron hits) in the coolest crystals (those furthest from the beam). It has been shown that the templates are insensitive to the positron energy, beam rate, and time in fill used to generate them [6, 91]. It is thus possible to choose a sample of late-time (i.e. low-pileup), high energy traces to compute the templates without loss of generality. Templates are built by identifying the peak time of each pulse and overlaying the normalized pulse shape for many pulses (see Figure 4.4 left). The profile of this histogram is used to create a cubic spline, which is saved to a ROOT file along with its cumulative distribution function (CDF). Two additional templates are also created for laser pulses: one for the standard laser, which illuminates the crystals every fill, and one for the ‘crossed’ laser, which is only used during specialized calibration runs (see Section 4.1.5).

Every time a crystal is swapped, and at the start of each Run year, a new set of templates is generated. These do not vary significantly from Run to Run, except in the case of crystals which have experienced some form of damage. For instance, the SiPM on Calorimeter 11/Crystal 18 had an amplifier which malfunctioned during Run-3. This dramatically altered the tail shape of the beam and laser pulses. Some crystals in Calorimeter 6 (0 and 9) were damaged by water infiltration[9] in between Run-1 and Run-2. The PbF_4 crystals, being moderately hydroscopic, develop a milky white layer on their surface after contact with water. These crystals were only slightly damaged, but in such a way that this milky white coating altered the amount of laser light they received. The template fitter module uses a database table to determine which template to use when fitting based on the run number of the island being fit.

An iterative fit procedure is performed using these templates to extract the integral ($\propto$ the deposited energy) and peak time of each pulse in the crystals [6]. The highest amplitude sample is identified and, if above a certain threshold, is used as the seed for the first fit. In Runs 1-3, this threshold was in hardware units, approximately 50 ADC counts. Due to differing energy/gain

---

[9] A polite term for 50 gallons of water falling onto calorimeters 5 and 6 from the ceiling.

calibrations, each crystal could have a slightly different minimum energy threshold. In the Run-4 reconstruction, this threshold was equalized to be ≈ 20 MeV for all crystals [142].

After the first pulse is found, the fitter repeats the process if any of the fit residuals are above that same amplitude threshold[10]. The process continues until the χ^2 of the fit no longer improves with any additional pulses above threshold. For islands in which a laser pulse is present (characterized by 50/54 of the crystals in a calorimeter being above threshold at once) the fitter is able to automatically select whether to use the beam or laser template when performing the fit, again based on whichever one results in a lower χ^2 value. An example of fits to beam data can be seen in Figures 4.4b and 4.4c.

4.1.3 Timing Corrections

For each calorimeter channel (crystal j in calorimeter i, for instance), the following correction to align all of the times is performed:

$$t'_{ij} = t - t_{\text{sync}} - \kappa_{\text{T0}}^{\text{sync - beam}} - \kappa_{\text{calo}}^{i} - \kappa_{\text{crystal}}^{j} \tag{4.1}$$

where t is the uncalibrated clock time, t_{sync} is the time that the laser sync pulse arrives at each detector, $\kappa_{T0}^{\text{sync - beam}}$ is the difference between when the sync pulse and beam pulse were observed in the T0 detector, and κ_{calo}^{i} ($\kappa_{\text{crystal}}^{j}$) are calorimeter (crystal) level constants calculated once per Run. These individual constants encapsulate both electronics and laser fiber length differences. Each of these constants is calculated using beam data.

4.1.3.1 Intra-Calorimeter Timing Corrections

The front face of the $g-2$ calorimeter crystals measures 25 mm on each side, which is comparable to the Molière radius $R_M^E = 22\,\text{mm}$ [108]. Because of this, the preponderance of showers will be shared amongst multiple crystals. In order to properly recombine these showers in the presence of pileup, the calorimeter crystals need to be aligned in time. The internal time alignment is bootstrapped

---

[10] In the Run-2/3 data, the primary and secondary fit thresholds in the UW reconstruction differed which contributed to a gain-like effect. See Section 4.1.6.1 and [141] for more details

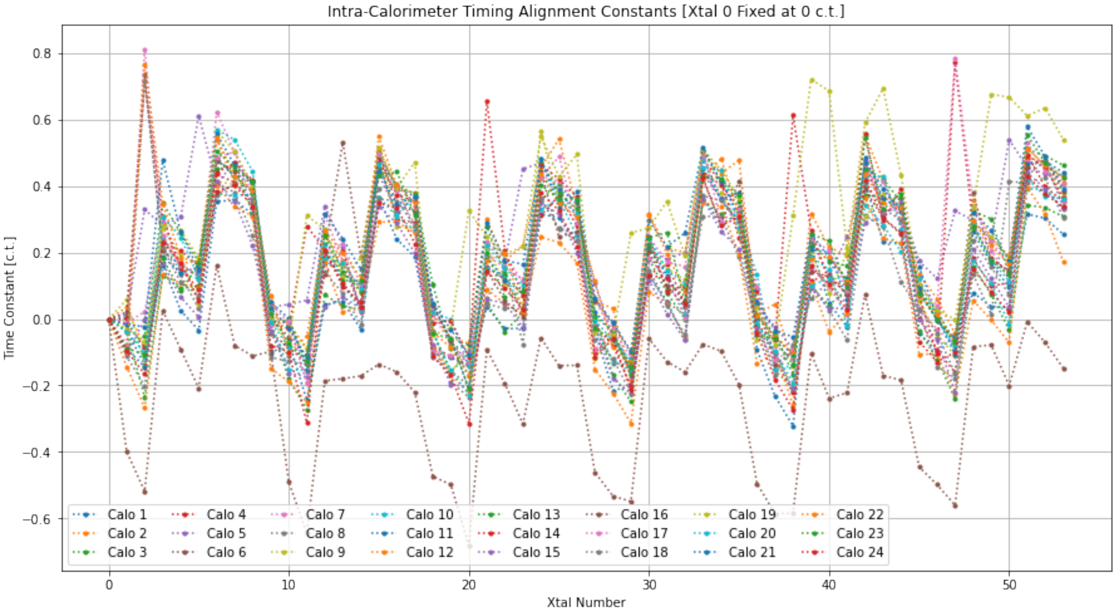

Figure 4.5: The intra-calorimeter timing offsets calculated for all calorimeters in Run-6. The relative offsets between crystals are tiny, usually < 0.5 clock ticks (1c.t. $= 1.25$ ns).

from the data itself. Showers which share energy across multiple crystals are identified, and the constraint that the time offset between their peaks should be 0 is imposed. From this, a system of equations is constructed:

$$\Delta_{ij} = \kappa^{i}_{\text{crystal}} - \kappa^{j}_{\text{crystal}} \tag{4.2}$$

for each pair of crystals that are aligned horizontally or vertically[11]. Since it is known that the time resolution of the detectors is energy dependant, a minimum energy threshold of 200 MeV is imposed in any given crystal used for this analysis [84, 91]. This system yields 93 equations which can be minimized via least squares. In this minimization, each side of Equation (4.2) is weighted by the inverse of the fitted error on the mean time difference to account for differences in statistics. By convention, $\kappa^{0}_{\text{crystal}} \equiv 0$ for each calorimeter. Two independent methods of performing this minimization were tested, one developed by J. Hempstead using Eigen [91, 143] and one by the author using scipy [144]. Both yielded consistent results. The time offsets extracted using this

---

[11] This is not exactly true, as it does take the shower some time to develop and spread through the crystals. However, this time is small compared to the time scales of the reconstruction and so it can safely be ignored.

procedure can be seen in Figure 4.5. All channels are offset by $< \pm 1$ c.t. from each another.

4.1.3.2 Inter-Calorimeter Timing Corrections

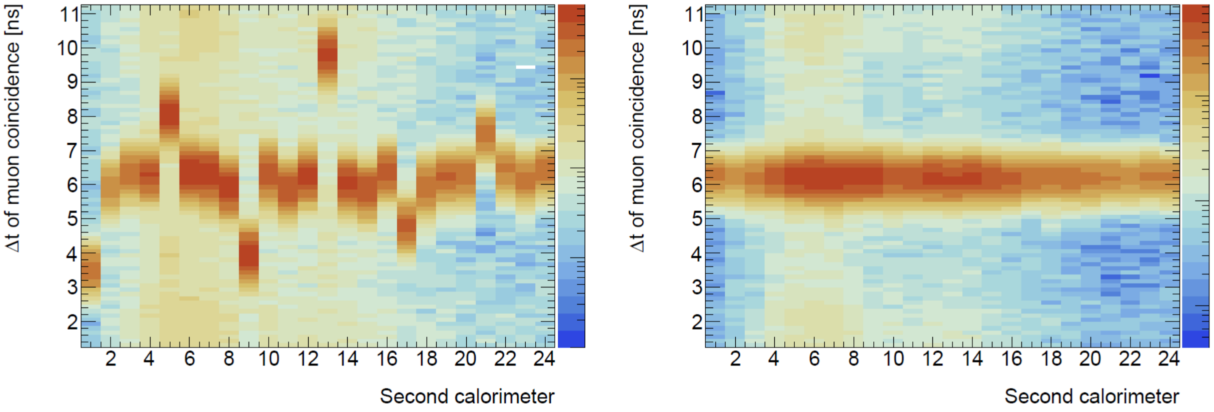

Figure 4.6: Inter-calorimeter time shifts before and after calibration. Reproduced from [91].

Once the crystals within the calorimeter are aligned, each of the calorimeters are aligned in time with respect to a common reference point. This point is chosen to be the intensity weighted maximum of the beam entrance pulse from the T0 detector. Since T0 and calorimeter 22 share a common laser fiber, all calorimeters are first aligned with respect to calorimeter 22 and then all calorimeters are globally aligned based on the common offset from calorimeter 22 to the T0 beam pulse.

A great deal of effort went into making sure the maximum number of muons which were injected are stored on stable orbits until they decay. To measure the relative offsets in time from one calorimeter to the next, however, this aspect of the experiment was made significantly worse. At the start of each data taking Run, a series of scattering targets were inserted. Muons which impact these targets lose energy and are knocked off their stable orbits. The effective muon lifetime in this mode drops from 64.4 μs to $\approx 35\,\mu$s. Muons which scatter off these targets will spiral inward and have a good chance of impacting the calorimeters. When they do, they deposit a distinct MIP (minimum ionizing particle) energy peak of $\approx$ 170 MeV. A clean sample of these muons is identified in the data by looking for triple coincidences of such energies in adjacent calorimeters (see Figure 4.7). Another system of equations is set up to solve for the relative time offsets of the

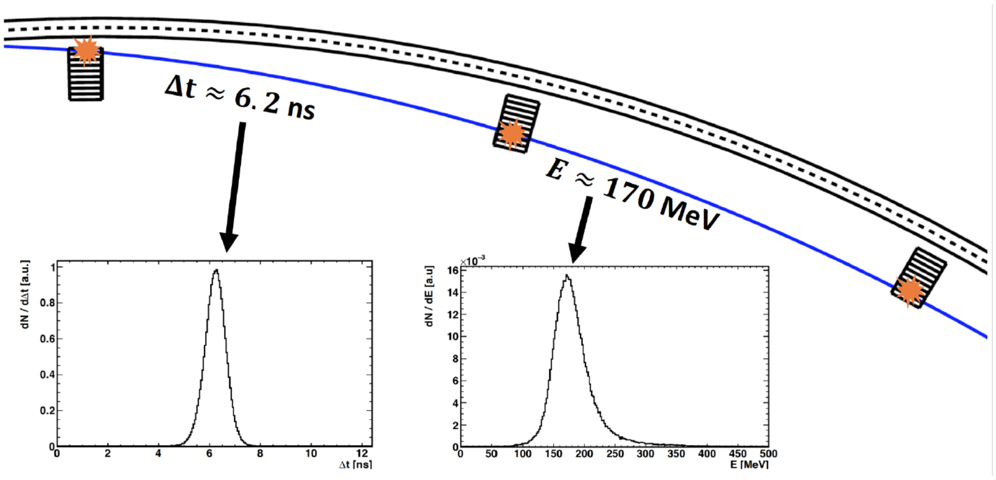

Figure 4.7: Diagram showing the trajectory of a typical lost muon triple coincidence, alongside the (calibrated) energy and δt distributions. Reproduced from [6].

different calorimeters:

$$\begin{aligned}\Delta t_{ij} &= t'_i - t'_j \\ &= (t_i - \kappa^i_{\text{calo}}) - (t_j - \kappa^j_{\text{calo}}) \\ &= \kappa^i_{\text{calo}} - \kappa^j_{\text{calo}} - \alpha \end{aligned} \tag{4.3}$$

where α represents the physical travel time between the detectors and κ^c_{calo} is the individual time offset for each calorimeter c. Setting $\kappa^{22}_{\text{calo}} \equiv 0$, this system of equations can be solved and the detectors aligned by subtracting their individual t constants. The time difference for triple coincidences before (left) and after (right) this procedure can be seen in Figure 4.6. The structure of the $g-2$ laser calibration system can be seen clearly in the before image: there are six laser heads and so at every fourth calorimeter a jump in the uncorrected time difference is seen. This corresponds to a slightly different path length in the laser fibers between each of the six laser heads. As a cross check, the value of α extracted from the system of equations above — 6.2 ns, as seen in the y-value of Figure 4.6 right — can be compared to the expectation from the travel time for a lost muon from the cyclotron period of the ring:

$$\frac{1}{24}T_{\text{cyc}} = \frac{1}{24}(149.2\ \text{ ns}) = 6.2\,\text{ns}\,\checkmark \tag{4.4}$$

4.1.4 Energy Calibration

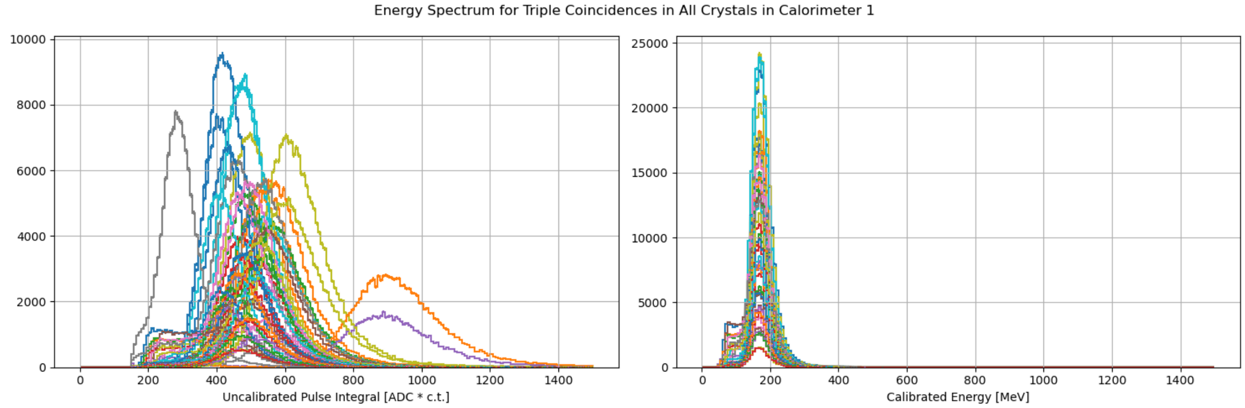

Figure 4.8: Pulse integrals for triple coincidences in Calorimeter 1 before and after energy calibration.

From the same lost muon data, an energy calibration for each of the crystals can be performed. In the monolithic calorimeters of the previous generation $g-2$ experiment, energy calibration was able to be performed using the positron energy spectrum itself [13]. In the current experiment, with the energy of a single positron being shared across multiple crystals, this was not nearly as straightforward. Instead the 170 MeV[12] peak that a throughgoing muon deposits in the 15 cm length of the calorimeter crystals was used. Only the energy deposited by the middle hit in a triple coincidence is used in this analysis, so that any average path length difference between crystals is minimized. Here, some care must be taken to avoid other particles which might also leave a MIP signature (such as deuterons or protons). Additional stringent time and energy cuts are used to remove them from the dataset as much as possible. Both of those species are subdominant, so fitting the highest intensity peak will still yield an excellent calibration. The energy spectrum of lost muons is created for each crystal and fit to a gaussian. The calibration constants are extracted from the mean of this gaussian fit: $170\,\mathrm{MeV}/\bar{E}$. The results of applying these calibration constants to the lost muon data can be seen in Figure 4.8.

---

[12] The value of this energy deposit is less important than having a standard candle that all crystals can be calibrated against.

4.1.5 Gain Corrections

Once the fit results are calibrated, a series of gain corrections to the reconstructed energies are required before data from the individual crystals can be combined. If uncorrected for, these gain effects could lead to a bias in the extracted value of the precession frequency. For instance, because of the gain sag in the detectors caused by the initial 'flash' of particles entering the ring, positrons which are detected earlier in the fill will be reconstructed with a different energy than those detected later in the fill (after the system has recovered). This effectively leads to an energy threshold change over the course of the fill. Since the observed $g-2$ phase is energy dependant (see Figure 5.37 in Section 5.2.5), a time changing energy threshold could introduce a time changing phase which pulls the fitted value of ω_a (as demonstrated in Equation (3.13))

The gain of each channel must be individually calibrated to a relative precision of better than 10^{-3} in order to meet design goals for gain related systematics [76]. The laser calibration system described in Section 3.4.3 is integral to the extraction of these gain calibrations. There are three timescales on which a gain correction must be done: $\mathcal{O}$(hours/days), $\mathcal{O}(\mu\text{s})$, and $\mathcal{O}$(ns)

Systematic effects stemming from these gain corrections are evaluated as part of the precession frequency analysis (see Section 6.4). A 'residual' gain-like effect not described here (and not tracked by the laser system) is observed in the calorimeter data, which is discussed in Section 5.4.2.1.

4.1.5.1 Hours to Days: Long Term Gain Correction (OOF)

The first correction is the long term gain correction, also known as the 'out of fill' or 'OOF' correction. This represents the long term drift of the gain of the system from a reference value determined at the start of each Run[13]. The gains of the $g-2$ SiPMs are highly temperature dependent (see Figure 4.9). In Runs 1 and 2, the temperature of the experimental hall was not well controlled. This led to large swings in temperature from the start of each Run (late fall) through the end (early summer). This overall shift, coupled with a diurnal oscillation of temperatures, meant that the OOF correction was important for being able to compare the energy scale of data taken many months apart. In Run-3, a new temperature control system was installed which eliminated

---

[13] By convention this is set to be the point where the lost muon data for the energy/timing calibration is acquired, but this is not required.

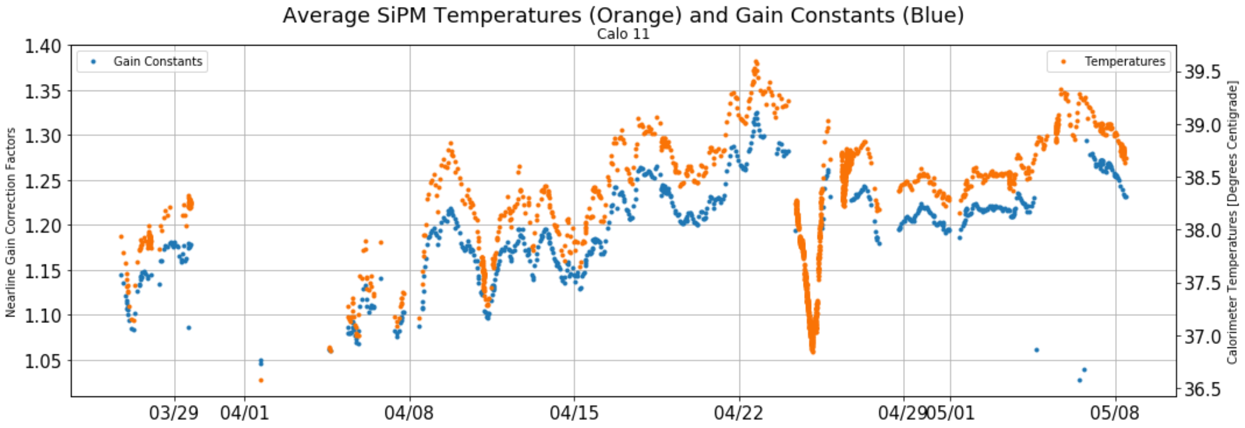

Figure 4.9: The long term gain drift of a single calorimeter compared with the average temperature reading for Run-2. Both diurnal oscillation and seasonal trends in temperature can be seen. Reproduced from [91].

the diurnal swings in temperature and removed the baseline shift for all but the hottest of months (some variation can be seen again at the end of Run-4 and 5 for instance, see Figure 4.10.).

This gain correction is monitored using 'out-of-fill' pulses from the laser calibration system (Section 3.4.3). In between muon injections, 4 laser pulses are sent to each of the 1296 crystals and a series of laser monitor detectors. The amplitude of the pulse at the current time, corrected for any drift in the laser itself as determined by the monitor detectors, is compared with the reference amplitude and a simple scale factor is applied [103, 110].

This effect does not couple to ω_a directly, except for its ability to dilute the ω_a oscillation signal. As will be described in Chapter 5, the statistical precision of the analysis is maximized with a precise weighting of different positron energies. An incorrect correction will simply apply sub-optimal weights to the combination of data across many months, resulting in a higher statistical uncertainty.

4.1.5.2 μs: In Fill Gain Correction (IFG)

The in-fill gain correction describes the change in the SiPM gain from the beginning to the end of the fill. When a pixel discharges, the bias voltage across the SiPM drops as the charge is replenished. When this happens for many pixels at once (for instance, during initial beam injection where the detector systems are overwhelmed), the change in the voltage across the SiPM can be significant.

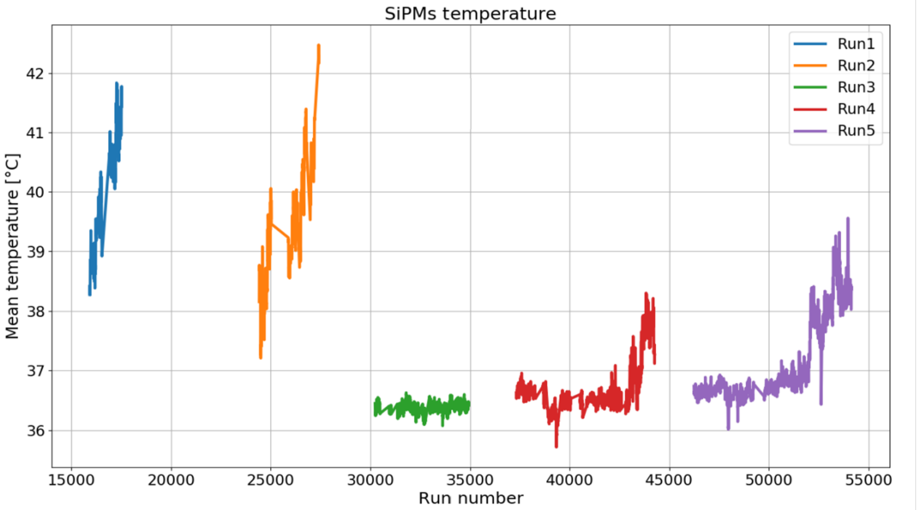

Figure 4.10: Average hall temperature for Run-1 through Run-6. Reproduced from P. Girotti [145].

This voltage sag reduces the response of the SiPM to subsequent pulses until the capacitors in the calorimeter electronics are able to re-establish the nominal bias voltage difference. The time scale at which the capacitors are able to deliver this charge to the SiPMs is $\mathcal{O}(10\ \mu\text{s})$.

Up to 9% of the positron data was sacrificed in order to measure this correction in-situ. Every N muon fills[14], 3 laser pulses are injected $185\,\mu s$ apart. These laser pulses are walked forward in time by $2.5\,\mu s$ after each subsequent laser fill. Using the response of the SiPMs at that time to the standard candle of the laser pulse, the gain sag for each SiPM is mapped throughout the fill. This is fit to:

$$g(t) = A\left(1 - ae^{-t/\tau}\right), \tag{4.5}$$

for each crystal. An example of a gain recovery curve for a single crystal can be seen in Figure 4.11. The a and τ parameters can vary significantly from crystal to crystal due to differences in the individual electronics chain as well as the amount of beam ‘splash’ each crystal sees. Crystals in the kicker region calorimeters (roughly calorimeters 5-8) are impacted the most by particles which are injected but are not stored, and so their IFG amplitudes are the highest. Calorimeters on the

---

[14] N varied across Run years. In Run-1/2, $N = 11$. Later in Run-3 N was raised to 22 [146]. N was chosen such that each of the 8-bunch shapes would be equally populated with laser pulses.

opposite side of the ring (roughly 18-22) see almost no splash and so are virtually unaffected.

The lifetimes (τ parameters) extracted from these in-situ curves are verified using specialized laser runs, where a burst of laser pulses are injected into the calorimeters from the 'crossed' laser head to simulate the injection splash, and then a probe pulse from the standard laser is injected in after a certain delay time [146]. Efforts have been made to quantify any effect these laser pulses introduce to the data, in order to recover this statistics from these fills (see Section 6.3).

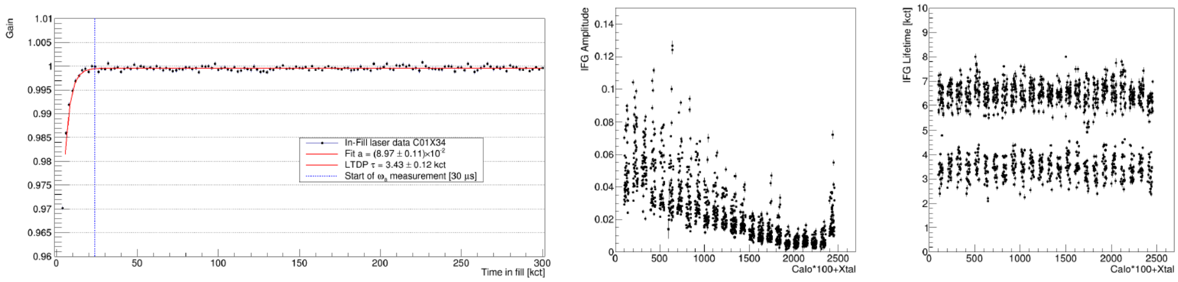

Figure 4.11: Left: An example of the IFG curve extracted for a single crystal. The effect has mostly dissipated by the time the ω_a measurement period starts at $30\mu s$ after injection. Center/Right: Extracted parameters for the IFG correction. The bi-modal distribution of lifetimes is a known effect of two slightly different electronics chains responsible for providing the bias voltage to the SiPMs. Reproduced from P. Girotti [146].

4.1.5.3 ns: Short Term Double Pulse Correction (STDP)

The final correction to be applied is the short term double pulse (STDP) correction. This is the shortest timescale correction, describing the gain sag experienced by a pileup pulse which arrives $\mathcal{O}$(ns) after an initial pulse. When a photon from an initial particle hits a SiPM pixel, it will cause it to discharge and deliver a pulse of charge to the on board amplifiers. Once a pixel fires, it requires a certain amount of time in order to recharge and re-enter Geiger mode. During this time such pixels are effectively inactive. A secondary particle which deposits energy in a crystal before all pixels in the SiPM recharge can therefore have its reconstructed energy artificially depressed by inactive pixels.

This recovery curve, which nominally[15] has the same functional form as the IFG function given in Equation (4.5), is measured using specialized laser runs. In these runs the standard and crossed

---

[15] This function has some additional temperature dependence, which modifies the simple recovery function and is beyond the scope of what is described here. See the following for more details: [17, 146].

lasers are fired sequentially with different time offsets: $1 < \Delta t[\text{ns}] < 100$. The reconstructed energy of the second laser pulse is compared to a reference amplitude absent the primary pulse. From this the gain sag is evaluated. The recovery time constants are $\mathcal{O}(10\,\text{ns})$. An example of the curve can be seen in Figure 4.12.

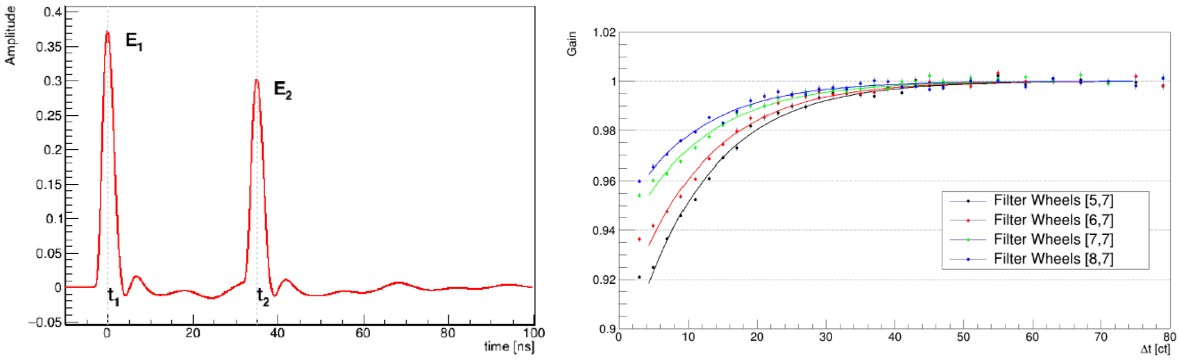

(a) **(b)**

Figure 4.12: (a) An example of the STDP data taking mode. E_1 and E_2 are pulses from the primary and crossed laser heads respectively. (b) The recovery curve for different laser intensities. The gain sag of the second pulse depends on the energy of the first pulse. Reproduced from P. Girotti [146].

4.1.6 Clustering in the UW Analysis

Once all of the timing and energy corrections are applied, the hits within a single island are combined together to form one or more clusters. The clustering algorithm described here was developed by A. Fienberg [6], with significant improvements made by H. Binney [84] for the Run-2/3 analysis. In Run-1, only the timing for the crystal hits was used when reconstructing clusters. However, the time resolution for low energy hits is known to be significantly worse than that of high energy events [108]. Thus for the Run-2/3 analysis, the clustering algorithm was altered to allow low energy hits more leeway to be included in a cluster. This was done by weighting the values used in the clustering by the inverse of the known timing resolution at that energy:

$$E_{eff} = \frac{E_1 E_2}{\sqrt{E_1^2 + E_2^2/2}} \tag{4.6}$$

$$\Delta t'(E_{eff}) = \frac{\Delta t}{\sigma_{\Delta t}(E_{eff})} \tag{4.7}$$

The logic for the clustering algorithm used in the Run-2/3 and Run-4+ analyses is as follows. There are two configurable timing thresholds t'_{low} and t'_{high}. A time ordered list of all of the reconstructed hits in a single island is created, and the first hit in this list is taken to be the ‘seed’ of of a new cluster. For each subsequent hit, the new effective energy and $\Delta t'$ is computed. The following algorithm determines whether this hit belongs in the cluster or whether a new cluster should be created:

$\Delta t' \leq t'_{low} \rightarrow$ This hit is added to the existing cluster

$t'_{low} < \Delta t' \leq t'_{high} \rightarrow$ The next hit in the list is examined. A new $\Delta t'_2$ is calculated, considering only this hit and the next hit. If $\Delta t' < \Delta t'_2$, this hit is added to the existing cluster. Otherwise, a new cluster is created this hit is treated as its seed.

$\Delta t' > t'_{high} \rightarrow$ A new cluster is created and this hit will be treated as that clusters seed.

These clusters are used in the creation of the analysis histograms (see Section 4.2.4). During the production, the same pulse fitting and clustering techniques described here are applied to pileup islands generated from the empirical pileup correction (see Section 5.2.2).

4.1.6.1 Reconstruction Comparisons in Run-1 and Beyond

In Run-1, the author was responsible for performing a comparison of two[16] parallel reconstruction algorithms. These algorithms were developed at UW and Cornell, and had a fundamental difference in their approach to reconstructing the positron energies and times. The UW reconstruction (‘Recon West’ or ‘RW’) described above fits each crystal individually and then combines the resulting fits together based on energy/timing information to form clusters. The Cornell reconstruction (‘Recon

---

[16] A third algorithm,‘ReconITA’, was not yet developed

East' or 'RE') performs a simultaneous fit to the highest energy crystal and all the crystals that surround it. The boundary of this fit can grow to accommodate showers which extend beyond a 3×3 grid, and can be done iteratively to pick up on pileup pulses. The advantage of this style of simultaneous fit, which locks all the peak times of the crystals together, is that it is more sensitive to low energy pulses on the edge of the shower which might be below the threshold of a standalone fit. It can also be less sensitive to noise, since it can fit arbitrarily small (or negative) pulses and on-average cancel out uncorrelated noise. Such an algorithm can also reject pileup at a much higher rate than a RW style fit due to its inherent spatial separation.

However, that spatial separation comes at a cost — a great deal of positrons will pass through material[17] on their way to the calorimeter, and thus there is a good opportunity for scattering to produce secondary particles. It has been shown that $\approx 1.5\%$ of the events in the calorimeter have spatially-separated, time-coincident 'secondaries' which are consistent with such scattering [84]. A RW style algorithm will properly handle these, as its clustering is based purely on time coincidences, while RE will potentially classify them as two distinct events.

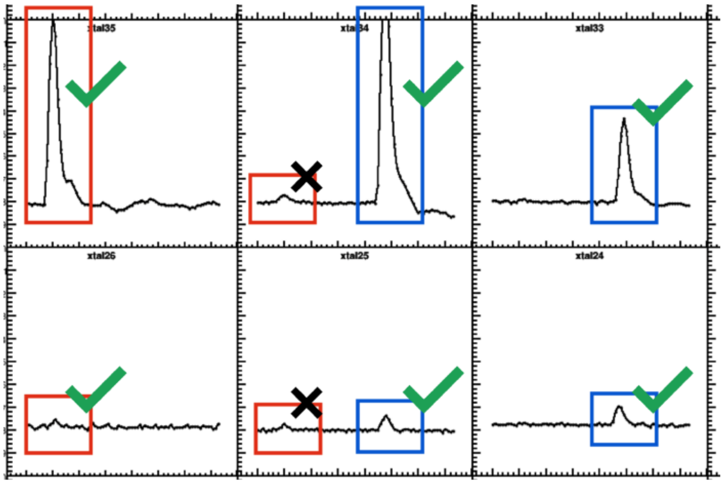

Figure 4.13: A graphic showing the effect of multi-cluster island bug in the Run-2/3 UW reconstruction. Reproduced from S. Foster [141].

Details of the comparison between the two reconstructions performed by the author can be found in reference [140]. At the level of the Run-1 analysis, no difference between the two reconstructions

---

[17] Kicker or ESQ plates primarily, or tracker chambers for those positrons behind a calorimeter.

was observed that would impact the physics result. However, with the higher statistics of Run-2/3 a new effort was made by others in the collaboration to re-evaluate these results, especially in light of the ‘residual gain’ effect (see Section 5.4.2.1). There it was discovered that the RW algorithm had a slight bias which was not present in RE. When fitting an island with multiple clusters, RW applied a different threshold to secondary pulses than it did to primary pulses (see Figure 4.13) [141]. The result of this configuration was that a pulse could be either fit or discarded depending on whether there was a pileup pulse in the same island. Since pileup is more likely early in the fill, this resulted in an effective change of the energy scale early to late in the fill. This was discovered after production of the Run-2/3 data was complete, so a correction was necessary to account for this effect in the data. In the UW analysis, it was shown that this bug would cause a gain-like effect consistent with the form of the ‘residual gain’ correction (see Section 5.4.2.1). It was determined that this was responsible for $\approx 70\%$ of the residual gain correction amplitude in the RW reconstruction. The source of the remaining $\approx 30\%$, common to both RW and RE, remains unknown and is under investigation. A fix for this bug was applied before the production of Run-4+ took place, which reduced the magnitude of the correction needed accordingly.

4.2 Many Fills: Multi-PB Data Handling

In total, excluding systematic runs and those data removed by Data Quality Control (DQC) cuts, in Run-2/3 there were $6.37 * 10^7$ muon fills and in Run-4/5/6 there were $> 2.35 * 10^8$ fills (a $> 3.5\times$ increase). This amounts to $> 7.3\,\text{PB}$ (1.5 PB for Run-2/3 vs. 5.8 PB for Run-4/5/6) of raw production data which needed to make its way through the full production chain to enter the final data analysis.

4.2.1 Nearline Analysis

The time scale for the full production to be ready, including final calibration constants and DQC from all aspects of the experiment was $\mathcal{O}(6\,\text{months})$ on average[18]. However, some systematic studies

---

[18] Although this time was reduced for every run, with great effort from the $g-2$ production team. In Run-6 a running production, keeping up with the data with only a couple weeks of delay, was achieved.

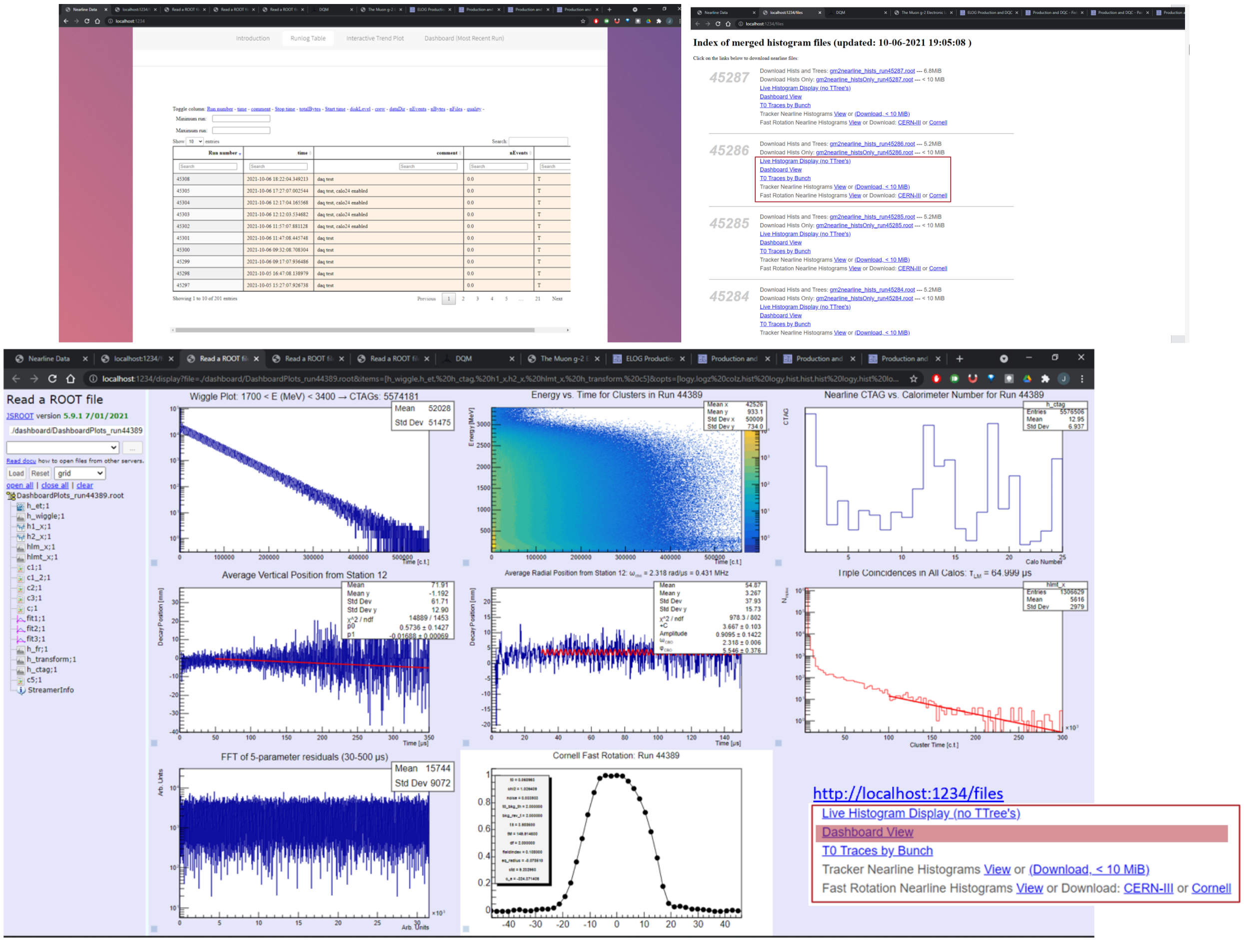

Introduction | Runlog Table | Interactive Trend Plot | Dashboard (Most Recent Run)

Toggle column: Run number - time - comment - Stop time - totalBytes - Start time - diskLevel - crew - dataDir - nEvents - nBytes - nFiles - quality -

Minimum run:

Maximum run:

Show 10 entries

Search:

Run number	time	comment	nEvents	
45308	2021-10-06 18:22:04.349213	daq test	0.0	T
45305	2021-10-06 17:27:07.002544	daq test, calo24 enabled	0.0	T
45304	2021-10-06 12:17:04.165568	daq test, calo24 enabled	0.0	T
45303	2021-10-06 12:12:03.534682	daq test, calo24 enabled	0.0	T
45302	2021-10-06 11:57:07.881128	daq test, calo24 enabled	0.0	T
45301	2021-10-06 11:47:08.445748	daq test	0.0	T
45300	2021-10-06 09:32:08.708304	daq test	0.0	T
45299	2021-10-06 09:17:07.936486	daq test	0.0	T
45298	2021-10-05 16:47:08.138979	daq test	0.0	T
45297	2021-10-05 15:27:07.926738	daq test	0.0	T

Showing 1 to 10 of 201 entries

Previous 1 2 3 4 5 … 21 Next

Index of merged histogram files (updated: 10-06-2021 19:05:08)

Click on the links below to download nearline files:

45287
Download Hists and Trees: gm2nearline_hists_run45287.root --- 6.8MiB
Download Hists Only: gm2nearline_histsOnly_run45287.root --- < 10 MiB
Live Histogram Display (no TTree's)
Dashboard View
T0 Traces by Bunch
Tracker Nearline Histograms View or (Download, < 10 MiB)
Fast Rotation Nearline Histograms View or Download: CERN-III or Cornell

45286
Download Hists and Trees: gm2nearline_hists_run45286.root --- 5.2MiB
Download Hists Only: gm2nearline_histsOnly_run45286.root --- < 10 MiB
Live Histogram Display (no TTree's)
Dashboard View
T0 Traces by Bunch
Tracker Nearline Histograms View or (Download, < 10 MiB)
Fast Rotation Nearline Histograms View or Download: CERN-III or Cornell

45285
Download Hists and Trees: gm2nearline_hists_run45285.root --- 5.2MiB
Download Hists Only: gm2nearline_histsOnly_run45285.root --- < 10 MiB
Live Histogram Display (no TTree's)
Dashboard View
T0 Traces by Bunch
Tracker Nearline Histograms View or (Download, < 10 MiB)
Fast Rotation Nearline Histograms View or Download: CERN-III or Cornell

45284
Download Hists and Trees: gm2nearline_hists_run45284.root --- 5.2MiB
Download Hists Only: gm2nearline_histsOnly_run45284.root --- < 10 MiB
Live Histogram Display (no TTree's)
Dashboard View
T0 Traces by Bunch
Tracker Nearline Histograms View or (Download, < 10 MiB)

localhost:1234/display?file=./dashboard/DashboardPlots_run44389.root&items=[h_wiggle,h_et,%20h_ctag,%20h1_x,h2_x,%20hlmt_x,%20h_transform,%20c5]&opts=[logy,logz%20colz,hist%20logy,hist,hist,hist%20logy,hist%20lo...

Read a ROOT file
JSROOT version 5.9.1 7/01/2021
./dashboard/DashboardPlots_run44389
Read docu how to open files from other servers.

DashboardPlots_run44389.root
- h_et;1
- h_wiggle;1
- h1_x;1
- h2_x;1
- hlm_x;1
- hlmt_x;1
- c1;1
- c1_2;1
- c2;1
- c3;1
- c;1
- fit1;1
- fit2;1
- fit3;1
- h_fr;1
- h_transform;1
- h_ctag;1
- c5;1
- StreamerInfo

http://localhost:1234/files
Live Histogram Display (no TTree's)
Dashboard View
T0 Traces by Bunch
Tracker Nearline Histograms View or (Download, < 10 MiB)
Fast Rotation Nearline Histograms View or Download: CERN-III or Cornell

Figure 4.14: A screenshot from the Nearline file interface, showing the various root files and histograms which were automatically produced.

required turnaround times on the order of hours or days to inform changes to running conditions. To that end, an abbreviated 'Nearline'[19] analysis chain was constructed. This analysis chain was developed for the 2017 commissioning run by K.S. Khaw [147] and was revamped and managed by the author from Run-2 through the end of Run-6. It consisted of simplified versions of the full *art*-based analysis code being run on two dedicated machines. Each of these machines would search for new midas data files periodically, the first on a $\mathcal{O}(2\,\text{minute})$ timescale and the second on a $\mathcal{O}(30\,\text{minute})$ timescale, and would process them continuously. The Nearline served a vital monitoring role for the experiment, allowing shifters and experts to verify the integrity of the data on short timescales and make any needed adjustments. For instance, if the ESQ system was set to an incorrect voltage, the nearline would show that from the data and a correction could be made. The effective muon lifetime and number of muon triple coincidences seen from the nearline could also indicate any issues with storage of the muons.

While taking production quality data, a new 2GB subrun file was created every 6-10 seconds. Each nearline machine could process a single one of these files in $\approx$ 45 seconds. The nearline machines thus averaged a $25 - 35\%$ data processing rate in normal operations. This level of data production was sufficient for monitoring of the beam and providing real time feedback on experimental systems. The same analysis code could be run on the Fermigrid to achieve a 100% production rate for those studies where greater statistical precision was required.

A web interface was constructed by the author to access and visualize the nearline data. This provided an interactive jsroot[20] [139] viewer for each of the run-level nearline files, as well as trend plots to track changes in the various beam parameters over time. Outputs from parallel nearline reconstructions for the field and tracker data, as well as additional reconstruction efforts from the calorimeter nearline (fast rotation momentum analyses, CBO measurements, amongst others), were incorporated into this website as well. These parameters (CTAGs, T0 integral, CBO frequency, etc.) are stored in a database for later analysis of long term trends. Some views of this can be seen in Figure 4.14.

---

[19] A play on the words indicating somewhere between the 'online' data quality monitor and the full 'offline' production.

[20] https://root.cern/js/

The phase-momentum systematic study detailed in Section 6.1 was undertaken entirely with the nearline data, processed to 100% completion on the Fermigrid.

4.2.2 Production Dataset Definition

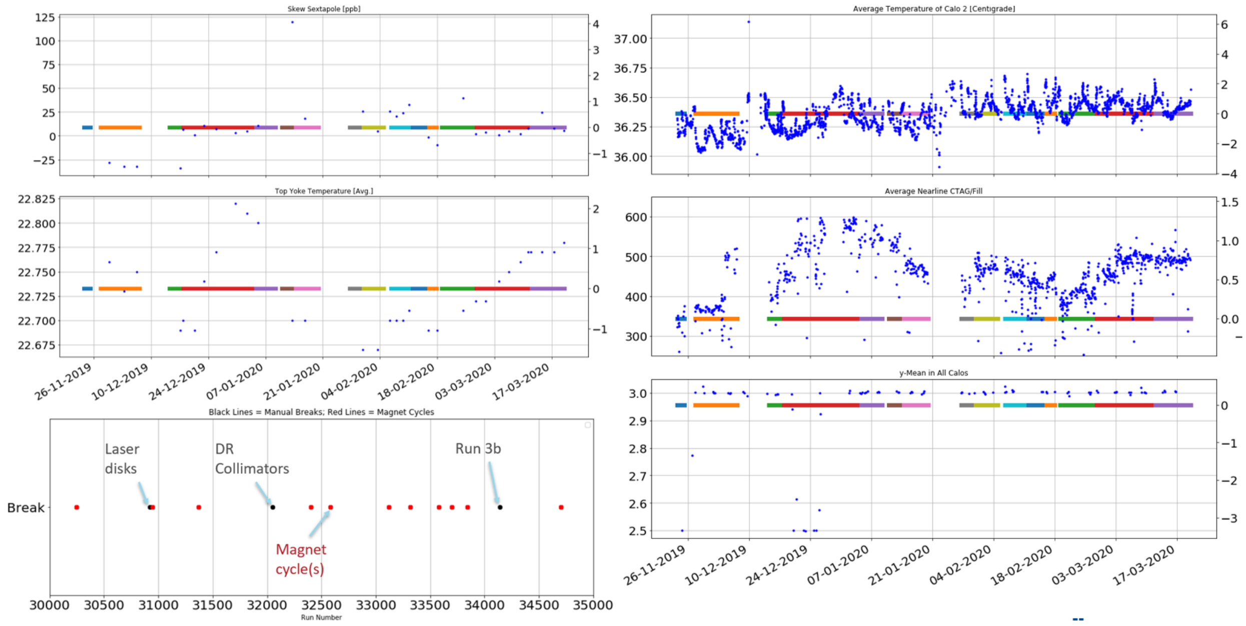

Figure 4.15: Standard trend plots showing stability of various field and calorimeter quantities over the course of the production datasets in Run-3.

The nearline data was also used for the initial definition of the full production datasets. These datasets, denoted by 'DS-___'[21], are sets of files which were taken with the same conditions at the same time. Creating these datasets is essential for building up a high statistics sample for the extraction of ω_a. The author, with input from several other system experts, was responsible for this procedure for Run-2 through Run-6. The algorithm for choosing the boundaries for specific datasets went roughly as follows:

- Datasets should begin and end with a trolley run, to make the combination of ω_a and ω_p as seamless as possible.
- Dataset boundaries should not include systematic studies. Systematic runs taken in the middle of the datasets can be excluded based on the documented run numbers.

---

[21] For Run-3, it goes as DS-3A, DS-3B, and so on.

- Datasets should have consistent field and beam conditions. Any significant changes in upstream conditions or experimental settings should denote a dataset boundary.

- Datasets should be as large as possible (up to 100,000 files, due to Fermilab file handling constraints).

With these criteria in mind, the datasets used in the production were created. First denoted any manual breaks in the data were denoted. These were somewhat rare, but included the insertion of the M5 beam cooling wedge partway through Run-2 (see Sections 3.1.3 and 6.1) and the kicker strength increase from Run-3a→3b. With these 'fixed' points in place, trends in the magnetic field data, tracker CBO measurements, and calorimeter behavior were analyzed. Only a few significant changes in field conditions were observed, which usually coincided with a magnet power cycle. CBO conditions, any difference in which could indicate ESQ voltage changes or other changes in beam storage, were also stable except for near documented (intentional) changes in experimental parameters.

Consulting with system-level experts led to some additional breakpoints being designated, but the majority of the dataset boundaries were driven simply by the file processing limits. As a result of this most of these dataset boundaries ended up being overly conservative. After careful investigation with the final production data, it was found that most were able to be recombined and fit together with no issue. The Run-2/3 analysis began with 20 sub-datasets (DS-2B-H and DS-3B-O[22]) and ended with 3 final datasets which were independently fit: Run-2, 3a, and 3b[23]. Run-4 is beginning with 21 datasets (DS-4AU), but it is expected those will be combined to a single fit. For Run-5/6, the differing ESQ RF settings (see Section 3.3.2) over the course of the run necessitate the data from the initial 35 datasets[24] be combined into two distinct groupings: DS-5A-L with horizontal RF only and DS-5M-O+DS-6A-N with both horizontal and vertical RF.

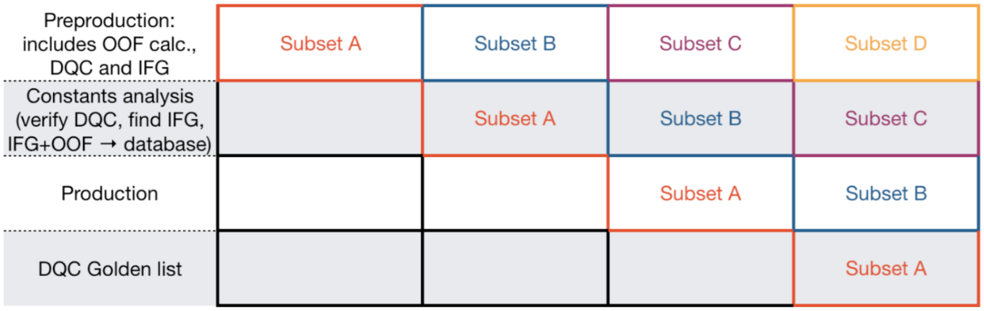

Preproduction: includes OOF calc., DQC and IFG	Subset A	Subset B	Subset C	Subset D
Constants analysis (verify DQC, find IFG, IFG+OOF → database)		Subset A	Subset B	Subset C
Production			Subset A	Subset B
DQC Golden list				Subset A

Figure 4.16: Diagram showing the rolling production scheme used for the Run-2+ data production. Reproduced from internal $g-2$ documentation.

4.2.3 Full Production

After the data is taken, it is transferred from the local drives in MC-1 to long-term tape storage (‘Enstore’) using Fermilab’s file transfer service (FTS). The latency associated with accessing data from the long term storage is a limiting factor in how quickly the data is analyzed. It can take multiple days for an entire dataset to be retrieved from the tape storage, and once it is staged it typically only remains accessible for ≈ 1 week. In order to not delay the overall analysis schedule, extreme care was taken to ensure that no time was wasted in the Run-2+ data production.

The $g-2$ production team consists of $3-4$ production experts, who manage the overall production timeline; a dozen or so system-level experts, who analyze the data quality of their individual systems and provide input to the settings used in the main production; and production shifters, which includes the entire collaboration to some extent. There are 7 major steps in the $g-2$ data production:

- Stage the raw data from long term tape storage to hard disks.
- Pre-production and fill-by-fill DQC
- Constants analysis and database management
- (Test) Production

---

[22] DS-2A and DS-3A contained only systematic runs and were not production quality data

[23] Again, the author apologizes for the capitalization convention. 3A and 3a are distinct objects. An attempt is made to distinguish between the two by appending ‘DS’ to the individual sub-datasets within a Run.

[24] 21 in Run-5 and 14 in Run-6

- (Test) Subrun DQC

where the last two steps are duplicated, first on a (randomly selected) subset of $\approx$ 10% of the files and then on the remaining 90% once the first set of files has been validated. Most problems with the DQC or software are able to be caught at this test production stage, saving valuable computing time. Each of these steps are independent across datasets and can happen in parallel (see Figure 4.16). Each step could take as little as one day or as much as a week to complete, depending on the size of the dataset and the complexity of the DQC checks needed.

4.2.3.1 Pre-Production, Constants Analysis, and Database Management

The first step in readying a dataset for analysis is the 'pre-production'. This is a nearline-like abbreviated analysis chain that extracts the minimum amount of information from the raw data to compute the various constants analyses and perform an initial round of DQC. Fill-by-fill DQC checks are performed at this stage:

- Were ESQs and kickers operating normally?
- Was a laser pulse found in all channels?
- Was a T0 beam pulse found for this fill?

Any fills which fail these checks are marked at this stage and will not proceed further in the production. Subrun files for which more than 5% of fills fail these cuts are excluded as well (as discussed later in Section 4.2.3.3). Typically these cuts reduce the number of fills by $\approx$ 8%, but reduce the number of CTAGs in a dataset by $< 1\%$.

At this point, the long term gain correction (Section 4.1.5.1) for each channel is extracted. This constant is calculated for each laser fill individually and then averaged over each subrun. The health of each calorimeter channel is determined from the out-of-fill laser data. Any channel which deviates by more than 10% from its reference value is investigated. Any channel which has an OOF correction of < 0.3 is excluded from the final analysis (this could be for as little as a single subrun or as long as an entire Run). Any calorimeter which has more than 3 such channels is also excluded entirely. The reason for this is due to the island chopping threshold. The hardware threshold of each of the crystals is nominally set to be ≈ 50 MeV. This threshold does not need to be exact, as long as it is far from the MIP peak used for energy calibration at ≈ 170 MeV. Once the gain correction reaches < 0.3, the effective hardware threshold has drifted from its setpoint to $\approx 50/0.3 = 167$ MeV. This cuts into the lost muon energy range quite severely and, since these lost muons typically deposit their energy in a single calorimeter crystal, limits the ability to reconstruct the lost muon spectrum. Positrons for which this crystal is not the trigger pulse are not as affected by this changing threshold. Such drifting gain values became more of a problem later in the experiments' lifetime, as equipment began to age. Where possible, the affected crystals or cables were replaced in between runs (for instance, significant maintenance was done on Calorimeter 9 in between Run-4 and Run-5).

Once all of the constants and conditions are computed, they are verified by system-level experts and uploaded to a database. The database keeps track of each set of constants and the interval over which each set is valid. Some constants may have an interval of validity spanning multiple runs, whereas some change at the subrun level.

4.2.3.2 Production: POMS Campaigns and Production Shifts

Once all of the required constants are uploaded and the integrity of the dataset has been checked, the full production of the data can proceed. For the calorimeters, this involves passing through the production chain described in Section 4.1. Similar production chains are defined by other reconstructions and for other ring systems (for instance, the straw tracking detectors and IBMS systems each have their own reconstruction chains).

In Run-1, this was the sole purview of the production team. After Run-1, a production shift schedule and institutional quota for such shifts was established[25]. Each shift lasted for one week, and involved 1-2 hours of monitoring data production and launching grid submissions (spread out over the course of each day) by non-computing-expert members of the collaboration. The introduction of the Production Operations Management Service (POMS) into the production workflow made these production shifts possible. POMS provides a GUI interface and multiple helper functions for

---

[25] Mirroring requirements for data-taking shifts.

large scale, repeated grid submissions. A ‘campaign’ can be set up with one or more steps, with each step taking as input the data produced by the previous step. This aligned well with the new rolling production scheme (Figure 4.16). Once the parameters of the campaign are defined POMS can automatically launch the processes across many grid nodes, monitor the outputs, perform any needed recoveries, and (when the stage is complete) signal the next stage of the campaign to proceed. This removed a huge manual burden from the experts, who now only needed to intervene if something went amiss. Once this workflow was introduced, each run was able to be processed in less time than the previous, even as the size of the overall datasets grew.

The dataproducts contained in the output files at the end of this stage are complete, and if all of the data were ‘physics quality’ no further action would be needed. Once experts verified that each stage of the production had completed successfully, the files were passed to the DQC team for final analysis and blessing.

4.2.3.3 Subrun Level DQC Analysis

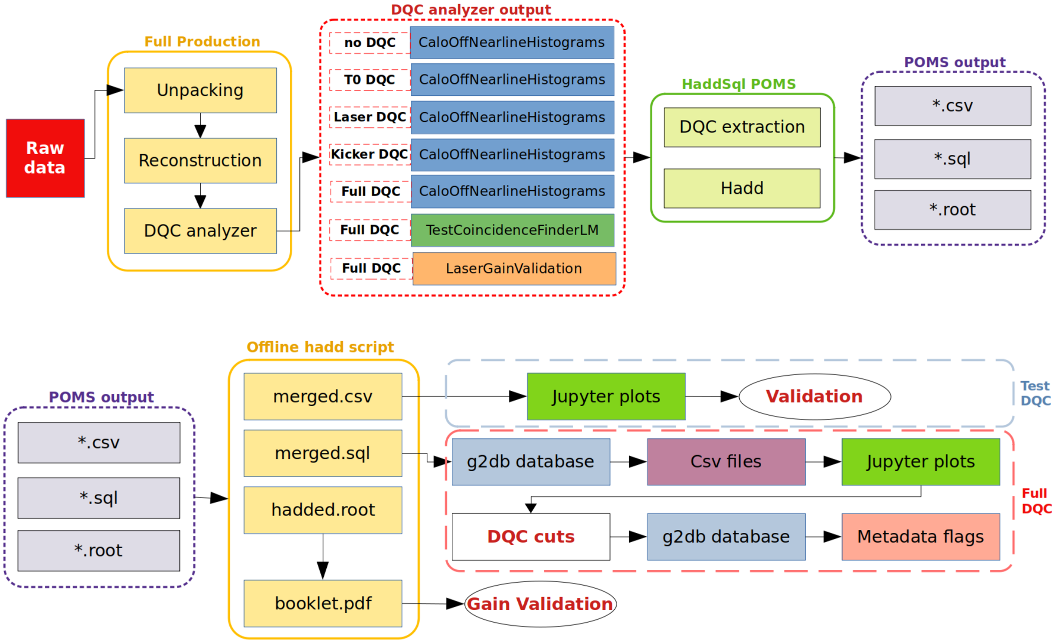

Figure 4.17: Flow of the data through the DQC analysis chain. The DQC analyzers are run as part of the full production workflow and the results are applied on the subrun level by excluding certain files from the datasets. Reproduced from internal $g - 2$ documentation.

Once the data production is complete, a number of subrun level DQC checks take place. The flow of the data through the DQC analysis chain in shown in Figure 4.17. The checks that are made at this stage include:

- Is the average CTAG/T0 ratio below the acceptable range of values?
- Is the average ratio of lost muons to positron hits below the upper acceptable limit?
- Do more than 95% of the fills in this subrun pass the fill-by-fill DQC cuts?
- Is this subrun in a range which has been marked 'bad' by the field, kicker, or ESQ teams?
- Do the three independent reconstruction algorithms display any difference in the trends above?
- Do the ring systems meet the qualifications for it being physics quality [148] data:
  - $\geq 22/24$ calorimeters are online.
  - $\geq 7/8$ tracker modules in each station are online.
  - All six laser heads, and associated monitors, are operational. Laser pulses are found in all calorimeters.
  - Slow control data is being recorded
  - The T0 bias voltage is on and data is being recorded

A jupyter notebook[26] [149] based analysis to make a standard set of DQC visualizations was developed by the author. This notebook plots the trends for these cuts across the run, as well as a histogram showing the total distribution. Some examples of these plots can be seen in Figure 4.18. In this figure, three sets of colored bands can be seen. The blue points represent the values for the DQC variables over all subruns in the dataset. Orange points are the points which pass the individual cut shown in that particular figure. For instance, in the bottom plot in Figure 4.18 the orange points all satisfy the condition that $N_{\text{triple}}/N_{\text{CTAG}} < 0.008$, indicating that muons were being properly stored. Green points, finally, are those which pass all DQC cuts with their current

---

[26] https://jupyter.org/

settings. The transparent red bands indicate regions where systematic studies took place, and all subruns within those bands will be manually marked as excluded from the final dataset.

The results of the cuts for DS-4CD are summarized in Table 4.1. In this case, only 0.476% of all CTAGs failed to be marked as quality production data. This level of data reduction was considered excellent. Some datasets had as much as 8% data reduction. Generally the percentage of data which passed all DQC cuts increased with each year the experiment was in operation.

Category	**DQC Type**	**Total**	**Lost**	**Remaining**	**Percentage Lost**
Subruns	Kicker	90554	0	90554	0.000%
	Laser	90554	0	90554	0.000%
	T0	90554	0	90554	0.000%
Fills	Kicker	8081725	42	8081683	0.001%
	Laser	8081725	0	8081725	0.000%
	T0	8081725	200397	7881328	2.480%
	All Fill-by-fill DQC	3574966033	29875	3574936158	0.001%
CTAGs	Kicker	3574966033	12014	3574954019	0.000%
	Laser	3574966033	0	3574966033	0.000%
	T0	3574966033	17861	3574948172	0.000%
	ESQ	3574936158	4801966	3570134192	0.134%
	Losses	3574936158	1272982	3573663176	0.036%
	CTAG/T0	3574936158	186300	3574749858	0.005%
	Fill-by-fill	3574936158	5883693	3569052465	0.165%
	Field	3574936158	6589611	3568346547	0.184%
	Final	**3574936158**	**17139930**	**3557796228**	**0.479%**

Table 4.1: Summary of the DQC Cuts made in DS-4CD. Only 0.479% of CTAGs failed the cuts.

4.2.3.4 Final Production Steps

All files in the Fermilab file handling system are managed using SAM (Serial Access to Metadata). This system is designed to do three things:

- Keep track of the locations of files based on a unique name;
- Keep track of metadata associated with a file; and
- Create datasets of files based on the metadata and serve them to users as requested.

The metadata associated with one of the production files can be seen in Figure 4.19.

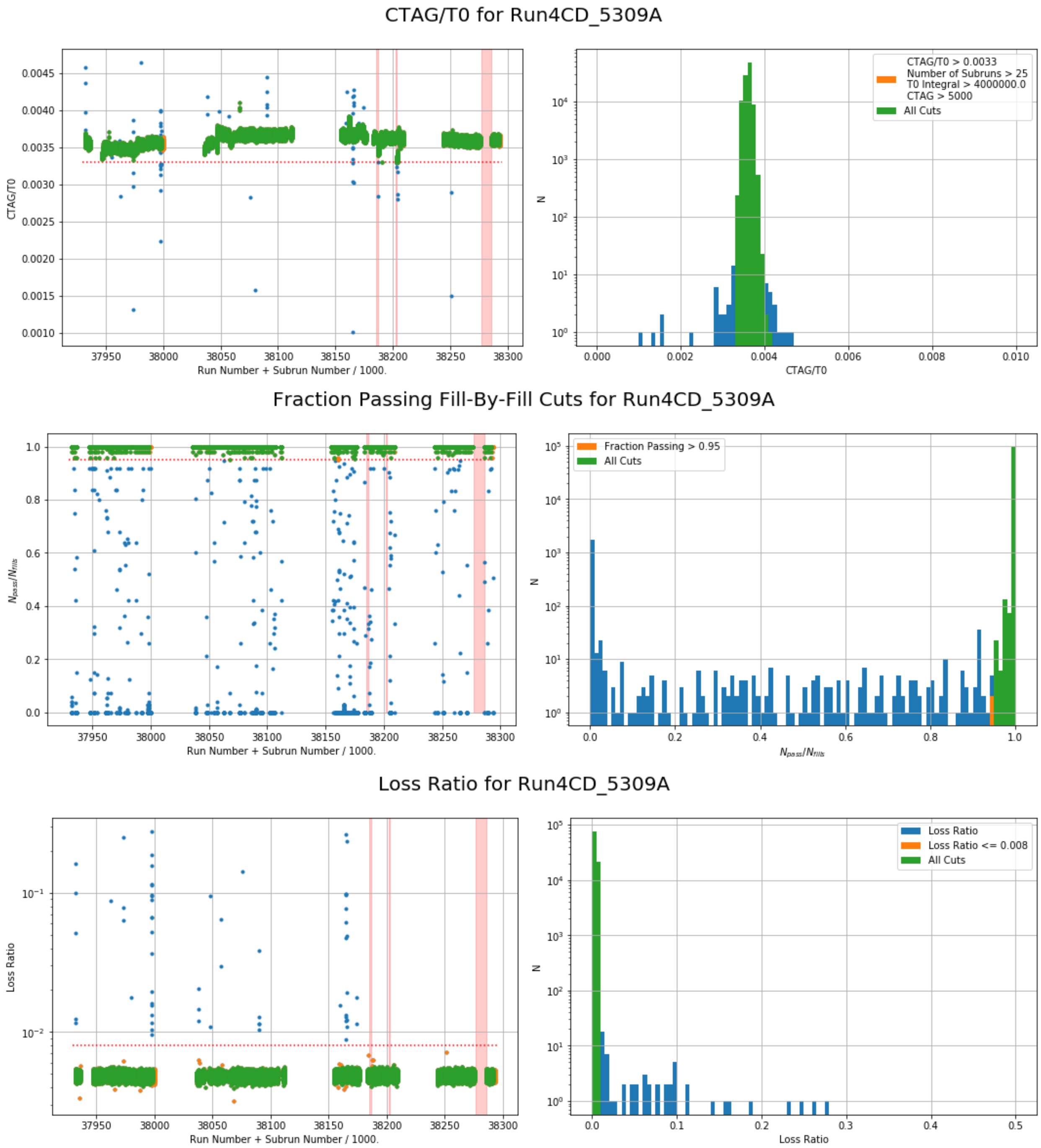

Figure 4.18: Standard Data Quality Control (DQC) plots showing the trends of calorimeter based cuts over a datasets evolution. Blue shows all data, while orange (green) curves indicate the data which remains after one (all) of the subrun level DQC cuts are applied. Descriptions of all of these cuts can be found in the text of Section 4.2.3.3.

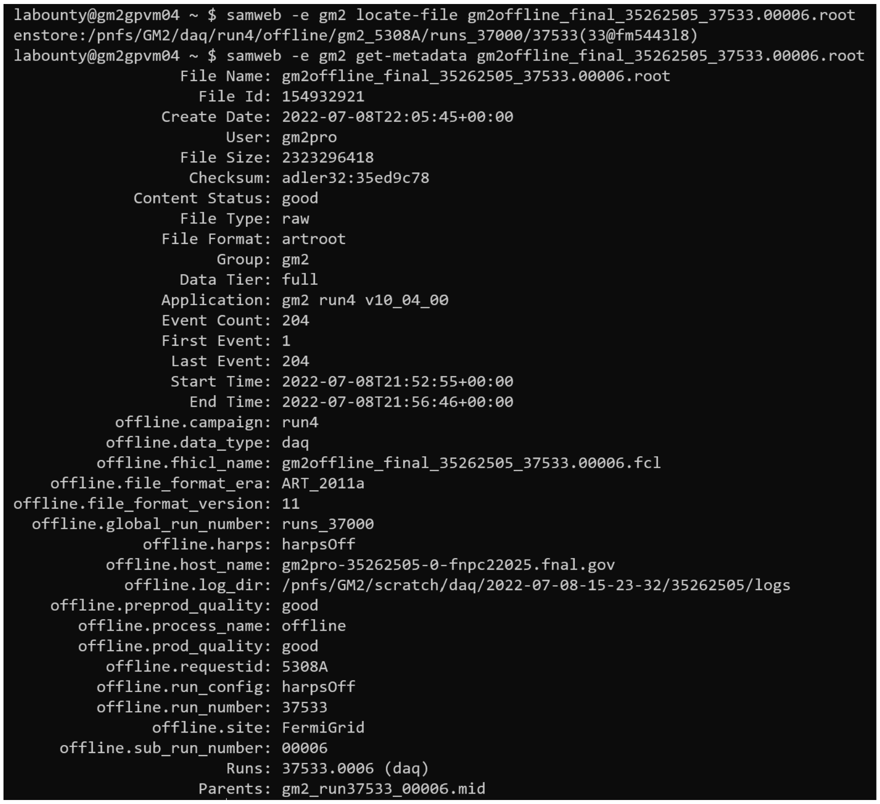

```
labounty@gm2gpvm04 ~ $ samweb -e gm2 locate-file gm2offline_final_35262505_37533.00006.root
enstore:/pnfs/GM2/daq/run4/offline/gm2_5308A/runs_37000/37533(33@fm5443l8)
labounty@gm2gpvm04 ~ $ samweb -e gm2 get-metadata gm2offline_final_35262505_37533.00006.root
                  File Name: gm2offline_final_35262505_37533.00006.root
                    File Id: 154932921
                Create Date: 2022-07-08T22:05:45+00:00
                       User: gm2pro
                  File Size: 2323296418
                   Checksum: adler32:35ed9c78
             Content Status: good
                  File Type: raw
                File Format: artroot
                      Group: gm2
                  Data Tier: full
                Application: gm2 run4 v10_04_00
                Event Count: 204
                First Event: 1
                 Last Event: 204
                 Start Time: 2022-07-08T21:52:55+00:00
                   End Time: 2022-07-08T21:56:46+00:00
           offline.campaign: run4
          offline.data_type: daq
         offline.fhicl_name: gm2offline_final_35262505_37533.00006.fcl
    offline.file_format_era: ART_2011a
offline.file_format_version: 11
  offline.global_run_number: runs_37000
              offline.harps: harpsOff
          offline.host_name: gm2pro-35262505-0-fnpc22025.fnal.gov
            offline.log_dir: /pnfs/GM2/scratch/daq/2022-07-08-15-23-32/35262505/logs
    offline.preprod_quality: good
       offline.process_name: offline
       offline.prod_quality: good
          offline.requestid: 5308A
         offline.run_config: harpsOff
         offline.run_number: 37533
               offline.site: FermiGrid
     offline.sub_run_number: 00006
                       Runs: 37533.0006 (daq)
                    Parents: gm2_run37533_00006.mid
```

Figure 4.19: SAM Metadata associated with one of the final production files in Run-4A. The variable `offline.prod_quality` indicates that this file has passed all DQC cuts.

SAM provides a single access point which obscures the need for any users (whether interactively or when using distributed computing resources) to keep track of the physical disks on which their files are stored or juggle lists of thousands of individual files to process a dataset.

Once the subrun-level DQC cuts are uploaded to the database, they are applied to the data as metadata quality flags (such as `offline.prod_quality` as shown in Figure 4.19) before a SAM dataset of all of the files is created. A final production dataset can be defined with just a run number range and quality flags. Updating the dataset definition (say to exclude a file later found to contain non-production data) is as simple as modifying the metadata of the files themselves. Analyzers can then request all of the files in a certain dataset using simply the dataset name, for example '`gm2pro_daq_offline_dqc_run4A_5308A`'. Here `5308A` is the software version with which the dataset was produced.

Once the DQC is applied, the dataset is essentially ready to use. In the Run-1 and 2/3 analysis, this was the final step. In Run-4+, an additional step was required due to the sheer volume of data. In previous runs the amount of of non-tape disk space available to the experiment was sufficient to keep all the final production files 100% staged, but with the threefold increase in data for Run-4/5/6 this was no longer sufficient. A set of 'skimmed' data files were therefore created. These files dropped some intermediate dataproducts and concatenated ≈ 10 subrun files (all from the same run) together. This both alleviated the storage space issue and massively improved the workflow for analysis submissions — it's much easier for each analyzer to wrangle 10,000 files than 100,000.

4.2.4 Analysis Submissions

The final step in preparing the data for an ω_a analysis is to histogram the data in preparation for fitting. As will be detailed next in Chapter 5, the extraction of ω_a is done from a fit of the precession frequency to a 1D histogram of positron arrival times. However in order to ensure that the precession frequency is extracted in an unbiased way, it is necessary to have multiple views of the data and perform cross checks vs. energy, individual calorimeter, etc. Each of the 6 independent analysis groups have their own methods for preparing these histograms, and so each group must analyze the raw data themselves to produce the particular inputs for their analysis.

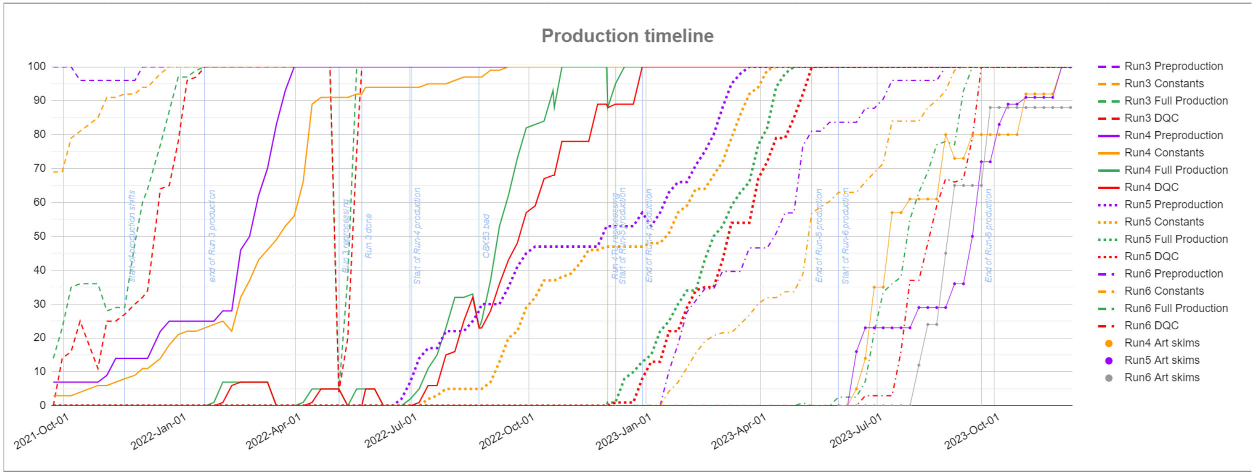

Figure 4.20: Timeline of the full production from the start of Run-2 data processing as of Jan. 5 2024. The y-axis here is percent completion.

The UW analysis uses an *art* analyzer to perform this histogramming. Using the Fermigrid, the $\mathcal{O}(10,000)$ files / dataset can be processed in parallel. The cost of this is that the analysis needs to conform to the constraints of that system. For instance, the majority of the grid nodes available to $g-2$ analyzers have no more than 4 GB of RAM available. This means that any job which requires more than 4GB to run will have to wait for extended periods of time to begin running, and is more likely to time out and fail. Since all ROOT histograms are memory resident, this creates a potential bottleneck. The UW analysis thus separates out different views of the data into different grid submissions, each requiring less than 4 GB of memory. Separate grid submissions are required for:

- The 'standard' analysis with 3D histograms of positron hit time, energy, and calorimeter number;
- 100 random seeds of the time randomization (described in Section 6.4);
- Systematic studies where the applied value of corrections like the IFG, OOF, etc. are varied;
- Energy leakage studies where the fiducial volume of the calorimeters is restricted;

among others. Some of these will be detailed in the following chapters. Each one of these submissions can take anywhere from 4-24 hours to fully process, depending on how 'crowded' the grid is at any given time. For systematic studies, it is often sufficient to process $\geq 95\%$ of the files in a dataset. This can typically be done in a single grid submission. For the full analysis, however, it is important to verify that every last positron is accounted for. Multiple 'recovery' submissions are typically required to make sure that the number of fills in the production dataset matches the number processed through the UW analysis chain.

The end result of this process is shown in Figure 4.21. From this dataset, the nominal value of ω_a can be extracted, and this process is described in the following chapters.

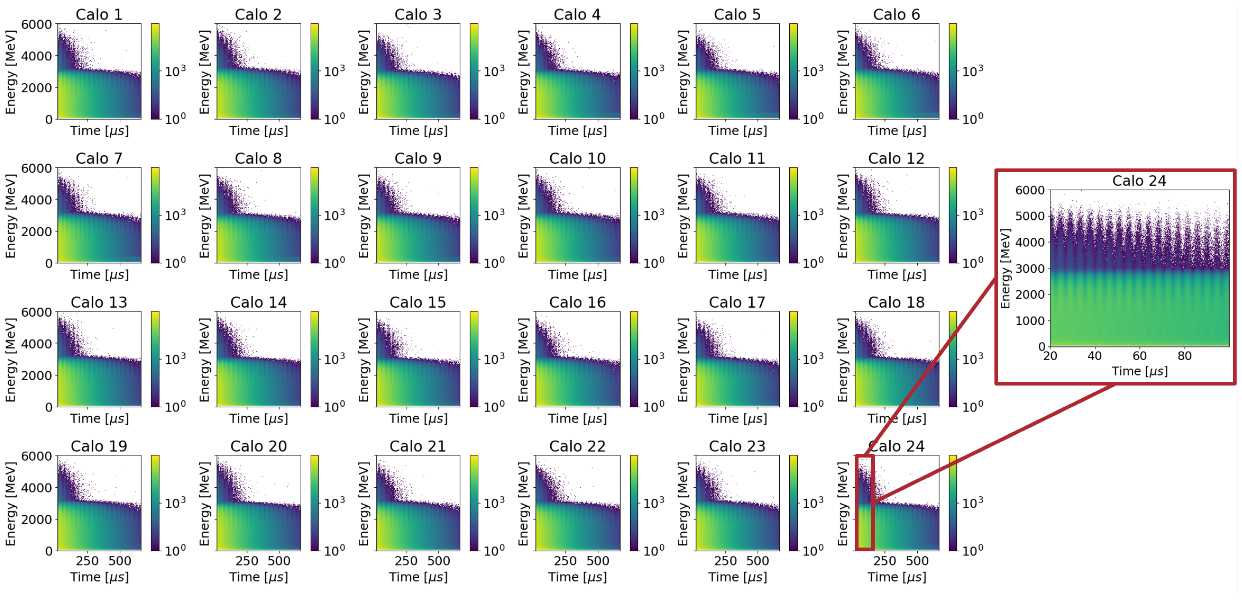

Figure 4.21: The output of the main analysis chain: a 3D histogram of positron hit time vs. deposited energy vs. calorimeter number.

Chapter 5

Data Analysis: Extraction of The Anomalous Precession Frequency ω_a

This chapter describes the current status of the UW analysis of ω_a. This analysis represents one of 6 analyses groups, each working semi-independently. In the sections to follow the iterative building of the fit and standard cross-checks performed as part of the ω_a analysis are discussed. Results from Run-4 will be presented here as the 'nominal' running conditions. Descriptions of how these conditions differ with respect to other running conditions will be mentioned (in brief) where relevant and will be discussed in more detail in Chapter 7.

5.1 Organizational Structure

The Run-2/3 UW analysis was performed primarily by H. Binney, with support in systematic studies and other analyses by S. Braun, J. Hempstead, and the author. The analysis was performed using a ROOT based package developed by many generations of UW graduate students [6, 84, 91]. For the Run-4+ analysis, the amount of technical debt in this codebase was assessed and the decision was made to re-implement the majority of the analysis code from scratch. This allowed for the piecemeal updates made from 2018-present to be more fully integrated into the analysis model. This update took place concurrently with the Run-2/3 analysis. The results from this new UW fitting module were checked against the original code using Monte Carlo samples and the Run-2/3 data. This upgrade process served as a crosscheck to the original analysis code for the Run-2/3 analysis. Some modifications to initial fit parameter guesses were required (due to differences in minimization strategies), but the final results agreed to well within the uncertainty on each of the fit parameters.

5.1.1 Run-4+ Fitting Module

Two Python packages were developed by the author for use in this analysis[1]. The first (‘`g2fit`’) performs a χ^2 minimization given an input set of data and a function of the form `func(x,p)`, where `x` are the bin centers and `p` a list of fit parameters. It provides a wrapper around the Python `iMinuit` library [150, 151]. By default, when fitting two rounds of minimization using the `MIGRAD` algorithm are performed. Uncertainties are them computed on each fit parameter using both the (somewhat less precise) `HESSE` algorithm and the (somewhat slower) `MINOS` algorithm[2]. The packages also provides a number of utilities for performing the $g-2$ fit, including the implementation of each of the fit functions detailed in Section 5.3. The second package (‘`g2_analysis`’) consists of two classes: `PrecessionAnalysis` and `AnalysisConfiguration`. These classes take in the raw histogram files, apply various corrections to the data, and then control the flow of the iterative fitting procedure to extract ω_a.

The flow of the analysis is controlled through a `toml` configuration file. This file contains each of the initial guesses for the parameters of the fit, which systematic scans are to be performed, which models for the various beam oscillations are to be included, and more. The analysis can be done interactively in a jupyter notebook session [149], or automatically from start to finish with a single command.

The results — each intermediate stage of the fit and systematic scans — are saved as `pickle` files, and can be reloaded across sessions or machines. This allows for resuming the analysis from an intermediate stage (or even just recreating a final plot) without having to repeat time-intensive

---

[1] The packages are located on GitHub, and access to the code is available upon request.

- `https://github.com/jlabounty/g2_analysis`
- `https://github.com/jlabounty/g2fit`

[2] This last step is only performed if a valid minimum has been identified by `MIGRAD`. A useful comparison of these two methods can be found at this page.

analysis steps.

5.1.2 Analyzer Level Blinding

The physical clock of the $g-2$ experiment is offset from 40 MHz by a factor unknown to anyone in the experiment[3], to prevent conscious or unconscious bias towards any particular result. The experiment is also blinded at the analyzer level. Each analyzer chooses a unique 'blinding phrase' which, through the `MD5` hashing algorithm, generates a unique blinding value: ΔR[4]. The parameter 'ω_a' is replaced in all fits by:

$$\omega_a \to 2\pi \times 0.2291\,\text{MHz} \times \left[1 - (R(\omega_a) - \Delta R) \times 10^{-6}\right]. \tag{5.1}$$

Where the quantity '$R(\omega_a)$' is left as the free parameter in the fit[5]. A shift of $R(\omega_a)$ by 1 unit, because of this definition, corresponds to a 1 ppm shift in ω_a. In the UW analysis the blinding phrase is read from a local text file specified in the fit configuration. This file is not committed to the repository.

5.2 Histogram Preparation

The output of the analysis submissions detailed in Section 4.2.4 consists of a series of 3D histograms — energy vs. time for each calorimeter — while the fits to $R(\omega_a)$ are performed on a 1D time spectrum. For the main analysis, the data from multiple calorimeters can be combined together simply by projecting the 3D histogram down to a 2D energy vs. time histogram. This section details the slightly more complex steps necessary to prepare the histograms and collapse the data along the energy axis in a statistically optimal way.

---

[3] Two Fermilab employees (not associated with $g-2$) set the initial value and monitor the offset weekly to ensure the clock blinding is stable.

[4] This can be thought of like an analysis 'password'. Any valid unicode sequence could be chosen, which will produce a unique ΔR. For example: 'correct horse battery staple'

[5] Note that figures may simply refer to this value as simply 'R', which should not be confused with $\mathcal{R} = {}^{\omega_a}/_{\omega_p}$.

5.2.1 Fast Rotation Removal

Since the muons are injected in a bunched structure, they do not uniformly fill the ring at the start of a fill. Therefore the calorimeters — especially at early times — see a stroboscopic image of the beam, with the intensity varying strongly at the cyclotron frequency. This fast oscillation is shown in the black curve in Figure 5.1. Precise modelling of this debunching is difficult to incorporate into the ω_a fit function, as it depends on the distribution of muon momenta in the ring and the initial injected bunch shape. Therefore to remove this effect and prevent this frequency from biasing the extraction of ω_a, a two step process is utilized in the UW analysis:

- The histograms are binned in time as closely to the cyclotron period as possible. For the UW analysis, $T_c = 149.2\,\text{ns}$ is chosen as the nominal cyclotron value. This removes the majority of the effect[6].

- To remove any remaining effect from the fast rotation, the arrival time of each positron is randomized by $\pm T_c/2$ before being histogrammed[7].

This procedure is effective in removing the effects of ω_c on ω_a[8]. A small residual effect on ω_a that is introduced by this randomization procedure is discussed in Section 6.4.

5.2.2 The Empirical Pileup Correction

The raw Run-4 data for all calorimeters can be seen in Figure 5.2a. Since the stored muons have a momentum of no more than $3.1\,\text{GeV}/c$, no energy deposits in the calorimeters should be visible with $E > 3.1\,\text{GeV}$[9]. The large number of positron hits reconstructed beyond this physical endpoint indicates the presence of pileup at early times.

---

[6] This also has the practical benefit of limiting the size of the analysis histograms. Binning finely enough to fit the cyclotron motion would quickly run up against the data size restrictions mentioned in Section 4.2.4.

[7] This can either be done on a per-positron or a per-fill (i.e. each of the positrons in the same fill will have the same time offset) basis.

[8] A similar randomization procedure is employed by other analysis groups to remove the effects of other frequencies as well. This is effective and does not dilute ω_a significantly so long as the frequency is $\gg 0.2291\,\text{MHz}$. One frequency which is often randomized is $\omega_{\text{vw}} = 2.3\,\text{MHz}$.

[9] While the energy and momentum of the relativistic beam particles can be used nearly interchangeably, we will strive to differentiate between them.

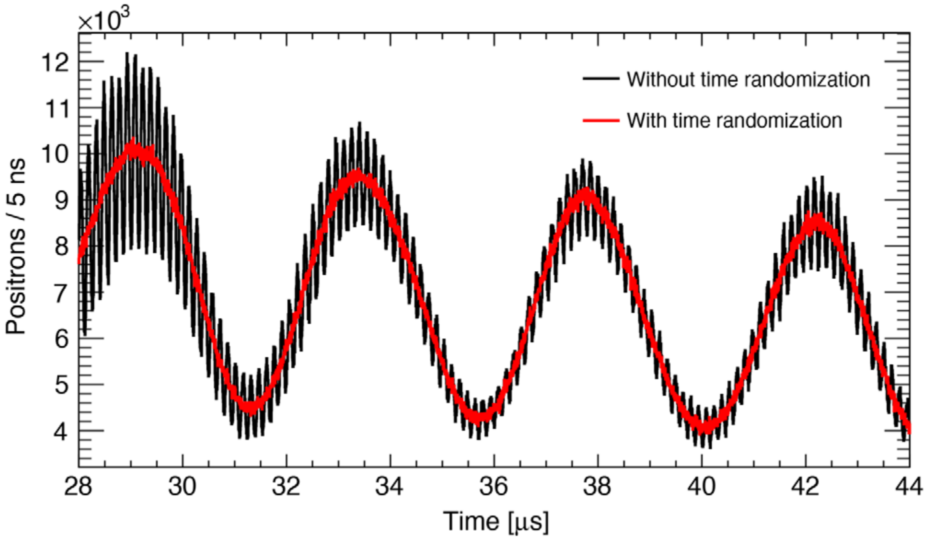

Figure 5.1: An example spectrum before (black) and after (red) the application of the fast rotation randomization. The randomization removes the high frequency cyclotron oscillation while leaving the main ω_a oscillation untouched.

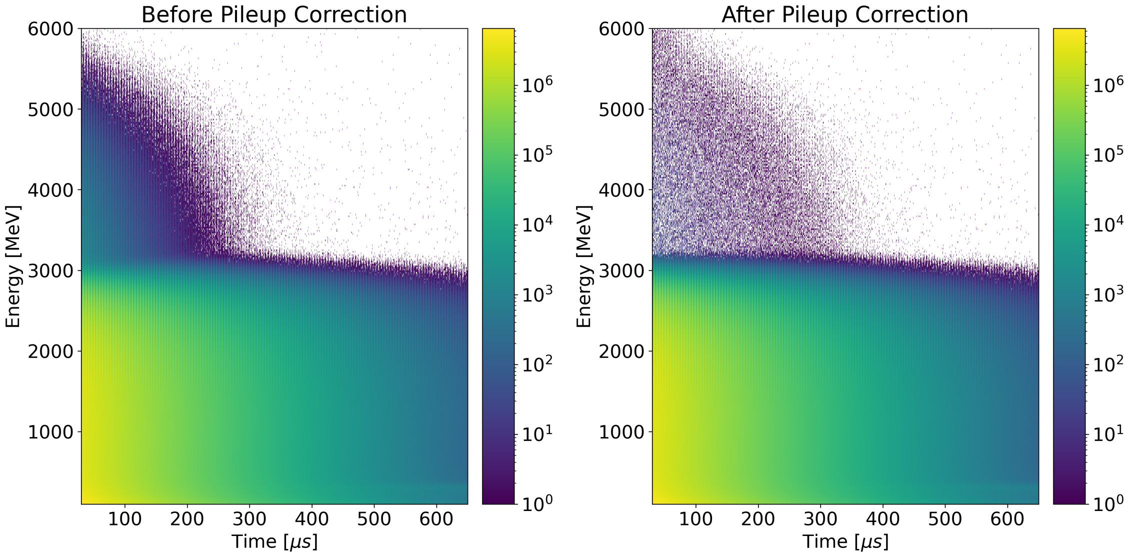

(a) **(b)**

Figure 5.2: (a) Uncorrected positron data for all calorimeters combined. The presence of positron clusters reconstructed with $E > 3.1\,\text{GeV}$ indicates the presence of pileup. (b) Positron data for all calorimeters after the application of the pileup correction detailed in Section 5.2.2. The high energy clusters have largely been removed.

Pileup clusters are those created by positrons that arrive close enough in time as to be indistinguishable by the fitting and clustering algorithms. Because the $g-2$ phase of the pileup hits will be (on average) different from a 'true' hit with that energy, and because the amount of pileup changes over the course of the fill[10], the presence of pileup in the data can bias the extraction of ω_a through a time dependent phase shift[11]. It is not generally possible to tag any individual cluster with $E < 3.1\,\mathrm{GeV}$ as likely consisting of pileup. Instead, statistical methods must be employed to remove pileup *on-average* from the distribution. The effectiveness of these algorithms is assessed by looking at the impact they have on the high energy clusters, comparing the early and late time energy spectra before and after the correction, and through Monte Carlo simulations [141].

In Run-1, the UW pileup correction was bootstrapped from the 2D energy/time histogram itself [6]. This method depended upon the fact that the clustering algorithm used only temporal information when determining whether hits belonged to one or many clusters. As a side effect of the updates to the clustering algorithm described in Section 4.1.6, some limited spatial dependence was introduced[12]. The effect was small, but rendered the Run-1 UW pileup reconstruction method obsolete. Starting from the Run-2/3 analysis, UW adopted an empirical pileup correction algorithm developed by D. Sweigart and S. Foster. The derivation for this correction is described in detail in references [84, 141, 152] and an abbreviated description of the method is given here.

The philosophy behind the empirical pileup correction can be summed up simply: it's difficult to model all of the detector and reconstruction dependant effects in order to construct the pileup spectrum that properly describes the data, so why bother? Instead, one can make use of the fact that the rate at which the muon intensity is changing (decaying with a lifetime $\gamma\tau_\mu \approx 64.4\,\mu\mathrm{s}$) is small compared to the scale of a few cyclotron periods ($T_c = 149.2\,\mathrm{ns}$). Thus the probability of a two hits appearing in the same island approximately[13] the same as the probability of a hit in one

---

[10] The amount of double pileup, for instance, scales as $[\mathrm{rate}]^2 \propto e^{-2t/\tau_a}$.

[11] See the argument in Section 3.6.3.

[12] The new algorithm introduced a slight difference in whether a pileup hit with the same energy and time would be included in a cluster if two pulses were in the same crystal or a different crystal. For more details, see reference [84].

[13] A small correction is necessary to account for the fact that this condition is not exactly true. This is incorporated into the systematic uncertainty from the pileup correction.

island being followed by another hit in a ‘shadow’ island one cyclotron period later:

$$\mathcal{P}(t,2) \approx \mathcal{P}(t,1) + \mathcal{P}(t+T_c,1) \tag{5.2}$$

Assuming the positron hits obey Poisson statistics, the probability of n hits to be reconstructed in an island with length l is given by:

$$\mathcal{P}(t,n) = \frac{e^{r(t)l}(r(t)l)^n}{n!} \tag{5.3}$$

where $r(t)$ is the instantaneous rate of positrons hitting the calorimeters. Letting the probability $r(t)l \equiv \lambda$, the raw pileup-contaminated positron spectrum (ρ_{raw}) can be described as a sum of islands which contain one positron hit (denoted $\hat{1}$), double pileup islands with two positron hits ($\hat{2}$), etc. This yields:

$$\begin{aligned}\rho_{\text{raw}} &= \sum_{i=1}^{N} \mathcal{P}(n) = (\lambda e^{-\lambda})\hat{1} + \frac{\lambda^2 e^{-\lambda}}{2}\hat{2} + \frac{\lambda^3 e^{-\lambda}}{6}\hat{3} + ... && (5.4)\\ &\approx \left(\lambda - \lambda^2 + \frac{\lambda^3}{2}\right)\hat{1} + \left(\frac{\lambda^2}{2} - \frac{\lambda^3}{2}\right)\hat{2} + \left(\frac{\lambda^3}{6}\right)\hat{3} + \mathcal{O}(\lambda^4)\,, && (5.5)\end{aligned}$$

where each island should be understood to contain clusters with individual energies and times, some of which are contaminated by pileup. The ‘hat’ notation here is used for bookkeeping, so that each term in the exponential sum is associated with the order of the island from which it originated. In the second line, the power series for the exponential[14] has been used to expand to $\mathcal{O}(\lambda^3)$. Were there to be no pileup, the hit spectrum would be given simply by $\lambda\hat{1}$. Any difference between this and ρ_{raw} is the pileup spectrum:

$$\rho_{\text{pu}} = \left(-\lambda^2 + \frac{\lambda^3}{2}\right)\hat{1} + \left(\frac{\lambda^2}{2} - \frac{\lambda^3}{2}\right)\hat{2} + \left(\frac{\lambda^3}{6}\right)\hat{3} + \mathcal{O}(\lambda^4)\,. \tag{5.6}$$

The pileup spectrum contains double/triple pileup events which must be subtracted from the data,

---

[14]

$$e^{\lambda} = \sum_{n=0}^{\infty} \frac{\lambda^n}{n!} \quad (\lambda \ll 1)$$

as well as single hits which must be added back in to correct for their misidentification. For instance, the $-\lambda^2\hat{1}$ term corresponds to two single islands which must be added back to the pileup contaminated spectrum to 'repair' the effect of a double pileup island in the $\lambda^2/2\hat{2}$ term [141]. By overlaying various combination of the islands in the real data, the pileup spectrum can be constructed and then subtracted from the underlying distribution.

The algorithm for construction of the double pileup spectrum from data, a schematic for which can be seen in Figure 5.3, is as follows. For each cluster in the data with time t_0, the algorithm looks forward in time and identifies any crystal hits which are are within the time range given by $t_0 + T_g \pm t_w$, where T_g is the 'gap time' equal to the cyclotron period and t_w is the 'window time' in which clusters are considered. Dedicated studies have shown that the RW pulse fitter is able to distinguish pulses of a wide energy range if they are separated by $> 5\,\mathrm{ns}$[15] [6, 152]. This is therefore taken to be the value of t_w, to ensure that any events which could possibly pile-up are properly considered. If there exists a 'shadow' island in this time window, the algorithm shifts said island back by T_g, and overlays it with the 'trigger' island to create an artificial pileup island. The noise level of the trigger and shadow island are then inflated artificially to match the noise level from the combined trace [152], and the three new islands are sent into the same fitting and clustering analysis chain that the unmodified calorimeter data flows through. If the fitter is no longer able to distinguish the two pulses in the combined island, this is considered a double pileup event. If the fitter is still able to distinguish the same number of pulses, then these are considered single events. Both sets of clusters are tracked, and the pileup spectrum is built from many such islands.

Given the assumption that $r(t) \approx r\left(t + T_g\right)$ and following the same logic as above this constructed double pileup spectrum can be shown to consist of [84, 141, 152]:

$$\rho_{\mathrm{pu,double}} = \left(-\lambda^2 + \frac{3}{2}\lambda^3\right)\hat{1} + \left(\frac{\lambda^2}{2} - \frac{3\lambda^3}{2}\right)\hat{2} + \left(\frac{\lambda^3}{2}\right)\hat{3} + ... \tag{5.7}$$

This equation takes into account the fact that the islands from which the double pileup spectrum is created themselves have some contamination from higher order pileup (hence the appearance

---

[15] This is intentionally taken to be much longer than the ADT of the fitting algorithm described in Section 4.1, so as to definitely include all 'possible' pileup events.

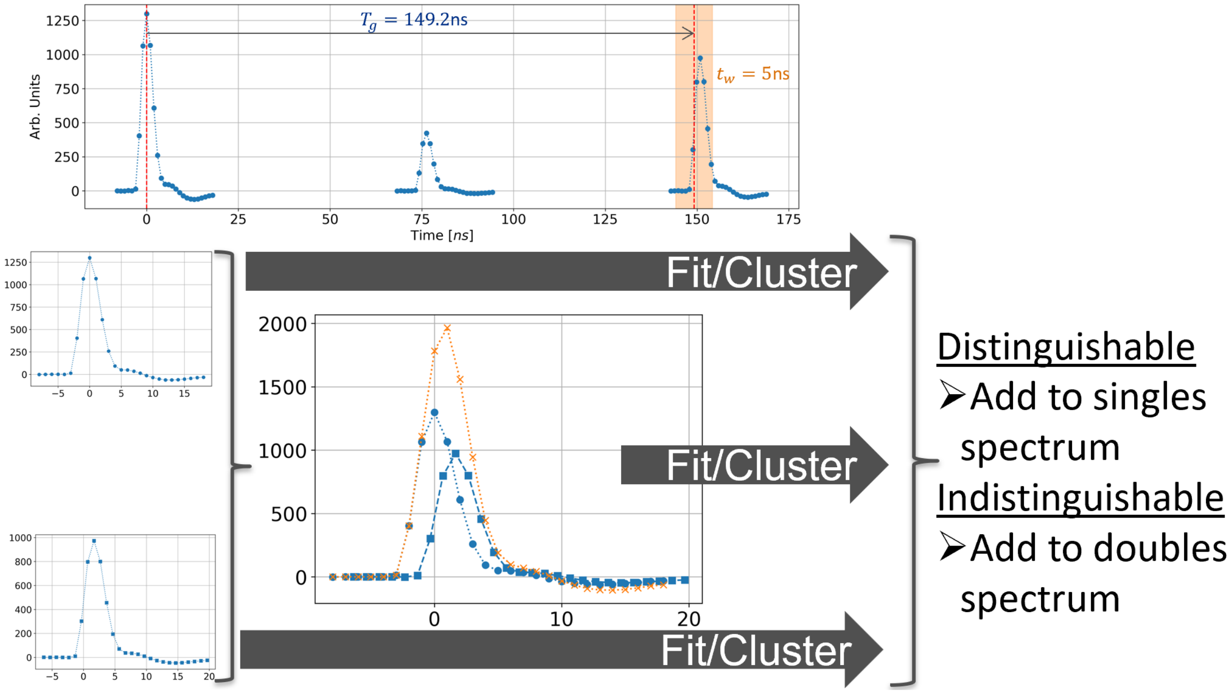

Figure 5.3: A diagram showing how the double pileup spectrum is constructed. For each positron, the algorithm looks forward in time to identify any clusters in the shadow window. If a cluster is found, as is the case here, then the later islands are shifted backwards in time, overlaid, and fit with the normal reconstruction process. If the newly constructed island is now indistinguishable from a single pulse, the reconstructed energy and time is added to the double pileup spectrum. Here, only clusters with $t > 30\,\mu$s are shown.

of $\hat{3}$ in Equation (5.7)). From this process, the pileup spectrum can be constructed to whatever order is deemed necessary by looking n additional shadow windows nT_g apart and analysing the combinatorics of overlaying the islands of that order. Studies have shown that beyond triple pileup, the effect on the extracted value of ω_a drops below a reasonable threshold for concern [152]. This process is repeated for every island in every fill, with the pileup clusters being computed alongside the data clusters in the main production chain.

The double and triple pileup correction histograms can be seen in Figure 5.4. These are both subtracted from Figure 5.2a to create the corrected spectrum shown in Figure 5.2b. The most noticeable effect is that the unphysical hits with $E > 3.1\,\text{GeV}$ are removed. The correction adds in a number of low energy pulses, which can be seen more clearly in Figure 5.5.

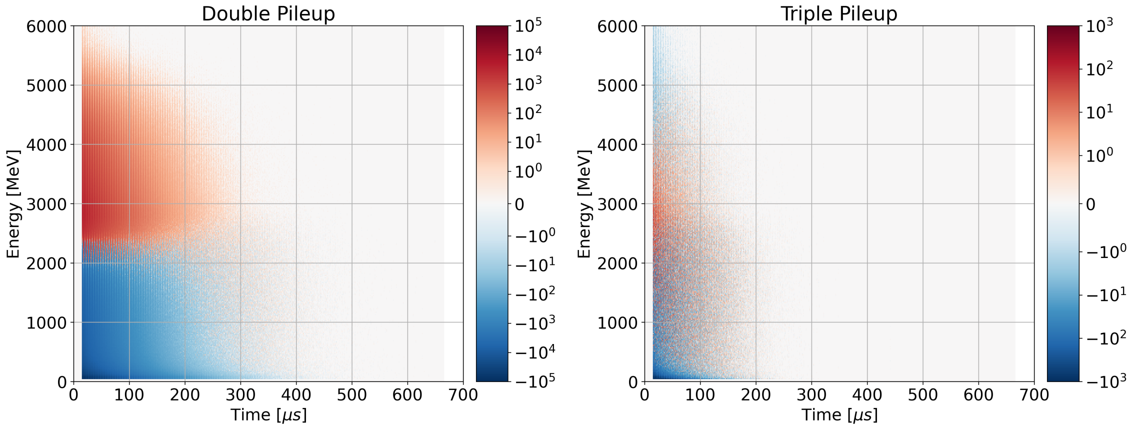

(a) **(b)**

Figure 5.4: Energy, time spectra for (a) double and (b) triple pileup. Note that some portions of the spectrum are negative and some are positive, indicating regions of this space where events were systematically higher/lower than required. The application of the pileup correction to the energy spectrum is shown in Figure 5.5b.

5.2.3 Residual Gain Correction

A correction for a 'residual' gain-like effect[16] is applied to the histograms at this stage. The perturbation to the energy spectrum from a gain change correlated with the instantaneous rate of high-energy positrons hitting the calorimeter face was derived in reference [6]. The energy-time

---

[16] i.e. an effect which is observed in the data but *not* tracked by the laser system, nor detailed in Section 4.1.5

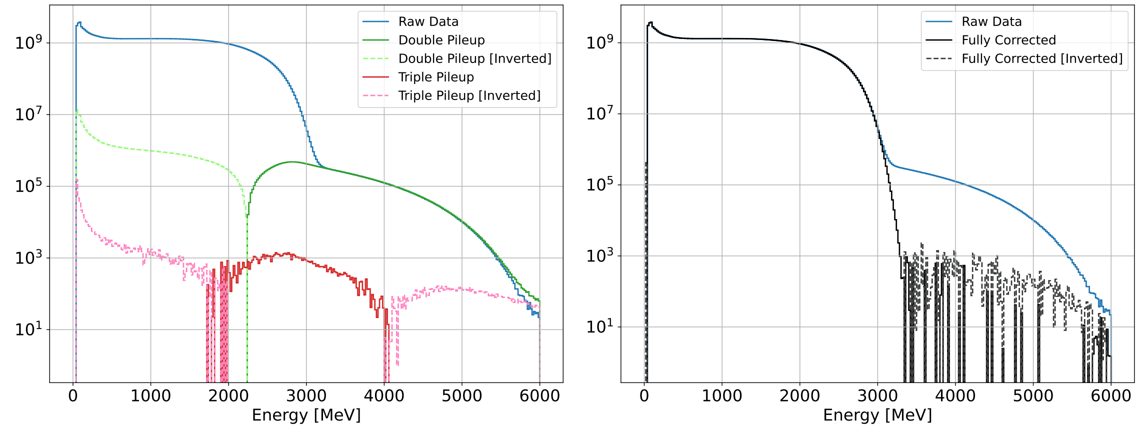

(a)

(b)

Figure 5.5: The uncorrected energy spectrum $[t > 30\,\mu\text{s}]$ overlaid with (a) double and triple pileup spectra, as well with as the (b) final corrected data. The double and triple corrections are both negative at certain points in the energy spectrum, indicating regions where data must systematically be added back in to correct for the effect of 'missing' pulses which became pileup.

spectrum is modified like so:

$$N(E,t) \rightarrow N(E,t)\left(1 + N_g\, e^{-t/\tau_a}\left[1 + A_g \cos\left(\omega_a t - \phi_a\right)\right]\right), \tag{5.8}$$

where τ_a, ϕ_a, and ω_a are taken from the values of the ω_a fit and N_g and A_g are determined using dedicated systematic studies (see Section 5.4.2.1). As of the writing of this thesis, the UW analysis takes the following as the nominal Run-4 values:

$$N_g = 0.00029, \tag{5.9}$$

$$A_g = 0.10, \tag{5.10}$$

The origin of this correction is under active investigation by a dedicated task force of analyzers as part of the Run-4+ analysis. This correction is discussed further in Section 5.4.2.1.

5.2.4 T-Method

The data thus far has been kept in the form of a 2D energy vs. time spectrum, while the nominal ω_a analysis is performed as a fit to a 1D time spectrum[17]. Collapsing the energy axis of this spectrum can be done with any number of thresholds and energy weights. The simplest choice is to place a lower energy threshold and integrate everything above. This is known as a threshold (or 'T-Method') analysis. As shown in Section 1.2.2.1, maximizing the integrated NA^2 in such a distribution will maximize the statistical power of our result. The probability distribution which describes muon decay is [153]:

$$dP = n(y)(1 + A(y)\cos(\omega t))dyd\Omega, \tag{5.11}$$

where $y \equiv {}^{p_e}/_{p_{\max}}$, p_e is the momentum of the decay positron, $p_{\max}$ is the maximum positron momentum (53 MeV/c), and $d\Omega$ is the differential solid angle of the decay. The Michel parameters are [154]:

$$n(y) = 2y^2(3 - 2y) \tag{5.12}$$

$$A(y) = \frac{2y-1}{3-2y} \tag{5.13}$$

These relations for n and a can be written in terms of the lab frame positron energy by applying a Lorentz transformation:

$$n(E) = \frac{2\pi}{3\gamma p_{\max}}(y' - 1)(4y'^2 - 5y' - 5) \tag{5.14}$$

$$A(E) = \frac{1 + y' - 8y'^2}{4y'^2 - 5y' - 5} \tag{5.15}$$

where $y' \equiv {}^{E}/_{E_{\max}}$ in the lab frame and $E_{\max} = 2\gamma p_{\max}$. Integrating above some energy threshold

---

[17] 2D methods for performing the fit could be performed in theory, but in practice these are limited by the knowledge of $A(E)$ (and higher order fit terms) in the presence of detector effects.

E_t yields the total number of positrons above that threshold and their average asymmetry:

$$\begin{aligned}\int_{E_t}^{E_{max}} n(E)dE &= N(E_t) \\ &= \frac{4\pi}{3}(y_t' - 1)^2(y_t' - (y_t')^2 + 3) \qquad (5.16) \\ \frac{\int_{E_t}^{E_{max}} n(e)A(E)dE}{\int_{E_t}^{E_{max}} n(e)dE} &= \bar{A}(E_t) \\ &= \frac{y_t'(2y_t' + 1)}{y_t' - (y_t')^2 + 3}. \qquad (5.17)\end{aligned}$$

where $y_t = E_t/E_{\text{max}}$.

Maximizing NA^2 for these theoretical forms yields the optimum energy threshold[18] of 1.9 GeV. This calculation is done in the absence of any detector acceptance effects, which perturb the measured forms of these parameters (as shown in Figure 5.6). In practice, the optimum energy threshold must therefore be found by scanning the threshold in this region and comparing the statistical power at each value. The result of this process is shown in Figure 5.8a, and yields an optimum threshold of 1.66 GeV in Run-4.

Reconstruction-level changes can affect the value of this optimum threshold. In Run-2/3 the threshold was closer to 1.69 GeV. The change between runs is attributed to the multi-cluster island fix perturbing the overall energy scale of high energy clusters (see Section 4.1.6.1). The threshold scan ensures that, no matter the changes, the analysis is taking place at the statistically optimal threshold.

5.2.5 A-Method

The argument in Section 5.2.4 holds so long as each positron is weighed equally. However, this is not the statistically optimal treatment of the data. Because the $g - 2$ asymmetry increases with positron energy[19], the ensemble of high energy decays contain more information about ω_a than those at lower energies. Extending the argument in Section 1.2.2.1 to account for nonuniform

---

[18] Including any positrons below this threshold (in this simple method where each positron is given the same weight in the final analysis) will 'dilute' the ω_a oscillation signal and thus lower the statistical precision of the result.

[19] This is just a restatement of the fact that the highest energy decay positrons are preferentially emitted in the direction of the muon's spin, as detailed in Chapter 1.

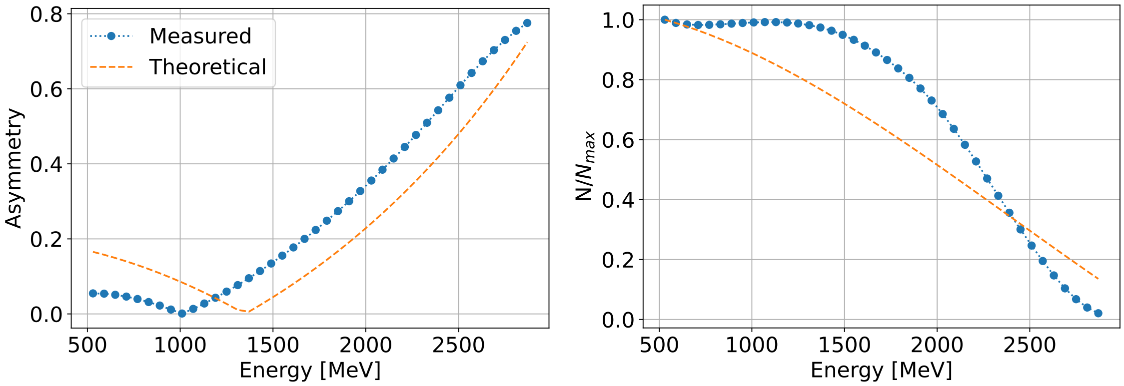

(a) **(b)**

Figure 5.6: Variation of the differential N(E) and A(E) as measured in the calorimeters vs. the theoretical forms in Equations (5.14) and (5.15). These are mapped empirically using the analysis shown in Figure 5.7.

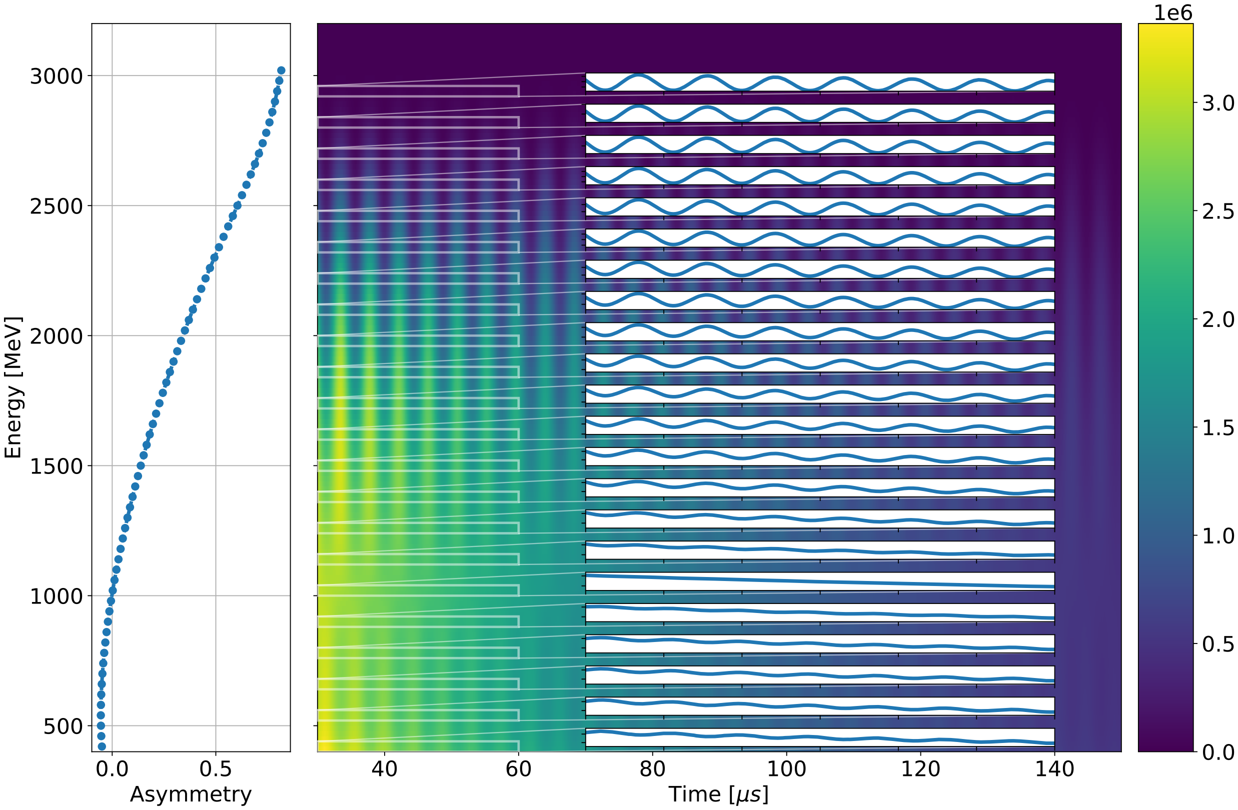

Figure 5.7: $A(E)$ is extracted by dividing the histogram into energy bins and fitting each one individually.

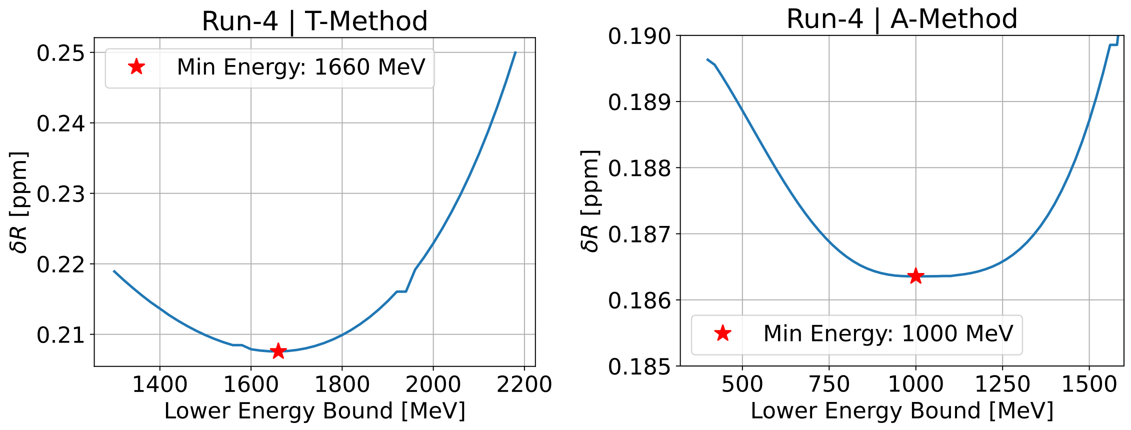

(a) **(b)**

Figure 5.8: Run-4 energy threshold scans vs. precision on $R(\omega_a)$ for (a) the T-Method and (b) the A-Method. Note the difference in the overall y-scales when comparing the T and A-Methods.

weights w:

$$N(t) \rightarrow N_0 e^{-\,t/\tau_a} \left[\langle w\rangle + \langle wA\rangle \cos\left(\omega_a t + \phi\right)\right], \tag{5.18}$$

it can be shown that the statistically optimal method for weighting is the $g-2$ asymmetry itself: $w(E) = A(E)$ [6]. $A(E)$ in the presence of detector effects is mapped empirically by dividing the calorimeter energy spectrum into 60 MeV bins. Each of these bins is fit to Equation (1.17)[20], as illustrated in Figure 5.7. The value of $A(E)$ extracted from each bin is interpolated using a cubic spline. This interpolation is then used to weight 2D histogram when collapsing the energy axis. Any 'incorrect' application of the weighting will result in a slight reduction of the statistical power of the measurement, but not any bias to $R(\omega_a)$. Studies have shown that the uncertainty associated with the exact application of the weighting (for instance, applying $A(E = E_{\text{bin center}})$ vs. $A(E = E_{\text{bin edge}})$) is less than $< 2\,\text{ppb}$. Another energy threshold sweep (Figure 5.8b) allows the optimum lower energy bound for the A-Method to be identified. This is found to be the point where the $g-2$ asymmetry goes to 0: $E_{\text{thresh}} = 1000\,\text{MeV}$.

$A(E)$ changes sign below this inflection point[21], therefore any added positrons from $E <$

---

[20] More precisely, the fit is performed to the blinded version introduced in the next section: Equation (5.19).

[21] Since the analysis code defines $A > 0$ by convention, this often appears in the fit results as a phase shift of ϕ_a by π.

1000 MeV can begin to dilute the ω_a oscillation signal. Some additional statistical power could be gained by a modification of the histogram construction technique to allow for negative positron weights and lowering this threshold further (Figure 5.9b). This is not performed for three reasons:

- Contamination from noise and low-energy MIP particles (see Section 6.2) is limited to low-energy bins, and so by introducing a lower energy cutoff any systematic effects from these particles can be eliminated.

- The energy dependence of some slowly varying terms in the final fit function can complicate the addition of positrons with negative weights.

- Statistical gains would be limited to the $\mathcal{O}(1-2\,\text{ppb})$ level.

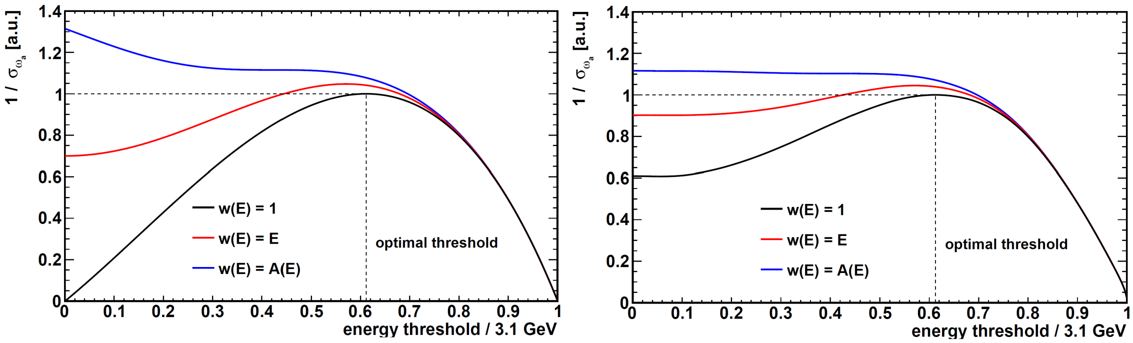

(a) Reproduced from [6].

(b) Reproduced from [6].

Figure 5.9: The precision on $R(\omega_a)$ obtained from the theoretical forms of $N(E_t)$ and $\bar{A}(E_t)$ (a) in the absence of detector effects and (b) with a simple model of detector effects included. Three different weighting schemes are shown: $w(E) = 1$ (T-Method), $w(E) = E$, and $w(E) = A(E)$ (A-Method). In all cases, and for all thresholds, the A-Method is the optimal weighting scheme. These plots do not include the practical limitations for setting the A-Method threshold to a lower bound discussed in Section 5.2.5, but illustrate the limited gains in statistical power that lowering the threshold below 1000 MeV can achieve in the presence of detector effects.

5.3 Building the ω_a Fit Function

5.3.1 First Model: Five Parameters

The simplest model for the extraction of ω_a is, as given in Section 1.2.2.1:

$$N(t) = N_0\, e^{-\,t/\tau_a} \left[1 + A_0 \cos\left(R(\omega_a)\, t + \phi_a\right)\right], \tag{5.19}$$

where N_0 is the overall normalization, τ_a is the effective muon lifetime, A_0 is the $g-2$ asymmetry parameter, ϕ_a is the phase of the $g-2$ oscillation, and the value of ω_a has been replaced with the blinded proxy $R(\omega_a)$.

Weighting the data as described in the previous Section and fitting with the five-parameter model above yields the results shown in Figure 5.10. It can be seen from Figure 5.10a that this functional form describes the data by eye quite well, yet the χ^2 of the fit is quite poor: $\chi^2/\text{NDF} = 12$. Looking at a fast Fourier transform (FFT) of the residuals shows that there are a number of frequencies which are present in the data and unaccounted for in the fit model. These are the BD oscillation frequencies created by the focusing of the ESQ system (see Section 3.3.2).

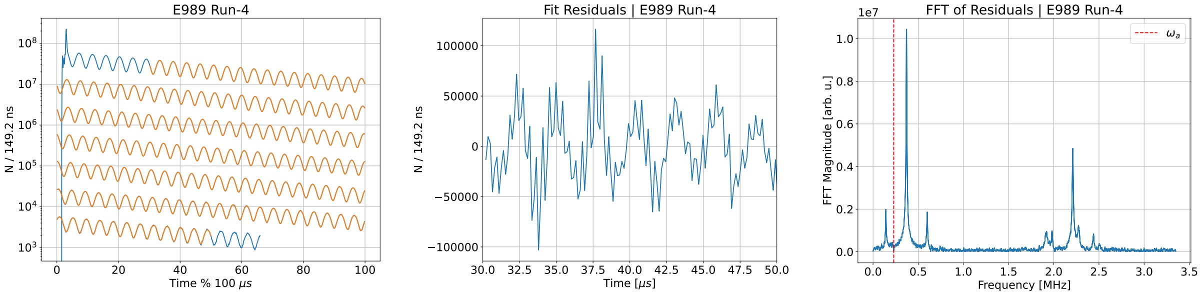

(a) **(b)** **(c)**

Figure 5.10: (a) Fit results, (b) fit residuals, and (c) the FFT of said residuals from fitting Run-4 to the five-parameter model in Equation (5.19). The CBO (low frequency) and y (high frequency) oscillations can clearly be seen in the residuals around 30 μs, corresponding to the highest and second highest peaks in the FFT respectively. Beating of these frequencies with the $g-2$ oscillation can be seen at $\omega_i \pm \omega_a$. The value of ω_a is indicated with the red line in (c).

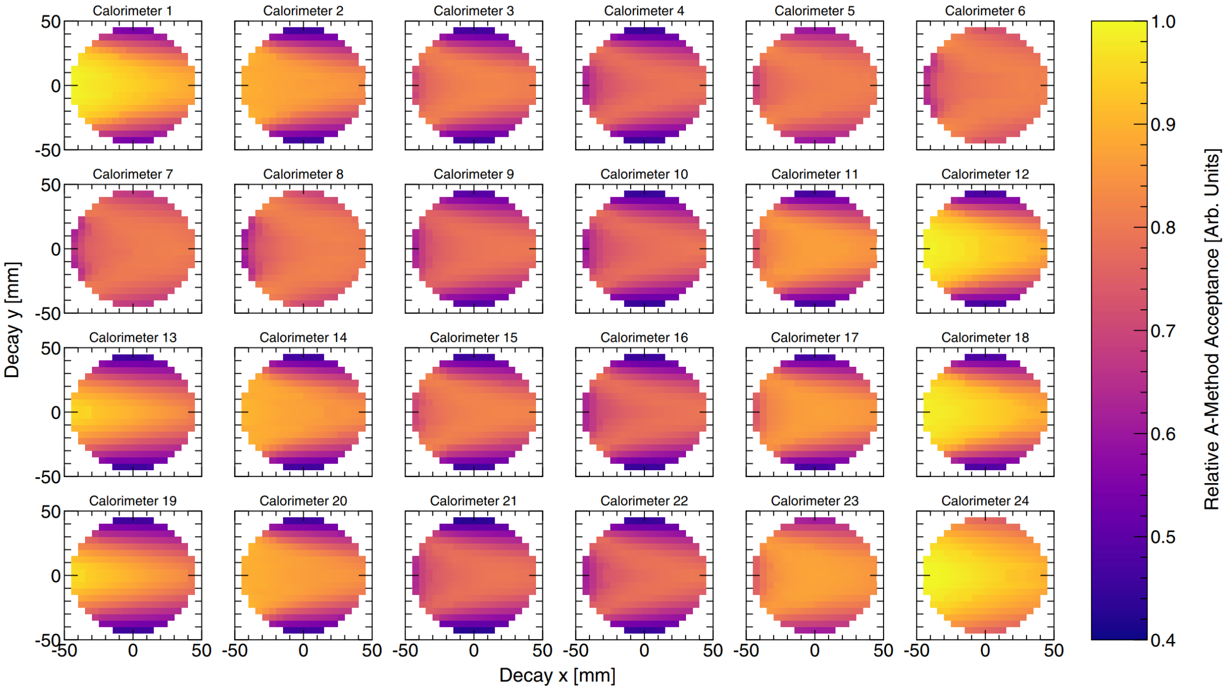

Figure 5.11: Relative acceptance (defined as $24 * N_{\text{detected}}/N_{\text{decayed}}$) for all calorimeters from simulation. The intra-calorimeter variation of these acceptance maps leads to the appearance of the BD frequencies in the positron data. The inter-calorimeter variation causes the BD frequencies to not be entirely cancelled when summing calorimeter data from around the ring. Reproduced from [105].

5.3.2 Beam Dynamics Frequencies: Predictions and Implications

The BD frequencies enter into the calorimeter data through detector acceptance effects. As shown in Figure 5.11, the probability of a positron being detected by the calorimeter varies as a function of the decay muon location in the storage ring: (r, y, θ). As the muons oscillate around their nominal orbits, the number of decay positrons seen by the calorimeters will also vary with the frequency of that oscillation[22]. If unaccounted for, these BD frequencies can bias the fit result by coupling to ω_a through their beat frequencies — $\omega_a \pm \omega_i$ — and pulling the best fit value of ω_a from its true value.

The various beam dynamics frequencies will decohere over the course of a fill as the muon beam debunches. The bias to ω_a will therefore also vary vs. time in fill. All such beam dynamics parameters which appear to an appreciable degree in the $g-2$ data must be explicitly included in the fit function in order to remove such bias[23]. In the UW analysis, this is done through a modification of the fit parameters in Equation (5.19):

$$\begin{aligned} X \rightarrow & X_0 X_i(t) && (5.20) \\ & = X_0 \left[1 + \mathcal{E}_i(t) \cos\left(\omega_i t - \phi_i\right)\right], && (5.21) \end{aligned}$$

where X could stand in for any of the parameters (N, A, ϕ) in Equation (5.19). The BD oscillation is captured in the cosine term and the 'envelope' $\mathcal{E}_i(t)$ describes how the amplitude of the oscillation evolves over the course of the fill. Were there no decoherence of these frequencies, this would simply be a constant: $\mathcal{E}_i(t) = A_i$. For most of the beam dynamics frequencies, the decoherence is modelled

---

[22] To a lesser extent the same is true for the observed asymmetry and phase, as described later in Section 5.3.7.

[23] Some frequencies can be removed by randomization rather than being fit directly, if they are sufficiently far from ω_a. This is done only for the cyclotron frequency in the UW analysis, but some analysis groups also employ this technique to remove high frequency vertical oscillations [155, 156].

simply by an exponential decay[24]:

$$\mathcal{E}_i(t) = A_i e^{-t/\tau_i}, \tag{5.22}$$

with a lifetimes ranging from $\mathcal{O}(10) - \mathcal{O}(100)\,\mu$s. To first order, the oscillatory terms are assumed to be independent such that the fit can be constructed as:

$$X \to X_0 * X_1(t) * X_2(t)...$$

for ω_1, ω_2, etc. This approximation provides a useful starting point, but breaks down in higher statistics datasets where higher order effects become apparent (see Section 5.3.6).

This is not the only possible model for incorporating these BD oscillations. Additional models based on beam moments [152] or deriving the forms of the envelopes from first principles [159] are explored by other analysis groups. The latter is a new approach for introduced for the Run-4 analysis, but the difference between the model presented here and the beam moment model has been studied in Runs 1-3. Less than a 5 ppb difference in the final value of $R(\omega_a)$ ($\ll 1\delta R(\omega_a)$) was found when comparing fit results using the two approaches [160].

The expected values of the BD frequencies (using the approximation of a continuous ESQ focusing field) can be calculated from the field index n (as given in Equation (3.8) in Section 3.3.2). The physical origin of these frequencies is confirmed using the two tracking stations and the MiniSciFi detectors, which observe the oscillations of the beam directly. In Run-4:

$$n = \frac{R_0}{vB_0}\frac{\partial E_y}{\partial y} \approx 0.107. \tag{5.23}$$

which yields:

---

[24] An empirical derivation of the envelope for the various BD frequencies is possible, but it requires detailed knowledge of the spread of the various frequencies in the ring ($\Delta\omega_i$) and the acceptance functions of the calorimeters [157, 158]. Each of these can be derived from simulation, but ultimately such a model results in a 7-12 parameter function of which 2-3 parameters remain floating in the fit. Such envelopes are explored as part of the systematic evaluations of the BD frequency terms, but are not implemented in the main analysis as of the writing of this thesis. Envelopes derived from interpolating sliding window fits to the data itself are also being explored.

$$f_c = \frac{1}{149.2\,\mathrm{ns}} = 6.702\,\mathrm{MHz}, \tag{5.24}$$

$$f_x = \sqrt{1-n}f_c = 6.333\,\mathrm{MHz}, \tag{5.25}$$

$$f_y = \sqrt{n}f_c = 2.197\,\mathrm{MHz}, \tag{5.26}$$

where (and generally throughout the text) $f_i \equiv \omega_i/2\pi$. The histogram bin width of 149.2 ns results in a Nyquist frequency of $f_{\mathrm{Nq}} = {}^{1}/_{(2*149.2\,\mathrm{ns})} = 3.35\,\mathrm{MHz}$. Frequencies higher than f_{Nq}, such as the cyclotron and x oscillation frequencies, therefore appear in the fit in aliased forms and beat frequencies[25]. Table 5.1 gives the values of the beam dynamics frequencies and their various sidebands in Run-4. The calculated frequencies can be seen overlaid with the residual FFT in Figure 5.12. The x-related terms agree well with the calculated values, while the y-related terms show a few percent deviation from the simple model of continuous ESQ plates. Because of this deviation, these frequencies are generally implemented as independent fit parameters rather than being derived from a common field index.

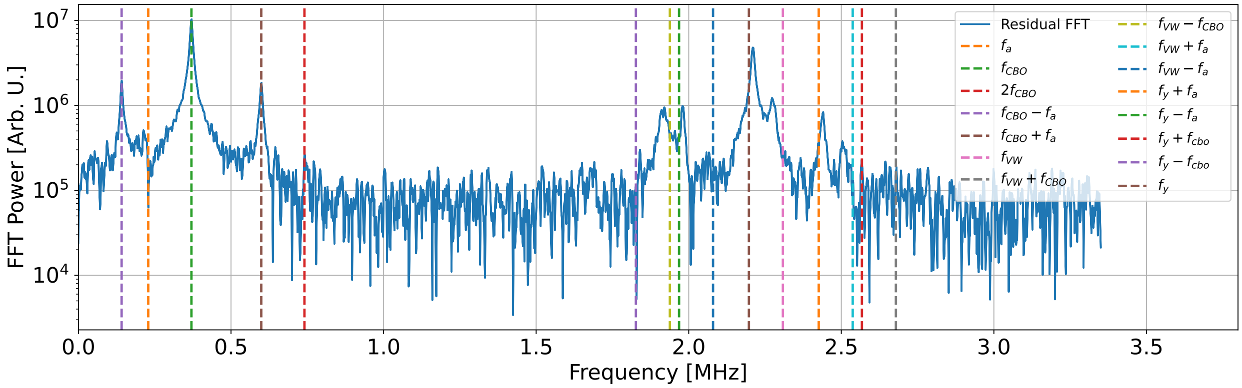

Figure 5.12: Calculated beam frequencies from Table 5.1 overlaid with the Run-4 5-parameter FFT. The largest peak is ω_{cbo}, from which the n value of the ring is extracted. This n value is used to calculate all other BD frequencies. The x frequencies agree well, but the y frequencies show a few percent deviation from their approximate values.

---

[25] Due to the stroboscopic nature of the calorimeter measurements, i.e. their observation of the 'same' beam modulo the cyclotron frequency as the muons circulate in the ring, even if the histogram were more finely binned the frequencies higher than $\omega_c/2$ would still appear in their aliased forms.

Name	Calculated Frequency [MHz]	Fitted Frequency [MHz]	Difference [%]
f_a	0.229	$R(\omega_a)$ **[blinded]**	—
f_c	6.703	—	—
f_x	6.333	—	—
f_y	2.197	**2.210**	0.59
$f_c - f_x \equiv f_{CBO}$	0.370	**0.370**	0.00
$2f_{CBO}$	0.741	0.741	0.00
$f_{CBO} - f_a$	0.142	0.142	0.00
$f_{CBO} + f_a$	0.599	0.599	0.00
$f_c - 2f_y \equiv f_{VW}$	2.309	**2.281**	-1.21
$f_{VW} + f_{CBO}$	2.679	2.651	-1.04
$f_{VW} - f_{CBO}$	1.938	1.911	-1.44
$f_{VW} + f_a$	2.537	2.510	-1.10
$f_{VW} - f_a$	2.080	2.052	-1.34
$f_y + f_a$	2.426	2.439	0.54
$f_y - f_a$	1.968	1.981	0.66
$f_y + f_{cbo}$	2.568	2.581	0.51
$f_y - f_{cbo}$	1.827	1.840	0.71
$f_c - f_y$	4.506	—	—

Table 5.1: Beam Dynamics frequencies observed in Run-4 vs. the approximate expected value from the continuous ESQ calculation (Equations (5.25) and (5.26)). The n value for the continuous ESQ calculation is calculated from the fitted value of ω_{cbo}. Some of these frequencies are not observed directly due to aliasing and the fast rotation randomization. The frequencies in bold are free fit parameters (taken from the full fit in Section 5.3.9), while the others are calculated from those values.

5.3.3 Iterative Fitting Approach

The full fit function used to extract $R(\omega_a)$ is constructed through an iterative process. Starting with the five-parameter functional form (Equation (5.19)), the steps are to:

1. Perform a fit to the data using the current functional form in the region $(30.2, 650]\,\mu$s

2. Examine an FFT of the fit residuals. Identify the physical cause of largest frequency peak (if any exist) and incorporate a model for this frequency into the full fit model[26]. Return to Item 1.

3. If there are no obvious peaks, examine the internal consistency checks detailed in Section 5.4. If parameters are not stable vs. any of these checks — particularly the fit start time and calorimeter-by-calorimeter fits — incorporate any additional changes into the fit model and return to Item 1

Once the fit is stable vs. all of the internal cross checks and a χ^2/NDF consistent with 1 has been achieved, the results are compared across the independent analysis group to rule out any analyzer-specific biases. The process of arriving at a stable fit model is still in progress for Run-4[27].

5.3.4 Coherent Horizontal Betatron Oscillation (CBO)

The largest frequency observed in the residual FFT is the 'coherent betatron oscillation' (CBO): $\omega_{\text{cbo}} \equiv \omega_c - \omega_x \approx 2\pi * 0.370\,\text{MHz}$. A schematic of how the CBO enters the data is shown in Figure 5.13a.

The calorimeters measure the beam in 24 locations, equally spaced out around the ring. As such, they observe a phase advance of the CBO at each station: $\phi_{\text{cbo,i}} \approx \phi_{\text{cbo,0}} + 2\pi N_{\text{calo}}/24$. If every calorimeter were to have an identical acceptance function, then the CBO would cancel around

---

[26] While each frequency incorporated into the model has a physical motivation, it is possible to imagine that such a peak in the FFT could be created coincidentally by a statistical fluctuation rather than a 'true' frequency. The effect of fitting such spurious frequencies has been evaluated using toy Monte Carlo and shown to be $\ll 5$ ppb on $R(\omega_a)$. This is supported by examining the scale at which real higher-order beam dynamics frequencies alter $R(\omega_a)$ (shown later in Table 5.2). In practice, attempting to blindly fit such fluctuations (which can sometimes appear in the various random seeds of the fast rotation randomization procedure) tends to lead to a fit which does not converge.

[27] The schedule for completion of the analysis (at UW) was driven in early to mid-2023 by availability of data and later by person-power having to be split between multiple experiments. It is expected that the fit model will be in a stable configuration by mid-to-late 2024, with systematic evaluations following soon after.

the ring and the peak would not appear in the calorimeter-summed data. Non-uniformities in the acceptance (driven by material effects) break the symmetry of the ring and result in a residual CBO oscillation. The amplitude of the CBO oscillation in the full fit is reduced by a factor of ≈ 5 compared to the calorimeter-by-calorimeter fits.

The CBO is incorporated into the fit model to first order by introducing a time dependence of the overall normalization:

$$N_0 \to N_0 N_x(t), \tag{5.27}$$

$$N_x(t)|_{1^{\text{st}}\ \text{Order CBO}} = 1 + \mathcal{E}_{\text{cbo}}(t) \cos\left(\omega_{\text{cbo}} t - \phi_{\text{cbo}}\right), \tag{5.28}$$

where ω_{cbo} and ϕ_{cbo} are the frequency and phase of the CBO oscillation and $\mathcal{E}_{\text{cbo}}(t)$ is the envelope which describes the decay of the oscillation vs. time in fill. The canonical choice of decoherence envelope for the CBO in Run-4 is:

$$\mathcal{E}_{\text{cbo}}(t) = A_{\text{cbo}} \left(e^{-\,{}^{t}\!/\!{}_{\tau_{\text{cbo}}}} + C_{cbo} \right). \tag{5.29}$$

This was the nominal model used in Run-3b, which has very similar conditions to Run-4. The impact of alternative envelope functions was heavily scrutinized as part of the Run-2/3 analysis [84]. Such evaluations are in progress for the Run-4+ analysis as well. With this first addition, the fit function becomes:

$$N(t) = N_0 N_x(t) e^{-\,{}^{t}\!/\!{}_{\tau}} \left[1 + A \cos\left(R(\omega_a)\, t - \phi\right)\right]. \tag{5.30}$$

Fitting the data using Equation (5.30) yields an improved reduced χ^2 (≈ 3.2) and largely eliminates the peaks at ω_{cbo} and $\omega_{\text{cbo}} \pm \omega_a$ in the residual FFT (Figure 5.13b).

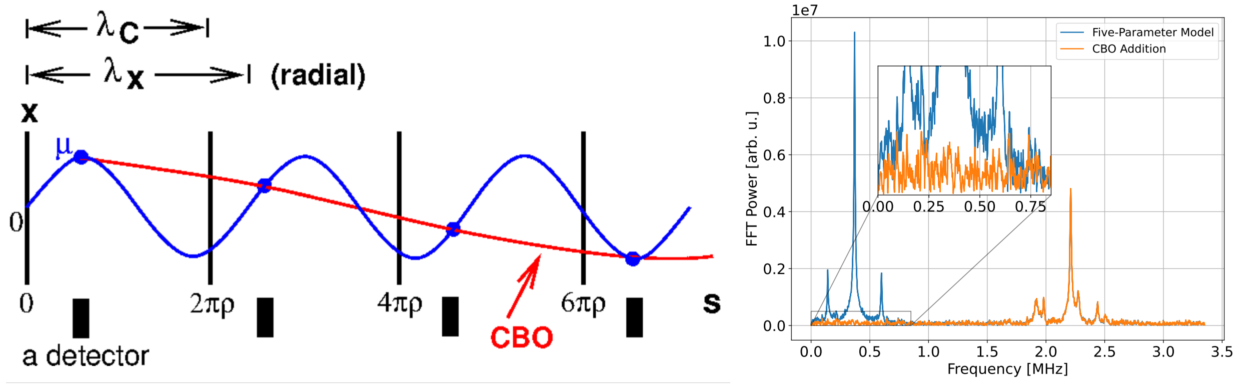

(a) Reproduced from [76]. **(b)**

Figure 5.13: (a) A cartoon showing the beating between the x and cyclotron frequencies which produces the CBO. A single calorimeter station views the beam every time it circumnavigates the ring (represented here as every $2\pi\rho$ distance travelled). (b) The effect of including the CBO oscillation in the fit function on the residual FFT. The peaks at ω_{cbo}, as well as $\omega_{\text{cbo}} \pm \omega_a$ disappear.

5.3.5 Vertical Frequencies

The next largest terms belong to the vertical frequencies. Two vertical frequencies are evident in the data: the unaliased vertical oscillation ω_y and the aliased vertical width[28] (VW) modulation $\omega_{\text{vw}} \equiv \omega_c - 2\omega_y$. These are accounted for by adding N modulations of the form:

$$N_y = 1 + \mathcal{E}_y(t)\cos\left(\omega_y t - \phi_y\right) \tag{5.31}$$

$$N_{\text{vw}} = 1 + \mathcal{E}_{\text{vw}}(t)\cos\left(\omega_{\text{vw}} t - \phi_{\text{vw}}\right) \tag{5.32}$$

where both $\mathcal{E}_y(t)$ and $\mathcal{E}_{\text{vw}}(t)$ are well-described by pure exponential decoherence:

$$\mathcal{E}_y(t) = A_y\, e^{-t/\tau_y}, \tag{5.33}$$

$$\mathcal{E}_{\text{vw}}(t) = A_{\text{vw}}\, e^{-t/\tau_{\text{vw}}}. \tag{5.34}$$

The VW oscillation is enhanced relative to the y-oscillation for all calorimeters because of the vertical symmetry of the calorimeter acceptance[29]. The presence of the kicker plates significantly

---

[28] Sometimes also referred to as ‘vertical waist’

[29] This is a fact that is made use of when constructing the phase-acceptance maps in Figure 5.11. The calorimeter can be ‘folded in half’ vertically to double the statistics.

perturbs the vertical acceptance of Calorimeters 5-8, leading to a local enhancement of the y-oscillation amplitude (see Figure 5.14b). Because these two frequencies are so close together, it is difficult for the fitter to definitively lock on to one or the other when they are included alone. They are therefore introduced together, and the full fit function becomes:

$$N(t) = N_0 N_x(t) N_y(t) N_{\text{vw}}(t) e^{-t/\tau} \left[1 + A\cos\left(R(\omega_a)\, t - \phi\right)\right]. \tag{5.35}$$

The results of including these terms in the fit can be seen in Figure 5.14a. The two main peaks corresponding to ω_y and ω_{vw}, as well as their beat frequencies with ω_a, have disappeared. However, a residual oscillation frequency at 1.9 MHz remains.

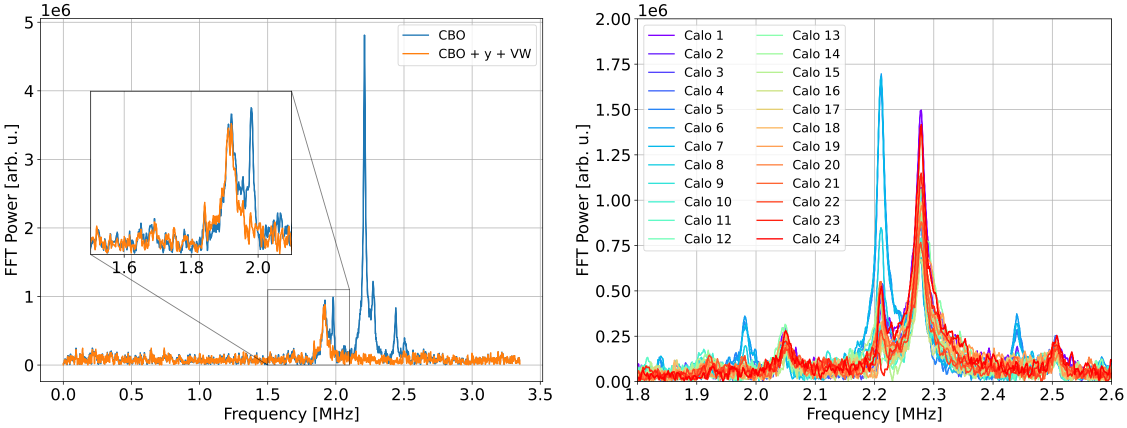

(a) (b)

Figure 5.14: (a) The addition of the y and VW oscillation terms in the fit reduces the magnitude of the peaks of the residuals in the FFT. (b) The relative magnitude of the vertical terms in the FFT of a calorimeter-by-calorimeter analysis. The VW oscillation (≈ 2.27 MHz) is present at the same approximate level in all calorimeters, while the y oscillation (≈ 2.20 MHz) is significantly more pronounced in the calorimeters located in the kicker region due to acceptance effects.

5.3.6 Coupled x/y Cross Terms

In the previous formalism, the radial and vertical oscillations were assumed to be independent, and thus able to be factored into $N_x(t)$ and $N_y(t)$ without loss of generality. This is not entirely correct. The coupling between these two factors can be seen from the acceptance maps generated for each calorimeter from simulation (as can be seen in Figure 5.11).

With the higher statistics of the Run-2/3 analysis, the higher-order coupling between the horizontal and vertical BD frequencies was visible in the fit residuals for the first time. The 1.9 MHz frequency in Figure 5.14a was identified as coming from beating between the VW ($\omega_c - 2\omega_y$) and the CBO ($\omega_c - \omega_x$) frequencies[30]. The presence of this peak was unexpected for two reasons:

- The lower frequency sideband ($\omega_{\text{vw}} - \omega_{\text{cbo}}$) was visible while the higher frequency sideband ($\omega_{\text{vw}} + \omega_{\text{cbo}}$) was not.
- Most beat frequencies are removed when the primary frequencies are included in the fit (as was the case for $\omega_{\text{cbo}} \pm \omega_a$, for instance). The 1.9 MHz peak remained even after ω_{cbo} and ω_{vw} were accounted for in the fit model.

The former effect can be understood as a consequence of the phase advance around the ring. Both ω_{vw} and ω_{cbo} advance by $2\pi{}^{N_{\text{calo}}}/_{24}$ at each calorimeter station around the ring. Therefore when $N_{\text{vw}}(t)$ and $N_{\text{cbo}}(t)$ are multiplied and expanded, the two phase advances cancel in the $\omega_{\text{vw}} - \omega_{\text{cbo}}$ term but sum to $4\pi{}^{N_{\text{calo}}}/_{24}$ in the $\omega_{\text{vw}} + \omega_{\text{cbo}}$ term [84, 161]. Therefore the positive sideband will experience the same cancellation as either of the two individual frequencies while the amplitude of the negative sideband will be unaffected by the summation. The latter effect was shown to both be due to acceptance, where the coupling of the x/y acceptances in the calorimeters could enhance the amplitude of an oscillation beyond what would be expected from the naive product of cosines (${}^{A_{\text{vw}}A_{\text{cbo}}}/_{2}$) [84, 162, 163]. Because of this enhancement, an additional degree of freedom in the amplitude was required to properly fit the peak.

To accommodate this coupling, the CBO and VW terms described in Sections 5.3.4 and 5.3.5 are combined to one N_{xy} term which allows the amplitude and phase of their beat cross terms to

---

[30] This can alternatively be interpreted as the $\omega_x - 2\omega_y$ beat frequency directly, rather than VW-CBO. The implication of this distinction would primarily be that it would be reasonable to allow the envelope and frequency of this cross term to float in the fit. This extension of the fit model is currently under investigation and is described briefly in Section 5.5.1. Preliminary results suggest this change can result in a $\Delta R(\omega_a) \approx 10\,\text{ppb}$ and a reduction in residual peaks in the final FFT.

float:

$$\begin{aligned} N_{xy}(t)|_{\text{Run-2/3}} = &\ (1+\mathcal{E}_{\text{cbo}}(t)\cos(\omega_{\text{cbo}}t-\phi_{\text{cbo}}))(1+\mathcal{E}_{\text{vw}}(t)\cos(\omega_{\text{vw}}t-\phi_{\text{vw}})) \\ &= 1+\mathcal{E}_{\text{cbo}}(t)\cos(\omega_{\text{cbo}}t-\phi_{\text{cbo}}) \\ &\quad + \mathcal{E}_{\text{vw}}(t)\cos(\omega_{\text{vw}}t-\phi_{\text{vw}}) \\ &\quad + \mathcal{E}_{\text{vw/cbo}}\left[A_{\text{VW+CBO}}\cos((\omega_{\text{vw}}+\omega_{\text{cbo}})t-\phi_{\text{VW+CBO}})\right] \\ &\quad + \mathcal{E}_{\text{vw/cbo}}\left[A_{\text{VW-CBO}}\cos((\omega_{\text{vw}}-\omega_{\text{cbo}})t-\phi_{\text{VW-CBO}})\right] + [\text{Higher Order}] \end{aligned} \tag{5.36}$$

where

$$\mathcal{E}_{\text{vw/cbo}} = e^{-t/\tau_{\text{cbo}}-t/\tau_{\text{vw}}}, \tag{5.37}$$

and the amplitude and phases of the two cross terms ($A_{\text{VW+CBO}}$, $A_{\text{VW-CBO}}$, $\phi_{\text{VW+CBO}}$, and $\phi_{\text{VW-CBO}}$) have been defined.

In Equation (5.36), the portion of the cross term arising from C_{cbo} is neglected. This had no measurable effect on the Run-2/3 analysis since $C_{\text{cbo}} \equiv 0$ in Run-2/3a and Run-3b did not have the statistical power required to be sensitive to such higher order terms. Fit models which include this portion of the cross term:

$$\begin{aligned} &+ C_{\text{cbo}}\mathcal{E}_{\text{vw}}\left[A_{\text{VW+CBO}}\cos((\omega_{\text{vw}}+\omega_{\text{cbo}})t-\phi_{\text{VW+CBO}})\right] \\ &+ C_{\text{cbo}}\mathcal{E}_{\text{vw}}\left[A_{\text{VW-CBO}}\cos((\omega_{\text{vw}}-\omega_{\text{cbo}})t-\phi_{\text{VW-CBO}})\right] \end{aligned}$$

are currently being explored.

Incorporating Equation (5.36) into the fit function yields an improvement in χ^2 and removes the 1.9 MHz peak from the residuals (Figure 5.15a). Although a prominent peak is not visible in the FFT, the fit does prefer a small positive value for $A_{\text{vw+cbo}}$ in Run-4, suppressed relative to $A_{\text{vw-cbo}}$ by approximately one order of magnitude. This is likely due to imperfect cancellation of the beat frequency around the ring. This can be seen in Figures 5.15b and 5.15c, where the χ^2 of the fit (leaving all other parameters to float) is scanned. The grey bands indicate the uncertainties as determined by `MINOS`. Both amplitudes are $> 2\sigma$ from 0.

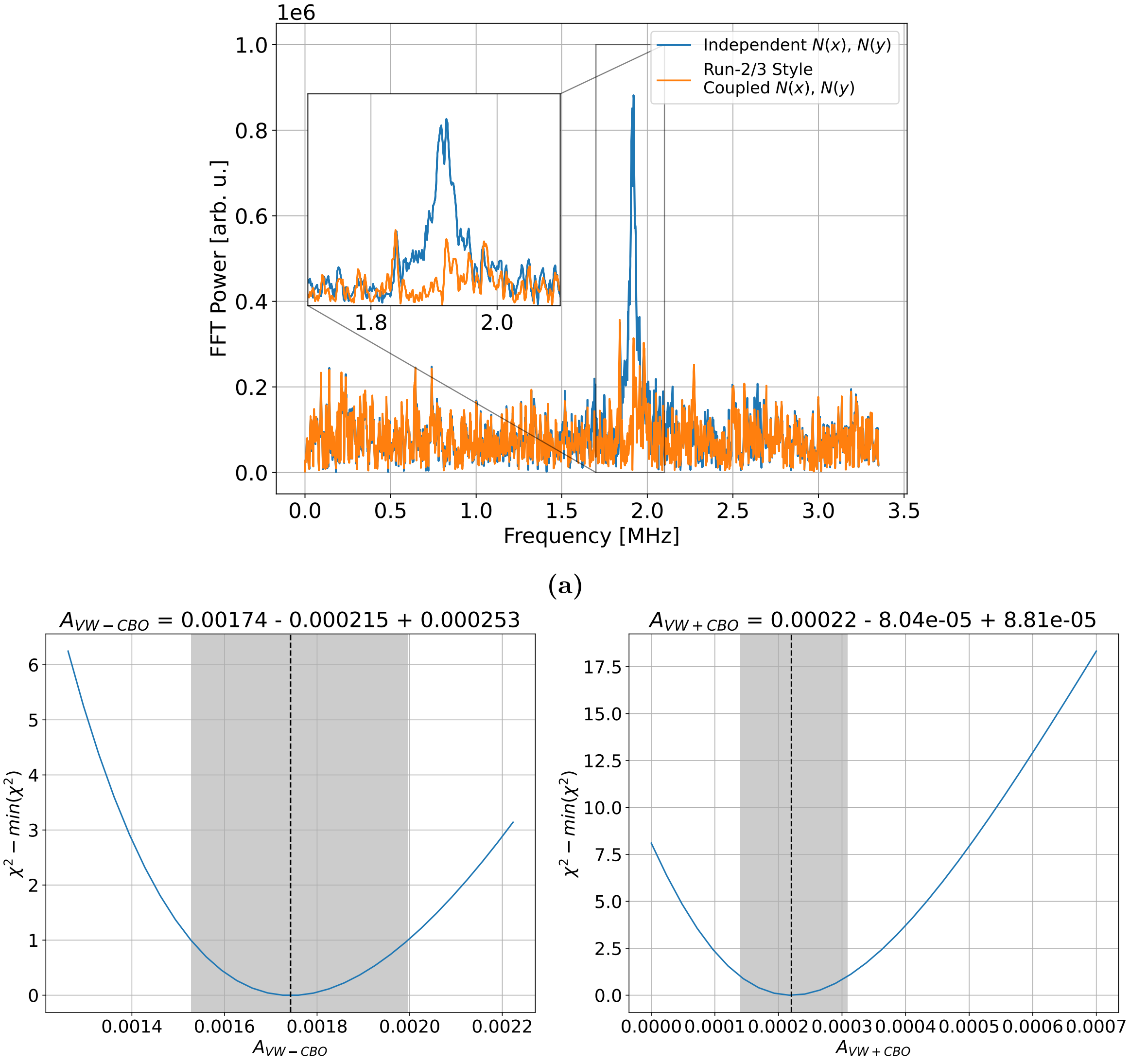

(a)

(b)

(c)

Figure 5.15: (a) The FFT of the fit results before and after the inclusion of the coupled N_{xy} term, as defined in Equation (5.36). The oscillation at $\omega_{\text{vw}} - \omega_{\text{cbo}} \approx 1.9\,\text{MHz}$ is eliminated. In Run-2, only the negative sideband was required. However, in Run-4 positive values for both $A_{\text{vw-cbo}}$ and $A_{\text{vw+cbo}}$ are preferred in the fit. This can be seen from the χ^2 scan of both parameters in (b) and (c).

In Run-4, the increased amplitude of the y-oscillation compared to Run-2/3 (see Figure 7.1 in Section 7.1) led to the appearance of a similar beat frequency between ω_y and ω_{cbo}. N_{xy} was further extended to encompass this coupling:

$$\begin{aligned} N_{xy}(t)|_{\text{Run-4}} = 1 &+ \mathcal{E}_{\text{cbo}}(t)\cos\left(\omega_{\text{cbo}}t - \phi_{\text{cbo}}\right) \\ &+ \mathcal{E}_{\text{vw}}(t)\cos\left(\omega_{\text{vw}}t - \phi_{\text{vw}}\right) \\ &+ \mathcal{E}_{\text{y}}(t)\cos\left(\omega_{\text{y}}t - \phi_{\text{y}}\right) \\ &+ \mathcal{E}_{\text{vw/cbo}}\left[A_{\text{VW+CBO}}\cos\left((\omega_{\text{vw}} + \omega_{\text{cbo}})t - \phi_{\text{VW+CBO}}\right)\right] \\ &+ \mathcal{E}_{\text{vw/cbo}}\left[A_{\text{VW-CBO}}\cos\left((\omega_{\text{vw}} - \omega_{\text{cbo}})t - \phi_{\text{VW-CBO}}\right)\right] \\ &+ \mathcal{E}_{\text{y/cbo}}\left[A_{\text{y+CBO}}\cos\left((\omega_{\text{y}} + \omega_{\text{cbo}})t - \phi_{\text{y+CBO}}\right)\right] \\ &+ \mathcal{E}_{\text{y/cbo}}\left[A_{\text{y-CBO}}\cos\left((\omega_{\text{y}} - \omega_{\text{cbo}})t - \phi_{\text{y-CBO}}\right)\right], \end{aligned} \tag{5.38}$$

where

$$\mathcal{E}_{\text{y/cbo}} = e^{-t/\tau_{\text{cbo}} - t/\tau_{\text{y}}}. \tag{5.39}$$

and again higher order terms have been dropped. With this addition, the full fit function becomes:

$$N(t) = N_0 N_{\text{xy}}(t) e^{-t/\tau}\left[1 + A\cos\left(R(\omega_a)\,t - \phi\right)\right]. \tag{5.40}$$

The results of including this term can be seen in Figure 5.16. Even with this addition, a number of frequency peaks are visible in the FFT in the $1.8 - 2.5\,\text{MHz}$ range. This is an indication that vertical frequency fit model remains incomplete.

5.3.7 Higher Order Beam Dynamics Terms

The effect of terms beyond this point is difficult to see in the FFT of lower statistics datasets, and is largely invisible in the calorimeter-summed FFT due to cancellation around the ring. However, evidence for these terms can be found by looking at the stability of the various parameters vs. the start time of the fit and by examining the calorimeter-by-calorimeter residuals. While individual calorimeter fits only have $1/24$ the statistics of the full fit, they are more sensitive to higher-order

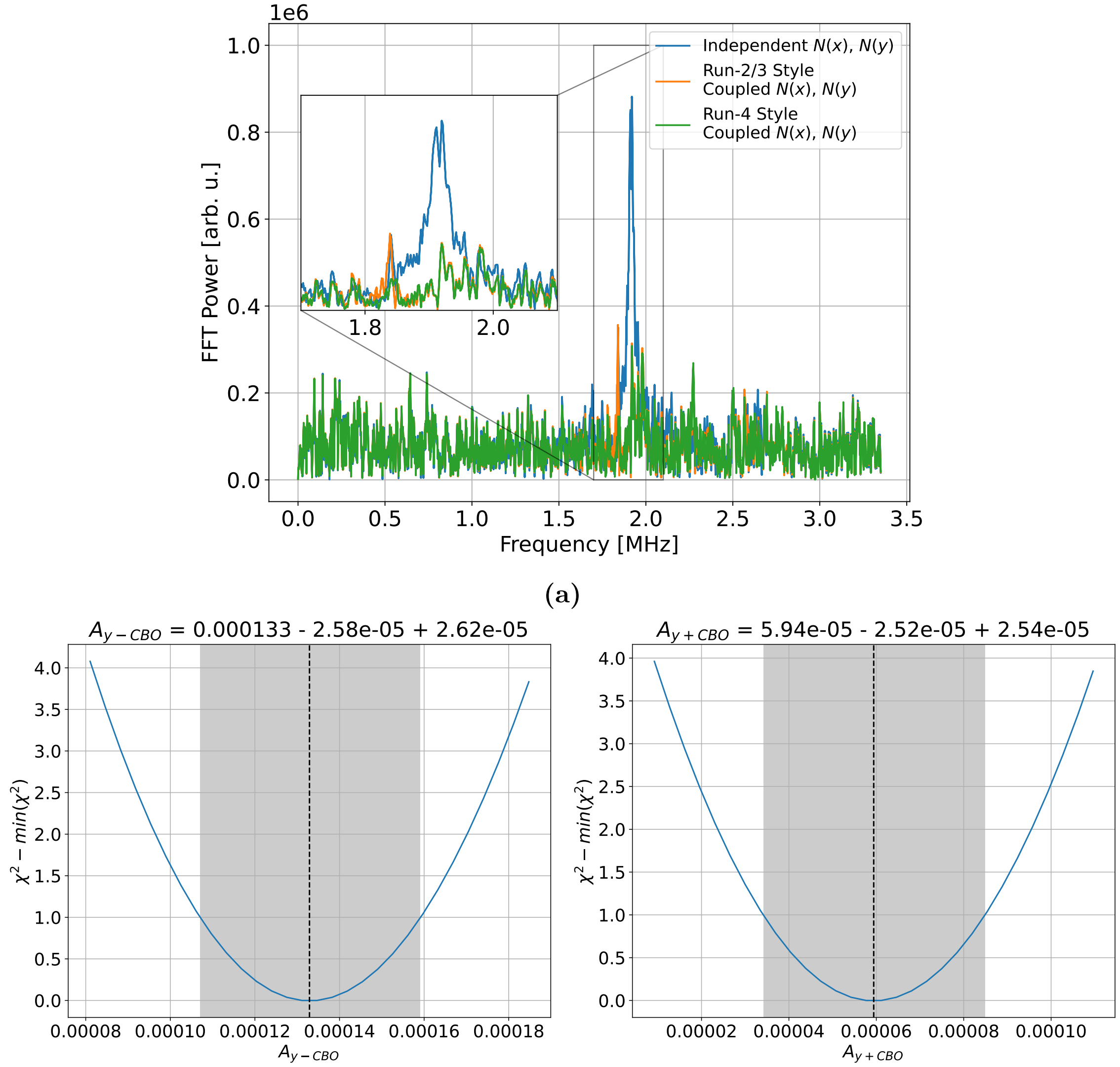

(a)

(b) **(c)**

Figure 5.16: The FFT of the fit residuals before and after the inclusion of the y-oscillation in the coupled N_{xy} term, as defined in Equation (5.38). The residual peak in the FFT (a) at $\omega_{\mathrm{y}} - \omega_{\mathrm{cbo}}$ is eliminated. Based on the χ^2 scans in (b) and (c), the fit prefers positive values for both the coupled $A_{\mathrm{y}\pm\mathrm{CBO}}$ amplitudes, suppressed by an order of magnitude relative to their vw±cbo counterparts.

beam dynamics effects. For instance, the residuals of the fits to the individual calorimeters using only the model up to Equations (5.38) and (5.40) can be seen in Figure 5.17. Clearly the fit model has not yet captured the full dynamics of the CBO or the vertical terms with just the function above.

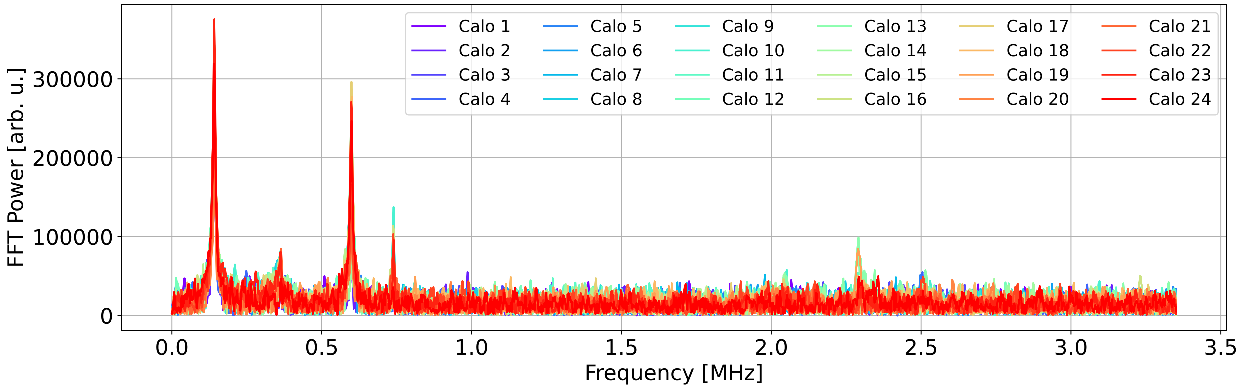

Figure 5.17: Calorimeter-by-calorimeter fit residual FFTs using the fit model in Equation (5.40). While this model describes the calorimeter-summed data quite well, it clearly does not capture the calorimeter-by-calorimeter dynamics. This is evidenced by the peaks in the residuals, the most prominent of which are at $\omega_{\text{cbo}} \pm \omega_a$.

5.3.7.1 CBO Modulations of A, ϕ

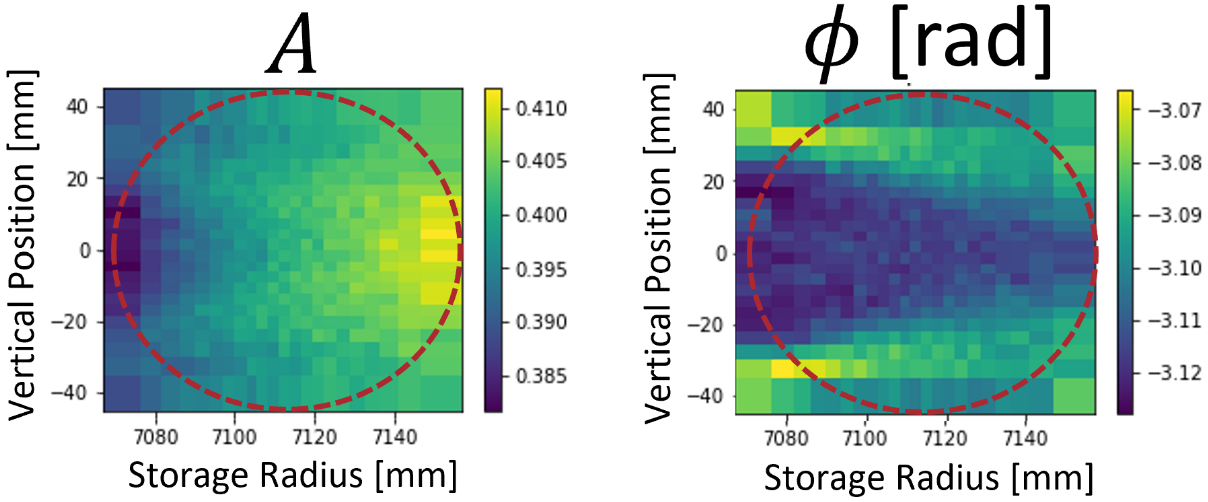

Figure 5.18: Average T-Method ϕ_a and A_0 measured by the calorimeters vs. the position in the storage region where the positrons were born, from simulation. Modified from [164].

While the main effect of the BD oscillations is seen in the modulation of the positron counts, $N(t)$, the observed $g-2$ asymmetry and phase also depend on the positron decay position (Figure 5.18) and therefore are modulated by the beam oscillations[31]. These terms are modified to include the effects of the CBO oscillations like so:

$$A_0 \to A_x(t) = A_0 \left[1 + e^{-t/\tau_{\mathrm{cbo}}} A_{\mathrm{AX11}} \cos\left(\omega_{\mathrm{cbo}}(t)t + \phi_{\mathrm{AX11}}\right)\right] \tag{5.41}$$

$$\phi_a \to \phi_x(t) = \phi_a + e^{-t/\tau_{\mathrm{cbo}}} A_{\phi X11} \cos\left(\omega_{\mathrm{cbo}}(t)t - \phi_{\phi X11}\right) \tag{5.42}$$

The notation for the fit parameters introduced here is slightly different from the previous sections[32]. Here the subscripts refer to the parameter which is being modulated, the beam moment, and the harmonic of that moment which is responsible for the modulation. For instance, the subscript 'AX11' refers to the modulation of A by the 1^{st} order x beam moment's first harmonic (i.e. the CBO). What has been referred to previously as A_{cbo} could be equivalently written in this notation as A_{NX11}.

The result of adding these additional modulation terms is shown in Figure 5.20 for Calorimeter 6. The amplitudes of these modulations are suppressed by 2 orders of magnitude compared to the amplitude of the CBO modulation of the normalization. The values of these parameters are allowed to float in the full fit, and the fit strongly prefers a non-zero value for both A_{AX11} and $A_{\phi\mathrm{X11}}$ (Figure 5.19).

5.3.7.2 CBO Harmonics: 2CBO and Beyond

A small residual peak can also be seen at $2\omega_{\mathrm{cbo}}$. This second harmonic of the CBO is incorporated into the fit in much the same way the first harmonic was:

$$N_{2CBO} = 1 + \mathcal{E}_{2CBO}(t) \cos\left(2\omega_{\mathrm{cbo}}t + \phi_{\mathrm{2CBO}}\right), \tag{5.43}$$

$$\mathcal{E}_{2CBO}(t) = A_{\mathrm{2CBO}} \left(e^{-t/2\tau_{cbo}} + C_{cbo}\right). \tag{5.44}$$

---

[31] This can equivalently be understood as (and implemented in the fits by) allowing the $\omega_{\mathrm{cbo}} \pm \omega_a$ sidebands to have independent amplitudes and phases.

[32] This is entirely due to historical naming conventions in the fitter code. This notation is largely made redundant by the inclusion of the higher order moments in the fit model directly.

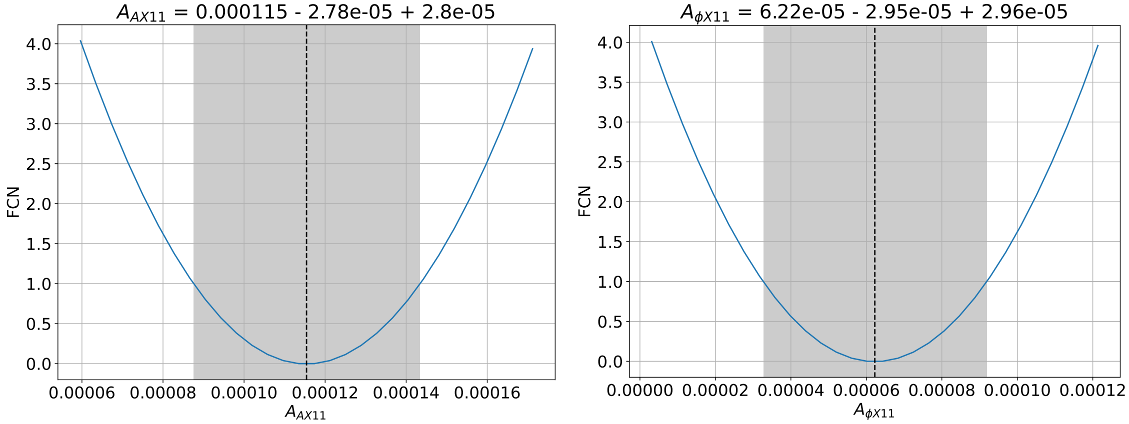

(a) **(b)**

Figure 5.19: A scan of the χ^2 parameter space for (a) A_{AX11} and (b) $A_{\phi\mathrm{X11}}$ in the full fit. While the effect of these terms is not obvious in the FFT, they are strongly preferred to have a non-zero amplitude.

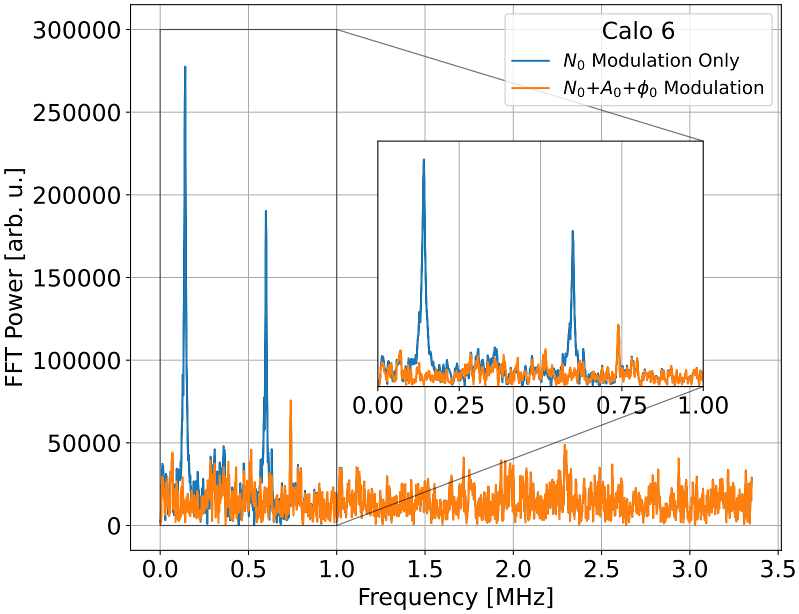

Figure 5.20: Effect of the addition of the $A_x(t)$ and $\phi_x(t)$ terms on the FFT of the residuals from Calorimeter 6.

Currently, this is kept as an N_x term rather than being folded into N_{xy}. This is a fairly arbitrary choice, and studies (using both real calorimeter data and Monte Carlo) are ongoing to determine the scale at which arbitrary choices like this impact the value of $R(\omega_a)$. As mentioned previously, similar studies performed for the Run-2/3 analysis suggest a $< 5\,\text{ppb}$ effect which largely averages out when combining the 6 analysis groups [160]. The effect of this additional term on the calorimeter 6 results is shown in Figure 5.21. The 2CBO terms are allowed to float in the full fit and a non-zero amplitude is strongly preferred.

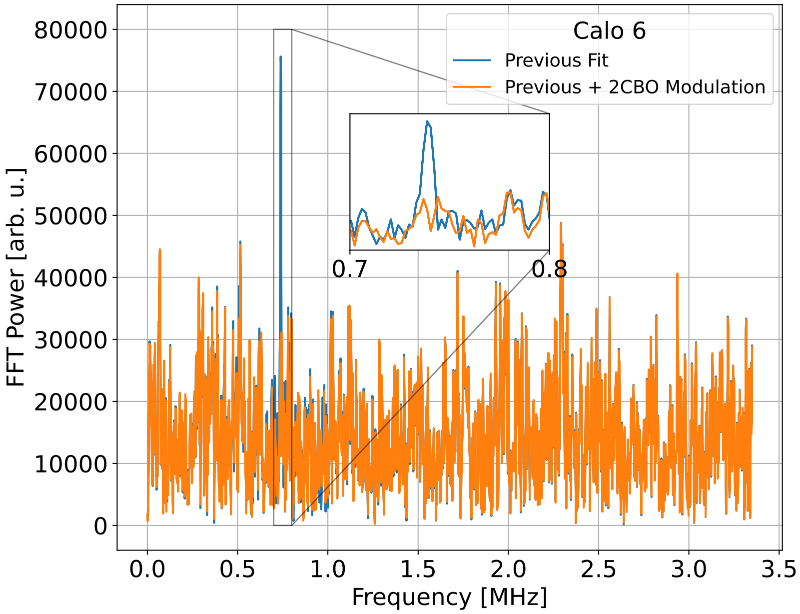

Figure 5.21: Effect of the addition of the N_{2CBO} term on the FFT of the residuals from Calorimeter 6.

5.3.7.3 Time Dependence of the Beam Dynamics Frequencies $\omega_{\mathbf{cbo}}$, $\omega_{\mathbf{vw}}$, and $\omega_{\mathbf{y}}$

Even after the addition of the higher order terms above, broad residual peaks at the CBO frequency remain in some calorimeters (Figure 5.22). Moreover, the magnitude of these peaks increases as the fit start time is moved backwards. This is evidence that these frequencies (or more exactly, the field index of the storage ring) are changing over the course of the fill.

In Runs 1-3 only a time varying ω_{cbo} was incorporated into the UW analysis, as this was the most prominent BD frequency and the analysis was not sensitive to changes in the vertical terms.

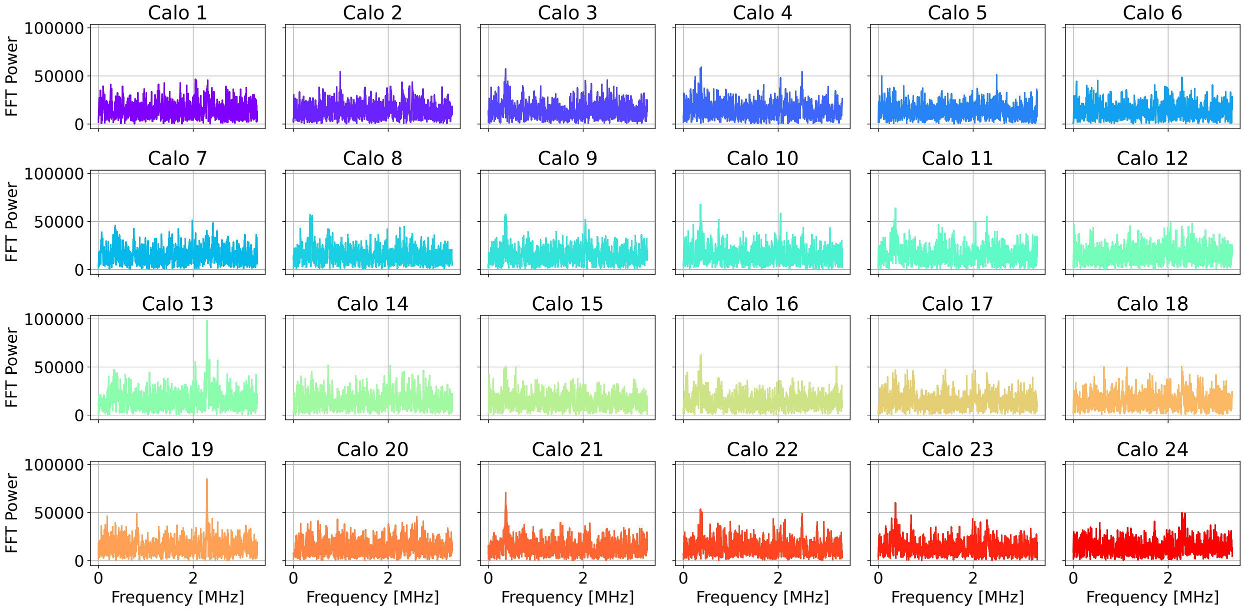

Figure 5.22: FFT of the calorimeter by calorimeter residuals with the fit model up to the 2CBO term in Equation (5.43). Residual behavior at ω_{cbo} can be seen in some calorimeters around the ring. Some peaks in the vertical region are also visible.

In Run-1, this effect was especially large due to damaged ESQ resistors. The form of ω_{cbo} in Run-1 was:

$$\omega_{\text{cbo}} \rightarrow \omega_{\text{cbo}}(t)|_{\text{Run-1}} = \omega_{\text{cbo},0} + \frac{a}{t}e^{-\,-\,t/\tau_a} + \frac{b}{t}e^{-\,-\,t/\tau_b} \tag{5.45}$$

where a/τ_a encapsulated the effect of intentional scraping and b/τ_b encapsulated the effect of unintentional beam motion from damaged ESQ resistors [6]. In Run-2/3, after the repair of the ESQ system, this was simplified to only include the scraping term.

$$\omega_{\text{cbo}}(t)|_{\text{Run-2/3}} = \omega_{\text{cbo},0} + \frac{a}{t}e^{-t/\tau_a} \tag{5.46}$$

$$\tag{5.47}$$

In both cases, the parameters were fixed to inputs from the tracker detectors:

$$a \equiv 6.87, \;\; \tau_a \equiv 6.0.$$

This form sufficed for the calorimeter-summed fits in Run-2/3. However, a residual form of the

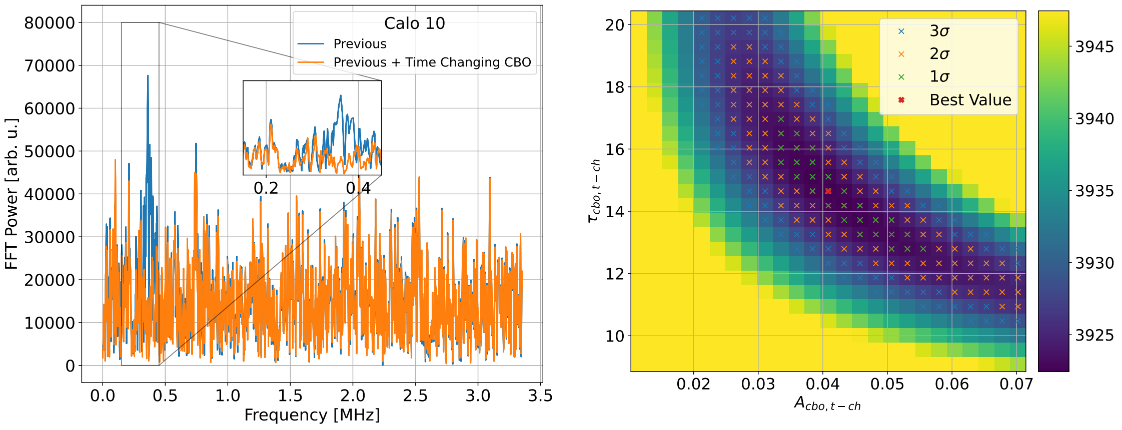

(a) **(b)**

Figure 5.23: (a) FFT of the fit residuals from Calorimeter 10 with and without the time changing CBO frequency. The peak in the residuals disappears with the additional degrees of freedom in the fit. (b) A scan of the χ^2 parameter space for the various values of $A_{\text{cbo,t-ch}}$ and $\tau_{\text{cbo,t-ch}}$. The color scale indicates the value of χ^2 for the fit minimum, and the x's in the legend indicate the regions which are $1 - 3\sigma$ from the minimum. The fit prefers a non-zero amplitude for this time changing frequency, but with a different lifetime to what was found in Run-2/3.

CBO frequency change was required in the calorimeter-by-calorimeter fits.

$$\omega_{\text{cbo}}(t) = \omega_{\text{cbo,tracker}}(t)\left(1 + A_{\text{cbo,t-ch}}\, e^{-t/\tau_{\text{cbo,t-ch}}}\right) \tag{5.48}$$

The amplitude $A_{\text{cbo,t-ch}}$ was allowed to float, while the lifetime in the UW analysis was fixed to 30 μs from dedicated studies [84]. Other groups (which did not include the tracker results as a fixed input in their fits) found a lifetime more consistent with 24.4 μs [165]. These differences caused no discernible impact to the fit quality nor value of $R(\omega_a)$ obtained when adding this term. Adding this residual frequency change to the fit removes the residual CBO peak in the FFTs of affected calorimeters, as can be seen for Calorimeter 10 in Figure 5.23. Preliminary results from Run-4 indicate that the residual CBO frequency change prefers a lifetime of $\tau_{cbo,t-ch} = 14.6\,\mu$s. This is shown in Figure 5.23b, where the χ^2 of the fit is mapped out vs the amplitude and lifetime of this time changing frequency.

Not evident in the Run-2/3 data was any residual behavior in the vertical terms. However, since ω_{cbo} and $\omega_{vw/y}$ are related through the field index, this was always expected. The magnitude of the expected change can be obtained by writing the field index in terms of ω_{cbo}:

$$n = 1 - \left(1 - \frac{\omega_{\text{cbo}}}{\omega_c}\right)^2 \tag{5.49}$$

and using the relations in Table 5.1. The results of this calculation are shown in Figure 5.24.

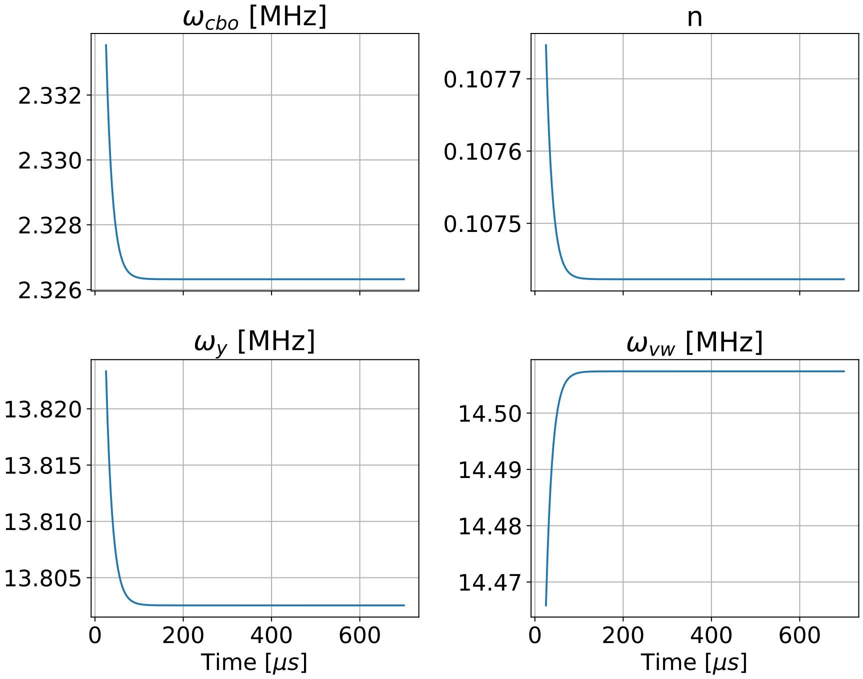

Figure 5.24: Calculated changes in ω_{vw} and ω_{y} based on the best fit value of $\omega_{\text{cbo}}(t)$ in Calorimeter 10. These time changes can be incorporated into the fit function as one time changing n value, with a scale factor to allow for non-continuous ESQ scaling.

Initial attempts to incorporate these vertical terms into the fit model have been met with limited success. While the fit prefers a non-zero value for the VW change, and the sign of the change matches what would be expected from the model above[33], the amplitude is not consistent with what can be derived from the model in Equation (5.49). This is not entirely unexpected, as the BD frequencies are modulated in different ways by the acceptance of the calorimeters. These can also be incorporated as standalone fit parameters. The inclusion of such a time changing ω_{vw} does not fully address the residual peak in Calorimeters 13 and 19. The modeling of the time dependence of the BD frequencies in Run-4 is a topic of active investigation. As such, this coupled

---

[33] That is to say, the opposite sign to the change in ω_{cbo}

x/y-frequency change, nor any form of $\omega_{\mathrm{y}}(t)/\omega_{\mathrm{vw}}(t)$, is not yet incorporated into the final fit model. Run-2/3 form of $\omega_{\mathrm{cbo}}(t)$ remains present as the default in the UW analysis.

5.3.8 Muon Losses

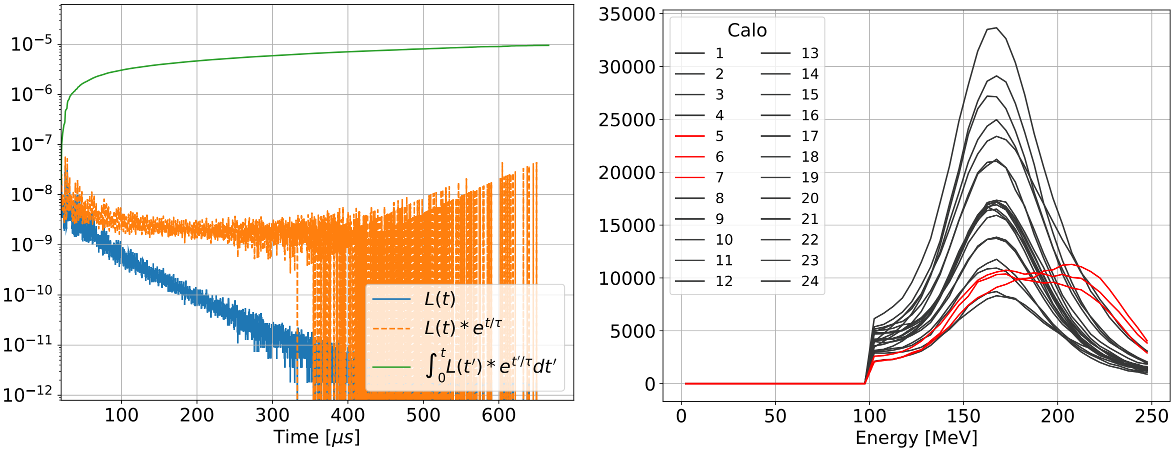

(a) **(b)**

Figure 5.25: (a) The muon loss spectrum for Run-4, constructed solely from calorimeters 14-24 and $100 < E$ [MeV] < 150. (b) The energy spectrum of triple coincidences in all calorimeters. The contamination from protons, which causes a double peak structure, can be seen in calorimeters 5-8 (indicated in red).

The final modification which must be made to the ω_a fit function concerns lost muons. In all of the previous formalism, it was assumed that muons only 'exited' the storage ring through decaying into positrons. That is not strictly true. As mentioned in Section 3.3.2, there exist a series of five aperture defining collimators spaced evenly around the ring. Passing through these collimators, or any of the other material in the storage region, can cause muons to be scattered out of the ring before they decay.

Up to this point, this effect has been absorbed into τ_a. However, if the probability of such losses is not strictly proportional to the number of muons in the ring (i.e. if the behavior is non-exponential) then this can lead to a term which biases ω_a. In the $g-2$ fits, this is combated by introducing the lost muon function $\Lambda(t)$:

$$\Lambda(t) = 1 - K_{\mathrm{loss}} \int_0^t e^{t/\tau_a} L(t') dt'. \tag{5.50}$$

$L(t)$ is the observed lost muon time spectrum in the calorimeters, measured from triple coincidences of MIPs in adjacent calorimeters. The integral quantity in $\Lambda(t)$, therefore, captures the integrated loss probability up to time t in the fit. The a-priori unknown efficiency for the detection of a given lost muon is absorbed into the overall scaling factor K_{loss}, which is allowed to float in the fit. Simulations have shown that the detection probability for all losses is approximately independent of muon momentum [166]. In these simulations, the observed time spectra of muon losses in the calorimeters has also been shown to be a representative subset of all losses.

To avoid a constant background caused by leakage of particles into the $g-2$ storage ring late in the fill (discussed later in Section 6.2), the $L(t)$ function used for the UW Run-4 analysis is constructed using only triple coincidence data from calorimeters 14-24. The form of $L(t)$ used in this analysis can be seen in Figure 5.25. The choice of loss function can significantly impact the value of K_{loss} preferred by the fit. This term does not strongly couple to $R(\omega_a)$, but nevertheless a small systematic associated with these choices is evaluated (Section 6.2.1). In Run-4, as in Run-3, the losses are largely exponential with some beam dynamics oscillations superimposed.

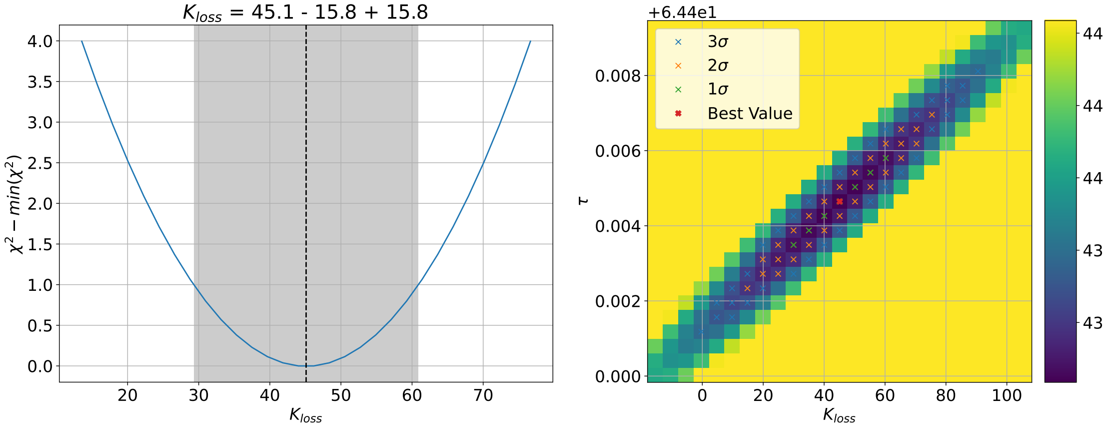

(a) **(b)**

Figure 5.26: (a) A χ^2 scan of K_{loss} in Run-4 using the form of $L(t)$ shown in Figure 5.25, leaving all other parameters free. The fit prefers a value of K_{loss} which is not consistent with 0 in this case. (b) A 2D χ^2 scan of K_{loss} vs. the muon lifetime. The two slow terms are highly correlated. This correlation is used to assign an uncertainty associated with muon losses. For the 2σ region of this χ^2 well, the value of $R(\omega_a)$ changes by 2 ppb.

As a result of the near-exponential behavior of $L(t)$, K_{loss} is highly correlated with τ and other slow terms in the ω_a fit. These correlations can be seen in Figure 5.26b. The value of K_{loss} preferred by the fit is > 0. This result, while consistent with expectations given the definition of K_{loss}, was surprising given that in Run-3 its preferred value was negative (in Run-3a, $K_{\text{loss}} \approx 2\sigma$ below 0). A negative K_{loss} is a non-physical value, and so K_{loss} was fixed to 0 in the Run-3 UW analysis. No clear explanation for why $K_{\text{loss}} < 0$ in Run-3 has yet been found, and similarly no explanation for the difference in behavior in Run-4 has been identified. At a surface level, the $L(t)$ functions look nearly identical. This is currently under active investigation as the behavior of K_{loss} couples strongly to the residual slow term in the data. Currently in Run-4, K_{loss} is allowed to float. Studies are underway to determine any differences in the Run-3 and Run-4 running conditions which could have contributed to the change in the sign of K_{loss}. The systematic associated with the muon losses are discussed in Section 6.2.1. The addition of the K_{loss} term changes the value of the muon lifetime preferred by the fit by $\approx 3\,\text{ns}$ ($2.6\delta_{\tau_a}$). Comparisons with the value of τ_a predicted by the fast rotation momentum analysis are in-progress.

5.3.9 The Current Picture: 33 Parameters

The UW ω_a fit function as of the writing of this thesis consists of 33 free parameters, and is shown in full in Equations (5.51) and (5.52).

$$N(t) = N_0 N_x(t) N_y(t) N_{xy}(t) \Lambda(t) e^{-\,t/\tau_a} \left[1 + A(t) \cos\left(R(\omega_a)\, t - \phi(t)\right)\right] \tag{5.51}$$

where

$$\begin{aligned}
N_x(t) &= 1 + e^{-2t/\tau_{\text{cbo}}} A_{\text{2CBO}} \cos\left(2\omega_{\text{cbo}}(t)t - \phi_{2CBO}\right) \\
N_y(t) &= 1 \\
N_{xy}(t) &= 1 + \mathcal{E}_{\text{cbo}}(t) \cos\left(\omega_{\text{cbo}}(t)t - \phi_{\text{cbo}}\right) \\
&\quad + e^{-t/\tau_{\text{vw}}} A_{\text{vw}} \cos\left(\omega_{\text{vw}}(t)t - \phi_{\text{vw}}\right) \\
&\quad + e^{-t/\tau_{\text{y}}} A_{\text{y}} \cos\left(\omega_{\text{y}}(t)t - \phi_{\text{y}}\right) \\
&\quad + e^{-t/\tau_{\text{cbo}} - t/\tau_{\text{vw}}} \left[A_{VW+CBO} \cos\left((\omega_{\text{vw}} + \omega_{\text{cbo}}(t))t - \phi_{VW+CBO}\right)\right] \\
&\quad + e^{-t/\tau_{\text{cbo}} - t/\tau_{\text{vw}}} \left[A_{VW-CBO} \cos\left((\omega_{\text{vw}} - \omega_{\text{cbo}}(t))t - \phi_{VW-CBO}\right)\right] \\
&\quad + e^{-t/\tau_{\text{cbo}} - t/\tau_{\text{y}}} \left[A_{y+CBO} \cos\left((\omega_{\text{y}} + \omega_{\text{cbo}}(t))t - \phi_{y+CBO}\right)\right] \\
&\quad + e^{-t/\tau_{\text{cbo}} - t/\tau_{\text{y}}} \left[A_{y-CBO} \cos\left((\omega_{\text{y}} - \omega_{\text{cbo}}(t))t - \phi_{y-CBO}\right)\right] \\
A(t) &= A_0 \left[1 + e^{-t/\tau_{\text{cbo}}} A_{\text{AX11}} \cos\left(\omega_{\text{cbo}}(t)t - \phi_{\text{AX11}}\right)\right] \\
\phi(t) &= \phi_a + e^{-t/\tau_{\text{cbo}}} A_{\phi X11} \cos\left(\omega_{\text{cbo}}(t)t - \phi_{\phi X11}\right) \\
\Lambda(t) &= 1 - K_{\text{loss}} \int_0^t e^{t/\tau_a} L(t')dt' \\
\mathcal{E}_{\text{cbo}}(t) &= A_{\text{cbo}} \left(e^{-t/\tau_{\text{cbo}}} + C_{cbo}\right) \\
\omega_{\text{cbo}}(t) &= \begin{cases} \omega_{\text{cbo}} + \frac{ae^{-t/\tau_a}}{t} & \text{Calorimeter summed fits} \\ \left(\omega_{\text{cbo}} + \frac{ae^{-t/\tau_a}}{t}\right)\left(1 + A_{\text{cbo,t-ch}} e^{-t/\tau_{\text{cbo,t-ch}}}\right) & \text{Calorimeter-by-calorimeter fits} \end{cases}
\end{aligned} \tag{5.52}$$

These equations describe all of the currently identified beam dynamics oscillations in the data, the current understanding of the time dependence and coupling of said oscillations, and any storage inefficiencies which might cause muons to be lost before they decay. The results of fitting the combined Run-4 dataset with these parameters is shown in Figure 5.28. The value of $R(\omega_a)$ found using Equation (5.51) for Run-4 is:

$$R(\omega_a) = -63.462 \pm 0.187 \quad [187\,\text{ppb}] \tag{5.53}$$

The change in $R(\omega_a)$, as well as the improvement in the fit quality, at each point in the iterative building of the fit can be seen in Table 5.2. Although a 'good' χ^2 value does not necessarily indicate a trustworthy fit result, a poor χ^2 value certainly indicates a problem. As it stands, the χ^2/NDF for this fit is still quite poor[34]: $4386/4122 \approx 1.06$, corresponding to a p-value of 2.2×10^{-3}. This is corroborated by the obvious residuals in the FFT around ω_{vw} which indicate that the modelling of the vertical motion of the beam requires improvement. Other analysis groups do not see an inflated χ^2 of this magnitude with a similar fit model, which indicates that some portion of the χ^2 inflation may be due to a data processing issue with the current histograms (this is discussed in Section 5.5.1).

Ongoing efforts to address the shortcomings of the fit model are underway, and the 'open questions' and ongoing developments for the Run-4 analysis are summarized in Section 5.5.1. The nominal Run-4 analysis is expected to be completed by the end of 2024.

Iteration	Description	Parameters	$\Delta R(\omega_a)$ [ppb]	$\Delta\chi^2$	χ^2/NDF
0	Basic Model	5	-911.31	48457.9	12.73
1	Addition of 1$^{\text{st}}$ order CBO, $\omega_{\text{cbo}}(t)$	10	-54.93	11076.9	3.73
2	Addition of ω_{y} and ω_{vw}.	18	11.94	586.9	1.20
3	Addition of K_{loss}.	19	10.65	577.3	1.20
4	Addition of 2CBO, $A_x(t)$, $\phi_x(t)$.	25	25.76	537.0	1.19
5	Addition of VW±CBO	29	-3.69	31.7	1.07
6	Addition of y±CBO	33	—	—	1.06

Table 5.2: $\Delta R(\omega_a)$ vs. the final fit from the addition of each of the terms of the A-Method fit. The improvement in χ^2 with each term of the fit is apparent. To aid in fit convergence, K_{loss} is applied at an intermediate stage of the fit, rather than at the last step as described in the text.

---

[34] A reasonable value for the χ^2/NDF for a fit of this size can be estimated by taking $1 + \sqrt{2/NDF} \approx 1.02$. Anything between this value and 1 would be roughly satisfactory.

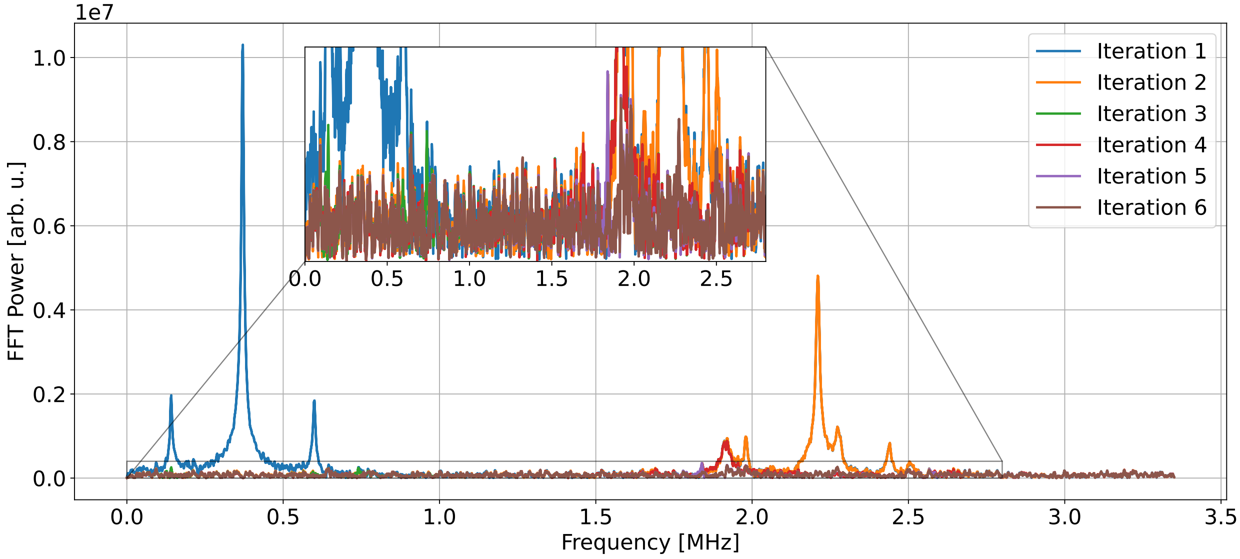

Figure 5.27: FFTs from each of the steps in the iterative fitting procedure for Run-4. As more beam dynamics terms are added, the corresponding peaks in the FFT are reduced and the fit quality improves.

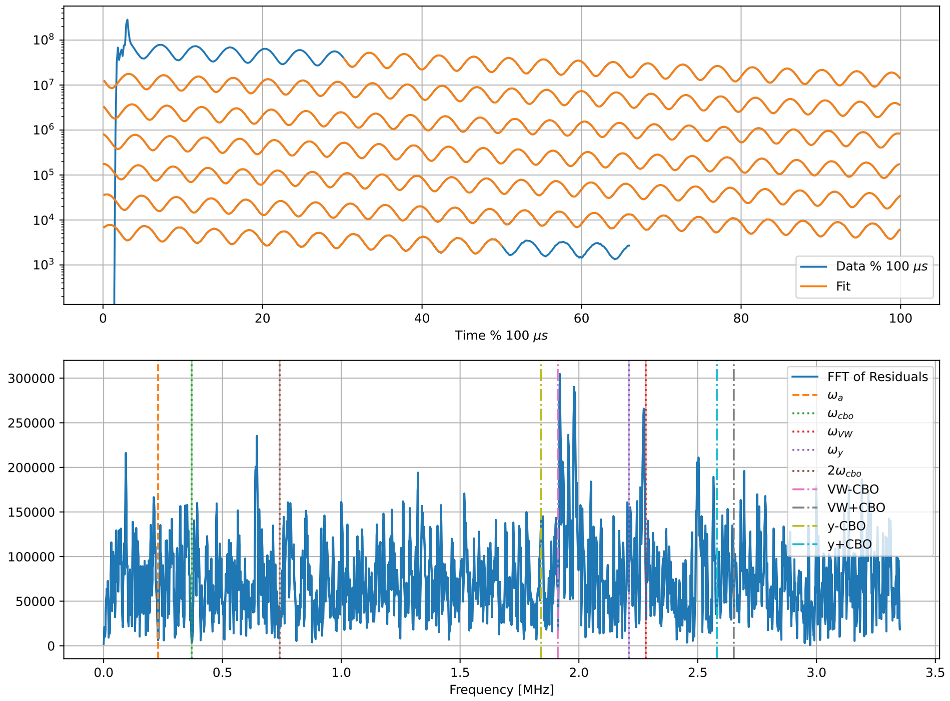

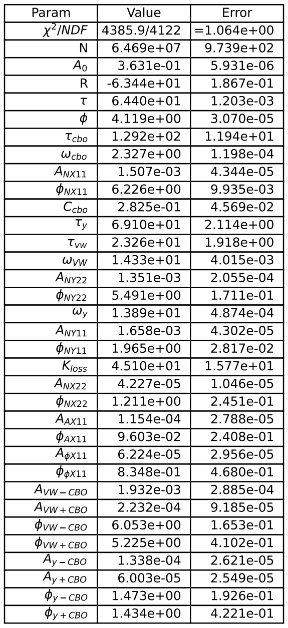

Param	Value	Error
χ^2/NDF	4385.9/4122	=1.064e+00
N	6.469e+07	9.739e+02
A_0	3.631e-01	5.931e-06
R	-6.344e+01	1.867e-01
τ	6.440e+01	1.203e-03
ϕ	4.119e+00	3.070e-05
τ_{cbo}	1.292e+02	1.194e+01
ω_{cbo}	2.327e+00	1.198e-04
A_{NX11}	1.507e-03	4.344e-05
ϕ_{NX11}	6.226e+00	9.935e-03
C_{cbo}	2.825e-01	4.569e-02
τ_y	6.910e+01	2.114e+00
τ_{vw}	2.326e+01	1.918e+00
ω_{VW}	1.433e+01	4.015e-03
A_{NY22}	1.351e-03	2.055e-04
ϕ_{NY22}	5.491e+00	1.711e-01
ω_y	1.389e+01	4.874e-04
A_{NY11}	1.658e-03	4.302e-05
ϕ_{NY11}	1.965e+00	2.817e-02
K_{loss}	4.510e+01	1.577e+01
A_{NX22}	4.227e-05	1.046e-05
ϕ_{NX22}	1.211e+00	2.451e-01
A_{AX11}	1.154e-04	2.788e-05
ϕ_{AX11}	9.603e-02	2.408e-01
$A_{\phi X11}$	6.224e-05	2.956e-05
$\phi_{\phi X11}$	8.348e-01	4.680e-01
A_{VW-CBO}	1.932e-03	2.885e-04
A_{VW+CBO}	2.232e-04	9.185e-05
ϕ_{VW-CBO}	6.053e+00	1.653e-01
ϕ_{VW+CBO}	5.225e+00	4.102e-01
A_{y-CBO}	1.338e-04	2.621e-05
A_{y+CBO}	6.003e-05	2.549e-05
ϕ_{y-CBO}	1.473e+00	1.926e-01
ϕ_{y+CBO}	1.434e+00	4.221e-01

Figure 5.28: A-Method fit of the Run-4 dataset to the model in Equations (5.51) and (5.52). The poor χ^2, as well as the residual behavior in the FFT in the $1.8 - 2.5$ MHz range indicates that the current fit model is not encapsulating all of the BD oscillations in the data. The values and uncertainties of the fit parameters can be found in Table 5.3.

	Name	Value	Hesse Error	Minos Error-	Minos Error+	Limit-	Limit+
0	$N \equiv N_0$	64.693e6	0.001e6	-0.001e6	0.001e6		
1	A_0	363.147e-3	0.006e-3	-0.006e-3	0.006e-3	0	
2	$R \equiv R(\omega_a)$	-63.44	0.19	-0.19	0.19		
3	$\tau \equiv \tau_a \equiv \langle\gamma\rangle\tau_\mu$	64.4046	0.0012	-0.0012	0.0012	10	100
4	$\phi \equiv \phi_a$	4.118904	0.000031	-0.000031	0.000031		
5	τ_{cbo}	129	12	-11	13	1	1E+03
6	ω_{cbo}	2.32692	0.00012	-0.00012	0.00012	2	2.9
7	$A_{cbo} \equiv A_{NX11}$	1.51e-3	0.04e-3	-0.04e-3	0.04e-3	0	
8	$\phi_{cbo} \equiv \phi_{NX11}$	6.226	0.010	-0.010	0.010		
9	C_{cbo}	0.28	0.05	-0.05	0.04	0	1
10	τ_y	69.1	2.1	-2.1	2.1	50	150
11	τ_{vw}	23.3	1.9	-1.7	1.9	10	50
12	ω_{vw}	14.334	0.004	-0.004	0.004	14	16
13	$A_{\mathrm{vw}} \equiv A_{NY22}$	1.35e-3	0.21e-3	-0.18e-3	0.21e-3	0	
14	$\phi_{\mathrm{vw}} \equiv \phi_{NY22}$	5.49	0.17	-0.17	0.17		
15	ω_y	13.8877	0.0005	-0.0005	0.0005	12	14
16	$A_{\mathrm{y}} \equiv A_{NY11}$	1.66e-3	0.04e-3	-0.04e-3	0.04e-3	0	
17	$\phi_{\mathrm{y}} \equiv \phi_{NY11}$	1.965	0.028	-0.028	0.028		
18	K_{loss}	45	16	-16	16		
19	$A_{\mathrm{2CBO}} \equiv A_{NX22}$	0.042e-3	0.010e-3	-0.010e-3	0.011e-3	0	
20	$\phi_{\mathrm{2CBO}} \equiv \phi_{NX22}$	1.21	0.24	-0.25	0.25		
21	A_{AX11}	0.115e-3	0.028e-3	-0.028e-3	0.028e-3	0	
22	ϕ_{AX11}	0.10	0.24	-0.24	0.24		
23	$A_{\phi X11}$	0.062e-3	0.030e-3	-0.029e-3	0.030e-3	0	
24	$\phi_{\phi X11}$	0.8	0.5	-0.5	0.5		
25	A_{VW-CBO}	1.93e-3	0.29e-3	-0.25e-3	0.30e-3	0	
26	A_{VW+CBO}	0.22e-3	0.09e-3	-0.09e-3	0.10e-3	0	
27	ϕ_{VW-CBO}	6.05	0.17	-0.16	0.17		
28	ϕ_{VW+CBO}	5.2	0.4	-0.4	0.4		
29	A_{y-CBO}	0.134e-3	0.026e-3	-0.026e-3	0.026e-3	0	
30	A_{y+CBO}	0.060e-3	0.025e-3	-0.025e-3	0.026e-3	0	
31	ϕ_{y-CBO}	1.47	0.19	-0.19	0.19		
32	ϕ_{y+CBO}	1.4	0.4	-0.4	0.4		

Table 5.3: Fit parameters for the final fit shown in Figure 5.28. The nominal fit values are computed by the `MIGRAD` minimization algorithm. The errors are calculated in two ways, by Hesse (which provides a fast, symmetric error estimate) and by `MINOS` (which maps out the χ^2 well for each parameter and yields a robust asymmetric error).

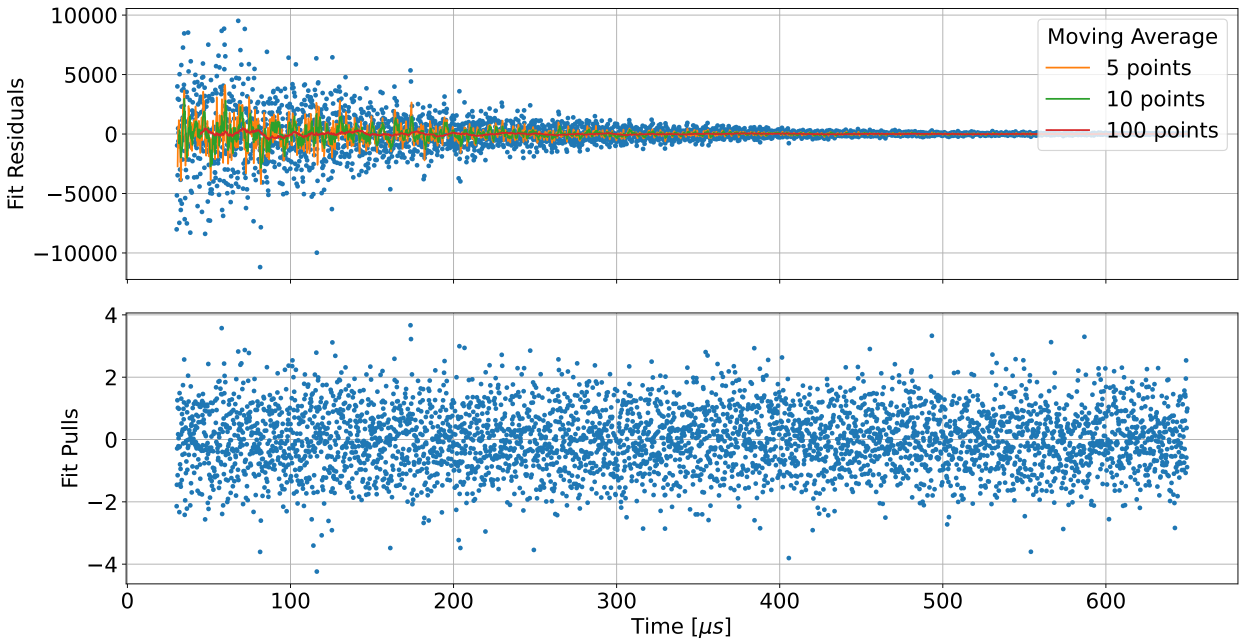

Figure 5.29: Residuals (Fit - Data) and Pulls ((Fit - Data) / Bin Error) of the A-Method fit of the Run-4 dataset to the model in Equations (5.51) and (5.52). The value for at each bins is shown in blue, and moving averages with different windows are overlaid. No clear trends are obvious in this plot which would indicate the cause of the poor χ^2.

5.4 Internal Consistency Checks

In addition to the analysis of the ‘full’ data described in the previous sections, the data are divided into different groupings — by energy, detector, etc. — and any inconsistencies in physical parameters are examined. As an example, the value of τ_a should not vary across calorimeter. Therefore any statistically significant shift between detectors could indicate the presence of an unmodelled slow effect in the data. Some of these checks are performed on the same nominal analysis histogram described in the previous section, while others require re-analysis of the raw data on the Fermigrid to construct new histograms (Section 4.2.4). Some completed cross checks are presented in detail here, while upcoming work is described briefly in Section 5.4.5

5.4.1 Fit Start/Stop Time

If the fit model is accurately describing the data, then the fit parameters — up to the limits of statistical fluctuations — should be independent of where the fit begins. To ensure this is true, the start and stop times of the fit are scanned. The set-subset statistical effects between a fit starting at t_i and one starting at t_j can be quantified via [11]:

$$\delta_{kw} = \sqrt{\left|\sigma_i^2 - \sigma_j^2\right|}, \tag{5.54}$$

where σ_i and σ_j are the fitted uncertainty on a given parameter with start time t_i and t_i respectively. This metric describes the amount by which two partially-correlated measurements of the same parameter can vary with respect to once another and still be consistent at the level of 1 (statistical) σ. These $\pm 1\sigma$ regions, referred to as 'Kawall bands', are indicated as shaded regions in the start-time scans to follow. The bands widen as the differences in the amount of data in the initial set and later-time subset grow.

Monte Carlo studies have been performed to quantify the variation outside this band which is acceptable. Generally all parameters remaining inside the Kawall bands for $> 75\%$ of a start-time scan is a necessary, but not sufficient, condition for a stable fit result. Some brief excursions are to be expected and are not necessarily cause for concern, but any parameter which sharply deviates from this band is cause for further investigation[35].

Multiple sets of start-time scans are performed. The first (Figure 5.30) leaves all of the parameters of the fit floating. This is the most sensitive to any instability in the fit. However, past $50\,\mu$s this fit can quickly fail to converge or fall into unstable local minima. This leads to the jagged Kawall bands and unstable fit errors which can be seen in some parameters (such as N, τ_a, or C_{cbo}). At later times, sub-leading-order beam dynamics oscillations have largely decayed away (The vw terms, for instance, have a lifetime of only $23\,\mu$s) and can become difficult to distinguish amongst statistical noise in the data. To examine further out in time, parameters like the lifetimes and frequencies of the BD terms can be fixed. With this approach, start-time scans out to $> 200\,\mu$s into the fill are possible (Figure 5.31).

Before the nominal start time of the fit ($30.1384\,\mu$s) the beam is still unstable, which can be seen in the rapidly changing N_0 and τ_a values before $\approx 25\,\mu$s into the fill. After the nominal fit start time (indicated in red in Figure 5.31), the fit results are generally stable. The parameter

---

[35] An example of such can be seen later in Figure 5.36 before the application of the residual gain correction.

whose stability is of utmost importance is $R(\omega_a)$. It can be seen in Figures 5.30 and 5.31c that $R(\omega_a)$ is stable out to $t_{\text{start}} = 220\,\mu\text{s}$. The other parameters of the five-parameter model remain largely stable as well. Stop time scans, not shown here, show similarly stable behavior.

Indications of the needed improvements in the handling of the vertical terms in the fit can be seen in Figure 5.30. In particular, the value of τ_{y} has a continual downward trend outside of the 1σ Kawall band. Updates to the fit model currently in progress (detailed in Section 5.5.1) are expected to resolve many of these effects.

The start-time scans inform the optimum starting point for the main fits. The canonical start time for the ω_a fits was Run-2/3 is $30.1384\,\mu\text{s}$. This time was chosen to be at a node of the ω_a oscillation, which reduces the sensitivity of the analysis to effects stemming from the pileup and gain systematics (as shown in Figure 5.33b). It was also chosen to be late enough in the fill to allow the beam to recover to a steady state after the ESQ scraping (as seen in Figure 5.31d). Figure 5.33a shows that moving the fit start time back to $25\,\mu\text{s}$ can yield an $\approx 5\,\text{ppb}$ increase in statistical power in Run-4. The balance of this statistical gain against systematic effects was studied for Run-4+ and it was concluded amongst the different analysis groups that the Run-4 analysis would retain the same fit start time as in Run-2/3 [167].

5.4.2 Energy-Binned Analysis

In addition to being used to generate the $A(E)$ function for the A-Method analysis (Section 5.2.5), the energy binned analysis is useful as an independent cross-check. Each energy bin yields an independent measurement of $R(\omega_a)$. The average of these values should therefore be consistent with the value obtained from the standard T/A-Method analyses.

5.4.2.1 Calculation of the Residual Gain Correction (RGC)

As mentioned in Section 5.2.3, a residual slow effect is present in the ω_a data. When not corrected for, this slow effect is most evident when looking at the behavior of K_{loss} vs. energy bin. Figure 5.35a shows that without the application of such a correction the value of K_{loss} decreases sharply for the highest energy bins. This is a non-physical result, since the number of lost muons is not truly

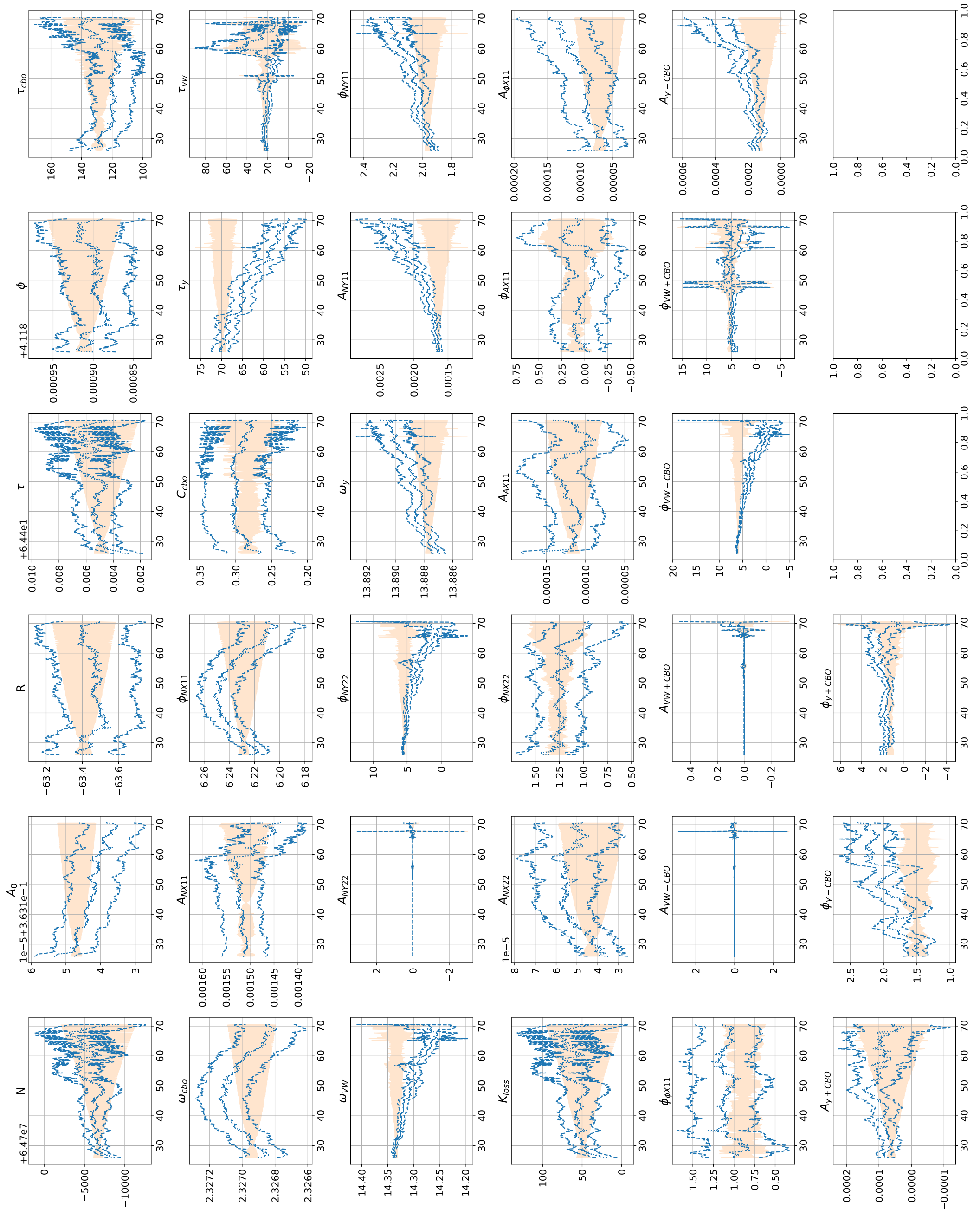

Figure 5.30: A-Method start-time scans with all parameters floating. The central blue curve is the value of the fit parameter, while the dashed curves above and below indicate $\pm 1\sigma$ from the fit. The shaded orange region indicates the Kawall band, which is computed with reference to the nominal start time of the fit. The instability of the BD frequencies and phases vs. fit start time is obvious, indicating a deficit in the modelling of the vertical terms. The instability of the overall fit can also be seen past $\approx 50\,\mu$s, indicated by the 'jumpiness' in the uncertainties on some parameters (such as N). Interpretation of the results past this point should be done with caution. The drift present in some of the vertical terms (particularly τ_y) is indicative of shortcoming of the current fit model. The updates in progress detailed in Section 5.5.1 are expected to resolve many of these effects.

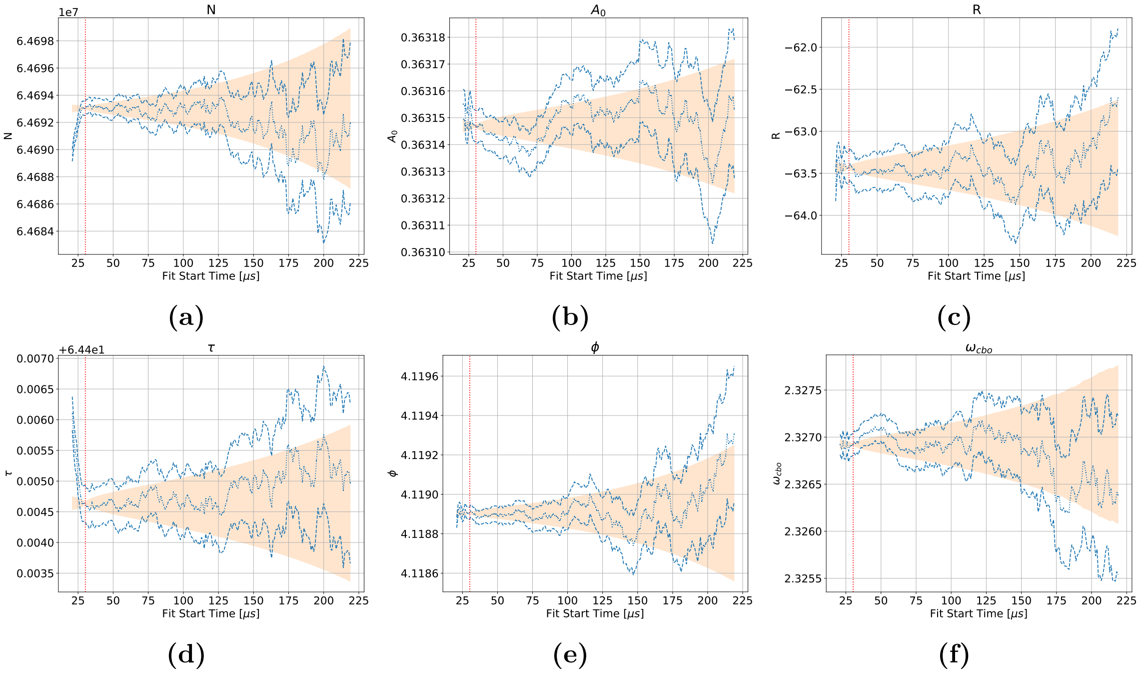

Figure 5.31: A-Method start-time scans for selected parameters in Run-4. The value of the fit parameter is shown in the central blue line, the $\pm 1\sigma$ fit errors are shown in the dashed blue lines, and the Kawall bands are indicated in orange. Higher order terms are fixed in this fit to avoid convergence issues. The dashed red line indicates the nominal fit start time of $30.2\,\mu$s. All parameters show good stability vs. fit start time.

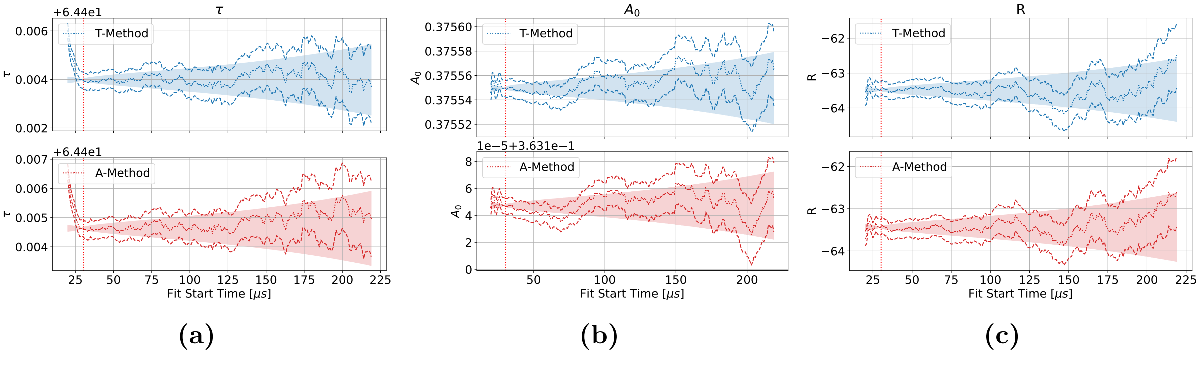

Figure 5.32: Comparison of selected parameters from start-time scans of the T- and A-Method fits to the full Run-4 data. The value of the fit parameter is shown in the blue line, the $\pm 1\sigma$ fit errors are shown in the dashed lines, and the Kawall bands are indicated with the shaded region. Both sets of scans show consistent, stable behavior.

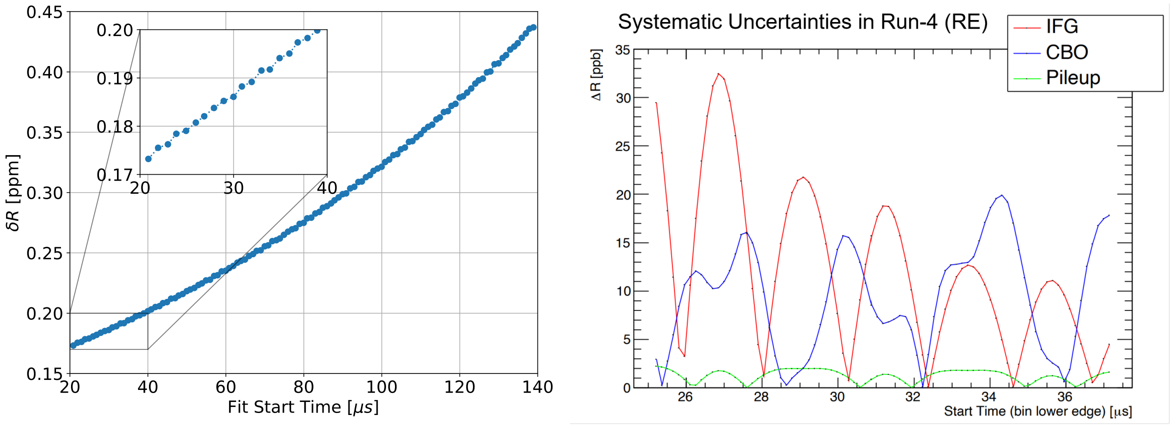

(a) **(b)** Reproduced from [167]

Figure 5.33: (a) Uncertainty on the fitted value of $R(\omega_a)$ vs. fit start time in the Run-4 A-Method analysis. (b) Sensitivity of $R(\omega_a)$ to systematics arising from the IFG (Section 4.1.5), CBO (Section 5.3.4), and Pileup (Section 5.2.2) in the Cornell ω_a analysis. The various systematics generally are minimized at the nodes of the ω_a oscillation.

correlated with the positron energy. The value of τ_a vs. fit start time shows similarly non-physical trends.

This residual slow effect has been present in ω_a analysis since Run-1, and has been the subject of much investigation [6, 84]. A gain change is postulated as the cause of the slow effect for the following reasons:

- The scale of the effect varies with the rate of high-energy events impacting the calorimeter.
- The effect of a small gain change would be more apparent in higher energy bins than in lower energy bins, matching the behavior observed in K_{loss}.
- The scale of the effect is consistent between reconstruction algorithms (in Run-4+), indicating a problem in the underlying data.
- The scale of a gain-like correction needed to repair the data is below that which could be measured by the laser system.

Other forms of corrections have also been proposed. These include an acceptance modulation caused by a change in the beam position, energy leakage out of the calorimeters varying vs. time in fill, or a remaining pulse-dependent energy threshold [152, 168–170]. Studies are underway across Run-4+ analysis groups to test these models and to identify the cause of this effect.

Pending these results, the form of the RGC from Runs 1-3 is implemented in the UW analysis as standard practice. The form of the correction is given in Equation (5.8). The values of the parameters N_g and A_g are determined empirically through the following process:

- A scan is performed over a wide range of N_g and A_g. At each point in the scan, the RGC is applied and a new T-Method fit is performed. Those values of N_g and A_g that minimize the χ^2 are taken as the nominal values[36].
- With this RGC applied, an energy binned analysis is conducted to ensure that these values indeed flattens $K_{\text{loss}}(E)$.
- A scan of the fit start time is performed to ensure the value of τ preferred by the fit is also stabilized by this choice.

The χ^2 scan performed on the full Run-4 data can be seen in Figure 5.34. The value of A_g is found to be consistent with previous runs, while N_g is reduced by $\approx 70\%$ compared to its Run-2/3 value. This is consistent with expectations from the fix of the multi-cluster island reconstruction bug (Section 4.1.6.1) which was implemented before Run-4+ data processing. A systematic uncertainty due to this residual slow effect was quantified for both the Run-1 [6, 103] and Run-2/3 publications [15, 84]. This was done by finding the difference in the value of $R(\omega_a)$ for different points in the scan within a range of $\Delta\chi^2 < 4\,\text{units}$ (2σ). As shown in Figure 5.34, in Run-4:

$$\delta R(\omega_a)|_{\text{RGC}} = 4\,\text{ppb}. \tag{5.55}$$

The value of $R(\omega_a)$ before and after the application of the RGC is changed by:

$$\Delta R(\omega_a)|_{\text{RGC, T-Method}} = 2.4\,\text{ppb} \tag{5.56}$$

$$\Delta R(\omega_a)|_{\text{RGC, A-Method}} = 9.4\,\text{ppb}. \tag{5.57}$$

---

[36] The same scan has been performed using the A-Method analysis, as well as with fit models of different order. All permutations tested thus far have yielded consistent results.

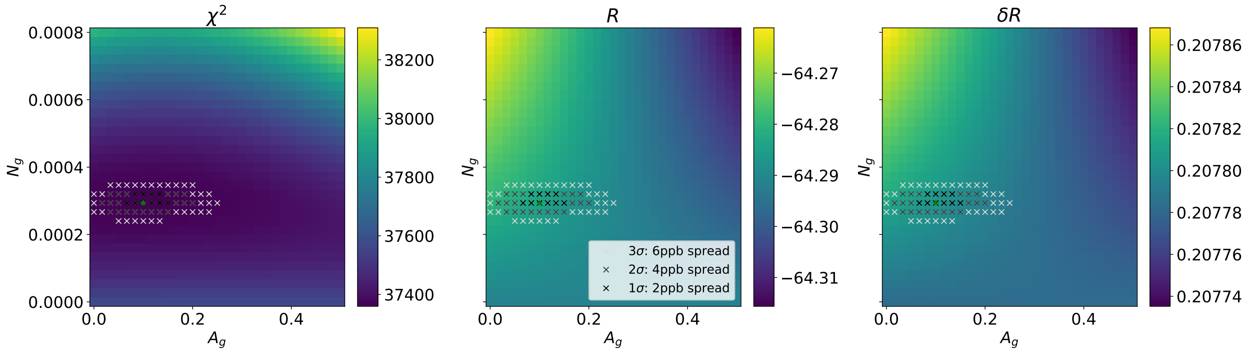

Figure 5.34: Five-parameter T-Method χ^2 scan for the various values of N_g and A_g for the RGC. The left plot shows the χ^2, while the middle and right plots show the effect on $R(\omega_a)$ and $\delta R(\omega_a)$ respectively. The optimum value is: $N_g = 0.00029$, $A_g = 0.10$.

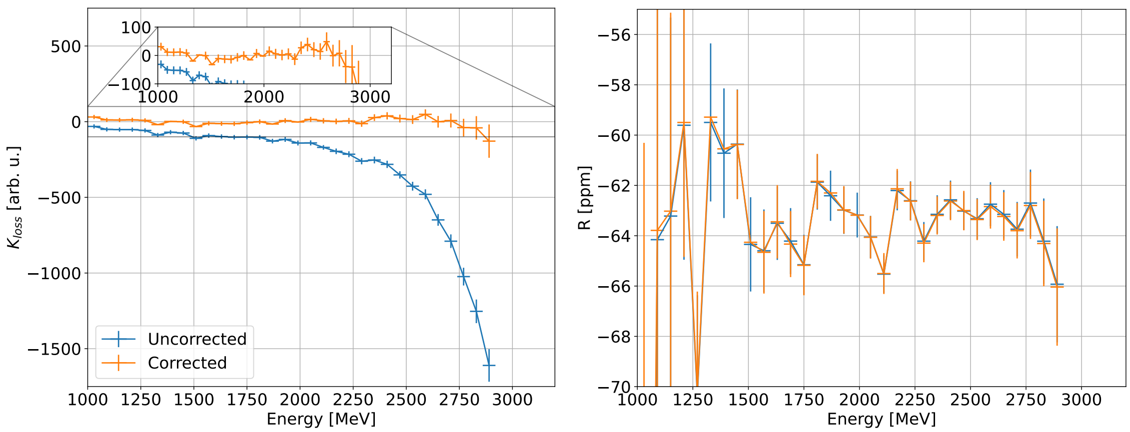

(a) **(b)**

Figure 5.35: Energy binned analyses before (blue) and after (orange) the application of the RGC. The value of $R(\omega_a)$ is virtually unchanged while K_{loss} is flattened. In these scans, τ_a is fixed to its value from the full fit.

5.4.2.2 After RGC Application

The results of the energy binned analysis after the application of the residual gain correction can be seen in Figure 5.37. The bin width for this scan is 60 MeV. Because of the lack of statistics in some energy bins, many higher order beam dynamics terms (such as $A(t)$ and $N_{2\text{CBO}}$) are neglected. The muon loss correction K_{loss} is included. An average of the $R(\omega_a)$ values from this analysis, fit

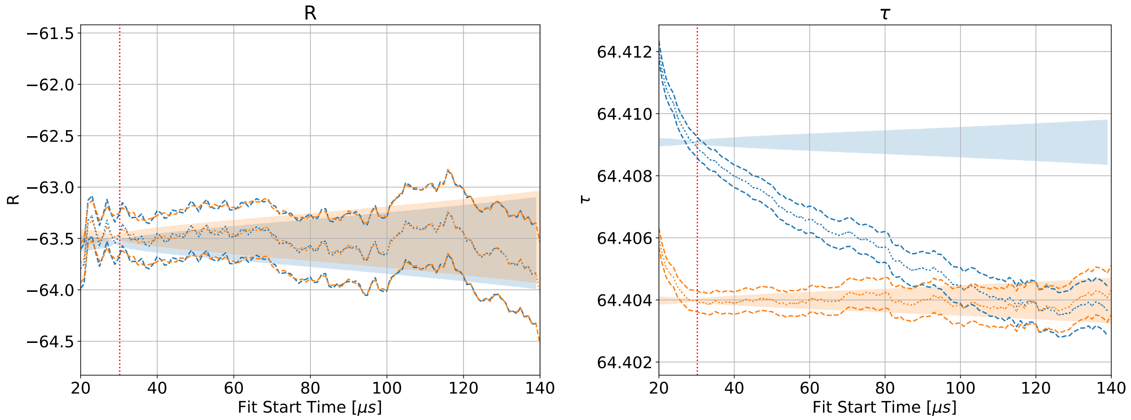

(a) **(b)**

Figure 5.36: T-Method start-time scans of τ_a and $R(\omega_a)$ before (blue) and after (orange) the application of the residual gain correction. The value of $R(\omega_a)$ is largely unaffected, while τ becomes fixed to its late time value.

to a constant value, is shown in Figure 5.38. This yields:

$$R(\omega_a)|_{\text{Energy Binned}} = -63.336 \pm 0.188 \; [188\,\text{ppb}] \tag{5.58}$$

Because of the lack of modelling of higher order terms, this result should not yet be taken as final. However, it is encouraging to note that even without higher-order terms this result is consistent with the A-Weighted value to within 1σ.

5.4.3 Calorimeter-by-Calorimeter Analysis

Splitting the data calorimeter-by-calorimeter also yields 24 quasi-independent measurements of ω_a. As stated in Section 5.3.7, these calorimeter-by-calorimeter measurements are more sensitive to the various beam dynamics terms which cancel in the calorimeter-summed fits. An example of this analysis is seen in Figure 5.39.

The $R(\omega_a)$ value which is seen by the calorimeters is consistent around the ring. Comparing the $R(\omega_a)$ value from the average of all calorimeters to the value from the full fit sets a scale for

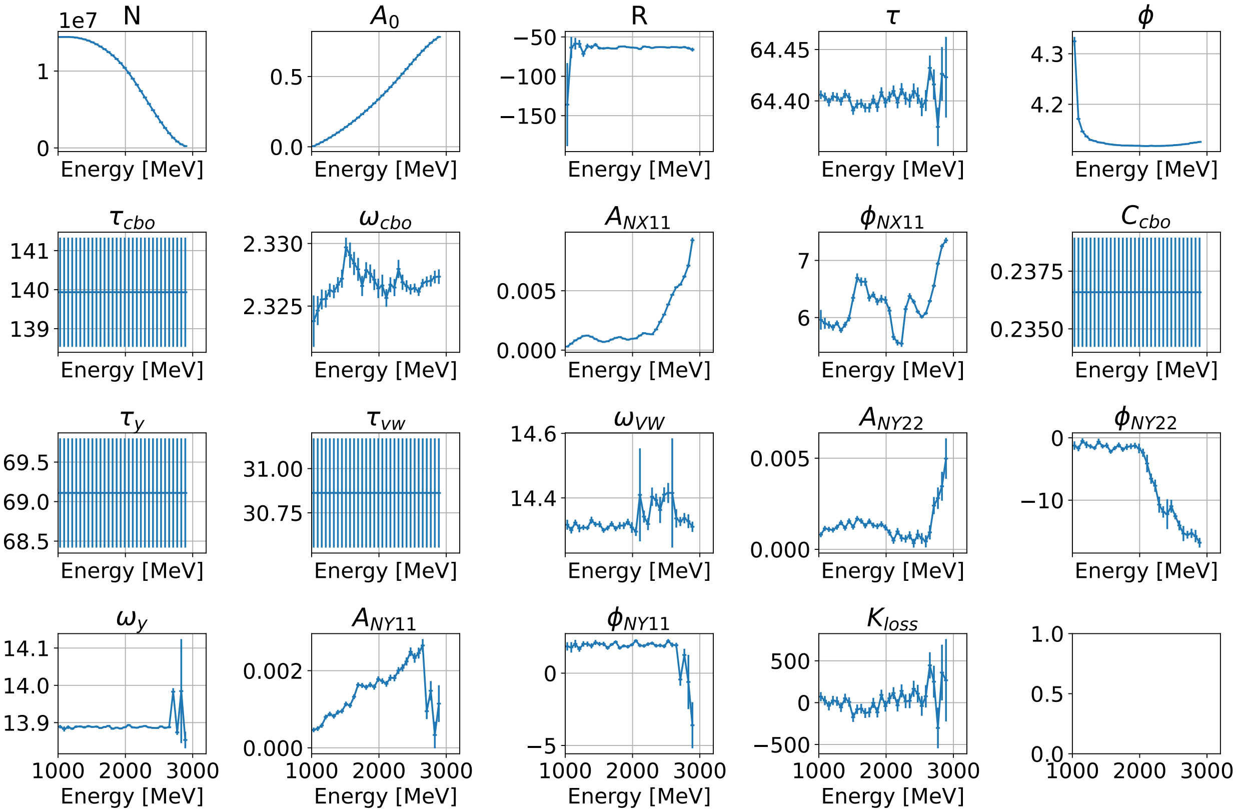

Figure 5.37: Energy binned analysis after the application of the residual gain correction. Low statistics in individual bins complicates analysis of the higher order BD terms.

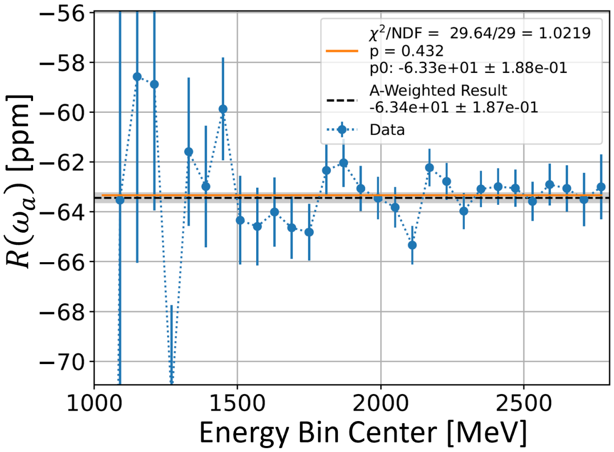

Figure 5.38: Value of $R(\omega_a)$ obtained from the energy binned analysis in Figure 5.37 compared with the value obtained from the full A-Weighted analysis. The average value of $R(\omega_a)$ is extracted from the energy binned data using a χ^2 minimization of the function $y = p_0$. Even with the lack of higher order BD modelling in the energy binned scan, the two are consistent at the level of $< 1\sigma$.

how much the modelling of the various beam dynamics parameters can perturb the value of $R(\omega_a)$:

$$\begin{aligned} R(\omega_a)|_{\text{Calo Avg.}} &= -63.439 \pm 0.187\,\text{ppm}, \\ \rightarrow \Delta R(\omega_a)|_{\text{Calo}} &\equiv R(\omega_a)|_{\text{Calo Sum}} - R(\omega_a)|_{\text{Calo Avg.}} \\ &= 0.0208\,\text{ppm} = 20.8\,\text{ppb}. \end{aligned} \tag{5.59}$$

The value of $\Delta R(\omega_a)|_{\text{Calo}}$ is reduced to 3 ppb when the effect of the time changing CBO frequency is introduced into the calorimeter-by-calorimeter fits. Because $K_{\text{loss}} \equiv 0$ in the calo-by-calo fits shown here, the muon lifetime absorbs any residual slow effect in the data. The variation in τ_a is largest in the kicker region (roughly calorimeters 5-8) but can be seen throughout the ring. Since this is where ω_{y} is most prominent, this is consistent with the hypothesis that an unmodelled vertical oscillation remains in the data. The χ^2 is approximately the same for all calorimeters, indicating that whatever effect is causing the overall worsening of the fit quality is not detector dependent.

Figure 5.40 shows the calorimeter-by-calorimeter results for all fit parameters. A number of interesting features of the data are present in these plots. Phase advances of the BD terms (typically $2\pi N_{\text{calo}}/24$) around the ring can be seen. Differences in the fitted values of various parameters driven by acceptance effects are also observed. Each calorimeter has a different acceptance function, which largely depends on its location in the ring and the presence of material between the detector and the storage region. Variation of terms like ϕ_a and A_{cbo} due to acceptance effects are therefore expected and can provide an important benchmark to simulations [158]. For example: calorimeters 13 and 19 have a restricted vertical acceptance compare to the other detectors due to their location behind the two tracker stations. This results in a different observed average $g-2$ phase (as could be inferred from Figure 5.18). The effect of unique acceptance in the kicker region (calorimeters 5-8) can be seen in the value of A_{y} in this region. This variation in the calorimeter acceptance functions leads to the imperfect cancellation of the beam dynamics oscillations when summing the calorimeter data together in the full fit. Calorimeters which observe a lower amplitude for certain beam dynamics oscillations (such as A_{y} in Calorimeter 2) may have difficulty fitting the lifetimes of such oscillations precisely. The effect of this can be seen in the increased uncertainty on τ_{y} in some calorimeters. This reduced sensitivity may result in such lifetimes needing to be measured using special systematic studies and then fixed in the final analysis[37].

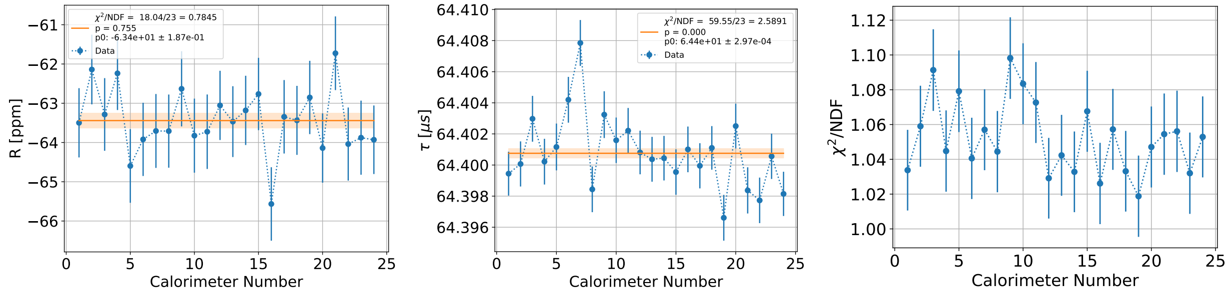

(a) **(b)** **(c)**

Figure 5.39: Calorimeter-by-calorimeter A-Method fit results for selected parameters. These fits use the model in Equations (5.51) and (5.52), with the exception that $K_{\text{loss}} \equiv 0$ and $A_{\text{cbo,t-ch}} \equiv 0$. Additional parameters can be seen in Figure 5.40. The poor χ^2 when fitting a constant value to τ_a is caused by unmodelled slow terms like muon losses, as well as any deficits in the modelling of the BD functions. The error bars shown on the reduced χ^2 values are $\sqrt{2/\text{NDF}}$, and should not be interpreted as 1σ fit uncertainties.

5.4.4 T/A-Comparison

The T and A-Method analyses should produce results which are statistically compatible. Since the T-Method only uses a subset of the data in the A-Method, some variation between the two can be expected. The results of performing the fit to the T-Method histogram using the full fit model in Equation (5.51) can be seen in Figure 5.41. This fit yields:

$$R(\omega_a)|_{\text{T-Method}} = -63.460 \pm 0.208 \ [208\,\text{ppb}]. \tag{5.60}$$

It has been shown that the ‘allowed’ difference between the $R(\omega_a)$ value obtained by these two analyses can be calculated using Equation (5.54) [171]. Comparing Equations (5.53) and (5.60):

$$\delta_{\text{kw}}|_{\text{T-A}} = \sqrt{|0.208^2 - 0.187^2|} = 0.092 \tag{5.61}$$

$$\Delta R(\omega_a)|_{\text{T-A}} = -0.021 = -0.23\delta_{\text{kw}}. \tag{5.62}$$

---

[37] This was the case for τ_{y} in the full fit in all of Run-2 [84]

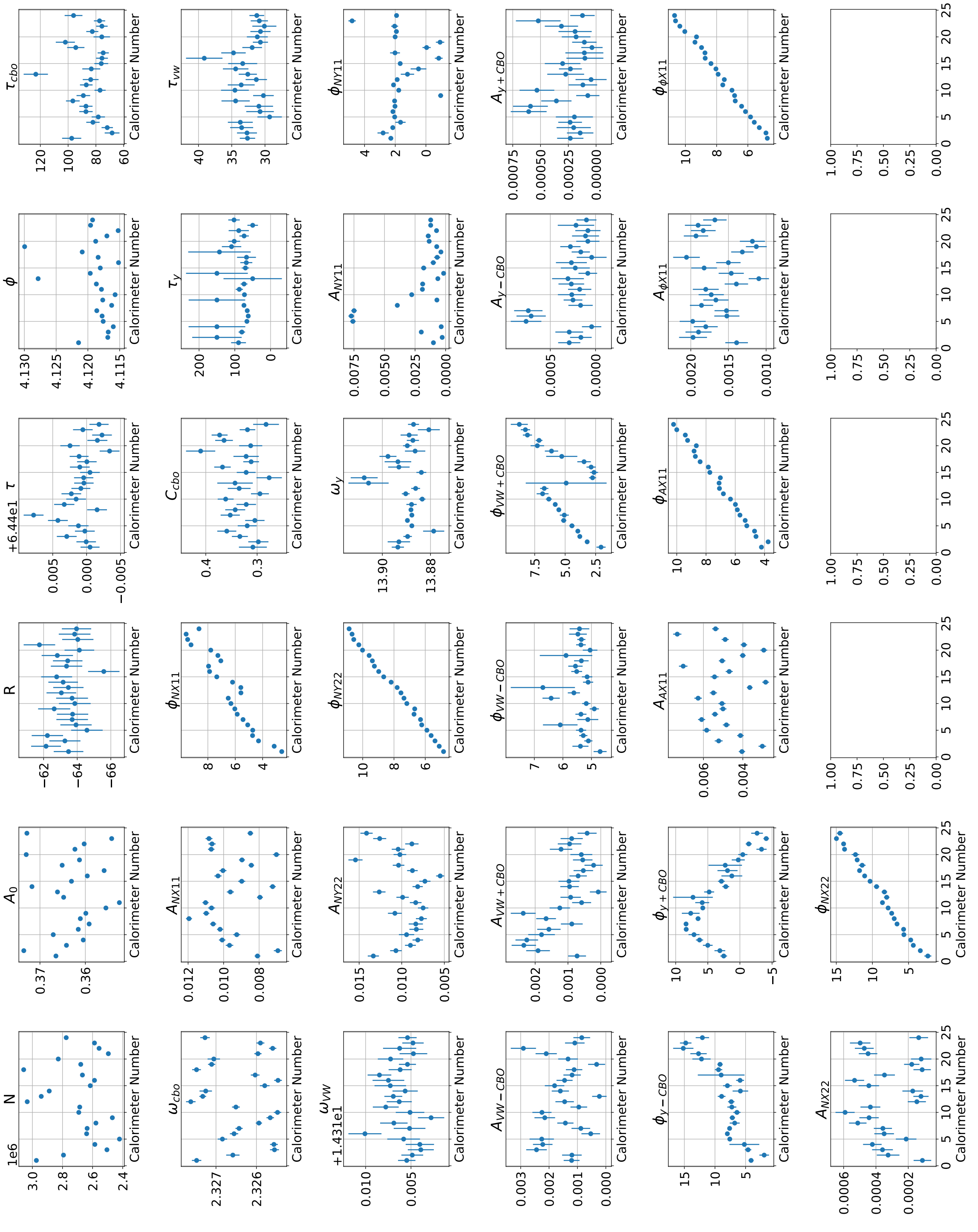

Figure 5.40: Fit parameters extracted from a calorimeter-by-calorimeter A-Method analysis of Run-4. These fits use the model in Equations (5.51) and (5.52), with the exception that $K_{\text{loss}} \equiv 0$ and $A_{\text{cbo,t-ch}} \equiv 0$. The consistency between the calorimeters in the $R(\omega_a)$ value sets the scale at which detector-dependent effect can perturb the measurement.

This difference is in line with the expected variation given the statistics of the measurement. Interestingly, the reduced χ^2 value for the T-Method (1.040) is improved compared to the A-Method. This may be a clue as to the cause of the cause of the poor χ^2, as the A-Method samples from a wider energy range than the T-Method does. Systematic sweeps of the energy-binned analysis are currently in progress to probe this difference deeper.

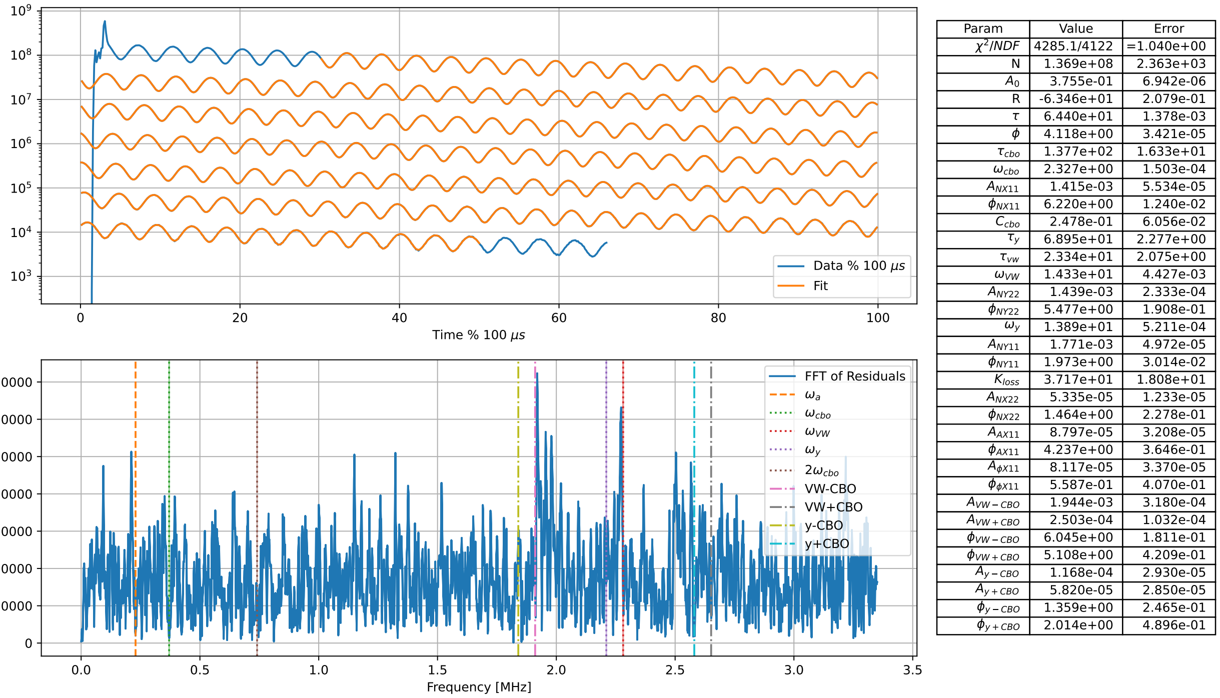

Param	Value	Error
χ^2/NDF	4285.1/4122	=1.040e+00
N	1.369e+08	2.363e+03
A_0	3.755e-01	6.942e-06
R	-6.346e+01	2.079e-01
τ	6.440e+01	1.378e-03
ϕ	4.118e+00	3.421e-05
τ_{cbo}	1.377e+02	1.633e+01
ω_{cbo}	2.327e+00	1.503e-04
A_{NX11}	1.415e-03	5.534e-05
ϕ_{NX11}	6.220e+00	1.240e-02
C_{cbo}	2.478e-01	6.056e-02
τ_y	6.895e+01	2.277e+00
τ_{vw}	2.334e+01	2.075e+00
ω_{VW}	1.433e+01	4.427e-03
A_{NY22}	1.439e-03	2.333e-04
ϕ_{NY22}	5.477e+00	1.908e-01
ω_y	1.389e+01	5.211e-04
A_{NY11}	1.771e-03	4.972e-05
ϕ_{NY11}	1.973e+00	3.014e-02
K_{loss}	3.717e+01	1.808e+01
A_{NX22}	5.335e-05	1.233e-05
ϕ_{NX22}	1.464e+00	2.278e-01
A_{AX11}	8.797e-05	3.208e-05
ϕ_{AX11}	4.237e+00	3.646e-01
$A_{\phi X11}$	8.117e-05	3.370e-05
$\phi_{\phi X11}$	5.587e-01	4.070e-01
A_{VW-CBO}	1.944e-03	3.180e-04
A_{VW+CBO}	2.503e-04	1.032e-04
ϕ_{VW-CBO}	6.045e+00	1.811e-01
ϕ_{VW+CBO}	5.108e+00	4.209e-01
A_{y-CBO}	1.168e-04	2.930e-05
A_{y+CBO}	5.820e-05	2.850e-05
ϕ_{y-CBO}	1.359e+00	2.465e-01
ϕ_{y+CBO}	2.014e+00	4.896e-01

Figure 5.41: A fit to the Run-4 T-Method histogram using the full fit model in Equation (5.51).

5.4.5 Studies in Progress

The following analyses are in-progress as of the writing of this thesis:

Calorimeter-by-calorimeter start time/energy binned scans Looking detector by detector may help to elucidate the cause of the residual gain correction. Preliminary results indicate the values of A_g and N_g can vary by detector.

Bunch-by-bunch scans No differences in the value of $R(\omega_a)$ vs. bunch number is expected, nor has any been observed in previous Runs. However, ϕ_a can vary by bunch and slightly dilute the overall ω_a signal. Quantifying the effect of this reduction is important.

Dataset-by-dataset scans Any shifts in the fit parameters over the course of a Run period (i.e. from DS-4A to 4U) could indicate an uncorrected hardware issue.

Energy binned analyses with higher order BD terms Work to integrate higher order BD terms into the energy binned analysis for the full Run-4 dataset is ongoing. This may help to shed light on the behavior of the unmodelled y-oscillations.

5.5 Summary

The UW Run-4 analysis is proceeding at a good pace, but the results shown in this thesis still represent a work in progress. The nominal analysis histograms have been produced, and data processing for special systematic studies (gain correction sensitivity scans, bunch-by-bunch analyses) is underway.

5.5.1 Open Run-4 Analysis Questions

While the Run-4 analysis is able to build upon the techniques used in the Run-1 [6] and Run-2/3 [84] analyses, it is the first set of data which is able to reach sub-200 ppb precision within a single fit. As a result, sub-dominant effects (which were likely always present in the previous analyses) now have the potential to impact final results. As of the writing of this thesis, a number of features remain under investigation:

- Many residual vertical frequencies are evident in the $1.8-2.6$ MHz range of the full-calorimeter FFT. These arise from incomplete modelling of the vertical terms. Extensions of the nominal fit model are currently under investigation, such as:
    - allowing the lifetime and frequency of the x/y cross terms to float (Figure 5.42, orange);
    - adding a modulation of the $g-2$ asymmetry and phase terms with the y-oscillations (Figure 5.42, green);
    - and adding a time dependence of the vertical frequencies (Section 5.3.7.3).

  These require additional systematic checks before being incorporated into the final fit model.

- Spikes in the Calorimeter 13 and Calorimeter 19 FFTs at just above ω_{vw} indicate unique behavior in those calorimeters which must be understood. These calorimeter are located just behind the two tracker stations, and so therefore have unique acceptance functions which may certainly factor into their unique sensitivity to these terms.
- Low frequency spikes in the full FFT are observed at 0.09 MHz and 0.64 MHz. These are not associated with any previously identified beam dynamics frequency. The amplitude of these peaks appears to vary with the value of the residual gain correction applied, as well as energy bin.
- Both the A-Method and T-Method analyses yield a reduced χ^2 which is not consistent with 1. This is partially due to the sub-optimal modelling of the higher-order vertical terms in the fit (the reduced χ^2 of the fits in Figure 5.42 decrease by ≈ 0.01), but could also be an indication of some unknown feature in the data. Current investigations show that this poor χ^2 was not present in fits performed to histograms produced from the same data a few months prior, indicating that the cause may simply be a data production error rather than any physics effect. Reprocessing of the data with a previous version of the analysis code to test this hypothesis is in progress.
- The residual gain correction has been found to prefer different values of N_g and A_g calorimeter by calorimeter. This could be due to the single-calorimeter enhancement of the BD oscillations affecting the results, but could also be an indication as to the cause of the RGC effect.

The author intends to continue work on these challenges after the completion of this thesis. It should be noted that the potential scale of these effects is small compared to the overall shift in $R(\omega_a)$ from the addition of the first order CBO term described in Section 5.3.7.3. In the authors estimation, each of the effects listed above has the potential to reasonably shift $R(\omega_a)$ by no more than 30 ppb — well within the statistical uncertainty of the measurement.

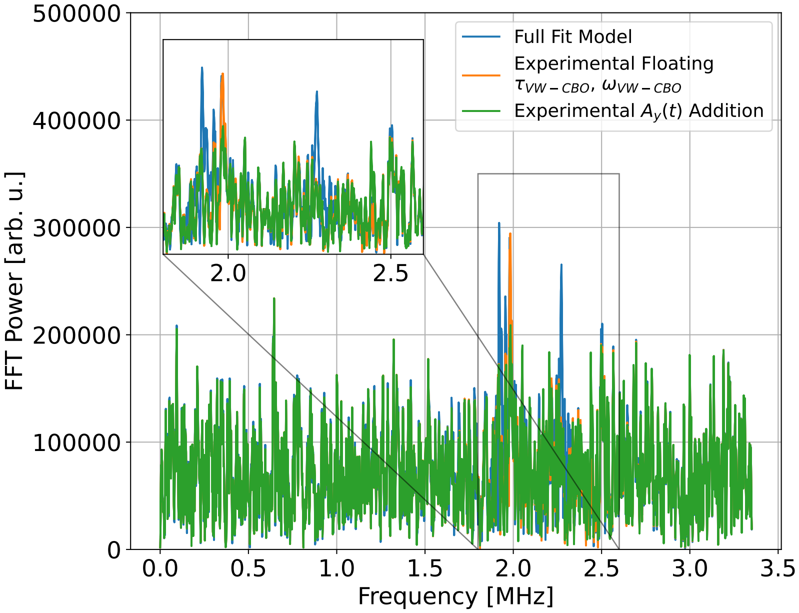

Figure 5.42: Freeing the lifetime and frequency of the VW-CBO cross term (orange) and the addition of a modulation of the $g-2$ asymmetry with ω_{y} (green) reduce the amplitude of the residual vertical oscillation peaks. Further extensions of the fit model like this are currently under investigation for the Run-4 analysis.

Chapter 6

Selected Systematic Studies

To quantify any bias in the measured value of ω_a, a series of systematic checks are performed across the various analysis teams. The philosophy behind the evaluation of the systematics in the Muon $g-2$ experiment is to be as robust as possible, with many independent cross checks for each value. On the precession frequency analysis side, each of the six independent ω_a analysis groups compute their own evaluations of the uncertainties, which are averaged together to yield the final result.

The effect of every correction (pileup, gain, etc.) on the final result is scrutinized intensely. Each correction is varied within its quoted uncertainties and the effect on $R(\omega_a)$ from this variation is taken as the overall systematic uncertainty. Where uncertainties are not well defined, for instance in the application of the residual gain correction, the correction is varied over a range of values where $\Delta\chi^2 < 4$ (2σ) for the final fit result. Additionally, for each of the terms of Equations (5.51) and (5.52), a series of questions are asked:

- How could this term introduce a bias to ω_a?
- How can such a bias be quantified?
- Can the analysis be modified to reduce such a bias?
- How do reasonable perturbations of this term alter the result?

This final question, for instance, led to the examination of many alternate CBO decoherence envelope models in the Run-2/3 analysis, which in turn led to a $\mathcal{O}(15\,\text{ppb})$ uncertainty.

The main drivers of the systematic uncertainties in the Run-2/3 analysis were CBO handling, pileup corrections, gain corrections, and the residual slow effect. All other effects were subdominant ($< 5\,\text{ppb}$ averaged across all analysis groups). This is expected to remain true in the Run-4+ analysis. For each of the beam dynamics corrections in Section 3.6.3, at least two independent analyses are performed. The systematics for such analyses are quantified using a similar philosophy to the ω_a systematics.

A selection of systematic studies performed by the author with relevance to the Run-4 analysis are presented in this chapter. The Run-4+ analysis is still a work in progress, and as such many values for systematic uncertainties which are evaluated as standard practice have not yet been computed. A summary of such systematics, their value in the Run-2/3 analysis, and their expected impacts on the Run-4+ analysis is presented in Section 6.4.

6.1 Phase-Momentum Relationship

As stated in Section 3.1.2, a relationship between the $g-2$ phase at injection and muon momentum — ${}^{d\phi_a}\!/_{dp}$ — is created in the delivery ring. Such a correlation can couple to changes in the momentum of the stored beam to produce a bias to ω_a. The stored momentum distribution in the ring can change over a single fill through two processes:

Momentum dependent muon losses: Lower momentum muons have a slightly higher probability of hitting aperture defining collimators and being ejected from the storage region before they can decay (see Section 3.6.3.3 and reference [122]).

Differential decay: Higher momentum muons have a slightly longer lifetime than low momentum muons, and so will make up a higher proportion of the stored population at later times (see Section 3.6.3.4).

Both of these effects are relatively small (each amounting to a difference in $R(\omega_a)$ of $< 20\,\text{ppb}$), but in order for them to be properly accounted for in systematic estimates this initial phase-momentum relationship must be known. As stated in Section 3.1.2.1, beamline simulations predict:

$$\left.\frac{d\langle\phi_a\rangle}{d\langle p\rangle}\right|_{\text{Sim.}} = -9.54\,\frac{\text{mrad}}{\%\Delta p/p}.$$

This relation is shown in Figure 6.1. Studies in Run-1 conditions were undertaken which confirmed this value [84]:

$$\left.\frac{d\langle\phi_a\rangle}{d\langle p\rangle}\right|_{\text{Run-1}} = -10 \pm 1.6\,\frac{\text{mrad}}{\%\Delta p/p}.$$

Here, studies undertaken in Run-6 to measure this relation for Run-4+ conditions[1] are described.

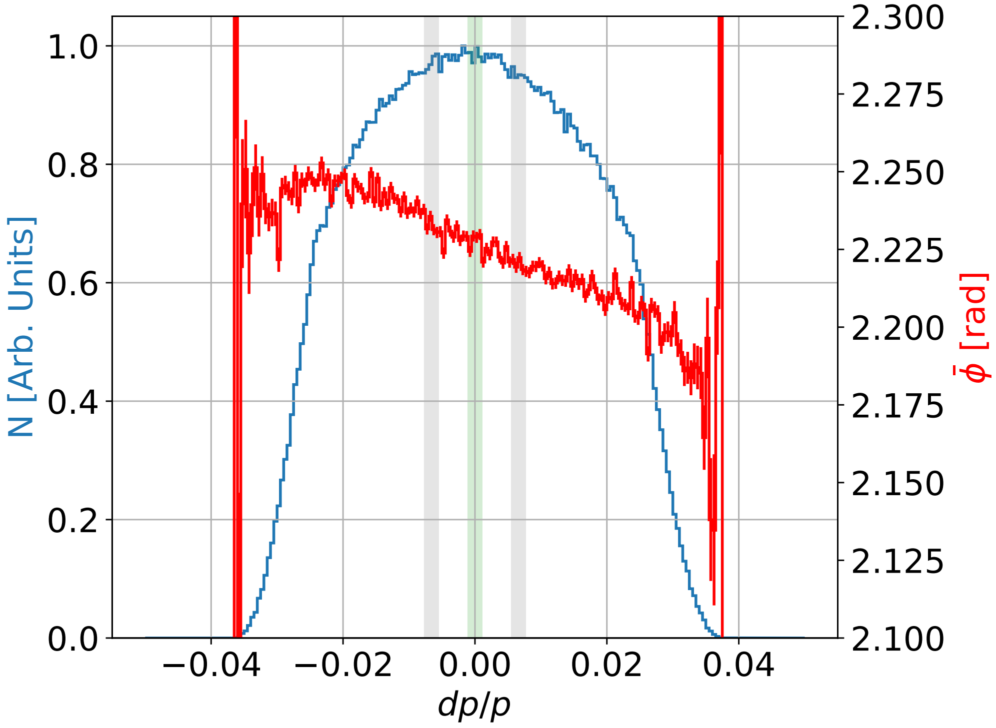

Figure 6.1: Simulated intensity (blue, left axis) and phase (red, right axis) distributions vs. momentum at the end of the M5 beamline, just before injection to the $g-2$ storage ring. The green band represents the region of this distribution which is selected in nominal operation, while the grey bands are the high and low momentum regions selected for this study.

The $g-2$ storage ring has a momentum acceptance of $\Delta p/p_0 = \pm 0.15\%$, while the overall

---

[1] To be precise, all storage conditions from Run-2 through Run-6 were studied.

momentum distribution of the incoming beam has $\Delta p/p_0 \approx \pm 2.5\%$ (as shown in Figure 6.1). By changing the magnetic field of the storage ring, a different subset of this incoming distribution can be selected and stored. For this study, the magnetic field of the storage ring was changed by $\pm 0.66\%$, which altered the central momentum p_0 by the same percentage. This is indicated by the grey bands in Figure 6.1. In total, 19 datasets (each totalling 6-12 hours of data taking) with a variety of settings were taken in Run-6. Nine of these datasets are part of the nominal analysis, while the others are used for systematic evaluations. The conditions within these datasets are summarized in Table 6.1.

The data from each set is divided by bunch[2] and a five-parameter ω_a analysis is performed on each of these subsets. The low statistics in each of these datasets means that the BD terms are not required in the fit function. Examples of such fits to each of the momenta are shown in Figure 6.2, illustrating the change in the precession frequency caused by the difference in the field. The value of ϕ_a extracted from these fits will be used to calculated ${}^{d\phi_a}/{}_{dp}$.

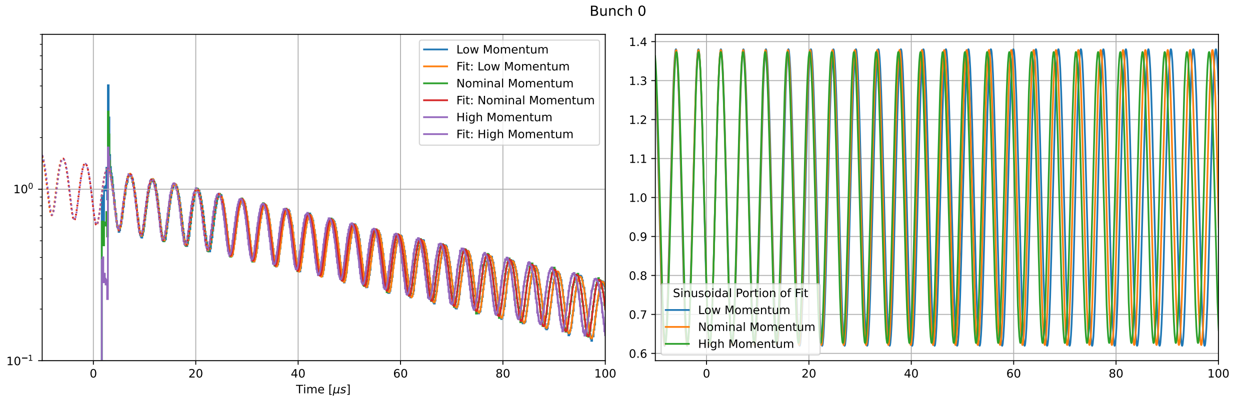

Figure 6.2: Example $g-2$ histograms from the high, nominal, and low momentum datasets. The precession frequency is altered by the change in magnetic field, which can be seen in the phase change at late times.

Changes in the accelerator systems upstream of the $g-2$ storage ring can cause slight changes in the arrival time and/or shape of the muon bunches. The T0 entrance counter is able to compensate for this at a level which is sufficient for the nominal ω_a analysis, but some effect on the observed entrance time of the muon bunch (t_0) remains at the ns-scale. If care is not taken, this spread in

---

[2] Bunches 0/8, 1/9, etc. are combined in this case, since their shapes have been shown to be identical.

Date	**Runs**	**Ring Field**	**M4/M5 Wedges**	**RF**	**Inflector Setpoint**	**Inflector Frozen Field**	**Kicker Setpoint**
2/28-3/1	57996 - 58003	-0.66%	IN	OFF	-0.67%	-0.66%	Run-6
3/1	58004 - 58015	+0.66%	IN	OFF	+0.66%	+0.66%	Run-6
3/3-3/4	58031 - 58035	Nominal	IN	OFF	Nominal	Nominal	Run-6
3/15-3/16	58209 - 58215	+0.66%	OUT	OFF	+0.66%	+0.66%	Run-6
3/16	58216 - 58219	+0.66%	IN	OFF	+0.66%	+0.66%	Run-6
3/18	58277 - 58279	Nominal	IN	OFF	Nominal	Nominal	Run-6
3/18-3/19	58285 - 58288	+0.66%	IN	OFF	+0.66%	Nominal	Run-6
3/19	58290 - 58293	+0.66%	OUT	OFF	+0.66%	Nominal	Run-6
3/22	58467 - 58471	-0.66%	IN	OFF	-0.66%	Nominal	Run-6
3/30-3/31	58823 - 58827	-0.66%	IN	OFF	-0.66%	Nominal	Run-6
3/31	58828 - 58831	-0.66%	IN	OFF	Nominal	Nominal	Run-6
4/14	59178 - 59181	Nominal	IN	ON	Nominal	Nominal	Run-6
4/14-4/15	59182 - 59187	Nominal	IN	OFF	Nominal	Nominal	Run-6
4/15	59189 - 59195	Nominal	OUT	OFF	Nominal	Nominal	Run-6
4/15	59197 - 59207	Nominal	IN	OFF	Nominal	Nominal	Run-2
4/15	59209 - 59214	-0.66%	IN	OFF	Nominal	Nominal	Run-2
4/15	59215 - 59221	-0.66%	IN	OFF	Nominal	Nominal	Run-2
4/16	59223 - 59226	+0.66%	IN	OFF	Nominal	Nominal	Run-2
4/16	59929 - 59232	Nominal	IN	OFF	Nominal	Nominal	Run-2

Table 6.1: The datasets used in the nominal phase-momentum analysis. Each one represents 6-12 hours of Run-6 data taking. Kicker strength, RF settings, and inflector settings were found not to impact the results in a significant way.

t_0 can cause a bias in the extracted value of ϕ_a of $\mathcal{O}(10\,\mathrm{mrad})$, exactly the scale which this study is attempting to measure.

To combat this, the value of t_0 for each bunch in every run is calculated using the Fourier fast rotation analysis. A full description of this analysis can be found in reference [172], but an abbreviated description of the relevant portions are given here. The spread in momenta in the ring yields a spread in the cyclotron periods of the stored muons. This signal can be seen in Figure 6.3a. By subtracting the exponential background and slowly varying ω_a signal from the hit times and performing a Fourier transform, the spread in cyclotron frequencies can be extracted.

Because of the initial flash of particles at injection, calorimeter digitization begins $\approx 4\,\mu$s into the fill. The analysis therefore cannot start at t_0 and must instead extrapolate back from a later time. As a consequence of this (and the fact that the signal exists in a finite time window), a non-physical background is introduced to the frequency extraction. With the proper choice of t_0, this background is parabolic and can be removed using a polynomial fit. An incorrect choice of t_0 introduces distortions to the background. The correct value of t_0 is obtained by a scan of the χ^2 of the parabolic background fit. The background fit is performed only in the non-physical region of the frequency space (i.e. frequencies which correspond to orbital radii outside the $\pm 45\,\mathrm{mm}$ muon storage region). Such a t_0 scan and the resulting parabolic background can be seen in Figures 6.3b and 6.3c. A distorted background resulting from an incorrect choice of t_0 can be seen in Figure 6.3d.

The t_0 extracted from this procedure on a run-by-run, bunch-by-bunch basis for a subset of the datasets in Table 6.1 can be seen in Figure 6.4b. The value of t_0 shifts throughout this study by up to 50 ns. This 'residual t_0' is subtracted from the positron hit times when creating the analysis histograms[3].

One additional complication in this analysis is that a field change of $\pm 0.66\%$ is outside the range which the fixed NMR probes are designed to measure. However, since the only parameter of interest in this analysis is ϕ_a, the muons themselves can be used as a magnetometer. The change

---

[3] Applying the phase change due to this residual t_0 as a correction to the fitted value of ϕ_a was also tested, and this yielded consistent results.

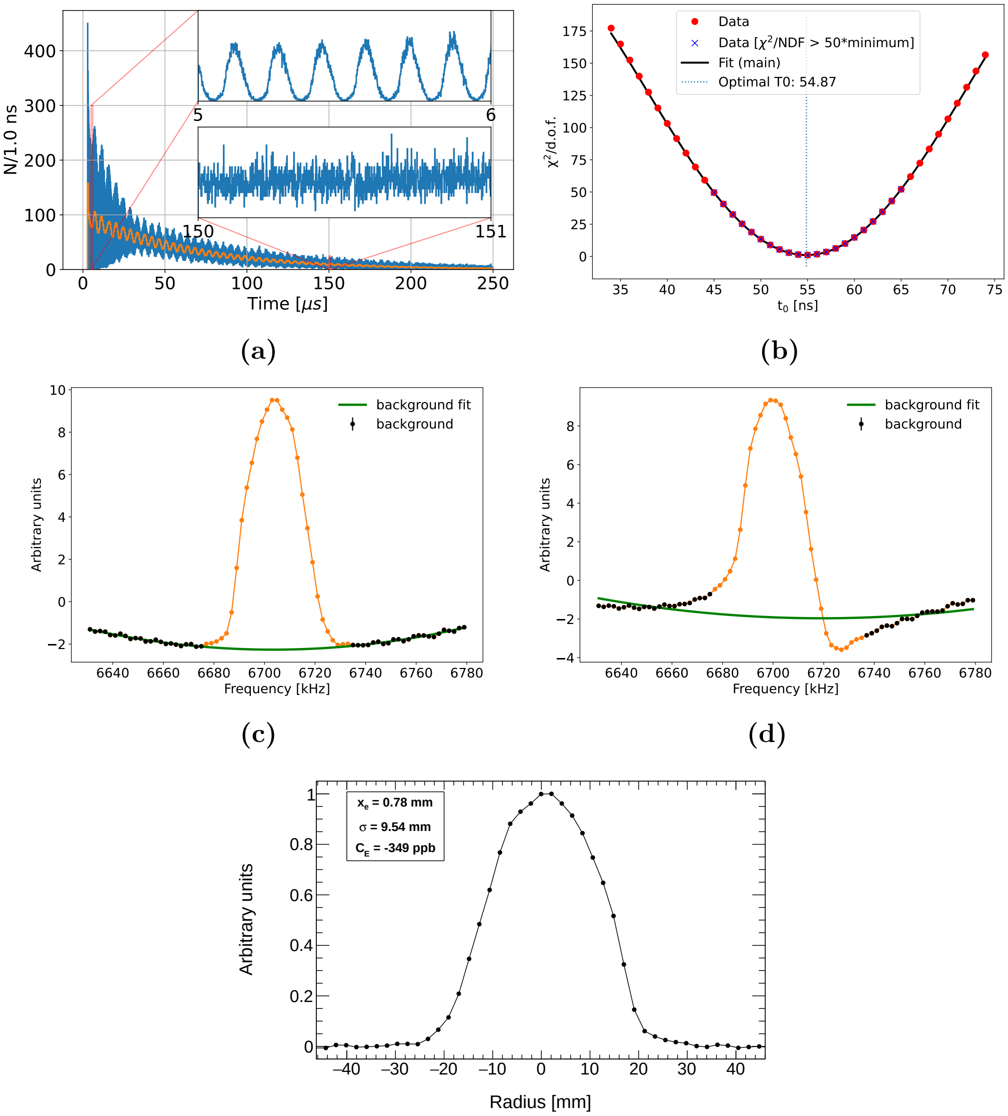

(a) **(b)**

(c) **(d)**

(e)

Figure 6.3: An example of the Fourier fast rotation analysis performed for run 59182, bunch 0. (a) The raw fast rotation signal. The finely binned data (blue) shows the cyclotron frequency modulation at early times. The decoherence of the cyclotron signal can be seen at late times. A smoothed version of the same data (orange) shows clearly the exponential decay and ω_a oscillation. (b) The result of the χ^2 scan for the t_0 background optimization procedure. (c) The resultant frequency distribution from the fourier analysis. The parabolic background can be seen with the properly optimized $t_0 = 54.87\,\text{ns}$. (d) The background fit to the same data when t_0 is fixed to 45 ns. A shift in the value of t_0 by 10 ns can result in a large distortion of the background. (e) The equilibrium radii extracted from the properly optimized frequency distribution.

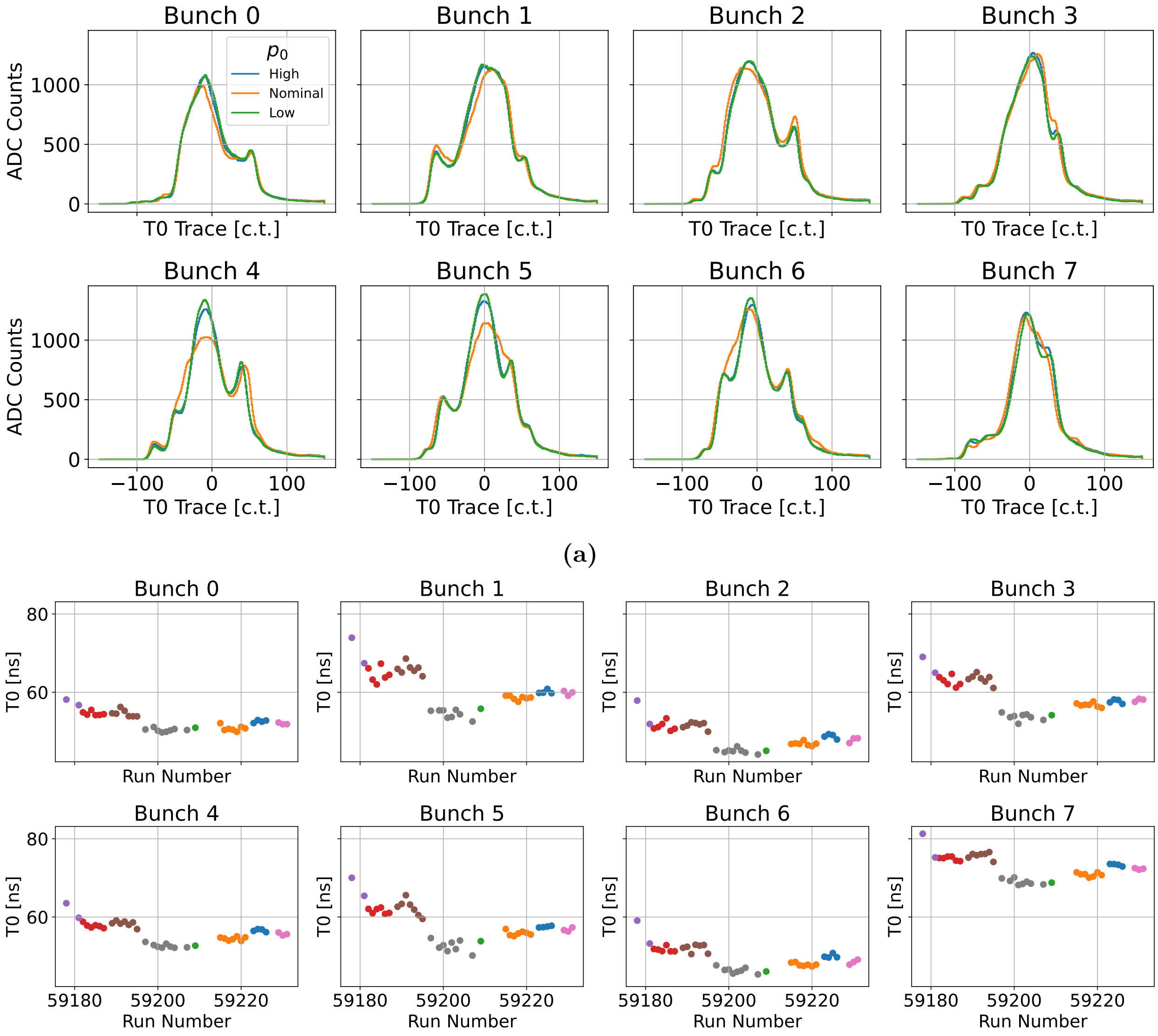

(a)

(b)

Figure 6.4: (a) Change in the shape of the beam entrance pulse as seen by the T0 detector between the first three datasets taken for this study. These changes are associated with upstream tuning of the beam, and can cause sudden changes in the value of t_0 and ϕ_a. (b) The value of t_0 also has been shown to slowly wander over the course of hours or days. This, combined with an overall offset by bunch, results in a bias to the value of ϕ_a in this study unless properly accounted for. Each point in these plots represents a full Fourier fast rotation analysis as shown in Figure 6.3. The colors represent different datasets in Table 6.1.

in $R(\omega_a)$ can be related to the change in field, and thus the change in stored momentum via:

$$\frac{\Delta p}{p}\ [\%] = \frac{\Delta B}{B}\ [\%] = \frac{\Delta R(\omega_a)}{10^6} * 100. \tag{6.1}$$

The correlation between ϕ_a and $p \propto R(\omega_a)$ in the fit is accounted for as a systematic error. This error, and others assessed as part of this study, are given in Table 6.2. Many of the non-fit errors listed there were not evaluated for the Run-1 version of this measurement. The muon lifetime can also be used to extract the momentum change, and this agrees with the values obtained from $R(\omega_a)$.

The values of ϕ_a are plotted vs. ${}^{\Delta p}/_{p_0}$ and fit to a linear function. The results of these fits can be seen in Figure 6.5. Two approaches are taken when combining the results from different bunches: fitting the bunches individually and taking the average and aligning the bunches by subtracting off their individual t_0 to fit them together. Both approaches yield consistent values of ${}^{d\langle\phi_a\rangle}/_{d\langle p\rangle}$. From this analysis:

$$\frac{d\langle\phi_a\rangle}{d\langle p\rangle} = -13.51 \pm 1.42\ \frac{\text{mrad}}{\%\Delta p/p}. \tag{6.2}$$

Error Source	**Value [mrad/(%dp/p)]**
Statistical uncertainty from the fit	0.54
Differences between the 9 datasets	0.25
Uncertainty in the magnetic field measurement	0.5
Changes in the detector gain between datasets	0.1
Bunch-by-bunch average vs. combined fit	0.03
Total	**1.42**

Table 6.2: Uncertainties associated with the extraction of the injection phase-momentum relationship. All uncertainties are taken as correlated, and so sum linearly.

The Run-6 measurement is 35 – 40% larger than the Run-1 measurement or the beamline simulation. The results are summarized in Figure 6.5. After repetition of the measurement confirmed these results, a thorough look at the simulation was undertaken to determine whether there had been any changes to the experimental setup since Run-1 which were not included in the latest model. Through this search, it was found that the beamline simulation model had not been updated to include the momentum cooling wedge inserted into the M4/M5 beamline in Run-2 [85].

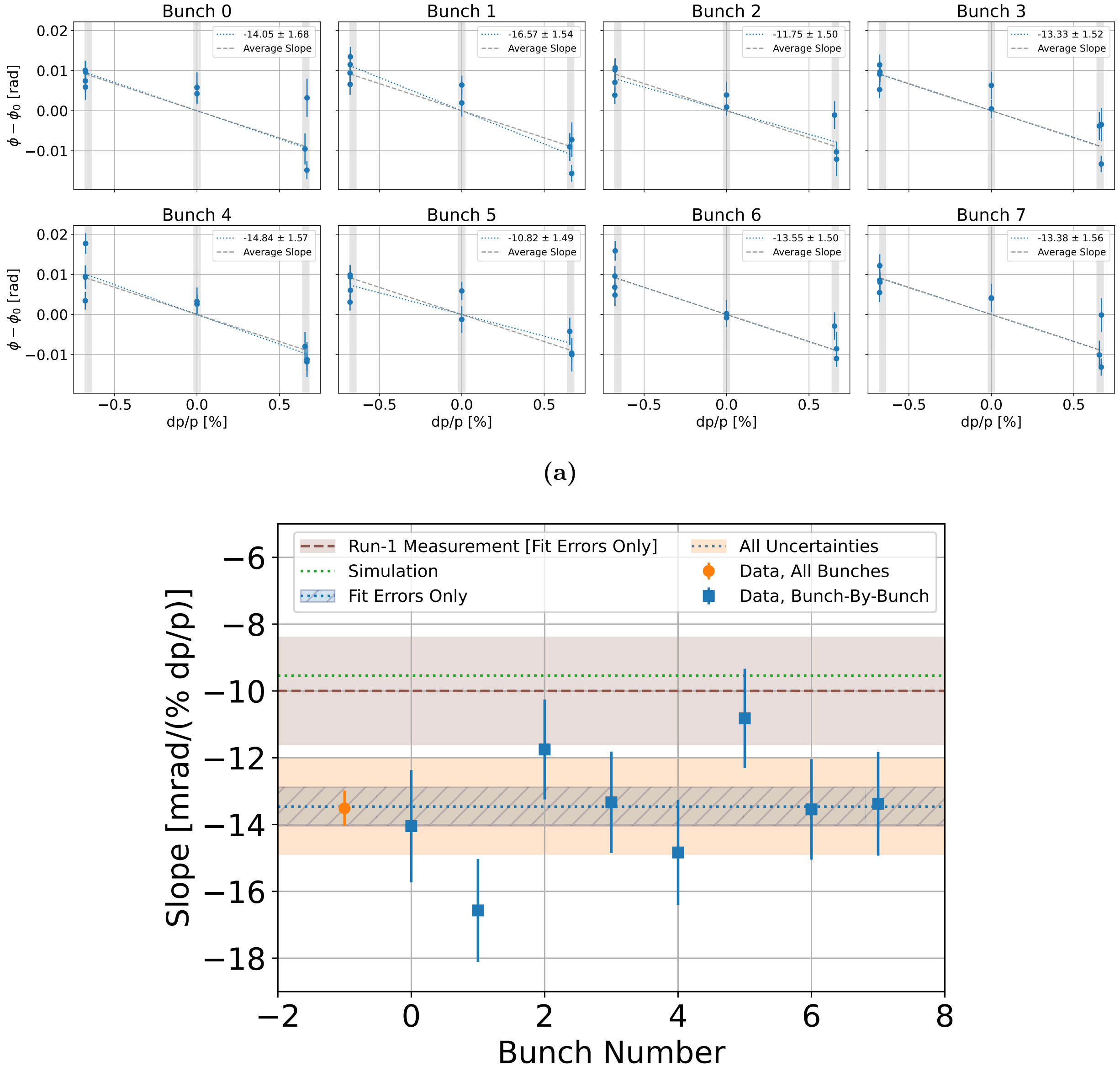

(a)

(b)

Figure 6.5: (a) Bunch-by-bunch linear fit results. (b) Results of the extracted slopes bunch by bunch compared with simulation. The simulation and the Run-1 result disagree with the updated measurement. ‘Bunch -1’ represents the combination of data from all bunches.

The wedge was inserted in an area of the beamline with high radial dispersion, and degraded high momentum muons to lower momentum with the goal of increasing overall storage efficiency (see Figure 3.5). This degradation could plausibly couple to, and enhance, the existing ${}^{d\phi_a}/_{dp}$

To test the hypothesis that the wedge was the direct cause of the increase in slope seen in this study, two studies have been performed: Toy Monte Carlo simulations of the effect of the wedge on the phase space of the beam [173], and back to back measurements of the $g-2$ phase with the wedge inserted vs. retracted. Both sets of studies indicate that the wedge can create a momentum dependent phase change and is responsible for the increase in the phase-momentum relationship.

For the data-driven test of this hypothesis, the difference between the $g-2$ phases with the M5 wedge inserted vs. retracted was measured for the nominal storage ring field and the +0.66% field (Figure 6.6a). The change in phase due to the insertion of the wedge was larger for high momentum muons. In Figure 6.6b, these observed shifts were applied as a correction to the data in Figure 6.5. With these correction factors applied, the Run-1 result was reproduced. This indicates that the wedge was the only cause of the difference between the Run-1 value and the value measured in Run-6. Updates to the full $g-2$ beamline simulation model are in progress to further test this hypothesis. These simulation results will be used as a cross check of these measurements when evaluating the final Run-4+ systematics.

The increase in slope directly couples C_{ml} and C_{dd}, increasing the magnitude of both by 35%. The value of C_{ml} is negligible post-Run-1 due to an overall decrease in $L(t)$ [17, 122], but the value of C_{dd} is not. The wedge was inserted just before DS-2E, and so this increase is reflected in the published values of C_{dd} for Run-2/3 [15, 17]. This will also be the case for the Run-4+ analyses.

6.2 Analysis of Non-Muon Events

Alongside muons, there are a few other particle species which make their way into the $g-2$ storage ring (Table 6.3). These are primarily protons and deuterons. These particles can be categorized based on their type of orbit: stable or unstable.

Stable beam contaminants arrive in time with the muon entrance pulse and thus can be kicked onto stable orbits within the storage ring. These particles then only appear in the detectors if

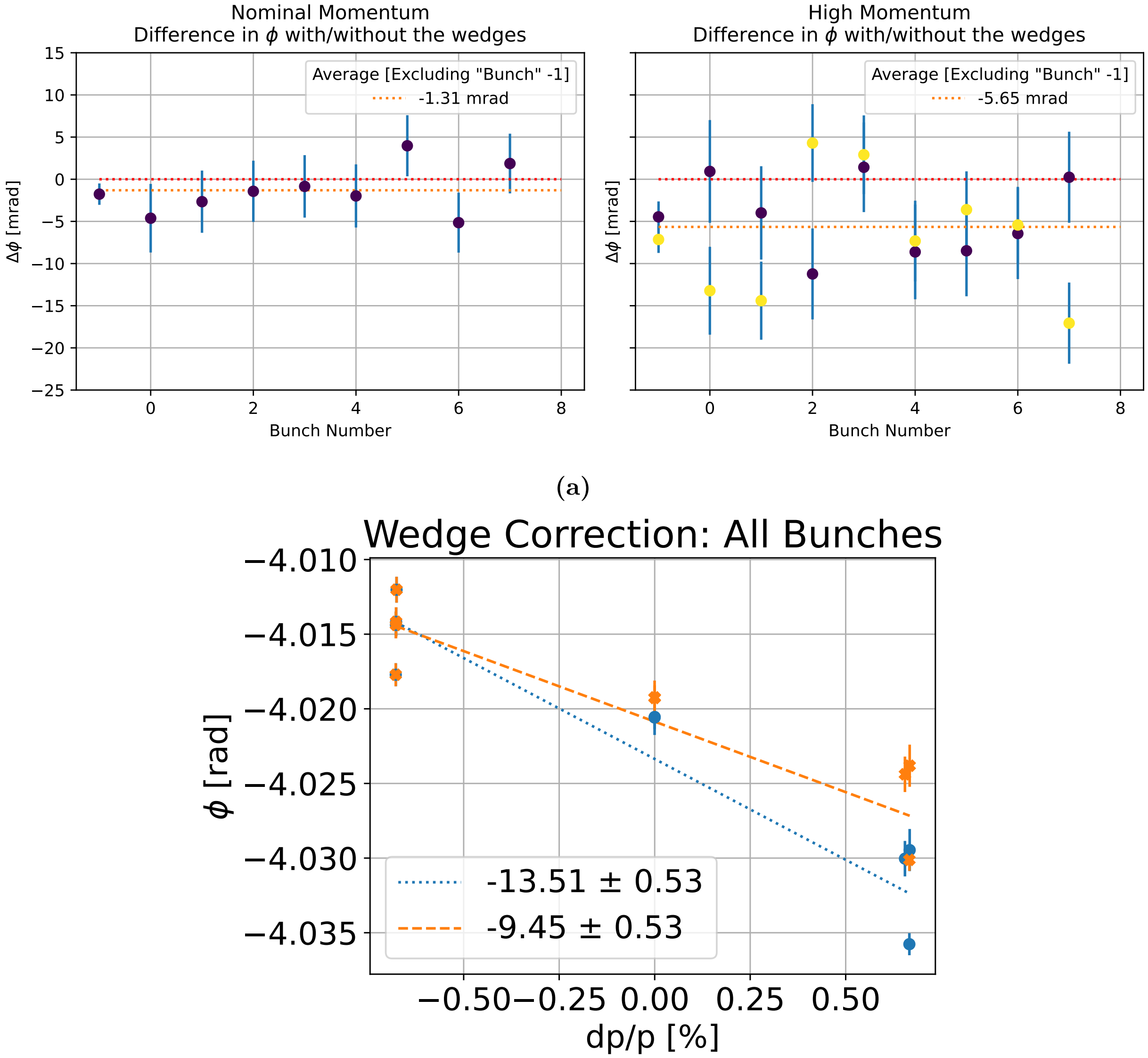

(a)

(b)

Figure 6.6: (a) Measured effect of inserting the wedge on the $g-2$ phase. (b) Measured slope, with (orange) and without (blue) a correction for wedge effects at high and nominal momenta.

Particle Species	Velocity [$\times c$]	DR Period [μs]	DR Frequency [MHz]	Energy Deposit in Calorimeter [MeV]	Seen In Stable Population	Seen in Unstable Population
Deuteron	0.8557	1.970	0.508	≈ 350	Yes	Yes
Proton	0.9571	1.761	0.568	≈ 200	No	Yes
Pion	0.9989	1.687	0.593	—	No	No
Muon	0.9994	1.686	0.593	≈ 170	Yes	No
Positron	1.0000	1.686	0.593	$0 - 3200$	No	No

Table 6.3: Properties of the particles seen in the $g - 2$ storage ring.

their orbits later become unstable; either due to energy loss from scattering (a la lost muons) or at the end of the fill when the ESQ voltages are discharged. Using this end of fill discharge, an estimate of the number of stable contaminants in the ring and their species can be formed. A study was performed where the calorimeter digitization window was extended and the ESQ system was discharged earlier and earlier in the fill. As the discharge of the ESQ was moved earlier, the observed late time excess moved with it (Figure 6.7b). After subtracting an exponential with the muon lifetime, this region was fit to an empirical functional form:

$$N(t) = \underbrace{\frac{A_{\mathrm{g}}}{1 + e^{-\alpha_{\mathrm{g}}(t-\bar{t}_{\mathrm{g}})}}}_{\text{Growth to plateau}} + \underbrace{A_{\mathrm{d}} e^{-(t-\bar{t}_{\mathrm{d}})/\tau_{\mathrm{d}}}}_{\text{Exponential decay}} + \underbrace{C}_{\text{Constant Background}}, \tag{6.3}$$

to model the behavior of the late time events and extrapolate past the end of digitization. This validity of this extrapolation was confirmed by comparing the predictions for the nominal ESQ shutoff data with that measured when the ESQ system was shut off earlier (Figure 6.7b). From this fit, the number of stable contaminants ($N_{\text{stable}} \equiv \int N(t)$) circulating in the ring was extracted. The conclusions from this study were:

- No difference was seen in the behavior of these contaminants with or without the ESQ RF.
- No difference was seen in the number of stable contaminants vs. bunch number.
- No peak was observed at $E \approx 200\,\text{MeV}$, and so the stored population of these particles consists of $\approx 100\%$ deuterons.

- These deuterons become the dominant species of particle in the ring as early as $\approx 300\,\mu$s into the fill as muons decay.

This analysis was important for understanding a constant background seen by the MiniSciFi detector, whose direct measurements of the stored beam are sensitive to these stably orbiting particles (as seen in Figure 6.8).

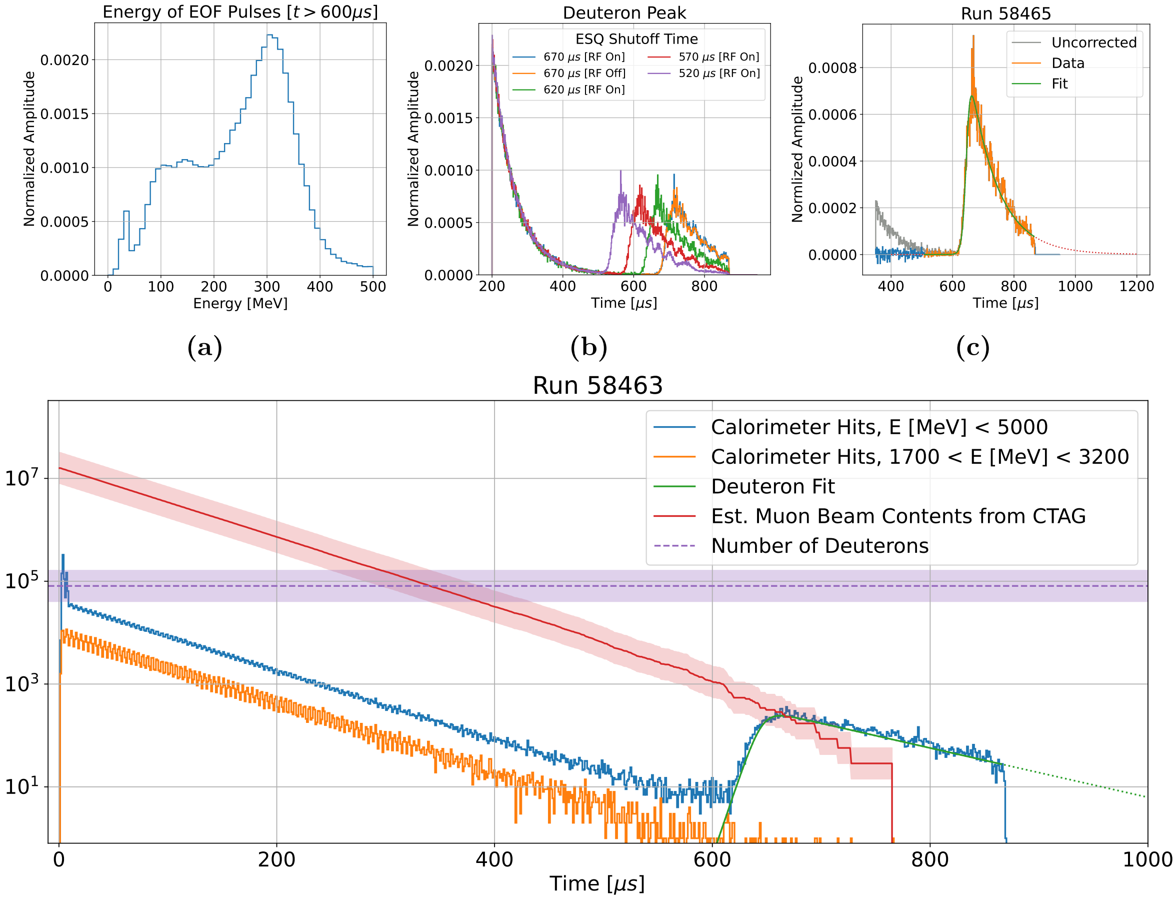

(a) **(b)** **(c)**

(d)

Figure 6.7: (a) Energies of the late time pulses. No evidence of any particles other than muons, positrons, and deuterons have been found. (b) As the ESQ system shut off is moved earlier, the late-time deuteron peak moves with it. (c) From an integral to a fit to this late time behavior, the total number of deuterons can be extracted. (d) Based on these estimates, the deuterons become the beam species in the ring where the red and purple bands cross. Based on assumptions about the detection efficiency for particles as the ESQ system shuts off, this can happen anywhere from $300 - 400\,\mu$s into the fill.

Unstable contaminants are those which arrive after injection has completed and while muons

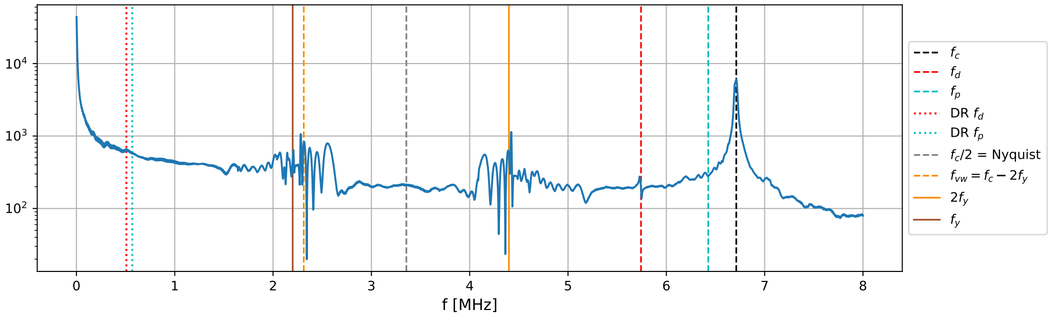

Figure 6.8: FFT of the signal seen by the MiniSciFi detector in Run-6. The revolution frequencies in the $g-2$ storage ring for muons, protons, and deuterons are indicated. No evidence of stable protons can be seen, but stable deuterons are present in the signal. Image: B. MacCoy.

are circulating in the storage ring. Because they do not receive a kick, as they exit the inflector they immediately spiral inwards towards the calorimeters in the kicker region[4]. They are predominantly seen in Calorimeters 5-8, and were quickly realized to come from leakage from the DR (Section 3.1.2). Muons are actively extracted from the DR, and whatever particles are not time coincident with the muon bunches are left behind. These remaining particles continue their orbits in the DR and, unlike in the $g-2$ storage ring where the ESQ system discharges and clears the ring at the end of each fill, can have a mean lifetime of up to 45 minutes. Every time these particles pass by the septem magnet which regulates passage down the M4/M5 beamlines, they have some small chance of passing through it[5] and propagating to the $g-2$ storage ring.

These particles can be seen in Figure 6.9. Two features are of note. First, both protons and deuterons can be seen in the unstable populations. This indicates that the abort kicker was not completely successful at removing the proton bunch from the DR. Second, the revolution frequency and debunching of these particles in the DR can be seen in their arrival times in the calorimeters.

The presence of these frequencies confirms their origin in the DR as well as their particle species. It also provides a potential explanation for how stable deuterons come to be in the storage ring. Deuterons lag behind muons in the DR, and so when the muons are extracted the deuterons formed from the same proton bunch would not be in a position to be extracted. They are also missed by

---

[4] Some small number of them may be on a trajectory which allows them to be stored for multiple turns, but such particles are very rare.

[5] This process, where particles accumulate in the DR and are slowly ('resonantly') extracted towards the muon campus, is quite similar to how the Mu2E experiment will perform its nominal injection process [174].

the proton abort kicker. These deuterons then debunch and uniformly fill the DR, so that when the next muon bunch is extracted a constant background of deuterons from previous bunches is extracted with it. Muon bunch i is contaminated by deuterons from bunch $i-1$.

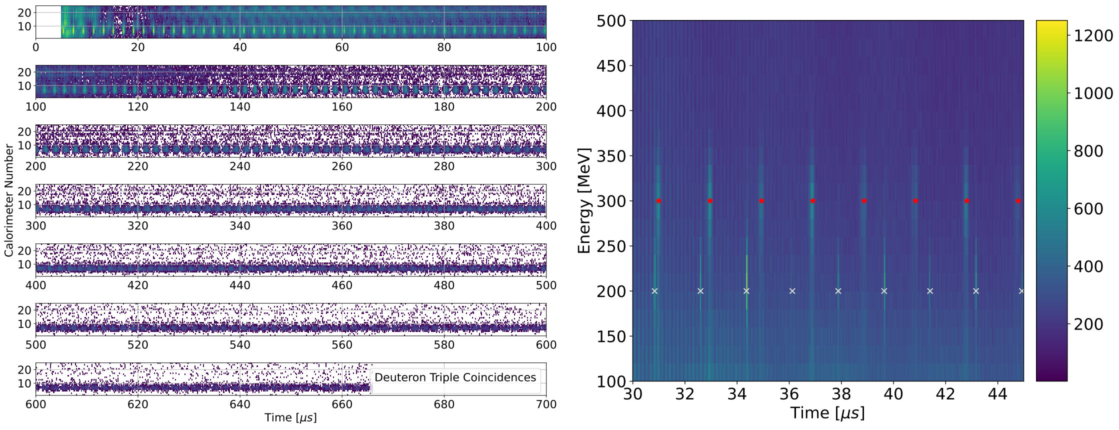

(a) **(b)**

Figure 6.9: (a) Debunching of the deuterons in Run-4. As they begin to uniformly fill the DR, their arrival times in the $g-2$ storage ring become more uniform. (b) DS-4A. Both protons (grey) and deuterons (red) can be seen in the low energy spectrum of Calorimeter 8. The markers are spaced uniformly at their respective DR periods and aligned to guide the eye.

The number of these unstable particles sharply increased at the start of Run-4, indicating an as yet unknown change in the muon campus beamline upstream of the storage ring. A downward trend in the number of protons entering the ring was observed over the course of Run-4, but they remained present throughout (see Figure 6.10). Since these particles typically deposit energies below 500 MeV in the calorimeters, and so to first order they do not enter into the nominal analysis. However, they can perturb the ω_a analysis if they:

- pile up with positrons and create clusters with an effective $E > 1000\,\mathrm{MeV}$;
- perturb the constructed pileup spectrum in such a way that it biases higher energy events;
- bias the lost muon spectrum $L(t)$ in a way which biases the ω_a fit; or
- shower hadronically and deposit $E > 1000\,\mathrm{MeV}$.

While such particles could easily perturb the UW Run-1 pileup construction, which relied on the final positron spectrum to bootstrap the pileup spectrum, the empirical pileup method is robust

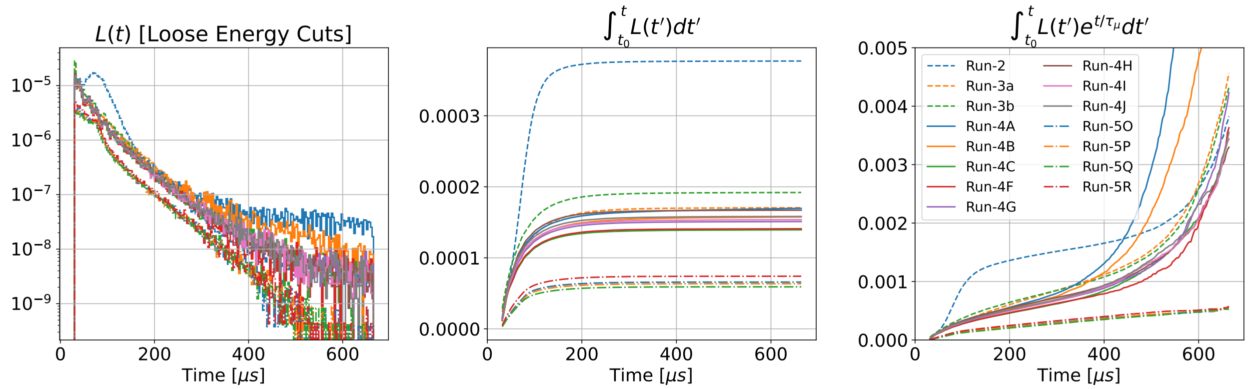

Figure 6.10: Trends in the $L(t)$ spectrum. Energy cuts are rather loose in this plot ($100 < E$ [MeV] < 250 to show the contamination from protons. The proton/deuteron contamination is visible in the late time uptick of the rightmost plot. It is largest in DS-4AB, and then decreases over the course of Run-4. Muon losses are the lowest in Run-5. The legend in the rightmost plot is common to all portions of this figure.

against such effects. No evidence of the characteristic frequencies of these particles in the nominal fit energy range were seen in the residuals or FFTs, which indicates that any effect they have is below the threshold of concern[6]. The construction of the lost muon function $L(t)$ can be biased by these particles (see Section 6.2.1).

Searches for higher energy hadronic showers in the calorimeter data correlated with these particles have been undertaken. A number of high energy ($E > 4.0\,\mathrm{GeV}$) candidates were identified in the Run-2/3 analysis, but were determined to likely be of cosmic origin based on event topology and their independence of beam flux [175]. This can account for some of the residual clusters in the high-energy 'pileup' region of the data. The effect of such high energy events was determined to be negligible: $\mathcal{O}(0.1\,\mathrm{ppb})$. No such events correlated with the revolution frequencies of particles of the DR have yet been identified. A similar study is in progress with the higher statistics of the Run-4+ data.

6.2.1 Contamination of the Muon Loss Spectrum

The loss probability (as defined in Section 5.3.8) is a physical quantity, and as such should be independent of how it is constructed. Contamination of the muon loss spectrum with other particles

---

[6] These particles can clearly be seen when conducting fits at very low energies [122].

has the potential to bias the extraction of $L(t)$. An example of this contamination in Run-4 is shown in Figure 6.11. In this figure, the triple coincidence spectrum for each calorimeter is shown for two energy regimes: a wide selection from $100 < E$ [MeV] < 250 and a narrow one from $100 < E$ [MeV] < 160. In the latter, contamination in the kicker region detectors due to upstream particles from the DR is visibly reduced but not eliminated. The effect of these particles on the fit result can be assessed by treating each of these spectra as the nominal form of $L(t)$ and performing the full fit. To equalize the normalization of K_{loss}, each of the triple coincidence spectra are normalized such that their integral is the same as the nominal $L(t)$.

The results of this study can be seen in Figure 6.12. The value of the muon lifetime and K_{loss} vary significantly in the region where the proton contamination is present. K_{loss} can also vary detector-to-detector due to detection efficiency differences or differences in losses azimuthally around the ring. This also results in a local worsening of the χ^2. However, the fitted value of $R(\omega_a)$ is robust against this contamination. Taking the difference between the maximum and minimum value of $R(\omega_a)$ from this study, a systematic error can be assigned:

$$\delta R(\omega_a)|_{\text{Choice of } L(t)} = 3.5\,\text{ppb} \tag{6.4}$$

This motivates the choice in the Run-4 analysis to construct $L(t)$ solely from the triple coincidence spectra of calorimeters 14-24.

6.3 Laser Fill Recovery

As mentioned in Section 4.1.5.1, the gain of the calorimeters is continuously monitored by a series of in-fill pulses. Three of these pulses are injected per ‘laser fill’ while the muons are stored. Depending on the Run, anywhere from $5 - 9\%$ of the data consisted of laser fills. In the Run-1 and Run-2/3 analysis, these fills were discarded. For the Run-4+ analysis, an investigation was undertaken to determine whether this data could be recovered. This investigation was performed in three ways:

- The crystal-level pulse fits immediately after the laser pulses were inspected manually for any deviation from pulses at similar times in non-laser fills.

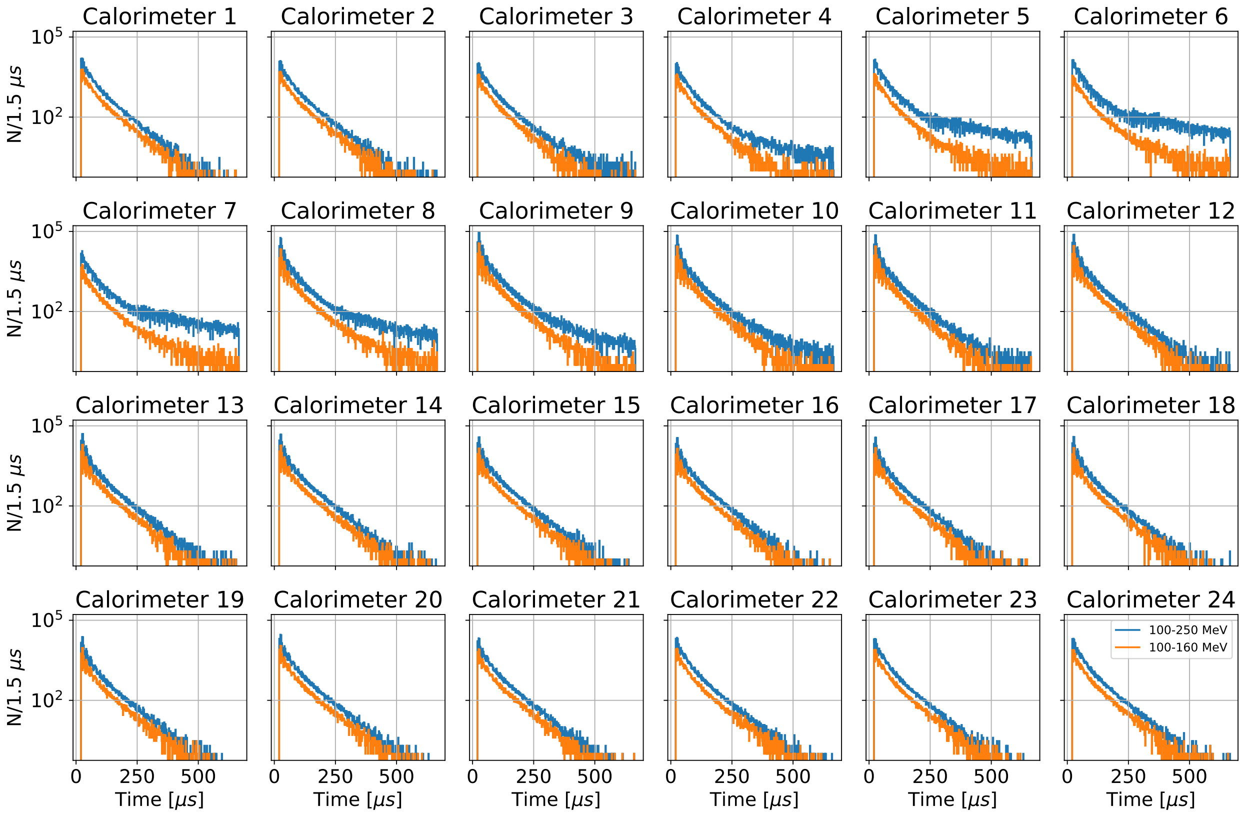

Figure 6.11: The time spectrum of triple coincidences ($L(t)$) centered on each calorimeter (i.e. for calorimeter 3, the coincidence consists of a signal in $2 \rightarrow 3 \rightarrow 4$) for two energy cuts. The contamination of this spectrum in calorimeters 4-10 with protons from the DR can be seen in the wide energy-cut spectrum (blue). It is reduced with a lower energy cut (orange), but is not entirely eliminated. Stricter timing cuts can also reduce the contamination, but similarly do not eliminate it entirely.

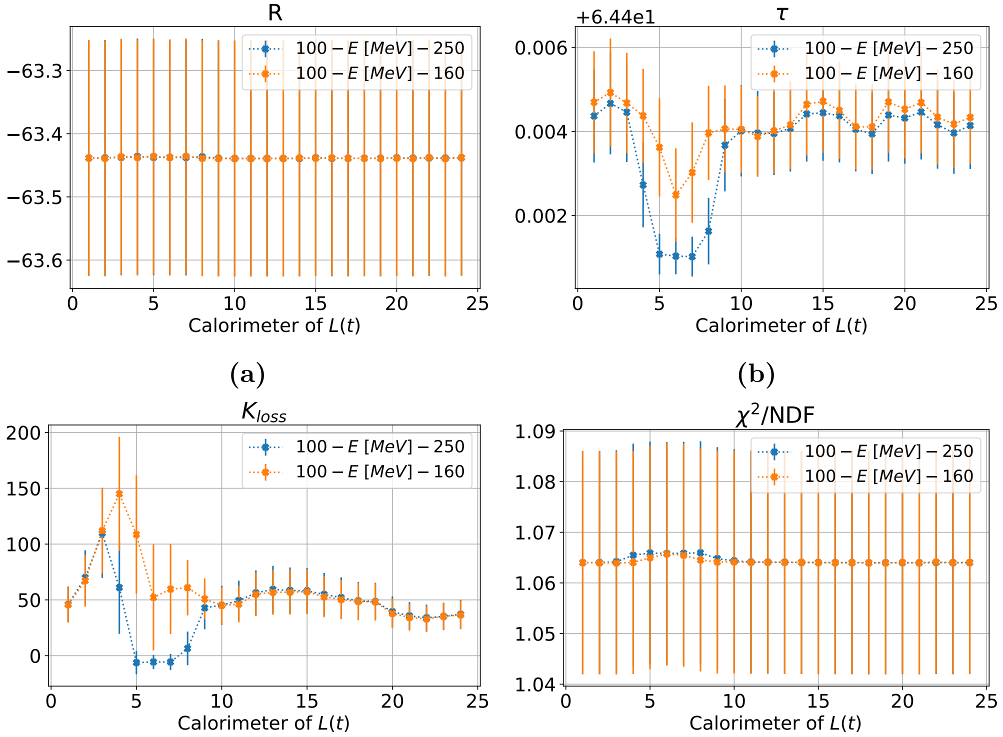

(a) **(b)**

(c) **(d)**

Figure 6.12: Values of the various fit parameters vs. the calorimeter and energy range from which $L(t)$ is derived. The effect of proton contamination in the kicker region can be observed in the instability of τ and K_{loss}. The instability is reduced when a more stringent energy cut is introduced.

- The non-laser data was randomly broken up into statistical subsets which were approximately the same size as the laser data. The same ω_a analysis was performed on each set, and statistical significance of any outliers (laser contaminated or otherwise) was assessed.
- A method of masking the histogram bins where laser pulses were present in laser fills was developed by the author.

The first two methods showed no significant perturbations to the value of $R(\omega_a)$. The final method was a novel approach to treating the $g-2$ data, analogous to the 'artificial dead time' implemented in the pulse fitter. When looping over the time-ordered clusters within a single fill, each time a laser cluster was identified[7], a dead-time was imposed. Any cluster (laser or positron) which would be placed in a time bin which overlapped with that dead time would not be counted. The number of fills for which any given bin in the histogram was masked/unmasked was tracked, and those counts were used to construct a scale factor with which the masked histogram was 'repaired:'

$$s_i = \frac{N^i_{\text{muon-fills}} + N^i_{\text{laser-fills-unmasked}} + N^i_{\text{laser-fills-masked}}}{N^i_{\text{muon-fills}} + N^i_{\text{laser-fills-unmasked}}}. \tag{6.5}$$

Each bin in the masked histogram was scaled such that:

$$N_i = s_i \left(N^i_{\text{muon}} + N^i_{\text{laser-unmasked}} \right) \tag{6.6}$$

$$\sigma_i = s_i \sqrt{N^i_{\text{muon}} + N^i_{\text{laser-unmasked}}}. \tag{6.7}$$

The result of this masking/repairing procedure can be seen schematically in Figure 6.13. This procedure was tested by scanning over many masking dead times and ensuring that the results agreed to within statistical precision (see Figure 6.14). Monte Carlo studies also confirmed that this masking procedure introduced no significant bias to the value of $R(\omega_a)$.

All three investigations yielded no signs that the laser fills would be incompatible with the main dataset. However, the following obstacles to including the laser fills in the analysis remained:

---

[7] A laser cluster was defined as any cluster with $N_{\text{crystals}} \geq 50$. The limit was not strictly 54 because some calorimeter channels were inactive. The odds of a pileup cluster after $t > 30\,\mu$s illuminating more than 50 calorimeter crystals at once are astronomically small, and so this is a safe limit to place.

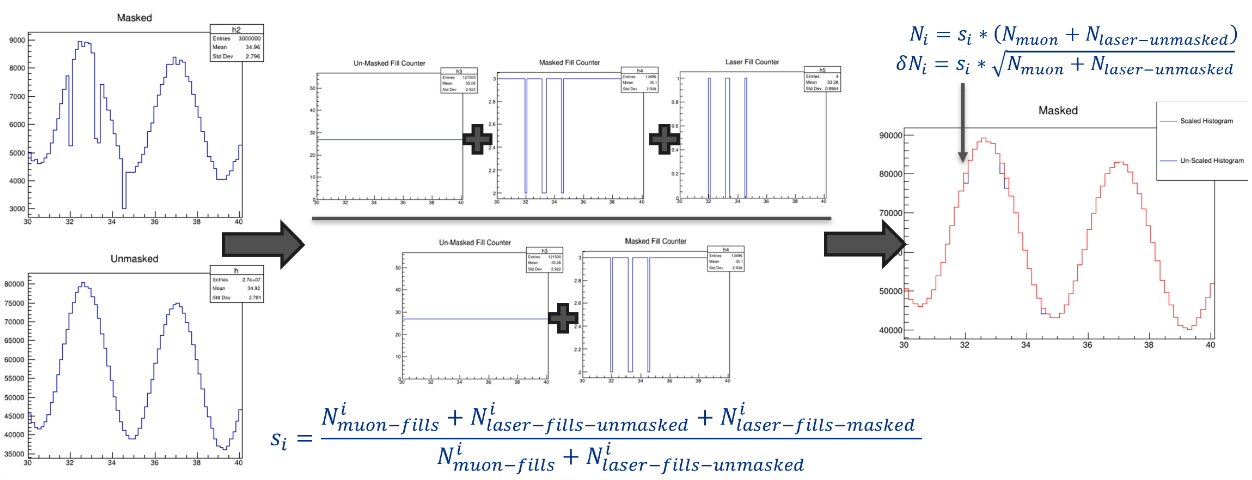

Figure 6.13: Schematic of the laser masking and re-weighting for $g-2$ histogram construction.

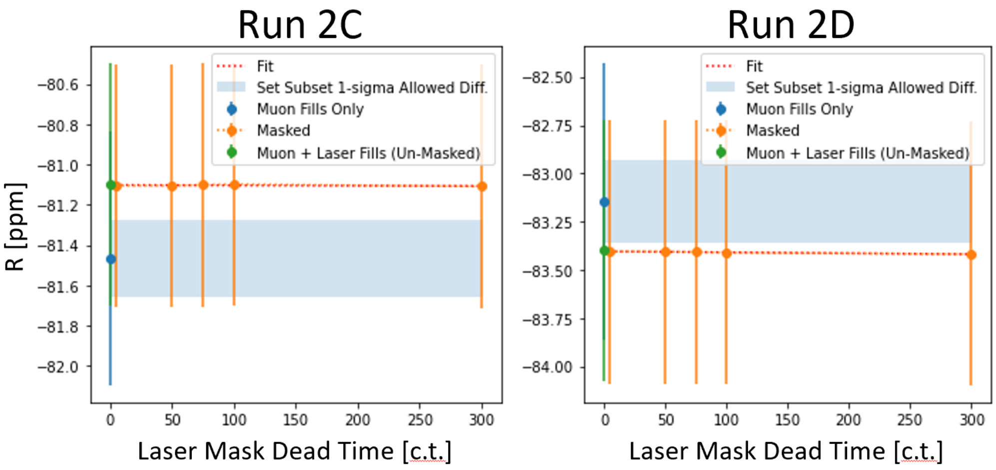

Figure 6.14: Results of the masking/re-weighting procedure performed on DS-2C and DS-2D. Muon fills only are shown in blue, Muon + laser with no masking procedure are shown in green, and Muon + masked/repaired laser are shown in orange for various dead time values. The differing sign of $\Delta R(\omega_a)$ indicates that there isn't a systematic bias from including these laser fills.

- This investigation took place after the production of the Run-2/3 data was $> 70\%$ complete. The laser fills were skipped in the nominal RE production chain, and so including them in the Run-2/3 analysis would have required significant reprocessing of the raw data to be performed.

- The statistical gain from just the Run-4+ data, after the laser prescale was significantly reduced, amounted to only $\approx 3\,\mathrm{ppb}$.

- Ensuring any systematic associated with the laser fills would be below their statistical gains for both the RE and RW reconstructions would require a significant time investment from multiple analysis groups while other higher-priority analyses are in progress.

For these reasons, the laser fills remain excluded from the nominal Run-4+ analysis.

6.4 Run-4+ Systematic Summary

Based on the values in references [17, 84], Table 6.4 shows an estimate for the values of the various ω_a systematics for the forthcoming runs. Where exact values are not given, these should be taken only as the author's best estimates for the future of this analysis based on the known condition changes between the running periods. The processes for evaluating the systematic categories given in Table 6.4 are as follows:

Fast Rotation Randomization A scan is performed where the nominal analysis histogram is produced using 100 unique random seeds for the ω_c time randomization. The average value of $R(\omega_a)$ obtained from fits to these histograms is extracted from a Gaussian fit. The error on the mean of that distribution is taken as the uncertainty associated with the randomization.

Gain The lifetime and amplitude parameters for each of the fill-scale gain corrections (IFG, STDP) are scanned. This process involves re-applying the corrections on the crystal level and re-clustering, which takes significant computation time. The difference in $R(\omega_a)$ from varying these parameters by 1σ is taken as the systematic.

Pileup As an initial estimate, the pileup correction is applied with a scaling factor ranging from 0-2× its nominal value. The fit is performed at each of these points, and the value of $R(\omega_a)$ and χ^2 are recorded. The $\Delta R(\omega_a)$ due to changing the pileup multiplier by a factor corresponding to ± 1 unit of χ^2 ($\pm 1\sigma$) is taken as the uncertainty. Results consistent with those found in Run-2/3 [84] have been obtained from these preliminary scans in Run-4. More detailed scans of the pileup correction parameters — which require re-clustering the raw data in a manner similar to the Gain analysis above — are in progress.

Muon Loss The portion associated with contamination is described in the text (Section 6.2.1). The portion associated with $K_{\text{loss}} < 0$, which was required for the Run-3 analysis, appears[8] to no longer be necessary in Run-4+.

CBO Model Different CBO models, each consistent with sliding window fits to the data, are incorporated into the main fit. Any model that results in a $\chi^2 \leq \min\left(\chi^2\right) + 3$ is accepted as a 'valid' description of the CBO behavior. The $\Delta R(\omega_a)$ between valid models is taken as the uncertainty. This is done for both the envelope and frequency portions of the fit.

y/VW Model The vertical terms can be perturbed in the same way as the CBO. This was not done in Runs 1-3, but will be required in Run-4+ due to the increased prominence of these frequencies and higher statistics. These are expected to be small.

Coupled x/y Model Differences in $R(\omega_a)$ will be assessed from reasonable perturbations of the cross term model. These include the addition of the $y \pm$ CBO terms,any terms from the non-exponential portions of $\mathcal{E}_{\text{cbo/vw/y}}$, and allowing the lifetimes or frequencies of the cross terms to float. These are expected to be small as well.

Residual Gain Correction (RGC) Described in the text (Section 5.4.2.1)

In Table 6.4, the BD (CBO, VW, and x/y) and RGC systematics have all been flagged (🚩) as areas where change from the Run-2/3 values is possible (in the author's estimation). The effect of the RF on the CBO and y oscillations in Run-5+ (discussed briefly in Chapter 7) will necessitate

---

[8] If K_{loss} returns to a value < 0, the uncertainty will be assessed as it was in Run-3: fixing $K_{\text{loss}} \equiv 0$ and taking the $\Delta R(\omega_a)$ from a 2σ region of a χ^2 scan of K_{loss} vs. τ_a as the uncertainty.

Category	Systematic	Run-2	Run-3a	Run-3b	Run-4 (Expectation)	Run-5/6 (Expectation)
Randomization	—	4	3	4	$\sim$	$\sim$
Gain	IFG amplitude	2.8	3.3	5.5	$\sim$	$\sim$
	STDP amplitude	1	1	1	$\sim$	$\sim$
Pileup	Amplitude	1	1	1	$\sim$	$\sim$
	Time/energy bias	2.5	1.8	2.1	$\sim$	$\sim$
	Rate error	1.5	0.2	0.8	$\sim$	$\sim$
Muon loss	Contamination	—	—	—	3.5	$\mathcal{O}(1\,\text{ppb})$
	K_{loss} negativity	—	11	9	—	—
CBO Terms	$\omega_{\text{cbo}}(t)$	3.6	7.9	6.4	$\sim$	⬇️🚩
	$\mathcal{E}_{\text{cbo}}$	12	13	16	$\sim$	⬇️🚩
y/VW Terms	$\mathcal{E}_{\text{y}},\ \mathcal{E}_{\text{vw}}$	—	—	—	$\mathcal{O}(2\,\text{ppb})$	$\mathcal{O}(2\,\text{ppb})$
	$\omega_{\text{y}}(t),\ \omega_{\text{vw}}(t)$	—	—	—	$\mathcal{O}(2\,\text{ppb})$	$\mathcal{O}(2\,\text{ppb})$
Coupled x/y	$y \pm$ CBO Addition	—	—	—	$\mathcal{O}(1\,\text{ppb})$	$\mathcal{O}(1\,\text{ppb})$
	$\mathcal{E}$ cross terms	—	—	—	$\mathcal{O}(5\,\text{ppb})$ 🚩	$\mathcal{O}(5\,\text{ppb})$ 🚩
RGC	—	8	5	12	4 🚩	⬇️🚩

Table 6.4: Expected values for the various systematic uncertainties in the ω_a analysis evaluated for Runs 2-6. All values here are given in terms of a ppb change on $R(\omega_a)$. Where numbers are not yet available, the author has indicated whether the expectation is that the value will increase (⬆️), decrease (⬇️), or remain approximately the same ($\sim$) compared to the Run-2/3 value. Areas where there is potential for a major difference, pending ongoing investigations, are indicated additionally with 🚩. Estimates as of March 2024.

new techniques for evaluating these uncertainties, which could in turn result in slight differences in the final values. Similarly, new ideas to assess and correct for the residual slow effect present in the data may lead to a change in the nominal procedure compared to Runs 1-3. Work on all of these studies is expected to complete by the end of 2024. The overall scale of these uncertainties is expected to remain small.

Chapter 7

Investigations in Progress for Run-4+

As it has been the main focus of the author in the months leading up to this thesis, the behavior seen in the Run-4 dataset has been presented as the ‘nominal’ set of conditions. In this chapter, some notable differences between the Runs are summarized and a picture of ongoing studies are presented. This chapter is indented to represent the current ‘state of play’ for the analysis, and to give a look towards the future work which will encompass the next steps of the analysis.

7.1 Prominence of Vertical Frequencies in Run-4 vs. Run-2/3

The prominence of the y-oscillation is greater in Run-4 than in previous runs. This can be seen in the five-parameter fit residuals (Figure 7.1a) and the amplitude of the ω_{y} peak in the residual FFTs (Figure 7.1). ω_{y} is most prominent in the calorimeters in the kicker region of the ring (Figure 5.14b). Acceptance of positrons born at large y is highly calorimeter dependent (Figure 5.11), and since calorimeters in the kicker region have the most uniform vertical acceptances they experience the largest enhancement.

One hypothesis to explain this increase in the prominence of ω_{y} is that the increased kick strength post Run-3b increased the vertical phase space available to the stored beam. When the beam is centered, a greater number of particles with large vertical betatron amplitudes can be stored without impacting the collimators. On the other hand, the vertical oscillations are not nearly as pronounced in Run-3b, which had an identical kick. This can be seen in Figure 7.2, where the calorimeter-by-calorimeter fitted amplitudes of the leading beam dynamics frequencies are compared. In these fits, the values of A_{cbo} are nearly identical across Run-3b and Run-4 while the values of A_{y} are quite different. The lower statistics in Run-3b can make drawing definitive conclusions difficult, but it is implausible that this difference could arise solely due to statistical effects.

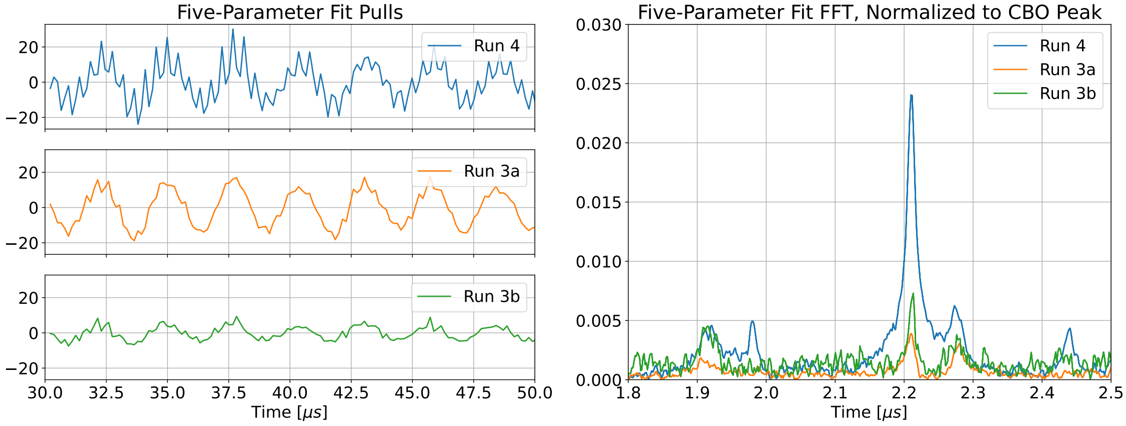

(a) **(b)**

Figure 7.1: Comparisons of the five-parameter (a) pulls (residuals / bin errors) and (b) FFTs for Run-3a, 3b, and Run-4. The magnitude of the vertical oscillations clearly increased between Run-3 and Run-4.

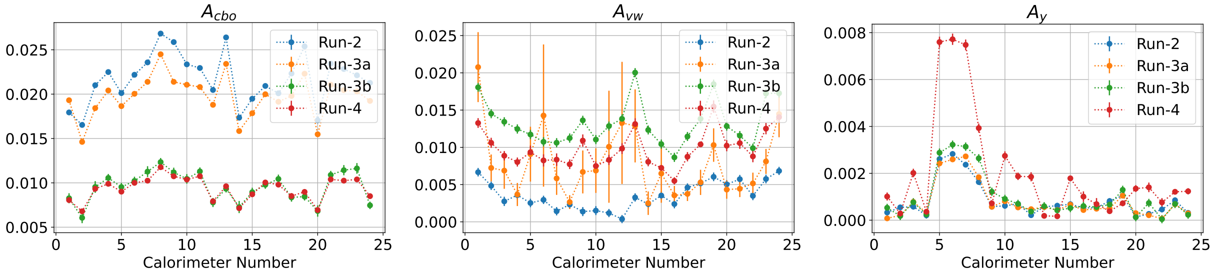

(a) **(b)** **(c)**

Figure 7.2: Comparison of the (a) CBO, (b) VW, and (c) y oscillation amplitudes in Runs 2-4. Clearly, the value of A_{y} is much more pronounced in the Run-4 kicker calorimeters than in previous runs. Run-2/3 values are taken from the work presented in reference [84].

One additional change which took place at the start of Run-4 was the modification of the surface coil settings to cancel the average radial field of the $g-2$ storage ring [176, 177]. While the radial field of the $g-2$ storage ring can not be measured directly by the NMR systems[1], the azimuthally averaged radial field can be measured by varying the ESQ HV while injecting an artificial radial field using the surface coil system. When the mean vertical position of the beam is independent of the ESQ HV, the average radial field is 0. The radial field at the start of Run-4 was found to be $\langle B_r \rangle = 15 \pm 1\,\mathrm{ppm}$. Using this measurement, the surface coil setpoints were tuned to remove this average field, and subsequent measurements with these changes found $\langle B_r \rangle = 0.4 \pm 0.6\,\mathrm{ppm}$. This process displaced the beam vertically by $\approx 1\,\mathrm{mm}$ [176]. Simulation studies are ongoing with updated kicker settings and radial field measurements to further investigate the effect of this change on the vertical oscillations seen by the calorimeters.

7.2 Impact of the ESQ RF in Run-5 on the BD Frequencies

The ESQ RF system described in Section 3.3.2 was activated starting in DS-5B. The resulting reduction in the prominence of the ω_{cbo} and ω_{y} frequencies can be seen in both the five-parameter fit residuals (Figure 7.3) as well as in the fitted amplitudes for each of the envelope functions (Table 7.1). The goal of the RF was to reduce the impact of the beam dynamics oscillations on the value of $R(\omega_a)$. The success of this effort is exemplified by comparing the difference in the value of $R(\omega_a)$ obtained when performing a fit with the five-parameter fit model and the five-parameter + CBO fit model in Run-4 and Run-5a:

$$\Delta R(\omega_a)|_{\text{CBO, Run-4}} = 856.4\,\mathrm{ppb} \tag{7.1}$$

$$\Delta R(\omega_a)|_{\text{CBO, Run-5a}} = 86.8\,\mathrm{ppb}. \tag{7.2}$$

This order of magnitude reduction in the impact of the BD frequencies on $R(\omega_a)$ similarly reduces the impact of the systematic uncertainties associated with the modelling of these terms.

The introduction of the ESQ RF was not without some side effects, however. While the BD terms in the calorimeter-summed data can still be adequately described by an exponential decoherence envelope, some fits to the individual calorimeters fail to converge with this parameterization.

---

[1] A full azimuthal map was measured using a specialized trolley and a 3-axis Hall probe before the installation of the vacuum chambers in 2016. This measurement was not able to be repeated with the vacuum systems in place [95].

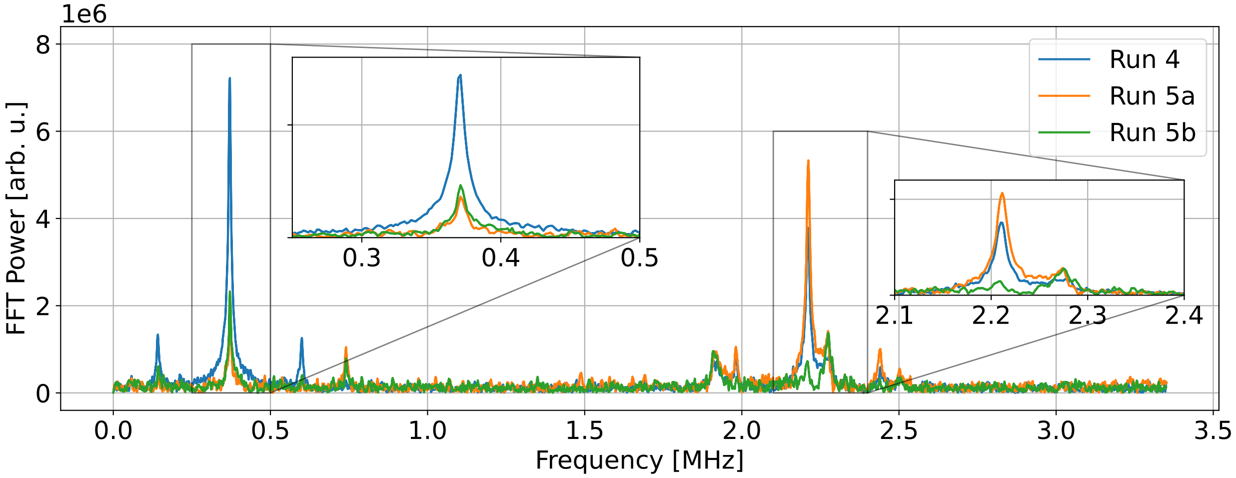

Figure 7.3: Comparison of the five-parameter fit residuals for Run-4, Run-5a, and Run-5b.

Dataset	Conditions	A_{cbo}	A_{y}	A_{vw}
4	No RF	1.43e-03	1.77e-03	9.14e-04
5a	x RF	**2.01e-04**	1.44e-03	3.43e-04
5b	xy RF	**2.48e-04**	**3.26e-04**	6.85e-04

Table 7.1: Fitted T-Method amplitudes of the BD frequency envelopes for Runs 4, 5a, and 5b. The reduction in amplitude due to the xRF and xyRF are highlighted. These values are taken from the fits in Figures 5.28 and 7.5.

Acceptance differences between the calorimeters, magnified by the overall decrease in the CBO amplitude, cause differences in the overall decoherence seen by the different detectors. The late time recoherence behavior of the CBO is also quite different in Run-5 compared to non-RF runs. Sliding window fits of the calorimeter-by-calorimeter envelopes are shown in Figure 7.4. In these fits, a constant A_{cbo} is assumed, ω_{cbo} is fixed to its value from the nominal fit, and a fit is performed in a window of 3 CBO periods. Using this method, the shape of the amplitude changes can be mapped out over the course of the fill without assuming any particular model. Some calorimeters remain well described by an exponential envelope, whereas others prefer a constant CBO amplitude or a decoherece/recoherence in the CBO over the course of the fill. These envelope functions are the subject of ongoing investigations across analysis groups.

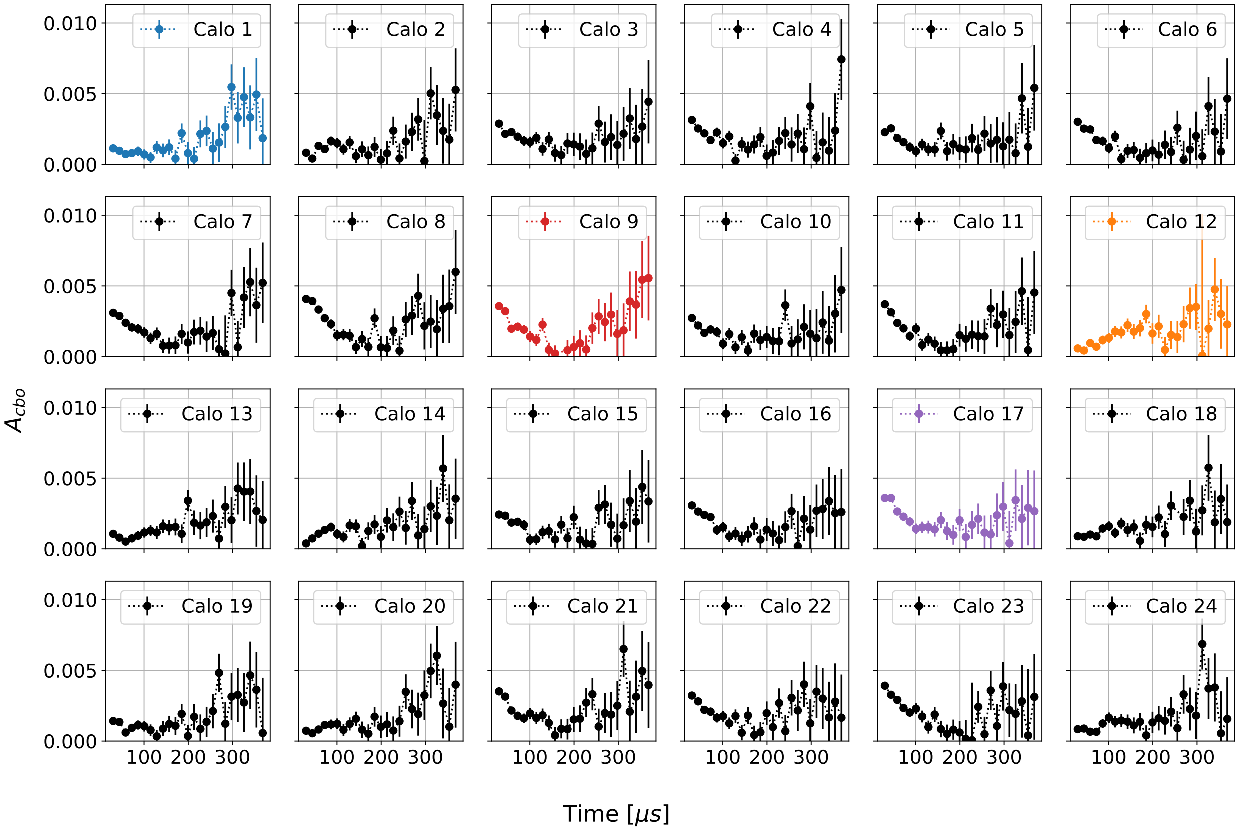

Figure 7.4: Sliding window fit results for the calorimeter-by-calorimeter fits in DS-5OR. In these fits, $\mathcal{E}_{\text{cbo}} = A_{\text{cbo}}$, and the data are fit in a time window of 3 CBO periods. Some calorimeters are highlighted as an example of the different CBO envelope behaviors: nearly flat (blue), de-/recoherence (red), exponential decay (purple), and growth (orange).

7.2.1 Preliminary Run-5 Analysis

Despite these challenges, an adequate 'Run-4 style' fit (with some limited modifications) can be conducted for Run-5 datasets. Preliminary fit results for Run-5a and 5b are shown in Figure 7.5. These fits show that, while work to understand the fine details of the Run-5 analysis is still ongoing, the majority of the changes necessary to the fit model are sub-leading order. A more detailed study of the BD envelopes will be required before these fits are finalized and comparisons across Run-4 and Run-5 can be performed.

7.3 Time Dependence of the CBO Frequency

As mentioned in Section 5.3.4, the measured CBO frequency is not constant over the course of each fill. This was especially true in Run-1, where changing ESQ voltages from damaged resistors dramatically altered the field index of the storage ring (and thus $\omega_{\rm cbo}$). In Runs 1-3, $\omega_{\rm cbo}(t)$ was incorporated into the UW ω_a fits as a fixed external input from the tracker (see Section 5.3.7.3). To measure this frequency change, the mean radial distribution from the tracker ($\bar{x}(t)$) was computed and a sliding window along the distribution was fit to the form:

$$\bar{x}(t) = A_i \cos\left(\omega_{\rm cbo,i} t + \phi_{\rm cbo,i}\right) + C_i, \tag{7.3}$$

The window for each fit i was $2-3$ CBO periods long, and incremented such that there was no overlap between adjacent points. From this, the phase advance relative to a constant frequency and phase was calculated:

$$\phi(t_i) = \omega_{\rm cbo,i} t - \phi_{\rm cbo,i}. \tag{7.4}$$

A model for the non-linear portion of the fit $\chi(t)$ is posited and the sliding window phase advance is fit to:

$$\phi(t) = \omega_{\rm cbo,0} t - \phi_{\rm cbo,0} + \chi(t). \tag{7.5}$$

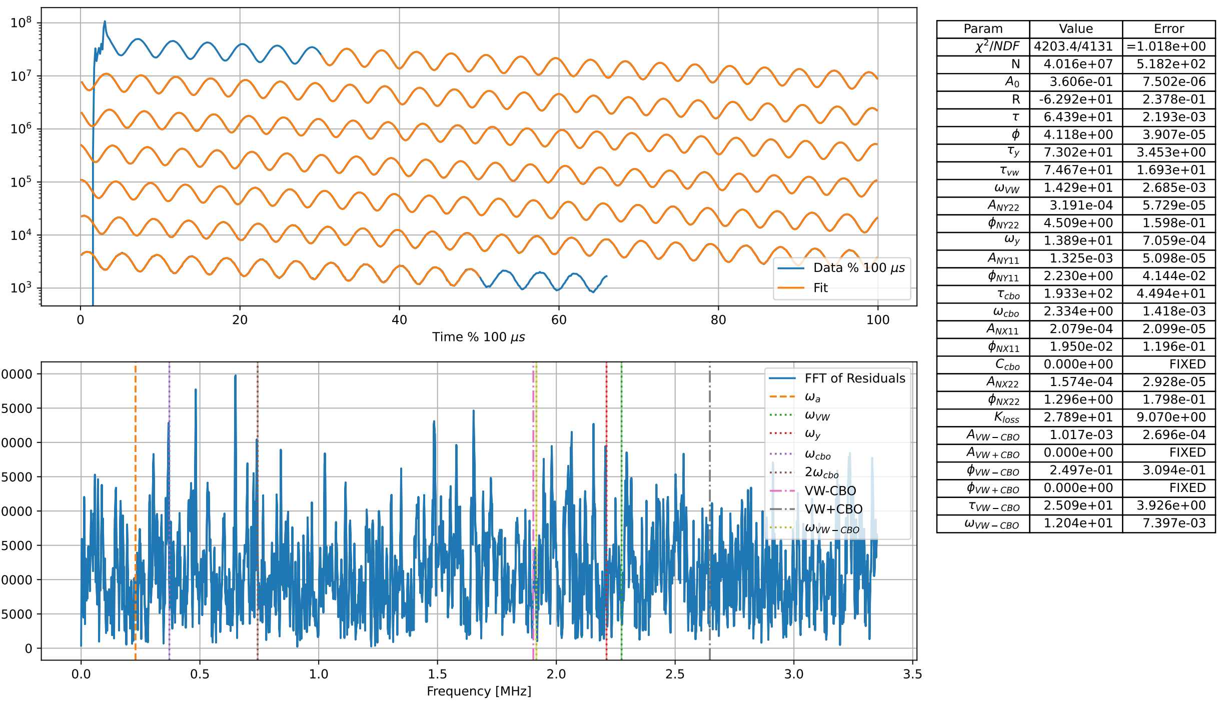

Param	Value	Error
χ^2/NDF	4203.4/4131	=1.018e+00
N	4.016e+07	5.182e+02
A_0	3.606e-01	7.502e-06
R	-6.292e+01	2.378e-01
τ	6.439e+01	2.193e-03
ϕ	4.118e+00	3.907e-05
τ_y	7.302e+01	3.453e+00
τ_{vw}	7.467e+01	1.693e+01
ω_{VW}	1.429e+01	2.685e-03
A_{NY22}	3.191e-04	5.729e-05
ϕ_{NY22}	4.509e+00	1.598e-01
ω_y	1.389e+01	7.059e-04
A_{NY11}	1.325e-03	5.098e-05
ϕ_{NY11}	2.230e+00	4.144e-02
τ_{cbo}	1.933e+02	4.494e+01
ω_{cbo}	2.334e+00	1.418e-03
A_{NX11}	2.079e-04	2.099e-05
ϕ_{NX11}	1.950e-02	1.196e-01
C_{cbo}	0.000e+00	FIXED
A_{NX22}	1.574e-04	2.928e-05
ϕ_{NX22}	1.296e+00	1.798e-01
K_{loss}	2.789e+01	9.070e+00
A_{VW-CBO}	1.017e-03	2.696e-04
A_{VW+CBO}	0.000e+00	FIXED
ϕ_{VW-CBO}	2.497e-01	3.094e-01
ϕ_{VW+CBO}	0.000e+00	FIXED
τ_{VW-CBO}	2.509e+01	3.926e+00
ω_{VW-CBO}	1.204e+01	7.397e-03

(a)

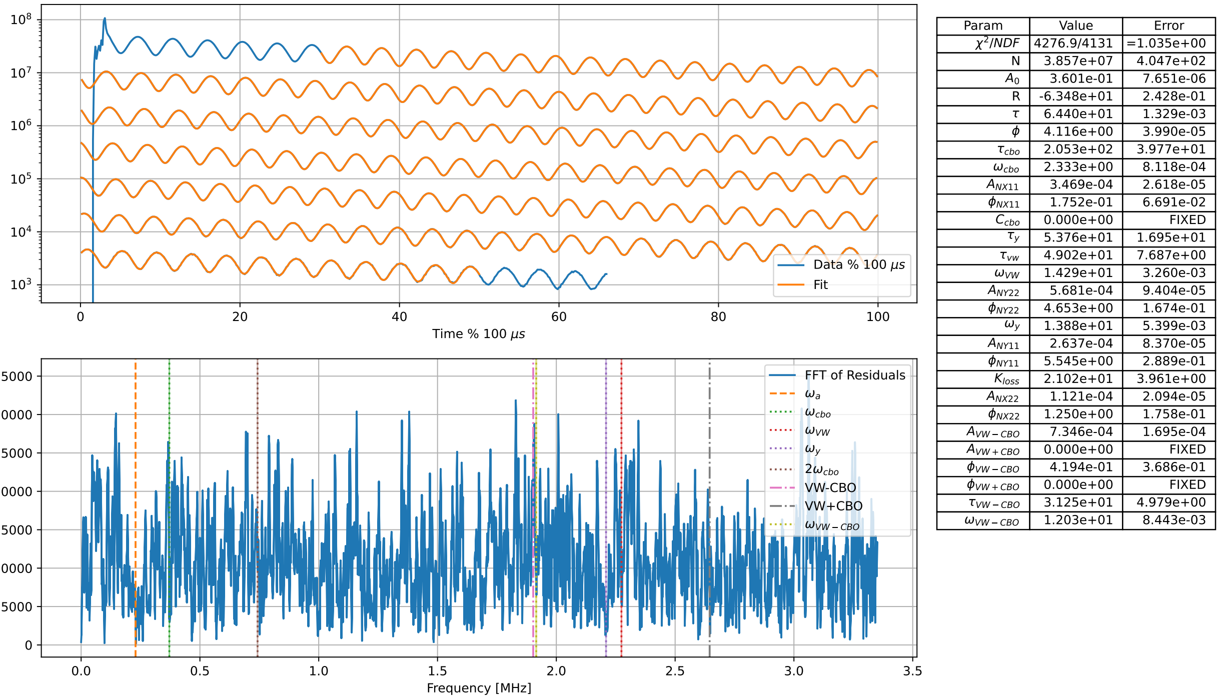

Param	Value	Error
χ^2/NDF	4276.9/4131	=1.035e+00
N	3.857e+07	4.047e+02
A_0	3.601e-01	7.651e-06
R	-6.348e+01	2.428e-01
τ	6.440e+01	1.329e-03
ϕ	4.116e+00	3.990e-05
τ_{cbo}	2.053e+02	3.977e+01
ω_{cbo}	2.333e+00	8.118e-04
A_{NX11}	3.469e-04	2.618e-05
ϕ_{NX11}	1.752e-01	6.691e-02
C_{cbo}	0.000e+00	FIXED
τ_y	5.376e+01	1.695e+01
τ_{vw}	4.902e+01	7.687e+00
ω_{VW}	1.429e+01	3.260e-03
A_{NY22}	5.681e-04	9.404e-05
ϕ_{NY22}	4.653e+00	1.674e-01
ω_y	1.388e+01	5.399e-03
A_{NY11}	2.637e-04	8.370e-05
ϕ_{NY11}	5.545e+00	2.889e-01
K_{loss}	2.102e+01	3.961e+00
A_{NX22}	1.121e-04	2.094e-05
ϕ_{NX22}	1.250e+00	1.758e-01
A_{VW-CBO}	7.346e-04	1.695e-04
A_{VW+CBO}	0.000e+00	FIXED
ϕ_{VW-CBO}	4.194e-01	3.686e-01
ϕ_{VW+CBO}	0.000e+00	FIXED
τ_{VW-CBO}	3.125e+01	4.979e+00
ω_{VW-CBO}	1.203e+01	8.443e-03

(b)

Figure 7.5: *Preliminary* first A-Method fits to (a) Run-5a and (b) Run-5b.

The linear portion of the fit is then subtracted for display. A schematic of this process is shown in Figure 7.6. The result of this analysis can be seen in Figure 7.7 for selected datasets from Runs

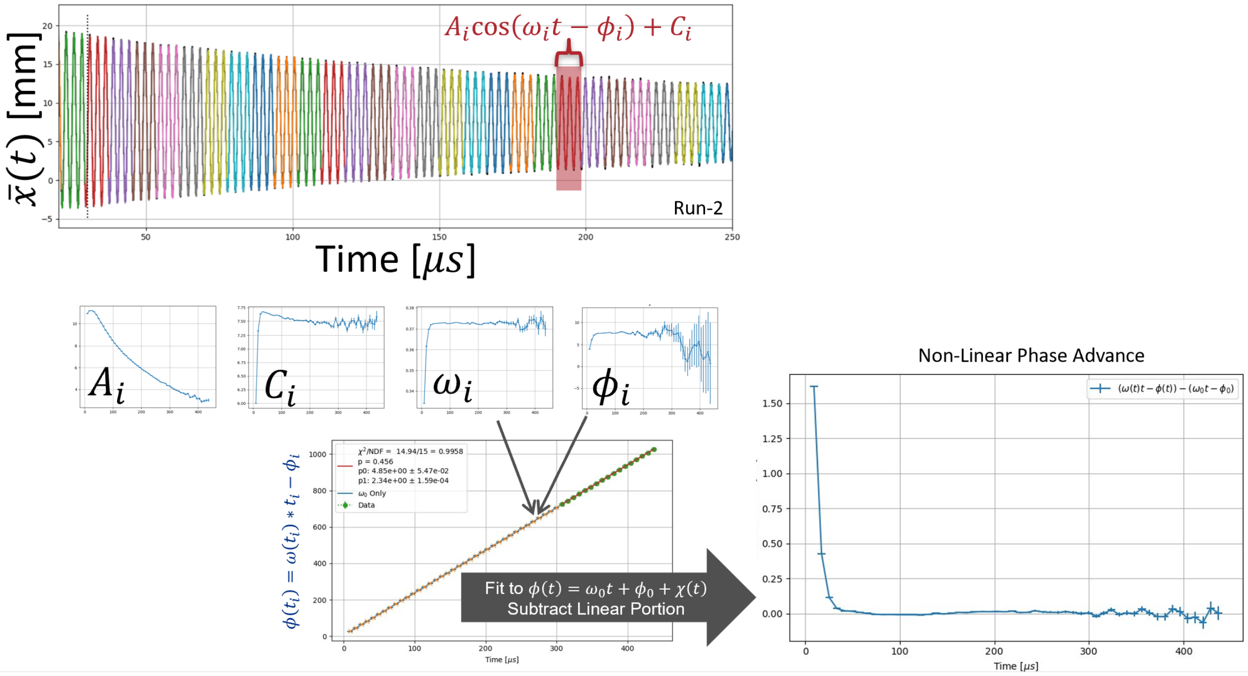

Figure 7.6: A diagram showing the extraction of the CBO phase advance from the radial profile. The average $x(t)$ distribution is divided up into windows, each of which are fit to the form in Equation (7.3). From these fits ω_{cbo,t_i} and ϕ_{cbo,t_i} are extracted. The resulting phase advance is fit to Equation (7.5) and the linear portion is subtracted for display. The data shown here are from Run-2.

1-5. Clearly, there exists very different CBO phase advance in each of these datasets.

It should be noted here that the choice of $\omega_{\text{cbo},0}$ and $\phi_{\text{cbo},0}$ have no a-priori physical basis. Therefore any linear function can be added to the distributions shown in Figure 7.7 to arrive at an equally 'correct' result. Fitting the $\chi(t)$ model at the same time as the linear phase advance was done in an attempt to reduce bias when interpreting the results of these sliding window scans. Alternatively, one coule assume a linear phase advance in some time region $(t_0, t_1]$, fit a linear function to only that region, and examine the shape of the residuals to interpret the non-linear portion of the phase advance. Figure 7.8 shows that the shape of such residuals can vary greatly depending only on the chosen values of t_0 and t_1, and thus how a bias can be introduced with such an approach. This underscores the fact that any model for the phase advance here must have some external input (another measurement, a physical model, etc.) to support it.

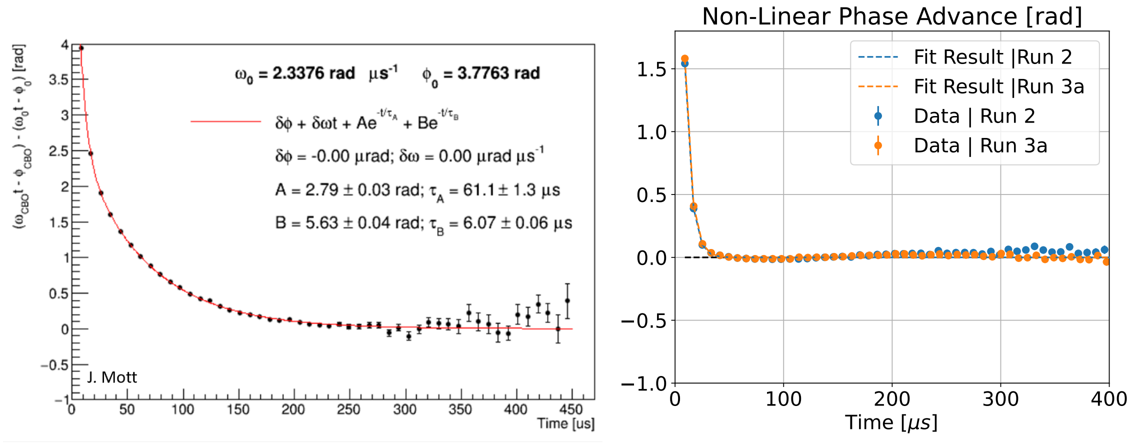

(a) Reproduced from [178].

(b)

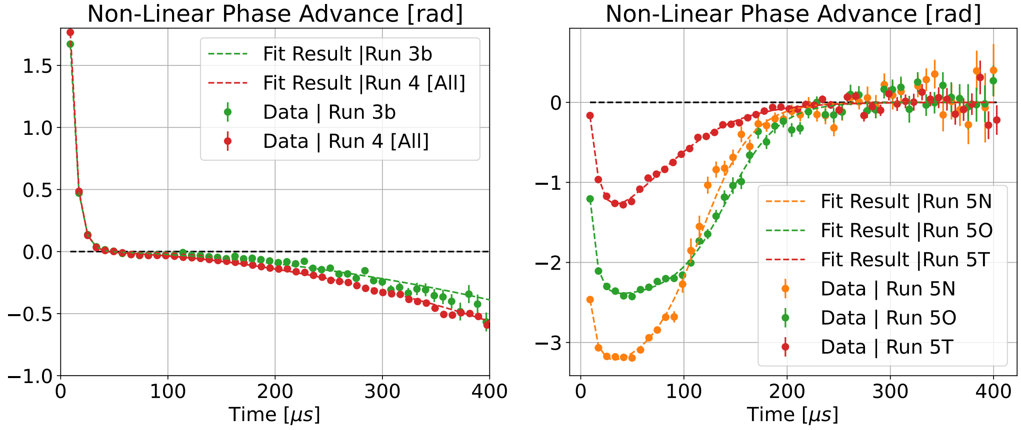

(c)

(d)

Figure 7.7: Non-linear CBO phase advance for (a) Run-1, (b) Run 2, (c) Run-3b/4, and (d) Run-5. The phase advance differs significantly from one Run period to another. The different $\chi(t)$ models used to fit these datasets are described in the text.

Here the various effects between runs are described, along with early modelling efforts which attempt to reconcile this behavior with the known beam dynamics of the system. In Run-2, a single exponential phase advance due to the ESQ scraping (Section 3.3.2) was sufficient to describe the observed behavior of $\omega_{\text{cbo}}(t)$ in all calorimeters:

$$\chi_{\text{scraping}}(t) = ae^{-t/t_a} \tag{7.6}$$

Some late time deviation in the non-linear portion of the fit from a pure exponential decay is visible,

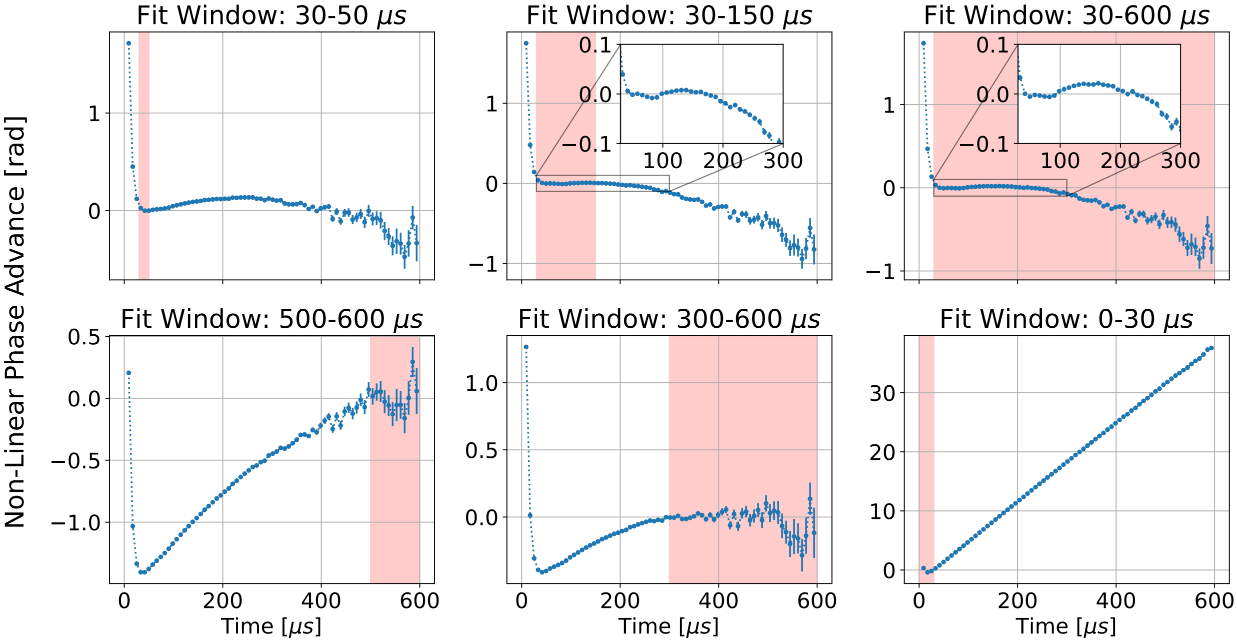

Figure 7.8: Residuals of a linear fit to the Run-4 tracker $\bar{x}(t)$ phase advance data when the fit is restricted to different ranges (indicated by the red bands). When this version of the analysis is used, the initial assumptions (i.e. is it assumed that the CBO is stable at late vs. early times) greatly impact the shape of the fit residuals. This has the potential to impact the interpretation of the data. Some of these choices are exaggerated to show the scale of the effect.

but was any reasonable threshold for concern in Run-2/3a.

7.3.1 Run-3b/4

In Run-3b and Run-4, significant, slowly-varying deviation from the simple scraping exponential was observed. Examination of the fit residuals motivated the addition of a quadratic term to the CBO frequency evolution:

$$\chi_{\text{Run-4}}(t) = \chi_{\text{scraping}}(t) + p_2 t^2 \tag{7.7}$$

The results of this fit can be seen in Figure 7.7c. This behavior is consistent across all of the datasets of Runs 3b-4.

The change in the CBO frequency can be interpreted as a slight drop (0.02 kV) in the ESQ voltage over the course of the fill ($\approx 3 * 10^{-5}\,\text{kV}/\mu\text{s}$). The electronic systems which maintain the voltage on the ESQ plates were built to a specification which allowed up to a 0.5% change in the voltage over 700 μs [76, 179]. A measurement was completed in 2017 which found a voltage *increase*[2] across the ESQ plates of less than this amount: ${}^{dV}\!/_{V} \approx 0.074\%/700\,\mu\text{s} \approx 1.9 * 10^{-5}\,\text{kV}/\mu\text{s}$ [180]. From these values, it can be concluded that such a drop in the ESQ voltage over the course of a single fill is, while unexpected, within reason. A measurement is planned post-Run-6 to determine the voltage drop across the ESQ plates over time vs. various running conditions (field, kicker HV, etc) to determine if this model holds and could potentially explain the difference from Run-3a→3b.

Pending the outcome of these investigations, a study was performed where the posited form of $\omega_{\text{cbo}}(t)$ was incorporated into the ω_a fit function:

$$\omega_{\text{cbo}} \rightarrow \omega_{\text{cbo},0} + \frac{a}{t} e^{-t/t_a} + p_2 t. \tag{7.8}$$

The value $p_2 \equiv -3.51 * 10^{-6}$ is obtained from the fits in Figure 7.7c. Implementing this function was found to shift $R(\omega_a)$ in DS-4AF by ≈ 1 ppb relative to the nominal $\omega_{\text{cbo}}(t)$ model, and resulted in a negligible decrease in the χ^2. This addition has not yet been incorporated into the nominal ω_a

---

[2] Such an increase was not unexpected, given the electronics of the ESQ pulser system.

fit function, but the systematic associated with the variable CBO may be inflated by this 1 ppb to encapsulate this effect.

7.3.2 Run-5

In Run-5, the behavior of the CBO phase advance is again quite different. The CBO extracted from $x(t)$ appears to experience a rapid change in phase anytime between 50 and 100 μs into the fill. The exact point in the fill where this change occurs and the difference between the early and late time phases differs from dataset to dataset. No difference in the general trends of the CBO frequency between the 5a and 5b datasets have been observed, indicating that the horizontal RF alone is the cause of this effect. A sliding window fit to a single Run-5 dataset (DS-5O) is shown in detail in Figure 7.9. From this, it is obvious that the CBO signal is still present at late times, and that this phase change is not simply a result of low statistics.

Across many datasets, it appears that at late times ($t > 300\,\mu$s) the phase advance seems to become nearly constant. Fitting the data to a single, constant frequency and phase works well at those late times. This observation led to the hypothesis that there exist two 'populations' of muons within the storage ring, each with slightly different CBO frequencies and/or phases: one that experiences a decoherence over the course of the fill and one that coheres at late times. Based on this hypothesis, a logistic[3] functional form was chosen entirely empirically to describe the data:

$$\chi_{\text{Run-5}}(t) = \chi_{\text{scraping}}(t) + \frac{L}{1 + e^{-k(t-t_0)}} \tag{7.9}$$

This model was found to fit the Run-5 data quite well across all Run-5 datasets. The value of $\phi_{\text{cbo}}(t)$ obtained with this functional form in Run-5 can be seen in Figure 7.7d. It has also been shown that the fitting the full time range of the $x(t)$ distribution directly with such a two population model can reproduce the observed non-linear behavior [181].

With slightly different values of $\omega_{\text{cbo},0}$ and $\phi_{\text{cbo},0}$, the Run-3b/4 CBO phase advance is also consistent with this model (see Figure 7.10), albeit with a smaller magnitude than is seen in Run-5.

---

[3] The logistic function is used to describe population growth towards a fixed plateau. The sigmoid function, commonly used in machine learning, is a generic case of the logistic function where $L = 1,\ k = 1,\ t_0 = 0$.

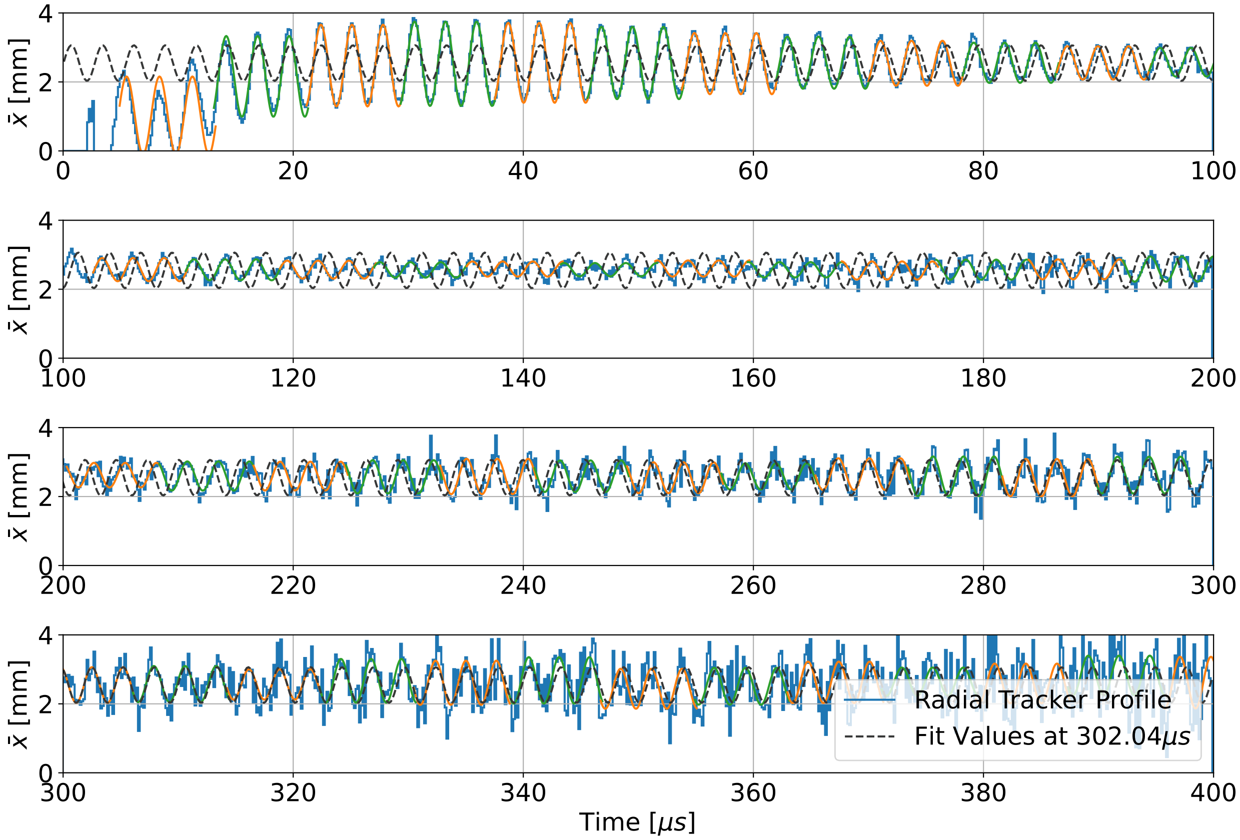

Figure 7.9: The CBO sliding window fit for the DS-5O tracker data. The fitted value at 300 μs is overlaid with the sliding windows of width $3/\omega_{\text{cbo}}$, to show the phase change over time in the fill. The ESQ scraping of the beam can be seen at early times.

The fact that both the models in Equations (7.8) and (7.9) describe the Run-4 data equally well again illustrates the fact that a good physical basis for any CBO phase advance model is required; simply arriving at a fit which describes the data is not sufficient[4].

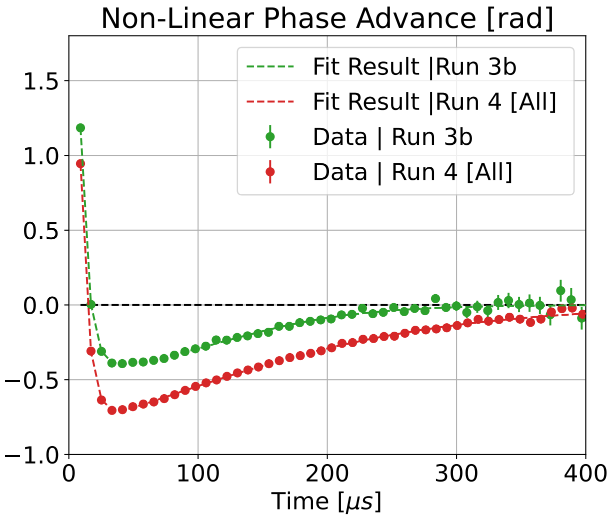

Figure 7.10: Non-linear fit result to the Run-3b and Run-4 data to the Logistic model in Equation (7.9). This model also provides a good description of the behavior of the non-linear CBO phase advance in these runs.

The physical reasoning behind there being two apparent populations of CBO behaviors in the ring is still under active investigation [183]. It is hypothesized that differences in the betatron oscillations of the muons could be introduced by a combination of the kicker and the ESQ RF systems, but it is premature to speculate further at the time of writing. High statistics simulations are in progress with Run-4 and Run-5-like conditions, which will help to disentangle the root cause of this variable CBO behavior.

Comparisons with calorimeter results are ongoing which will aid in this effort, although the calorimeters are less sensitive to the motion of the beam than the trackers. Such comparisons are complicated by the different acceptances of the different detectors, and between $x(t)$ and $N(t)$ measurements. Regardless of the outcome of these studies, the Run-5 CBO in general is suppressed by an order of magnitude relative to Run-4. Therefore any uncertainty on $R(\omega_a)$ arising from these new CBO effects will have a limited effect compared to the CBO in previous runs.

---

[4] We must be careful here to step lightly around Von Neumann's elephant [182].

7.4 Outlook

Run-4 in many ways remains an extension of Run-3b, and therefore many features present in this dataset have been explored and incorporated into the nominal fit model. The refinement of such models required for a final analysis is ongoing. The modelling of the unique BD behavior in Run-5+ provides a challenge for the completion of the final $g-2$ analysis. In particular, the per-calorimeter dependence of the BD envelope functions mean that additional work is required in order to perform some of the same cross-checks described in Section 5.4. The nominal analysis flow may need to be altered to accommodate this fact, incorporating more inputs from systematic studies (sliding windows, calorimeter-by-calorimeter fits, etc. which are more sensitive to the BD terms) into the main fit. An excellent team of analyzers from across the collaboration has been assembled and is actively tackling the challenges laid out in this chapter and in Section 5.5.1. Every technique used in the previous publications is being heavily scrutinized before the next (final) release. Work on the ω_a analysis is on track to be completed by the end of 2024.

Chapter 8

Conclusion

This thesis has presented the current status of the UW analysis of the final runs of the Muon $g-2$ Experiment at Fermilab. Runs 1-3 of the experiment have been published and have a yielded a total uncertainty of 203 ppb (with ≈ 182 ppb arising purely from statistics) on the value of a_μ [17]. Analysis of the remaining data from Runs 4-6 ($\approx 73\%$ of the total data collected) is well underway and is expected to yield a final statistical uncertainty of < 100 ppb (Table 8.1).

Dataset	Individual Precision [ppb]	Cumulative Precision [ppb]
Run 1	434	—
Run 2	337	267
Run 3	248	182
Run 4*	184	129
Run 5*	168	102
Run 6*	269	96

Table 8.1: A-Method precision (*statistical-only*) on ω_a for each Run year individually, as well as the cumulative statistical gains from each additional year of running. The values indicated with an asterisk have not been finalized and may change if the DQC cuts for any of the datasets are altered significantly.

It is expected that, once systematic uncertainties are fully evaluated, the experiment is well positioned to meet or better its stated goal of 140 ppb uncertainty on a_μ. While a number of avenues of study remain, no issues have yet been noted which are expected to significantly delay the results nor alter conclusions reached in previous analyses.

8.1 BSM Speculation

Up to this point, speculation regarding the implications of the measurement has been avoided due to the tumult in the SM calculations. However, the potential of Muon $g-2$ as a signal for physics beyond the standard model bears some discussion. This section is presented with the caveat that it likely will be outdated by the end of the year in which this document is published.

Assuming that the $\Delta a_\mu \equiv a_\mu^{\mathrm{exp}} - a_\mu^{\mathrm{SM}}$ calculated from the WP20 SM evaluation holds for the moment, the contribution to a_μ from physics beyond the standard model is:

$$a_\mu^{\mathrm{BSM}} \approx 1.5 \times a_\mu^{\mathrm{EW}}. \tag{8.1}$$

Because of their similar scale, it is useful to think of potential BSM models as scaling relative to the EW contribution. In a large variety of models of BSM physics[1], the contribution to a_μ scales like:

$$a_\mu^{\mathrm{BSM}} \propto a_\mu^{\mathrm{EW}} \times \left(\frac{M_{\mathrm{W}}}{M_{\mathrm{BSM}}}\right)^2 \times [\text{couplings}]. \tag{8.2}$$

This implies that the BSM signal in a_μ arises from either:

- Rather light, electrically-neutral particles which benefit from a large enhancement due to the ratio of masses in Equation (8.2) (while evading traditional detection efforts).
- Some other mechanism with a heavy mediator and a large enhancement to its coupling (chirality flipping, muophilic interactions, etc.)

An excellent review of BSM models which are compatible with the this value of Δa_μ can be found in reference [184]. Most 'simple' extensions of the SM have been largely excluded, and current models require some fine tuning of parameters to avoid constraints from detector experiments. Some of the notable models which have been explored include:

Axion Like Particles (ALPs) While the QCD Axion was originally proposed as a solution to the strong CP problem, a wide range of 'axion-like' particles are a good candidate for dark

---

[1] Those with so-called 'natural scaling'

matter and solutions to various anomalies in the SM. Because of their (potentially) low mass, this class of BSM particles can benefit from a large mass enhancement [185].

Two-Higgs Doublet Extensions of the standard model with an additional Higgs doublet have been motivated by supersymmetry, as well as explanations for the observed baryon asymmetry of the universe [186]. This is one of the only remaining single-field extensions of the SM which can explain a_μ while remaining consistent with collider limits (in a limited parameter space) [184, 187, 188].

Leptoquarks Scalar muophilic leptoquarks — particles which carry both color charge and lepton number — can explain Δa_μ while evading constraints from $\mu \to e\gamma$ limits and direct detection at the LHC in limited mass ranges [184]. Many models were proposed which could simultaneously explain Δa_μ and the reported B-anomalies from the LHC, but such models have fallen by the wayside in the last few years as the latter has been resolved.

Supersymmetry There remain versions of the Minimally Supersymmetric Standard Model (MSSM) which can evade constraints placed by the LHC. In some versions of these models, both Δa_μ and the relic dark matter density can be explained as one [184]. The grey band in Figure 8.1 corresponds to a range of generic SUSY models with $5 < \tan(\beta) < 50$.

As the constraints from other experiments become more strict in the coming years, many of these models will continue to be excluded.

In light of the tension between the updated lattice results and the R-Ratio calculations of a_μ^{HVP} the following question can also be asked: is it possible that the experiment and the lattice HVP results are correctly describing the SM, but there exists BSM physics ‘hiding’ in the e^+e^- collider data? Comparisons between data-driven and lattice results have found that the discrepancy between the two lies primarily in the low-energy regime, where the available parameter space for new physics is even more limited than for the standard interpretation of Muon $g-2$ results. Most models for new physics in that region are already excluded by existing experimental constraints [189, 190]. Within these severe bounds some possibilities remain, an example of which can be found in reference [191].

Finally, assuming there is no new physics in the e^+e^- collider data and the lattice (or CMD-3) results for a_μ^{HVP} hold[2], the value of Δa_μ does not go entirely to 0. This can be seen in Figure 8.1. The significance of the signal in Δa_μ drops from $> 5\sigma$ to $\approx 1.8\sigma$. The blue band represents the value of Δa_μ calculated between the experimental average and the WP [1] while the orange band represents the value of Δa_μ found when replacing $a_\mu^{\text{HVP, LO}}$ with that calculated by the BMW collaboration [56]. The values of the BSM mass scales preferred by the lattice value are generally pushed higher by this decrease in Δa_μ. Should this reduced discrepancy hold, it could serve as motivation for a next generation $g-2$ experiment to probe this smaller difference with an even greater precision (see Section 8.2).

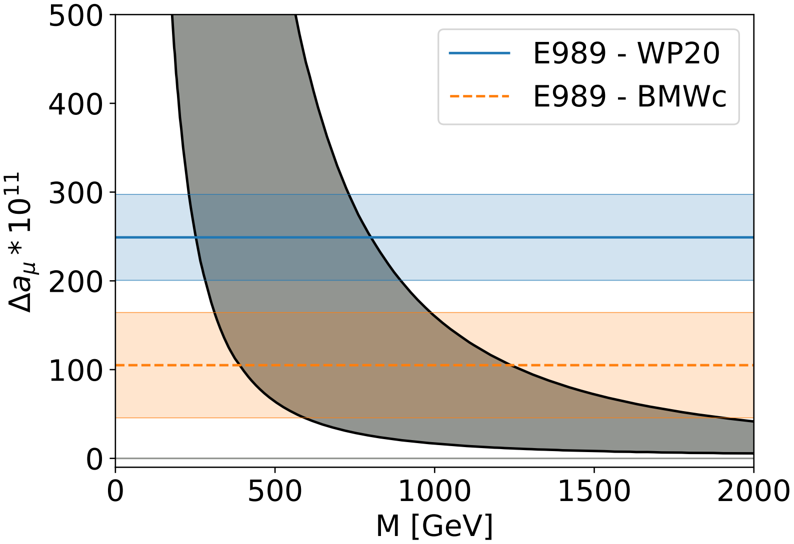

Figure 8.1: Illustration of the compatibility of the values of Δa_μ from the WP [1] (blue) and from the BMW lattice evaluation of a_μ^{HVP} [56] (orange) with a range of BSM models. The grey band represents models like supersymmetry with a large enhancement ($5 < \tan(\beta) < 50$). From these curves, it can be seen that the value of Δa_μ compatible with the lattice result generally pushes the mass scale of new physics higher. BSM curves are adapted from [192] (in this reference they were courtesy of D. Stöckinger).

The outcome of the theoretical questions detailed in Section 2.2 will hopefully be resolved in the next few years. Once that is complete, the comparison between Muon $g-2$ experiment and theory will once again be able to act as a strong test of the standard model of particle physics.

---

[2] As mentioned in Section 2.3.4, new inputs from the MUonE experiment and τ decay measurements will become available in the coming years, which may help to provide clarity in this area of the theoretical calculation.

8.2 A Next Generation Muon $g-2$ Experiment

The Run-4+ results from the Muon $g-2$ Experiment at Fermilab will likely be the final word on the anomalous magnetic moment of the muon for the next decade or more. The E34 J-PARC experiment will provide an excellent, independent test of the measurement technique, but the technique employed there is unlikely to be able to be competitive with storage ring results in the near future. In the coming years, as exascale computational facilities become available, it is highly probable that lattice-based calculations of a_μ^{HVP} and a_μ^{HLbL} with uncertainties at the $< 50\,\text{ppb}$ level can be achieved. Since these quantities are the main drivers of the theoretical uncertainty, this would allow for a strong test of the standard model even considering the reduced difference between a_μ^{SM} and a_μ^{exp} shown in Figures 2.10 and 8.1. Soon after the conclusion of the BNL E821 Muon $g-2$ experiment, members of that collaboration came together to imagine what a next generation $g-2$ measurement would look like. The Fermilab E989 experiment was born in large part from those discussions. Asking a similar question now is interesting as a thought experiment[3].

It is useful to choose a (somewhat arbitrary) goal of a final uncertainty of 60 ppb on $\mathcal{R}$ — more than a factor of two improvement from the projected E989 final uncertainty[4]. Following the argument in the E989 proposal documents, this can be divided this evenly into a statistical and systematic portion, and the systematic portion divided further between ω_a and ω_p (as shown in Table 8.2). Each of these are assumed to be totally uncorrelated.

Category		**Budget [ppb]**
Statistical		42.4
Systematic	ω_a	30
	ω_p	30
Total		60

Table 8.2: Proposed statistical and systematic error budget for a next generation Muon $g-2$ experiment.

---

[3] The values here are presented with the caveat that they represent only the speculations of the author. A survey of 50 members of the collaboration would likely return 50 distinct ideas about how such a next generation experiment could be performed.

[4] One could, of course, be more aggressive. This number is useful to set the scale of needed improvements, but should not be taken as a limiting factor. From Figure 8.2b, the impact of either additional statistics being accumulated or additional improvements in the systematics can be assessed. This can then be compared to the tensions in Figure 8.3.

The total systematic uncertainty for Runs 2 and 3 of the current experiment was 70 ppb: 25 ppb from ω_a systematics, 40 ppb from ω_a correction terms ($C\_$, see Section 3.6.3), 46 ppb from $\tilde{\omega}_p$, and 24 ppb from ω_p correction terms ($B\_$, see Section 3.6.1). For a 60 ppb measurement to be possible, each of these contributions would need to be reduced by a factor of two or more. Table 8.3 shows the largest contributions from each of the error tables for each of those contributions.

Systematic		Uncertainty [ppb]
ω_a	CBO Handling	**21**
	Slow Effects	10
$C\_$	C_e	**32**
	C_p	10
	C_{pa}	13
	C_{dd}	**17**
ω_p	Probe calibration	**17.8**
	Motional trolley effects	**18**
	Ring configuration changes	**22**
	Temperature dependence	9−15
	Field tracking	**16−17**
$B\_$	B_q	**19.5**
	B_k	13.3

Table 8.3: Largest ($>$ 10 ppb) individual contributions to the various categories of systematic uncertainties in the Run-2/3 measurement. Values reproduced from tables in [17].

The easiest way to reduce the systematic uncertainty of the measurement — albeit at a heavy statistical cost — is to restrict the diameter of the storage region. Many of the largest systematics in the experiment couple to the width of the stored beam in some way:

- C_e and C_{dd} are both directly proportional to the spread of momenta in the storage ring. Reducing the width of the storage region decreases this spread and directly reduces the corresponding uncertainties.
- C_p is proportional to the average amplitude of the vertical oscillations of the beam. Decreasing this amplitude similarly decreases the magnitude of the correction and its uncertainties.
- C_{pa} is driven by differences in acceptance between different muon decay locations. These differences are greatest near the edges of the current storage region.
- The largest uncertainties in the ω_a analysis are related to the CBO and other beam dynamics

effects. Muons with large CBO/vertical oscillation amplitudes would not be compatible with storage in this updated configuration, thereby reducing these systematics.

- Reducing the radius of the storage region while keeping the same size ESQ plates will reduce the effects of any non-linearities in the E field. These non-linearities alter the effective field index of the ring at large amplitudes and contribute to the decoherence of the CBO over time.
- Without any adjustments to the ring, the uniformity of the magnetic field over a smaller storage region is more uniform. From this alone, the uncertainties in $\tilde{\omega}_p$ can be reduced. With a smaller storage region to focus on, improved passive shimming of the magnetic field could also yield an average uniformity beyond what was achieved at E989.

Other systematics could be reduced with a next-generation upgrade to the associated hardware:

Optimized Kicker The ringing tail of the kicker pulse was responsible for large portions of B_k, and can also influence the BD corrections through unintentional residual kicking of the stored beam. A next generation design of the kicker electronics could aid in reducing these uncertainties.

Optimized ESQ System Optimized placement of standoffs to reduce sparks and vibrations can be employed in a new ESQ system. Investigations into different modes of ESQ pulsing (different patterns, RF-Only scraping, etc.) can be undertaken to reduce the impact of B_q in the next experiment.

Additional Fixed NMR Probes The position and layout of the fixed NMR probes (above/below the ESQ plates, far from the muon storage region) results in a limited ability to track the field in the muon storage region. These limitations can be addressed with additional fixed NMR probes placed within the vacuum chamber of the storage ring. Such probes within the vacuum chambers, or even within the ESQ boundaries[5], arranged as to be sensitive to higher-order multipoles would potentially reduce interpolation related uncertainties and could reduce the frequency at which trolley runs are required.

---

[5] Pulsing the ESQ system with such obstacles in place would be a challenge and require (at the very least) a vacuum pressure and order of magnitude lower than in the current generation experiment.

Updated Trolley System A large contribution to the overall uncertainty on the magnetic field extraction came from trolley system itself — motional effects, temperature variations, etc. [17]. An updated trolley system would likely be required to accommodate the changes to the storage region layout, and many of these systematics could be addressed in such an update.

Improved Proton Bunch Shaping Restricting the time width of the proton bunches (and thus the muon bunches) can reduce the value of $C_{dd}^{p-t_0}$. The E989 bunches were $\approx 120\,\text{ns}$ long (almost one full cyclotron period of the ring). Cutting this width in half with improved RF shaping in the recycler ring (or equivalent) would aid in all uncertainties related to the non-uniformity of the kicker pulse over the length of the injected bunch.

Presuming that these improvements are possible, the accumulation of data can be considered. The curve of number of measured positrons vs. the increase in statistical power is shown in Figure 8.2a. From this it can be seen that such an experiment would be able to reach its statistical goal after accumulating 5.5× the Fermilab statistics. The statistical 'hit' from the reduced beam aperture compared to the current generation experiment would need to be compensated for in order for this accumulation to happen in a reasonable time frame. This could be done in a number of ways:

Earlier Fit Start Time Replacing traditional ESQ scraping (physically moving the beam centroid) with RF scraping alone could yield a more stable beam earlier in the fill, allowing the start time to be pushed back and more stored muons to be included in the fit range.

Improved Injection Efficiency The upgraded inflector magnet designed for this generation $g-2$ experiment could be employed in the next, allowing for lower scattering of the muon beam and a $\approx 20\%$ greater flux of muons injected into the storage ring.

Increased Fill Rate The fill structure of the $g-2$ experiment (as seen in Figure 3.3c) is rather inefficient. To accommodate other users of the Fermilab accelerator complex, the E989 Muon $g-2$ program takes only 4 out of 20 available batches of protons, resulting in 16 muon bunches each 1.4 second booster cycle ($\approx 11.4\,\text{Hz}$). The maximum rate which is compatible with the current operation of the experiment (roughly 1 ms of muon fill combined with 1 ms of recovery) is 500 Hz. The E989 fill rate could therefore be increased significantly without any impact to the systematics of the experiment, nor any significant changes to the E989 operational mode.

Increased Beam Flux An increase in the number of protons on target[6], or an increase in the efficiency of the conversion of protons into stored muons[7] would be required for such a next generation experiment to be able to accumulate statistics efficiently. The $g - 2$ calorimeters were designed for pileup at double the rate at which they were operated. A slight increase in instantaneous rate can easily be accommodated in a next-generation experiment.

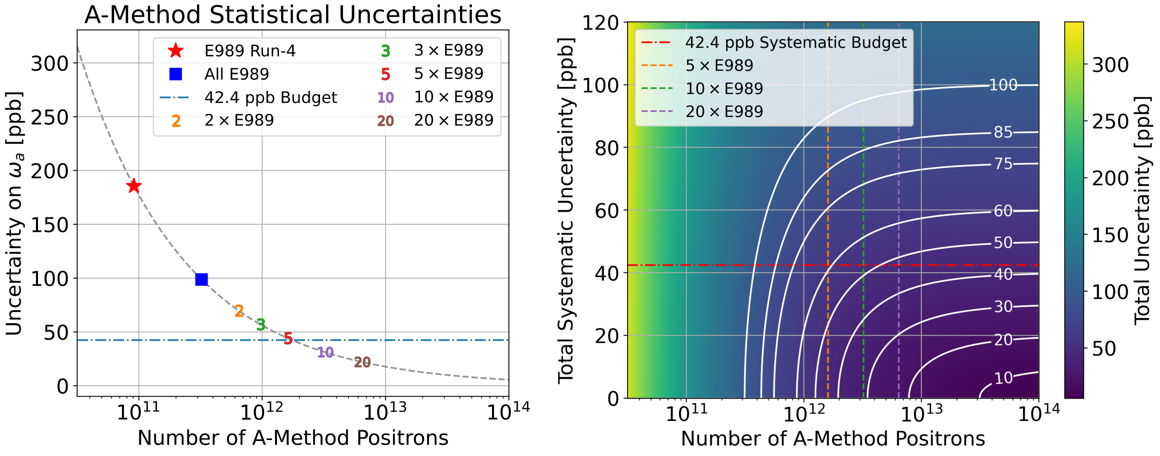

(a) **(b)**

Figure 8.2: (a) Projected A-Method statistical precision, obtained by scaling the total number of positrons collected by the E989 experiment. The goal of 42.4 ppb uncertainty (indicated with the blue dashed line) can be achieved with 5.5× the statistics of the Fermilab experiment. (b) Total projected uncertainty for the experiment vs. the total number of positrons accumulated and the total systematic uncertainty. The 42.4 ppb budget is indicated in red. The white lines are contours of the colored z-axis corresponding to the total uncertainty.

Over the course of Run-4 data taking (Dec. 4th of 2020 to June 27th of 2021), the E989 Muon $g - 2$ experiment averaged a rate of ≈ 2100 physics-quality CTAGs acquired every second[8]. This rate includes downtime from trolley runs, systematic studies, and the inherent ≈ 11.4 Hz repetition rate of muon fills from the Fermilab accelerator complex. Should the improvements above be able

---

[6] The E821 experiment at BNL utilized proton bunches which were a factor of 4 larger than the E989 experiment (4×10^{12} vs. 1×10^{12}).

[7] The E989 experiment yielded ≈ 300 CTAGs for each 1×10^{12} protons on target.

[8] This can roughly be related to the weighted count of A-Weighted positrons by multiplying by a factor of ≈ 2.27.

to yield a net factor of four increase in the number of stored muons every second, and assuming $\approx 65\%$ average uptime over the course of a calendar year, a next generation experiment would be able to accumulate equivalent statistics to the entire E989 experiment in a single year. After 6 years of running, such an experiment would achieve its statistical goal[9].

As a final note, on the scale of such an improved measurement the 22 ppb uncertainty coming from ${}^{m_\mu}/_{m_e}$ (needed for the conversion of $\mathcal{R}$ to a_μ, see Section 3.7) is significant. A new measurement of muonium hyperfine splitting could reduce this uncertainty (the one currently used by CODATA comes from 1999 [131, 193]).

With all of these factors in mind — each one of which requiring a great deal of dedicated design work to achieve — a 60 ppb measurement of a_μ can plausibly be realized. Such an experiment would allow for a strong test of the standard model, even considering the reduced scale of Δa_μ suggested by the current lattice results (Figure 8.3). These basic ideas could be used to guide the design of such an experiment should the discrepancy between a_μ^{SM} and a_μ^{exp} continue to puzzle the next generation of theorists and experimentalists.

8.3 Final Thoughts

The final results of the Muon $g-2$ Experiment are on track to be published by late 2025. By that time, the upheaval in the SM prediction will hopefully have been resolved, allowing for a comparison between the theoretical and measured value of a_μ at the $\mathcal{O}(140\,\mathrm{ppb})$ level. Only time will tell whether the story of the Muon $g-2$ measurements will be that of a signal of BSM physics or of the resurgence of the standard model. In either case, however, the experiment will stand as a monumental achievement of precision measurement and of pushing forward our understanding of the universe.

---

[9] Assuming no improvement in the efficiency of CTAG/p^+ compared to E989, this would require $\approx 5.8 \times 10^{20}\, p^+$ delivered on target per year. The number of available protons would likely be a limiting factor in any next generation experiment.

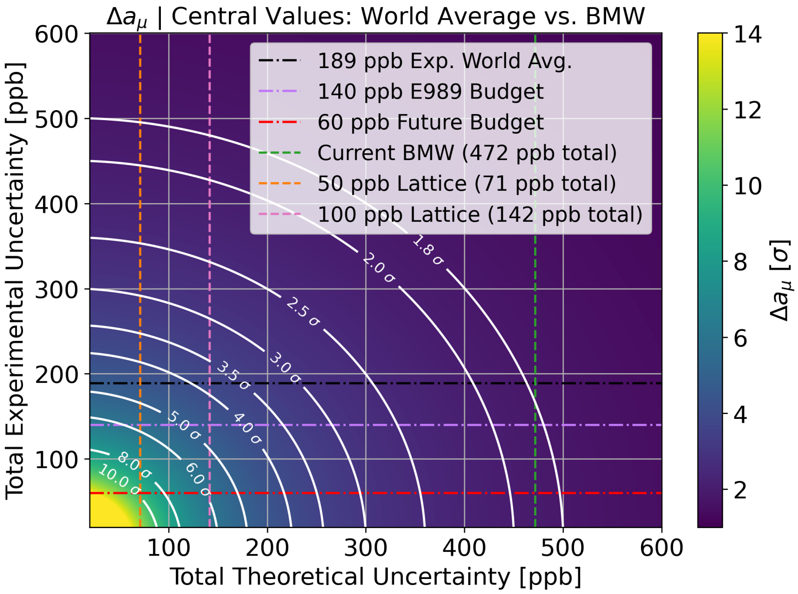

Figure 8.3: Illustration of the potential tension between a next generation $g-2$ experiment and future theoretical evaluations of $a_\mu^{\rm SM}$, assuming the central values from the current BMW evaluation of $a_\mu^{\rm HVP}$ [56] and the world average experimental value are unchanged. The vertical lines of 100 ppb and 50 ppb lattice uncertainties assume equal contributions from $a_\mu^{\rm HLbL}$ and $a_\mu^{\rm HVP}$.

Bibliography

[1] T. Aoyama, N. Asmussen, M. Benayoun, J. Bijnens, T. Blum, M. Bruno, I. Caprini, C.M. Carloni Calame, M. Cè, G. Colangelo, F. Curciarello, H. Czyż, I. Danilkin, M. Davier, C.T.H. Davies, M. Della Morte, S.I. Eidelman, A.X. El-Khadra, A. Gérardin, D. Giusti, M. Golterman, Steven Gottlieb, V. Gülpers, F. Hagelstein, M. Hayakawa, G. Herdoíza, D.W. Hertzog, A. Hoecker, M. Hoferichter, B.-L. Hoid, R.J. Hudspith, F. Ignatov, T. Izubuchi, F. Jegerlehner, L. Jin, A. Keshavarzi, T. Kinoshita, B. Kubis, A. Kupich, A. Kupść, L. Laub, C. Lehner, L. Lellouch, I. Logashenko, B. Malaescu, K. Maltman, M.K. Marinković, P. Masjuan, A.S. Meyer, H.B. Meyer, T. Mibe, K. Miura, S.E. Müller, M. Nio, D. Nomura, A. Nyffeler, V. Pascalutsa, M. Passera, E. Perez del Rio, S. Peris, A. Portelli, M. Procura, C.F. Redmer, B.L. Roberts, P. Sánchez-Puertas, S. Serednyakov, B. Shwartz, S. Simula, D. Stöckinger, H. Stöckinger-Kim, P. Stoffer, T. Teubner, R. Van de Water, M. Vanderhaeghen, G. Venanzoni, G. von Hippel, H. Wittig, Z. Zhang, M.N. Achasov, A. Bashir, N. Cardoso, B. Chakraborty, E.-H. Chao, J. Charles, A. Crivellin, O. Deineka, A. Denig, C. DeTar, C.A. Dominguez, A.E. Dorokhov, V.P. Druzhinin, G. Eichmann, M. Fael, C.S. Fischer, E. Gámiz, Z. Gelzer, J.R. Green, S. Guellati-Khelifa, D. Hatton, N. Hermansson-Truedsson, S. Holz, B. Hörz, M. Knecht, J. Koponen, A.S. Kronfeld, J. Laiho, S. Leupold, P.B. Mackenzie, W.J. Marciano, C. McNeile, D. Mohler, J. Monnard, E.T. Neil, A.V. Nesterenko, K. Ottnad, V. Pauk, A.E. Radzhabov, E. de Rafael, K. Raya, A. Risch, A. Rodríguez-Sánchez, P. Roig, T. San José, E.P. Solodov, R. Sugar, K. Yu. Todyshev, A. Vainshtein, A. Vaquero Avilés-Casco, E. Weil, J. Wilhelm, R. Williams, and A.S. Zhevlakov. The anomalous magnetic moment of the muon in the standard model. *Physics Re-*

ports, 887:1–166, 2020. ISSN 0370-1573. doi:https://doi.org/10.1016/j.physrep.2020.07.006. URL `https://www.sciencedirect.com/science/article/pii/S0370157320302556`. The anomalous magnetic moment of the muon in the Standard Model.

[2] John David Jackson. *Classical Electrodynamics*. Wiley, New York, NY, 3rd ed. edition, 1999.

[3] Matthew D. Schwartz. *Quantum Field Theory and the Standard Model*. Cambridge University Press, 2013.

[4] G. W. Bennett, B. Bousquet, H. N. Brown, G. Bunce, R. M. Carey, P. Cushman, G. T. Danby, P. T. Debevec, M. Deile, H. Deng, W. Deninger, S. K. Dhawan, V. P. Druzhinin, L. Duong, E. Efstathiadis, F. J. M. Farley, G. V. Fedotovich, S. Giron, F. E. Gray, D. Grigoriev, M. Grosse-Perdekamp, A. Grossmann, M. F. Hare, D. W. Hertzog, X. Huang, V. W. Hughes, M. Iwasaki, K. Jungmann, D. Kawall, M. Kawamura, B. I. Khazin, J. Kindem, F. Krienen, I. Kronkvist, A. Lam, R. Larsen, Y. Y. Lee, I. Logashenko, R. McNabb, W. Meng, J. Mi, J. P. Miller, Y. Mizumachi, W. M. Morse, D. Nikas, C. J. G. Onderwater, Y. Orlov, C. S. Özben, J. M. Paley, Q. Peng, C. C. Polly, J. Pretz, R. Prigl, G. zu Putlitz, T. Qian, S. I. Redin, O. Rind, B. L. Roberts, N. Ryskulov, S. Sedykh, Y. K. Semertzidis, P. Shagin, Yu. M. Shatunov, E. P. Sichtermann, E. Solodov, M. Sossong, A. Steinmetz, L. R. Sulak, C. Timmermans, A. Trofimov, D. Urner, P. von Walter, D. Warburton, D. Winn, A. Yamamoto, and D. Zimmerman. Improved limit on the muon electric dipole moment. *Phys. Rev. D*, 80:052008, Sep 2009. doi:10.1103/PhysRevD.80.052008. URL `https://link.aps.org/doi/10.1103/PhysRevD.80.052008`.

[5] R. L. Workman and Others. Review of Particle Physics. *PTEP*, 2022:083C01, 2022. doi:10.1093/ptep/ptac097.

[6] A. Fienberg. *Measuring the Precession Frequency in the E989 Muon g − 2 Experiment*. PhD thesis, University of Washington, 2019. URL `https://doi.org/10.2172/1515050`.

[7] T. D. Lee and C. N. Yang. Question of parity conservation in weak interactions. *Phys. Rev.*,

104:254–258, Oct 1956. doi:10.1103/PhysRev.104.254. URL `https://link.aps.org/doi/10.1103/PhysRev.104.254`.

[8] Richard L. Garwin, Leon M. Lederman, and Marcel Weinrich. Observations of the failure of conservation of parity and charge conjugation in meson decays: the magnetic moment of the free muon. *Phys. Rev.*, 105:1415–1417, Feb 1957. doi:10.1103/PhysRev.105.1415. URL `https://link.aps.org/doi/10.1103/PhysRev.105.1415`.

[9] R. L. Garwin, D. P. Hutchinson, S. Penman, and G. Shapiro. Accurate determination of the μ^+ magnetic moment. *Phys. Rev.*, 118:271–283, Apr 1960. doi:10.1103/PhysRev.118.271. URL `https://link.aps.org/doi/10.1103/PhysRev.118.271`.

[10] B. Lee Roberts. The history of the muon (g-2) experiments, 2018.

[11] D Kawall. Statistical and Systematic Errors on Fitting ω_a. E821 Note 322, 1998.

[12] J.R. Taylor. *An Introduction to Error Analysis: The Study of Uncertainties in Physical Measurements.* University Science Books, Sausalito, 1997.

[13] Christopher Polly. *A MEASUREMENT OF THE ANOMALOUS MAGNETIC MOMENT OF THE NEGATIVE MUON TO 0.7 PPM.* PhD thesis, University of Illinois at Urbana-Champaign, 2005.

[14] F Combley, F.J.M Farley, and E Picasso. The cern muon (g-2) experiments. *Physics Reports*, 68(2):93–119, 1981. ISSN 0370-1573. doi:https://doi.org/10.1016/0370-1573(81)90028-4. URL `https://www.sciencedirect.com/science/article/pii/0370157381900284`.

[15] D. P. Aguillard, T. Albahri, D. Allspach, A. Anisenkov, K. Badgley, S. Baeßler, I. Bailey, L. Bailey, V. A. Baranov, E. Barlas-Yucel, T. Barrett, E. Barzi, F. Bedeschi, M. Berz, M. Bhattacharya, H. P. Binney, P. Bloom, J. Bono, E. Bottalico, T. Bowcock, S. Braun, M. Bressler, G. Cantatore, R. M. Carey, B. C. K. Casey, D. Cauz, R. Chakraborty, A. Chapelain, S. Chappa, S. Charity, C. Chen, M. Cheng, R. Chislett, Z. Chu, T. E. Chupp, C. Claessens, M. E. Convery, S. Corrodi, L. Cotrozzi, J. D. Crnkovic, S. Dabagov, P. T.

Debevec, S. Di Falco, G. Di Sciascio, B. Drendel, A. Driutti, V. N. Duginov, M. Eads, A. Edmonds, J. Esquivel, M. Farooq, R. Fatemi, C. Ferrari, M. Fertl, A. T. Fienberg, A. Fioretti, D. Flay, S. B. Foster, H. Friedsam, N. S. Froemming, C. Gabbanini, I. Gaines, M. D. Galati, S. Ganguly, A. Garcia, J. George, L. K. Gibbons, A. Gioiosa, K. L. Giovanetti, P. Girotti, W. Gohn, L. Goodenough, T. Gorringe, J. Grange, S. Grant, F. Gray, S. Haciomeroglu, T. Halewood-Leagas, D. Hampai, F. Han, J. Hempstead, D. W. Hertzog, G. Hesketh, E. Hess, A. Hibbert, Z. Hodge, K. W. Hong, R. Hong, T. Hu, Y. Hu, M. Iacovacci, M. Incagli, P. Kammel, M. Kargiantoulakis, M. Karuza, J. Kaspar, D. Kawall, L. Kelton, A. Keshavarzi, D. S. Kessler, K. S. Khaw, Z. Khechadoorian, N. V. Khomutov, B. Kiburg, M. Kiburg, O. Kim, N. Kinnaird, E. Kraegeloh, V. A. Krylov, N. A. Kuchinskiy, K. R. Labe, J. LaBounty, M. Lancaster, S. Lee, B. Li, D. Li, L. Li, I. Logashenko, A. Lorente Campos, Z. Lu, A. Lucà, G. Lukicov, A. Lusiani, A. L. Lyon, B. MacCoy, R. Madrak, K. Makino, S. Mastroianni, J. P. Miller, S. Miozzi, B. Mitra, J. P. Morgan, W. M. Morse, J. Mott, A. Nath, J. K. Ng, H. Nguyen, Y. Oksuzian, Z. Omarov, R. Osofsky, S. Park, G. Pauletta, G. M. Piacentino, R. N. Pilato, K. T. Pitts, B. Plaster, D. Počanić, N. Pohlman, C. C. Polly, J. Price, B. Quinn, M. U. H. Qureshi, S. Ramachandran, E. Ramberg, R. Reimann, B. L. Roberts, D. L. Rubin, L. Santi, C. Schlesier, A. Schreckenberger, Y. K. Semertzidis, D. Shemyakin, M. Sorbara, D. Stöckinger, J. Stapleton, D. Still, C. Stoughton, D. Stratakis, H. E. Swanson, G. Sweetmore, D. A. Sweigart, M. J. Syphers, D. A. Tarazona, T. Teubner, A. E. Tewsley-Booth, V. Tishchenko, N. H. Tran, W. Turner, E. Valetov, D. Vasilkova, G. Venanzoni, V. P. Volnykh, T. Walton, A. Weisskopf, L. Welty-Rieger, P. Winter, Y. Wu, B. Yu, M. Yucel, Y. Zeng, and C. Zhang. Measurement of the positive muon anomalous magnetic moment to 0.20 ppm. *Phys. Rev. Lett.*, 131:161802, Oct 2023. doi:10.1103/PhysRevLett.131.161802. URL `https://link.aps.org/doi/10.1103/PhysRevLett.131.161802`.

[16] B. Abi, T. Albahri, S. Al-Kilani, D. Allspach, L. P. Alonzi, A. Anastasi, A. Anisenkov, F. Azfar, K. Badgley, S. Baeßler, I. Bailey, V. A. Baranov, E. Barlas-Yucel, T. Barrett, E. Barzi, A. Basti, F. Bedeschi, A. Behnke, M. Berz, M. Bhattacharya, H. P. Binney, R. Bjorkquist, P. Bloom, J. Bono, E. Bottalico, T. Bowcock, D. Boyden, G. Cantatore, R. M. Carey, J. Car-

roll, B. C. K. Casey, D. Cauz, S. Ceravolo, R. Chakraborty, S. P. Chang, A. Chapelain, S. Chappa, S. Charity, R. Chislett, J. Choi, Z. Chu, T. E. Chupp, M. E. Convery, A. Conway, G. Corradi, S. Corrodi, L. Cotrozzi, J. D. Crnkovic, S. Dabagov, P. M. De Lurgio, P. T. Debevec, S. Di Falco, P. Di Meo, G. Di Sciascio, R. Di Stefano, B. Drendel, A. Driutti, V. N. Duginov, M. Eads, N. Eggert, A. Epps, J. Esquivel, M. Farooq, R. Fatemi, C. Ferrari, M. Fertl, A. Fiedler, A. T. Fienberg, A. Fioretti, D. Flay, S. B. Foster, H. Friedsam, E. Frlež, N. S. Froemming, J. Fry, C. Fu, C. Gabbanini, M. D. Galati, S. Ganguly, A. Garcia, D. E. Gastler, J. George, L. K. Gibbons, A. Gioiosa, K. L. Giovanetti, P. Girotti, W. Gohn, T. Gorringe, J. Grange, S. Grant, F. Gray, S. Haciomeroglu, D. Hahn, T. Halewood-Leagas, D. Hampai, F. Han, E. Hazen, J. Hempstead, S. Henry, A. T. Herrod, D. W. Hertzog, G. Hesketh, A. Hibbert, Z. Hodge, J. L. Holzbauer, K. W. Hong, R. Hong, M. Iacovacci, M. Incagli, C. Johnstone, J. A. Johnstone, P. Kammel, M. Kargiantoulakis, M. Karuza, J. Kaspar, D. Kawall, L. Kelton, A. Keshavarzi, D. Kessler, K. S. Khaw, Z. Khechadoorian, N. V. Khomutov, B. Kiburg, M. Kiburg, O. Kim, S. C. Kim, Y. I. Kim, B. King, N. Kinnaird, M. Korostelev, I. Kourbanis, E. Kraegeloh, V. A. Krylov, A. Kuchibhotla, N. A. Kuchinskiy, K. R. Labe, J. LaBounty, M. Lancaster, M. J. Lee, S. Lee, S. Leo, B. Li, D. Li, L. Li, I. Logashenko, A. Lorente Campos, A. Lucà, G. Lukicov, G. Luo, A. Lusiani, A. L. Lyon, B. MacCoy, R. Madrak, K. Makino, F. Marignetti, S. Mastroianni, S. Maxfield, M. McEvoy, W. Merritt, A. A. Mikhailichenko, J. P. Miller, S. Miozzi, J. P. Morgan, W. M. Morse, J. Mott, E. Motuk, A. Nath, D. Newton, H. Nguyen, M. Oberling, R. Osofsky, J.-F. Ostiguy, S. Park, G. Pauletta, G. M. Piacentino, R. N. Pilato, K. T. Pitts, B. Plaster, D. Počanić, N. Pohlman, C. C. Polly, M. Popovic, J. Price, B. Quinn, N. Raha, S. Ramachandran, E. Ramberg, N. T. Rider, J. L. Ritchie, B. L. Roberts, D. L. Rubin, L. Santi, D. Sathyan, H. Schellman, C. Schlesier, A. Schreckenberger, Y. K. Semertzidis, Y. M. Shatunov, D. Shemyakin, M. Shenk, D. Sim, M. W. Smith, A. Smith, A. K. Soha, M. Sorbara, D. Stöckinger, J. Stapleton, D. Still, C. Stoughton, D. Stratakis, C. Strohman, T. Stuttard, H. E. Swanson, G. Sweetmore, D. A. Sweigart, M. J. Syphers, D. A. Tarazona, T. Teubner, A. E. Tewsley-Booth, K. Thomson, V. Tishchenko, N. H. Tran, W. Turner, E. Valetov, D. Vasilkova, G. Venanzoni, V. P. Volnykh, T. Walton, M. Warren,

A. Weisskopf, L. Welty-Rieger, M. Whitley, P. Winter, A. Wolski, M. Wormald, W. Wu, and C. Yoshikawa. Measurement of the positive muon anomalous magnetic moment to 0.46 ppm. *Phys. Rev. Lett.*, 126:141801, Apr 2021. doi:10.1103/PhysRevLett.126.141801. URL `https://link.aps.org/doi/10.1103/PhysRevLett.126.141801`.

[17] D. P. Aguillard, T. Albahri, D. Allspach, A. Anisenkov, K. Badgley, S. Baeßler, I. Bailey, L. Bailey, V. A. Baranov, E. Barlas-Yucel, T. Barrett, E. Barzi, F. Bedeschi, M. Berz, M. Bhattacharya, H. P. Binney, P. Bloom, J. Bono, E. Bottalico, T. Bowcock, S. Braun, M. Bressler, G. Cantatore, R. M. Carey, B. C. K. Casey, D. Cauz, R. Chakraborty, A. Chapelain, S. Chappa, S. Charity, C. Chen, M. Cheng, R. Chislett, Z. Chu, T. E. Chupp, C. Claessens, M. E. Convery, S. Corrodi, L. Cotrozzi, J. D. Crnkovic, S. Dabagov, P. T. Debevec, S. Di Falco, G. Di Sciascio, S. Donati, B. Drendel, A. Driutti, V. N. Duginov, M. Eads, A. Edmonds, J. Esquivel, M. Farooq, R. Fatemi, C. Ferrari, M. Fertl, A. T. Fienberg, A. Fioretti, D. Flay, S. B. Foster, H. Friedsam, N. S. Froemming, C. Gabbanini, I. Gaines, M. D. Galati, S. Ganguly, A. Garcia, J. George, L. K. Gibbons, A. Gioiosa, K. L. Giovanetti, P. Girotti, W. Gohn, L. Goodenough, T. Gorringe, J. Grange, S. Grant, F. Gray, S. Haciomeroglu, T. Halewood-Leagas, D. Hampai, F. Han, J. Hempstead, D. W. Hertzog, G. Hesketh, E. Hess, A. Hibbert, Z. Hodge, K. W. Hong, R. Hong, T. Hu, Y. Hu, M. Iacovacci, M. Incagli, P. Kammel, M. Kargiantoulakis, M. Karuza, J. Kaspar, D. Kawall, L. Kelton, A. Keshavarzi, D. S. Kessler, K. S. Khaw, Z. Khechadoorian, N. V. Khomutov, B. Kiburg, M. Kiburg, O. Kim, N. Kinnaird, E. Kraegeloh, V. A. Krylov, N. A. Kuchinskiy, K. R. Labe, J. LaBounty, M. Lancaster, S. Lee, B. Li, D. Li, L. Li, I. Logashenko, A. Lorente Campos, Z. Lu, A. Lucà, G. Lukicov, A. Lusiani, A. L. Lyon, B. MacCoy, R. Madrak, K. Makino, S. Mastroianni, J. P. Miller, S. Miozzi, B. Mitra, J. P. Morgan, W. M. Morse, J. Mott, A. Nath, J. K. Ng, H. Nguyen, Y. Oksuzian, Z. Omarov, R. Osofsky, S. Park, G. Pauletta, G. M. Piacentino, R. N. Pilato, K. T. Pitts, B. Plaster, D. Počanić, N. Pohlman, C. C. Polly, J. Price, B. Quinn, M. U. H. Qureshi, S. Ramachandran, E. Ramberg, R. Reimann, B. L. Roberts, D. L. Rubin, M. Sakurai, L. Santi, C. Schlesier, A. Schreckenberger, Y. K. Semertzidis, D. Shemyakin, M. Sorbara, J. Stapleton, D. Still, D. Stöckinger, C. Stoughton,

D. Stratakis, H. E. Swanson, G. Sweetmore, D. A. Sweigart, M. J. Syphers, D. A. Tarazona, T. Teubner, A. E. Tewsley-Booth, V. Tishchenko, N. H. Tran, W. Turner, E. Valetov, D. Vasilkova, G. Venanzoni, V. P. Volnykh, T. Walton, A. Weisskopf, L. Welty-Rieger, P. Winter, Y. Wu, B. Yu, M. Yucel, Y. Zeng, and C. Zhang. Detailed report on the measurement of the positive muon anomalous magnetic moment to 0.20 ppm, 2024.

[18] Tatsumi Aoyama, Masashi Hayakawa, Toichiro Kinoshita, and Makiko Nio. Complete Tenth-Order QED Contribution to the Muon $g-2$. *Phys. Rev. Lett.*, 109:111808, 2012. doi:10.1103/PhysRevLett.109.111808.

[19] Tatsumi Aoyama, Toichiro Kinoshita, and Makiko Nio. Theory of the Anomalous Magnetic Moment of the Electron. *Atoms*, 7(1):28, 2019. doi:10.3390/atoms7010028.

[20] Andrzej Czarnecki, William J. Marciano, and Arkady Vainshtein. Refinements in electroweak contributions to the muon anomalous magnetic moment. *Phys. Rev.*, D67:073006, 2003. doi:10.1103/PhysRevD.67.073006. [Erratum: Phys. Rev. **D73**, 119901 (2006)].

[21] C. Gnendiger, D. Stoeckinger, and H. Stoeckinger-Kim. The electroweak contributions to $(g-2)_\mu$ after the Higgs boson mass measurement. *Phys. Rev.*, D88:053005, 2013. doi:10.1103/PhysRevD.88.053005.

[22] Michel Davier, Andreas Hoecker, Bogdan Malaescu, and Zhiqing Zhang. Reevaluation of the hadronic vacuum polarisation contributions to the Standard Model predictions of the muon $g-2$ and $\alpha(m_Z^2)$ using newest hadronic cross-section data. *Eur. Phys. J.*, C77(12):827, 2017. doi:10.1140/epjc/s10052-017-5161-6.

[23] Alexander Keshavarzi, Daisuke Nomura, and Thomas Teubner. Muon $g-2$ and $\alpha(M_Z^2)$: a new data-based analysis. *Phys. Rev.*, D97(11):114025, 2018. doi:10.1103/PhysRevD.97.114025.

[24] Gilberto Colangelo, Martin Hoferichter, and Peter Stoffer. Two-pion contribution to hadronic vacuum polarization. *JHEP*, 02:006, 2019. doi:10.1007/JHEP02(2019)006.

[25] Martin Hoferichter, Bai-Long Hoid, and Bastian Kubis. Three-pion contribution to hadronic vacuum polarization. *JHEP*, 08:137, 2019. doi:10.1007/JHEP08(2019)137.

[26] M. Davier, A. Hoecker, B. Malaescu, and Z. Zhang. A new evaluation of the hadronic vacuum polarisation contributions to the muon anomalous magnetic moment and to $\alpha(m_Z^2)$. *Eur. Phys. J. C*, 80(3):241, 2020. doi:10.1140/epjc/s10052-020-7792-2. [Erratum: Eur.Phys.J.C 80, 410 (2020)].

[27] Alexander Keshavarzi, Daisuke Nomura, and Thomas Teubner. The $g-2$ of charged leptons, $\alpha(M_Z^2)$ and the hyperfine splitting of muonium. *Phys. Rev.*, D101:014029, 2020. doi:10.1103/PhysRevD.101.014029.

[28] Alexander Kurz, Tao Liu, Peter Marquard, and Matthias Steinhauser. Hadronic contribution to the muon anomalous magnetic moment to next-to-next-to-leading order. *Phys. Lett.*, B734: 144–147, 2014. doi:10.1016/j.physletb.2014.05.043.

[29] Kirill Melnikov and Arkady Vainshtein. Hadronic light-by-light scattering contribution to the muon anomalous magnetic moment revisited. *Phys. Rev.*, D70:113006, 2004. doi:10.1103/PhysRevD.70.113006.

[30] Pere Masjuan and Pablo Sánchez-Puertas. Pseudoscalar-pole contribution to the $(g_\mu - 2)$: a rational approach. *Phys. Rev.*, D95(5):054026, 2017. doi:10.1103/PhysRevD.95.054026.

[31] Gilberto Colangelo, Martin Hoferichter, Massimiliano Procura, and Peter Stoffer. Dispersion relation for hadronic light-by-light scattering: two-pion contributions. *JHEP*, 04:161, 2017. doi:10.1007/JHEP04(2017)161.

[32] Martin Hoferichter, Bai-Long Hoid, Bastian Kubis, Stefan Leupold, and Sebastian P. Schneider. Dispersion relation for hadronic light-by-light scattering: pion pole. *JHEP*, 10:141, 2018. doi:10.1007/JHEP10(2018)141.

[33] Antoine Gérardin, Harvey B. Meyer, and Andreas Nyffeler. Lattice calculation of the pion transition form factor with $N_f = 2+1$ Wilson quarks. *Phys. Rev.*, D100(3):034520, 2019. doi:10.1103/PhysRevD.100.034520.

[34] Johan Bijnens, Nils Hermansson-Truedsson, and Antonio Rodríguez-Sánchez. Short-distance

constraints for the HLbL contribution to the muon anomalous magnetic moment. *Phys. Lett.*, B798:134994, 2019. doi:10.1016/j.physletb.2019.134994.

[35] Gilberto Colangelo, Franziska Hagelstein, Martin Hoferichter, Laetitia Laub, and Peter Stoffer. Longitudinal short-distance constraints for the hadronic light-by-light contribution to $(g-2)_\mu$ with large-N_c Regge models. *JHEP*, 03:101, 2020. doi:10.1007/JHEP03(2020)101.

[36] Thomas Blum, Norman Christ, Masashi Hayakawa, Taku Izubuchi, Luchang Jin, Chulwoo Jung, and Christoph Lehner. The hadronic light-by-light scattering contribution to the muon anomalous magnetic moment from lattice QCD. *Phys. Rev. Lett.*, 124(13):132002, 2020. doi:10.1103/PhysRevLett.124.132002.

[37] Gilberto Colangelo, Martin Hoferichter, Andreas Nyffeler, Massimo Passera, and Peter Stoffer. Remarks on higher-order hadronic corrections to the muon $g-2$. *Phys. Lett.*, B735: 90–91, 2014. doi:10.1016/j.physletb.2014.06.012.

[38] Yutaro Sato. *J-PARC Muon g− 2/EDM Experiment*. 2021. doi:10.7566/JPSCP.33.011110. URL `https://journals.jps.jp/doi/abs/10.7566/JPSCP.33.011110`.

[39] W. Pauli. Zur quantenmechanik des magnetischen elektrons. *Physik 43, 601–623*, 1927. doi:https://doi.org/10.1007/BF01397326.

[40] P. Kusch and H. M. Foley. Precision measurement of the ratio of the atomic 'g values' in the ${}^2p_{\frac{3}{2}}$ and ${}^2p_{\frac{1}{2}}$ states of gallium. *Phys. Rev.*, 72:1256–1257, Dec 1947. doi:10.1103/PhysRev.72.1256.2. URL `https://link.aps.org/doi/10.1103/PhysRev.72.1256.2`.

[41] Julian S. Schwinger. On Quantum electrodynamics and the magnetic moment of the electron. *Phys. Rev.*, 73:416–417, 1948. doi:10.1103/PhysRev.73.416.

[42] A. Petermann. Fourth order magnetic moment of the electron. *Helv. Phys. Acta*, 30:407–408, 1957. doi:10.5169/seals-112823.

[43] Charles M Sommerfield. The magnetic moment of the electron. *Annals of Physics*, 5(1):26–57,

1958. ISSN 0003-4916. doi:https://doi.org/10.1016/0003-4916(58)90003-4. URL `https://www.sciencedirect.com/science/article/pii/0003491658900034`.

[44] S. Laporta and E. Remiddi. The analytical value of the electron (g − 2) at order 3 in qed. *Physics Letters B*, 379(1–4):283–291, June 1996. ISSN 0370-2693. doi:10.1016/0370-2693(96)00439-x. URL `http://dx.doi.org/10.1016/0370-2693(96)00439-X`.

[45] Stefano Laporta. High-precision calculation of the 4-loop contribution to the electron g-2 in qed. *Physics Letters B*, 772:232–238, 2017. ISSN 0370-2693. doi:https://doi.org/10.1016/j.physletb.2017.06.056. URL `https://www.sciencedirect.com/science/article/pii/S0370269317305324`.

[46] Richard H. Parker, Chenghui Yu, Weicheng Zhong, Brian Estey, and Holger Müller. Measurement of the fine-structure constant as a test of the Standard Model. *Science*, 360:191, 2018. doi:10.1126/science.aap7706.

[47] Rym Bouchendira, Pierre Cladé, Saïda Guellati-Khélifa, Fran çois Nez, and Fran çois Biraben. New determination of the fine structure constant and test of the quantum electrodynamics. *Phys. Rev. Lett.*, 106:080801, Feb 2011. doi:10.1103/PhysRevLett.106.080801. URL `https://link.aps.org/doi/10.1103/PhysRevLett.106.080801`.

[48] X. Fan, T. G. Myers, B. A. D. Sukra, and G. Gabrielse. Measurement of the electron magnetic moment. *Phys. Rev. Lett.*, 130:071801, Feb 2023. doi:10.1103/PhysRevLett.130.071801. URL `https://link.aps.org/doi/10.1103/PhysRevLett.130.071801`.

[49] Stanley J. Brodsky and Eduardo de Rafael. Suggested boson-lepton pair couplings and the anomalous magnetic moment of the muon. *Phys. Rev.*, 168:1620–1622, Apr 1968. doi:10.1103/PhysRev.168.1620. URL `https://link.aps.org/doi/10.1103/PhysRev.168.1620`.

[50] B. E. Lautrup and E. de Rafael. Calculation of the sixth-order contribution from the fourth-order vacuum polarization to the difference of the anomalous magnetic moments of muon

and electron. *Phys. Rev.*, 174:1835–1842, Oct 1968. doi:10.1103/PhysRev.174.1835. URL `https://link.aps.org/doi/10.1103/PhysRev.174.1835`.

[51] Alexander Keshavarzi, Daisuke Nomura, and Thomas Teubner. $g-2$ of charged leptons, $\alpha(M_Z^2)$, and the hyperfine splitting of muonium. *Phys. Rev. D*, 101:014029, Jan 2020. doi:10.1103/PhysRevD.101.014029. URL `https://link.aps.org/doi/10.1103/PhysRevD.101.014029`.

[52] J. P. Lees, V. Poireau, V. Tisserand, J. Garra Tico, E. Grauges, A. Palano, G. Eigen, B. Stugu, D. N. Brown, L. T. Kerth, Yu. G. Kolomensky, G. Lynch, H. Koch, T. Schroeder, D. J. Asgeirsson, C. Hearty, T. S. Mattison, J. A. McKenna, A. Khan, V. E. Blinov, A. R. Buzykaev, V. P. Druzhinin, V. B. Golubev, E. A. Kravchenko, A. P. Onuchin, S. I. Serednyakov, Yu. I. Skovpen, E. P. Solodov, K. Yu. Todyshev, A. N. Yushkov, M. Bondioli, D. Kirkby, A. J. Lankford, M. Mandelkern, H. Atmacan, J. W. Gary, F. Liu, O. Long, G. M. Vitug, C. Campagnari, T. M. Hong, D. Kovalskyi, J. D. Richman, C. A. West, A. M. Eisner, J. Kroseberg, W. S. Lockman, A. J. Martinez, B. A. Schumm, A. Seiden, D. S. Chao, C. H. Cheng, B. Echenard, K. T. Flood, D. G. Hitlin, P. Ongmongkolkul, F. C. Porter, A. Y. Rakitin, R. Andreassen, Z. Huard, B. T. Meadows, M. D. Sokoloff, L. Sun, P. C. Bloom, W. T. Ford, A. Gaz, U. Nauenberg, J. G. Smith, S. R. Wagner, R. Ayad, W. H. Toki, B. Spaan, K. R. Schubert, R. Schwierz, D. Bernard, M. Verderi, P. J. Clark, S. Playfer, D. Bettoni, C. Bozzi, R. Calabrese, G. Cibinetto, E. Fioravanti, I. Garzia, E. Luppi, M. Munerato, M. Negrini, L. Piemontese, V. Santoro, R. Baldini-Ferroli, A. Calcaterra, R. de Sangro, G. Finocchiaro, P. Patteri, I. M. Peruzzi, M. Piccolo, M. Rama, A. Zallo, R. Contri, E. Guido, M. Lo Vetere, M. R. Monge, S. Passaggio, C. Patrignani, E. Robutti, B. Bhuyan, V. Prasad, C. L. Lee, M. Morii, A. J. Edwards, A. Adametz, U. Uwer, H. M. Lacker, T. Lueck, P. D. Dauncey, P. K. Behera, U. Mallik, C. Chen, J. Cochran, W. T. Meyer, S. Prell, A. E. Rubin, A. V. Gritsan, Z. J. Guo, N. Arnaud, M. Davier, D. Derkach, G. Grosdidier, F. Le Diberder, A. M. Lutz, B. Malaescu, P. Roudeau, M. H. Schune, A. Stocchi, L. L. Wang, G. Wormser, D. J. Lange, D. M. Wright, C. A. Chavez, J. P. Coleman, J. R. Fry, E. Gabathuler, D. E. Hutchcroft, D. J. Payne, C. Touramanis, A. J. Bevan, F. Di Lodovico, R. Sacco, M. Sigamani, G. Cowan,

D. N. Brown, C. L. Davis, A. G. Denig, M. Fritsch, W. Gradl, K. Griessinger, A. Hafner, E. Prencipe, R. J. Barlow, G. Jackson, G. D. Lafferty, E. Behn, R. Cenci, B. Hamilton, A. Jawahery, D. A. Roberts, C. Dallapiccola, R. Cowan, D. Dujmic, G. Sciolla, R. Cheaib, D. Lindemann, P. M. Patel, S. H. Robertson, P. Biassoni, N. Neri, F. Palombo, S. Stracka, L. Cremaldi, R. Godang, R. Kroeger, P. Sonnek, D. J. Summers, X. Nguyen, M. Simard, P. Taras, G. De Nardo, D. Monorchio, G. Onorato, C. Sciacca, M. Martinelli, G. Raven, C. P. Jessop, J. M. LoSecco, W. F. Wang, K. Honscheid, R. Kass, J. Brau, R. Frey, N. B. Sinev, D. Strom, E. Torrence, E. Feltresi, N. Gagliardi, M. Margoni, M. Morandin, M. Posocco, M. Rotondo, G. Simi, F. Simonetto, R. Stroili, S. Akar, E. Ben-Haim, M. Bomben, G. R. Bonneaud, H. Briand, G. Calderini, J. Chauveau, O. Hamon, Ph. Leruste, G. Marchiori, J. Ocariz, S. Sitt, M. Biasini, E. Manoni, S. Pacetti, A. Rossi, C. Angelini, G. Batignani, S. Bettarini, M. Carpinelli, G. Casarosa, A. Cervelli, F. Forti, M. A. Giorgi, A. Lusiani, B. Oberhof, E. Paoloni, A. Perez, G. Rizzo, J. J. Walsh, D. Lopes Pegna, J. Olsen, A. J. S. Smith, A. V. Telnov, F. Anulli, R. Faccini, F. Ferrarotto, F. Ferroni, M. Gaspero, L. Li Gioi, M. A. Mazzoni, G. Piredda, C. Bünger, O. Grünberg, T. Hartmann, T. Leddig, H. Schröder, C. Voss, R. Waldi, T. Adye, E. O. Olaiya, F. F. Wilson, S. Emery, G. Hamel de Monchenault, G. Vasseur, Ch. Yèche, D. Aston, D. J. Bard, R. Bartoldus, J. F. Benitez, C. Cartaro, M. R. Convery, J. Dorfan, G. P. Dubois-Felsmann, W. Dunwoodie, M. Ebert, R. C. Field, M. Franco Sevilla, B. G. Fulsom, A. M. Gabareen, M. T. Graham, P. Grenier, C. Hast, W. R. Innes, M. H. Kelsey, P. Kim, M. L. Kocian, D. W. G. S. Leith, P. Lewis, B. Lindquist, S. Luitz, V. Luth, H. L. Lynch, D. B. MacFarlane, D. R. Muller, H. Neal, S. Nelson, M. Perl, T. Pulliam, B. N. Ratcliff, A. Roodman, A. A. Salnikov, R. H. Schindler, A. Snyder, D. Su, M. K. Sullivan, J. Va'vra, A. P. Wagner, W. J. Wisniewski, M. Wittgen, D. H. Wright, H. W. Wulsin, C. C. Young, V. Ziegler, W. Park, M. V. Purohit, R. M. White, J. R. Wilson, A. Randle-Conde, S. J. Sekula, M. Bellis, P. R. Burchat, T. S. Miyashita, M. S. Alam, J. A. Ernst, R. Gorodeisky, N. Guttman, D. R. Peimer, A. Soffer, P. Lund, S. M. Spanier, J. L. Ritchie, A. M. Ruland, R. F. Schwitters, B. C. Wray, J. M. Izen, X. C. Lou, F. Bianchi, D. Gamba, L. Lanceri, L. Vitale, F. Martinez-Vidal, A. Oyanguren, H. Ahmed, J. Albert,

Sw. Banerjee, F. U. Bernlochner, H. H. F. Choi, G. J. King, R. Kowalewski, M. J. Lewczuk, I. M. Nugent, J. M. Roney, R. J. Sobie, N. Tasneem, T. J. Gershon, P. F. Harrison, T. E. Latham, E. M. T. Puccio, H. R. Band, S. Dasu, Y. Pan, R. Prepost, and S. L. Wu. Precise measurement of the $e^+e^- \to \pi^+\pi^-(\gamma)$ cross section with the initial-state radiation method at babar. *Phys. Rev. D*, 86:032013, Aug 2012. doi:10.1103/PhysRevD.86.032013. URL `https://link.aps.org/doi/10.1103/PhysRevD.86.032013`.

[53] F. Ambrosino, F. Archilli, P. Beltrame, G. Bencivenni, C. Bini, C. Bloise, S. Bocchetta, F. Bossi, P. Branchini, G. Capon, T. Capussela, F. Ceradini, P. Ciambrone, E. De Lucia, A. De Santis, P. De Simone, G. De Zorzi, A. Denig, A. Di Domenico, C. Di Donato, B. Di Micco, M. Dreucci, G. Felici, S. Fiore, P. Franzini, C. Gatti, P. Gauzzi, S. Giovannella, E. Graziani, M. Jacewicz, W. Kluge, J. Lee-Franzini, D. Leone, P. Massarotti, S. Meola, S. Miscetti, S. Müller, F. Murtas, M. Napolitano, F. Nguyen, A. Passeri, V. Patera, P. Santangelo, C. Taccini, L. Tortora, G. Venanzoni, and R. Versaci. Measurement of (e+e−−→ + −) from threshold to 0.85 gev2 using initial state radiation with the kloe detector. *Physics Letters B*, 700(2):102–110, 2011. ISSN 0370-2693. doi:https://doi.org/10.1016/j.physletb.2011.04.055. URL `https://www.sciencedirect.com/science/article/pii/S0370269311004679`.

[54] D. Babusci, D. Badoni, I. Balwierz-Pytko, G. Bencivenni, C. Bini, C. Bloise, F. Bossi, P. Branchini, A. Budano, L. Caldeira Balkeståhl, G. Capon, F. Ceradini, P. Ciambrone, F. Curciarello, E. Czerwiński, E. Dané, V. De Leo, E. De Lucia, G. De Robertis, A. De Santis, P. De Simone, A. Di Domenico, C. Di Donato, D. Domenici, O. Erriquez, G. Fanizzi, G. Felici, S. Fiore, P. Franzini, P. Gauzzi, G. Giardina, S. Giovannella, F. Gonnella, E. Graziani, F. Happacher, L. Heijkenskjöld, B. Höistad, L. Iafolla, E. Iarocci, M. Jacewicz, T. Johansson, W. Kluge, A. Kupsc, J. Lee-Franzini, F. Loddo, P. Lukin, G. Mandaglio, M. Martemianov, M. Martini, M. Mascolo, R. Messi, S. Miscetti, G. Morello, D. Moricciani, P. Moskal, S. Müller, F. Nguyen, A. Passeri, V. Patera, I. Prado Longhi, A. Ranieri, C.F. Redmer, P. Santangelo, I. Sarra, M. Schioppa, B. Sciascia, M. Silarski, C. Taccini, L. Tortora, G. Venanzoni, R. Versaci, W. Wiślicki, M. Wolke, and J. Zdebik. Precision measurement of (e+e−−→ + −)/ (e+e−−→ + −) and determination of the + − contribu-

tion to the muon anomaly with the kloe detector. *Physics Letters B*, 720(4):336–343, 2013. ISSN 0370-2693. doi:https://doi.org/10.1016/j.physletb.2013.02.029. URL `https://www.sciencedirect.com/science/article/pii/S0370269313001585`.

[55] 2 Collaboration, A. Anastasi, D. Babusci, M. Berlowski, C. Bloise, F. Bossi, P. Branchini, A. Budano, L. Caldeira Balkeståhl, B. Cao, F. Ceradini, P. Ciambrone, F. Curciarello, E. Czerwiński, G. D'Agostini, E. Danè, V. De Leo, E. De Lucia, A. De Santis, P. De Simone, A. Di Cicco, A. Di Domenico, D. Domenici, A. D'Uffizi, A. Fantini, G. Fantini, P. Fermani, S. Fiore, A. Gajos, P. Gauzzi, S. Giovannella, E. Graziani, V. L. Ivanov, T. Johansson, D. Kisielewska-Kamińska, X. Kang, E. A. Kozyrev, W. Krzemien, A. Kupsc, S. Loffredo, P. A. Lukin, G. Mandaglio, M. Martini, R. Messi, S. Miscetti, G. Morello, D. Moricciani, P. Moskal, A. Passeri, V. Patera, E. Perez del Rio, N. Raha, P. Santangelo, M. Schioppa, A. Selce, M. Silarski, F. Sirghi, E. P. Solodov, L. Tortora, G. Venanzoni, W. Wiślicki, M. Wolke, A. Keshavarzi, S. E. Müller, and T. Teubner. Combination of kloe $\sigma\big(e^+e^- \to \pi^+\pi^-\gamma(\gamma)\big)$ measurements and determination of $a_\mu^{\pi^+\pi^-}$ in the energy range $0.10 < s < 0.95$ gev^2, 2018.

[56] Sz. Borsanyi, Z. Fodor, J. N. Guenther, C. Hoelbling, S. D. Katz, L. Lellouch, T. Lippert, K. Miura, L. Parato, K. K. Szabo, F. Stokes, B. C. Toth, Cs. Torok, and L. Varnhorst. Leading hadronic contribution to the muon magnetic moment from lattice qcd. *Nature*, 593 (7857):51–55, May 2021. ISSN 1476-4687. doi:10.1038/s41586-021-03418-1. URL `https://doi.org/10.1038/s41586-021-03418-1`.

[57] F. V. Ignatov et al. Measurement of the $e^+e^- \to \pi^+\pi^-$ cross section from threshold to 1.2 GeV with the CMD-3 detector. 2 2023.

[58] Vladyslav Pauk and Marc Vanderhaeghen. Single meson contributions to the muon's anomalous magnetic moment. *Eur. Phys. J.*, C74(8):3008, 2014. doi:10.1140/epjc/s10052-014-3008-y.

[59] Igor Danilkin and Marc Vanderhaeghen. Light-by-light scattering sum rules in light of new data. *Phys. Rev.*, D95(1):014019, 2017. doi:10.1103/PhysRevD.95.014019.

[60] Friedrich Jegerlehner. *The Anomalous Magnetic Moment of the Muon*, volume 274. Springer, Cham, 2017. doi:10.1007/978-3-319-63577-4.

[61] M. Knecht, S. Narison, A. Rabemananjara, and D. Rabetiarivony. Scalar meson contributions to a_μ from hadronic light-by-light scattering. *Phys. Lett.*, B787:111–123, 2018. doi:10.1016/j.physletb.2018.10.048.

[62] Gernot Eichmann, Christian S. Fischer, and Richard Williams. Kaon-box contribution to the anomalous magnetic moment of the muon. *Phys. Rev.*, D101(5):054015, 2020. doi:10.1103/PhysRevD.101.054015.

[63] Pablo Roig and Pablo Sánchez-Puertas. Axial-vector exchange contribution to the hadronic light-by-light piece of the muon anomalous magnetic moment. *Phys. Rev.*, D101(7):074019, 2020. doi:10.1103/PhysRevD.101.074019.

[64] G. Peter Lepage. Lattice qcd for novices, 2005.

[65] Genessa Benton, Diogo Boito, Maarten Golterman, Alexander Keshavarzi, Kim Maltman, and Santiago Peris. Data-driven determination of the light-quark connected component of the intermediate-window contribution to the muon $g-2$, 2023.

[66] A. Gérardin. Hadronic contributions to the anomalous magnetic moment of the muon. URL `https://indico.fnal.gov/event/57249/contributions/271164/`.

[67] Maarten Golterman. Data-driven determination of the light-quark connected component of the intermediate-window contribution to $g_\mu - 2$. URL `https://indico.fnal.gov/event/57249/contributions/270697/`.

[68] Martin Hoferichter, Peter Stoffer, and Maximilian Zillinger. An optimized basis for hadronic light-by-light scattering. 2 2024.

[69] Peter Stoffer, Gilberto Colangelo, and Martin Hoferichter. Puzzles in the hadronic contributions to the muon anomalous magnetic moment. *JINST*, 18(10):C10021, 2023. doi:10.1088/1748-0221/18/10/C10021.

[70] En-Hung Chao, Renwick J. Hudspith, Antoine Gérardin, Jeremy R. Green, Harvey B. Meyer, and Konstantin Ottnad. Hadronic light-by-light contribution to

$$(g-2)_\mu$$

from lattice qcd: a complete calculation. *The European Physical Journal C*, 81(7), July 2021. ISSN 1434-6052. doi:10.1140/epjc/s10052-021-09455-4. URL `http://dx.doi.org/10.1140/epjc/s10052-021-09455-4`.

[71] En-Hung Chao, Renwick J. Hudspith, Antoine Gérardin, Jeremy R. Green, and Harvey B. Meyer. The charm-quark contribution to light-by-light scattering in the muon

$$(g-2)$$

from lattice qcd. *The European Physical Journal C*, 82(8), August 2022. ISSN 1434-6052. doi:10.1140/epjc/s10052-022-10589-2. URL `http://dx.doi.org/10.1140/epjc/s10052-022-10589-2`.

[72] Thomas Blum, Norman Christ, Masashi Hayakawa, Taku Izubuchi, Luchang Jin, Chulwoo Jung, Christoph Lehner, and Cheng Tu. Hadronic light-by-light contribution to the muon anomaly from lattice qcd with infinite volume qed at physical pion mass, 2023.

[73] G. Colangelo et al. Prospects for precise predictions of a_μ in the Standard Model. 3 2022.

[74] G. Abbiendi, C. M. Carloni Calame, U. Marconi, C. Matteuzzi, G. Montagna, O. Nicrosini, M. Passera, F. Piccinini, R. Tenchini, L. Trentadue, and G. Venanzoni. Measuring the leading hadronic contribution to the muon g-2 via μescattering. *The European Physical Journal C*, 77(3):139, Mar 2017. ISSN 1434-6052. doi:10.1140/epjc/s10052-017-4633-z. URL `https://doi.org/10.1140/epjc/s10052-017-4633-z`.

[75] Pere Masjuan, Alejandro Miranda, and Pablo Roig. Tau data-driven evaluation of the hadronic vacuum polarization *. *Nuclear and Particle Physics Proceedings*, 2023. ISSN

2405-6014. doi:https://doi.org/10.1016/j.nuclphysbps.2023.12.001. URL `https://www.sciencedirect.com/science/article/pii/S2405601423002687`.

[76] J. Grange, V. Guarino, P. Winter, K. Wood, H. Zhao, R. M. Carey, D. Gastler, E. Hazen, N. Kinnaird, J. P. Miller, J. Mott, B. L. Roberts, J. Benante, J. Crnkovic, W. M. Morse, H. Sayed, V. Tishchenko, V. P. Druzhinin, B. I. Khazin, I. A. Koop, I. Logashenko, Y. M. Shatunov, E. Solodov, M. Korostelev, D. Newton, A. Wolski, A. Chapelain, R. Bjorkquist, N. Eggert, A. Frankenthal, L. Gibbons, S. Kim, A. Mikhailichenko, Y. Orlov, D. Rubin, D. Sweigart, D. Allspach, G. Annala, E. Barzi, K. Bourland, G. Brown, B. C. K. Casey, S. Chappa, M. E. Convery, B. Drendel, H. Friedsam, T. Gadfort, K. Hardin, S. Hawke, S. Hayes, W. Jaskierny, C. Johnstone, J. Johnstone, V. Kashikhin, C. Kendziora, B. Kiburg, A. Klebaner, I. Kourbanis, J. Kyle, N. Larson, A. Leveling, A. L. Lyon, D. Markley, D. McArthur, K. W. Merritt, N. Mokhov, J. P. Morgan, H. Nguyen, J-F. Ostiguy, A. Para, C. C. Polly M. Popovic, E. Ramberg, M. Rominsky, D. Schoo, R. Schultz, D. Still, A. K. Soha, S. Strigonov, G. Tassotto, D. Turrioni, E. Villegas, E. Voirin, G. Velev, L. Welty-Rieger, D. Wolff, C. Worel, J-Y. Wu, R. Zifko, K. Jungmann, C. J. G. Onderwater, P. T. Debevec, S. Ganguly, M. Kasten, S. Leo, K. Pitts, C. Schlesier, M. Gaisser, S. Haciomeroglu, Y-I. Kim, S. Lee, M-J Lee, Y. K. Semertzidis, K. Giovanetti, V. A. Baranov, V. N. Duginov, N. V. Khomutov, V. A. Krylov, N. A. Kuchinskiy, V. P. Volnykh, C. Crawford, R. Fatemi, W. P. Gohn, T. P. Gorringe, W. Korsch, B. Plaster, A. Anastasi, D. Babusci, S. Dabagov, C. Ferrari, A. Fioretti, C. Gabbanini, D. Hampai, A. Palladino, G. Venanzoni, T. Bowcock, J. Carroll, B. King, S. Maxfield, K. McCormick, J. Price, D. Sim, A. Smith, T. Teubner, W. Turner, M. Whitley, M. Wormald, R. Chislett, S. Kilani, M. Lancaster, E. Motuk, T. Stuttard, M. Warren, D. Flay, D. Kawall, Z. Meadows, T. Chupp, R. Raymond, A. Tewlsey-Booth, M. J. Syphers, D. Tarazona, S. Catalonotti, R. Di Stefano, M. Iacovacci, S. Mastroianni, S. Chattopadhyay, M. Eads, M. Fortner, D. Hedin, N. Pohlman, A. de Gouvea, H. Schellman, L. Welty-Rieger, F. Azfar, S. Henry, G. D. Alkhazov, V. L. Golovtsov, P. V. Neustroev, L. N. Uvarov, A. A. Vasilyev, A. A. Vorobyov, M. B. Zhalov, L. Cerrito, F. Gray, G. Di Sciascio, D. Moricciani, C. Fu, X. Ji, L. Li, H. Yang, D. Stöckinger, G. Cantatore, D. Cauz,

M. Karuza, G. Pauletta, L. Santi, S. Baeßler, M. Bychkov, E. Frlez, D. Pocanic, L. P. Alonzi, M. Fertl, A. Fienberg, N. Froemming, A. Garcia, D. W. Hertzog J. Kaspar, P. Kammel, R. Osofsky, M. Smith, E. Swanson, T. van Wechel, and K. Lynch. Muon (g-2) technical design report, 2018.

[77] Sudeshna Ganguly. Muon g-2 Beam At Fermilab. E989 DocDB 29832, 2023. URL `https://gm2-docdb.fnal.gov/cgi-bin/sso/ShowDocument?docid=29832`.

[78] Jim Morgan. Accelerator Status and Plans. E989 DocDB 15241, 2018. URL `https://gm2-docdb.fnal.gov/cgi-bin/sso/ShowDocument?docid=15241`.

[79] Eremey Valetov. E989 Note 223: Muon g-2 End-to-End Beamline Simulations, and Systematic Analyses of Muon Losses and Origin Effects. E989 DocDB 19979, 2020. URL `https://gm2-docdb.fnal.gov/cgi-bin/sso/ShowDocument?docid=19979`.

[80] N. Froemming. *Optimization of Muon Injection and Storage in the Fermilab g-2 Experiment: From Simulation to Reality.* PhD thesis, University of Washington, 2018. URL `http://hdl.handle.net/1773/43445`.

[81] B. MacCoy. *Beam Dynamics Challenges in the Muon g-2 Experiment.* PhD thesis, University of Washington, 2023. URL `http://hdl.handle.net/1773/50899`.

[82] Jim Morgan. Deuterons to the g-2 Ring. E989 DocDB 23188, 2020. URL `https://gm2-docdb.fnal.gov/cgi-bin/sso/ShowDocument?docid=23188`.

[83] G. W. Bennett, B. Bousquet, H. N. Brown, G. Bunce, R. M. Carey, P. Cushman, G. T. Danby, P. T. Debevec, M. Deile, H. Deng, W. Deninger, S. K. Dhawan, V. P. Druzhinin, L. Duong, E. Efstathiadis, F. J. M. Farley, G. V. Fedotovich, S. Giron, F. E. Gray, D. Grigoriev, M. Grosse-Perdekamp, A. Grossmann, M. F. Hare, D. W. Hertzog, X. Huang, V. W. Hughes, M. Iwasaki, K. Jungmann, D. Kawall, M. Kawamura, B. I. Khazin, J. Kindem, F. Krienen, I. Kronkvist, A. Lam, R. Larsen, Y. Y. Lee, I. Logashenko, R. McNabb, W. Meng, J. Mi, J. P. Miller, Y. Mizumachi, W. M. Morse, D. Nikas, C. J. G. Onderwater, Y. Orlov, C. S. Özben, J. M. Paley, Q. Peng, C. C. Polly, J. Pretz, R. Prigl, G. zu Putlitz, T. Qian, S. I.

Redin, O. Rind, B. L. Roberts, N. Ryskulov, S. Sedykh, Y. K. Semertzidis, P. Shagin, Yu. M. Shatunov, E. P. Sichtermann, E. Solodov, M. Sossong, A. Steinmetz, L. R. Sulak, C. Timmermans, A. Trofimov, D. Urner, P. von Walter, D. Warburton, D. Winn, A. Yamamoto, and D. Zimmerman. Final report of the e821 muon anomalous magnetic moment measurement at bnl. *Phys. Rev. D*, 73:072003, Apr 2006. doi:10.1103/PhysRevD.73.072003. URL `https://link.aps.org/doi/10.1103/PhysRevD.73.072003`.

[84] Hannah Binney. *Precession frequency analysis for Run-2 and Run-3 of the Muon g-2 experiment*. PhD thesis, University of Washington, 2022. URL `http://hdl.handle.net/1773/49743`.

[85] Diktys Stratakis. Optimizing Injection: with wedge and new inflector. E989 DocDB 24444, 2020. URL `https://gm2-docdb.fnal.gov/cgi-bin/sso/ShowDocument?docid=24444`.

[86] Andy Edmonds. Run-4 T0 Traces for Simulation Tuning. E989 DocDB 29577, 2023. URL `https://gm2-docdb.fnal.gov/cgi-bin/sso/ShowDocument?docid=29577`.

[87] Dave Rubin. Estimating Differential Decay From the Stored Beam - update. E989 DocDB 29145, 2023. URL `https://gm2-docdb.fnal.gov/cgi-bin/sso/ShowDocument?docid=29145`.

[88] Dave Rubin. E989 Note 291:Spin -Transverse Coordinate Correlation. E989 DocDB 28011, 2022. URL `https://gm2-docdb.fnal.gov/cgi-bin/sso/ShowDocument?docid=28011`.

[89] A Yamamoto, Y Makida, K Tanaka, F Krienen, B.L Roberts, H.N Brown, G Bunce, G.T Danby, M G-Perdekamp, H Hseuh, L Jia, Y.Y Lee, M Mapes, W Meng, W Morse, C Pai, R Prigl, W Sampson, J Sandberg, M Suenaga, T Tallerico, F Toldo, K Woodle, M.A Green, I Itoh, H Otsuka, Y Saito, T Ozawa, Y Tachiya, H Tanaka, A Grossmann, K Jungmann, G zu Putlitz, H Deng, S Dhawan, V Hughes, D Kawall, J Pretz, S Redin, E Sichtermann, and A Steinmetz. The superconducting inflector for the bnl g-2 experiment. *Nuclear Instruments and Methods in Physics Research Section A: Accelerators, Spectrometers, Detectors and Associated Equipment*, 491(1):23–40, 2002. ISSN 0168-9002. doi:https://-

doi.org/10.1016/S0168-9002(02)01232-9. URL `https://www.sciencedirect.com/science/article/pii/S0168900202012329`.

[90] Nathan Froemming, Karie Badgley, Jason Crnkovic, Laura Kelton, Hogan Nguyen, Diktys Stratakis, and Michael Syphers. Commissioning the superconducting magnetic inflector system for the muon g-2 experiment. 6 2018. doi:10.18429/JACoW-IPAC2018-WEPAF014. URL `https://www.osti.gov/biblio/1478036`.

[91] Jason Hempstead. *Measuring the anomalous precession frequency ω_a for the Muon $g-2$ experiment.* PhD thesis, University of Washington, 2021. URL `http://hdl.handle.net/1773/47677`.

[92] T. Albahri, A. Anastasi, K. Badgley, et al. Magnetic-field measurement and analysis for the Muon $g-2$ Experiment at Fermilab. *Phys. Rev. A*, 103:042208, Apr 2021. doi:10.1103/PhysRevA.103.042208.

[93] G.T. Danby, L. Addessi, Z. Armoza, J. Benante, H.N. Brown, G. Bunce, J.C. Cottingham, J. Cullen, J. Geller, H. Hseuh, J.W. Jackson, L. Jia, S. Kochis, D. Koniczny, R. Larsen, Y.Y. Lee, M. Mapes, R.E. Meier, W. Meng, W.M. Morse, M. O'Toole, C. Pai, I. Polk, R. Prigl, Y.K. Semertzidis, R. Shutt, L. Snydstrup, A. Soukas, T. Tallerico, F. Toldo, D.Von Lintig, K. Woodle, R.M. Carey, W. Earle, E.S. Hazen, F. Krienen, J.P. Miller, J. Ouyang, B.L. Roberts, L.R. Sulak, W.A. Worstell, Y. Orlov, D. Winn, A. Grossmann, K. Jungmann, G. zu Putlitz, P. von Walter, P.T. Debevec, W.J. Deninger, D.W. Hertzog, S. Sedykh, D. Urner, M.A. Green, U. Haeberlen, P. Cushman, S. Giron, J. Kindem, D. Miller, C. Timmermans, D. Zimmerman, V.P. Druzhinin, G.V. Fedotovich, D.N. Grigorev, B.I. Khazin, N.M. Ryskulov, S. Serednyakov, Yu.M. Shatunov, E. Solodov, K. Endo, H. Hirabayashi, Y. Mizumachi, A. Yamamoto, S.K. Dhawan, A. Disco, F.J.M. Farley, X. Fei, M. Grosse-Perdekamp, V.W. Hughes, D. Kawall, and S.I. Redin. The brookhaven muon storage ring magnet. *Nuclear Instruments and Methods in Physics Research Section A: Accelerators, Spectrometers, Detectors and Associated Equipment*, 457(1):

151–174, 2001. ISSN 0168-9002. doi:https://doi.org/10.1016/S0168-9002(00)00704-X. URL `https://www.sciencedirect.com/science/article/pii/S016890020000704X`.

[94] Rachel Osofsky. Improving Magnetic Field Uniformity in the Muon g-2 Storage Ring, APS April Meeting 2018. E989 DocDB 11439, 2018. URL `https://gm2-docdb.fnal.gov/cgi-bin/sso/ShowDocument?docid=11439`.

[95] Rachel Osofsky. *Magnetic Field Determination for Run 1 of the Fermilab Muon $g-2$ Experiment*. PhD thesis, University of Washington, 2019. URL `https://www.osti.gov/biblio/1833583`.

[96] F. Bloch, W. W. Hansen, and Martin Packard. Nuclear induction. *Phys. Rev.*, 69:127–127, Feb 1946. doi:10.1103/PhysRev.69.127. URL `https://link.aps.org/doi/10.1103/PhysRev.69.127`.

[97] E. M. Purcell, H. C. Torrey, and R. V. Pound. Resonance absorption by nuclear magnetic moments in a solid. *Phys. Rev.*, 69:37–38, Jan 1946. doi:10.1103/PhysRev.69.37. URL `https://link.aps.org/doi/10.1103/PhysRev.69.37`.

[98] Rene Reimann. E989 Note 283: Magnetic Field Derived from Fixed Probe Stations - Uncertainties and Correlations. E989 DocDB 26890, 2022. URL `https://gm2-docdb.fnal.gov/cgi-bin/sso/ShowDocument?docid=26890`.

[99] David P Aguillard et al. E989 Note 294: Run 2/3 Field Documentation: Review. E989 DocDB 28082, 2023. URL `https://gm2-docdb.fnal.gov/cgi-bin/sso/ShowDocument?docid=28082`.

[100] Bingzhi Li. E989 Note 230: Trolley Calibration Analysis for Run1. E989 DocDB 22947, 2020. URL `https://gm2-docdb.fnal.gov/cgi-bin/sso/ShowDocument?docid=22947`.

[101] Rachel Osofsky. Improving Magnetic Field Uniformity in the g-2 Storage Ring (2018 Users Meeting poster). E989 DocDB 12497, 2018. URL `https://gm2-docdb.fnal.gov/cgi-bin/sso/ShowDocument?docid=12497`.

[102] Alex Keshavarzi. Measurement of the kicker field and pulse shape. E989 DocDB 9398, 2017. URL `https://gm2-docdb.fnal.gov/cgi-bin/sso/ShowDocument?docid=9398`.

[103] T. Albahri, A. Anastasi, A. Anisenkov, K. Badgley, S. Baeßler, I. Bailey, V. A. Baranov, E. Barlas-Yucel, T. Barrett, A. Basti, F. Bedeschi, M. Berz, M. Bhattacharya, H. P. Binney, P. Bloom, J. Bono, E. Bottalico, T. Bowcock, G. Cantatore, R. M. Carey, B. C. K. Casey, D. Cauz, R. Chakraborty, S. P. Chang, A. Chapelain, S. Charity, R. Chislett, J. Choi, Z. Chu, T. E. Chupp, S. Corrodi, L. Cotrozzi, J. D. Crnkovic, S. Dabagov, P. T. Debevec, S. Di Falco, P. Di Meo, G. Di Sciascio, R. Di Stefano, A. Driutti, V. N. Duginov, M. Eads, J. Esquivel, M. Farooq, R. Fatemi, C. Ferrari, M. Fertl, A. T. Fienberg, A. Fioretti, D. Flay, E. Frlež, N. S. Froemming, J. Fry, C. Gabbanini, M. D. Galati, S. Ganguly, A. Garcia, J. George, L. K. Gibbons, A. Gioiosa, K. L. Giovanetti, P. Girotti, W. Gohn, T. Gorringe, J. Grange, S. Grant, F. Gray, S. Haciomeroglu, T. Halewood-Leagas, D. Hampai, F. Han, J. Hempstead, A. T. Herrod, D. W. Hertzog, G. Hesketh, A. Hibbert, Z. Hodge, J. L. Holzbauer, K. W. Hong, R. Hong, M. Iacovacci, M. Incagli, P. Kammel, M. Kargiantoulakis, M. Karuza, J. Kaspar, D. Kawall, L. Kelton, A. Keshavarzi, D. Kessler, K. S. Khaw, Z. Khechadoorian, N. V. Khomutov, B. Kiburg, M. Kiburg, O. Kim, Y. I. Kim, B. King, N. Kinnaird, E. Kraegeloh, A. Kuchibhotla, N. A. Kuchinskiy, K. R. Labe, J. LaBounty, M. Lancaster, M. J. Lee, S. Lee, S. Leo, B. Li, D. Li, L. Li, I. Logashenko, A. Lorente Campos, A. Lucà, G. Lukicov, A. Lusiani, A. L. Lyon, B. MacCoy, R. Madrak, K. Makino, F. Marignetti, S. Mastroianni, J. P. Miller, S. Miozzi, W. M. Morse, J. Mott, A. Nath, H. Nguyen, R. Osofsky, S. Park, G. Pauletta, G. M. Piacentino, R. N. Pilato, K. T. Pitts, B. Plaster, D. Počanić, N. Pohlman, C. C. Polly, J. Price, B. Quinn, N. Raha, S. Ramachandran, E. Ramberg, J. L. Ritchie, B. L. Roberts, D. L. Rubin, L. Santi, C. Schlesier, A. Schreckenberger, Y. K. Semertzidis, D. Shemyakin, M. W. Smith, M. Sorbara, D. Stöckinger, J. Stapleton, C. Stoughton, D. Stratakis, T. Stuttard, H. E. Swanson, G. Sweetmore, D. A. Sweigart, M. J. Syphers, D. A. Tarazona, T. Teubner, A. E. Tewsley-Booth, K. Thomson, V. Tishchenko, N. H. Tran, W. Turner, E. Valetov, D. Vasilkova, G. Venanzoni, T. Walton, A. Weisskopf, L. Welty-Rieger, P. Winter, A. Wolski, and W. Wu. Measurement of the anomalous precession frequency of the muon in the fermilab muon $g-2$

experiment. *Phys. Rev. D*, 103:072002, Apr 2021. doi:10.1103/PhysRevD.103.072002. URL `https://link.aps.org/doi/10.1103/PhysRevD.103.072002`.

[104] A.P. Schreckenberger, D. Allspach, D. Barak, J. Bohn, C. Bradford, D. Cauz, S.P. Chang, A. Chapelain, S. Chappa, S. Charity, R. Chislett, J. Esquivel, C. Ferrari, A. Fioretti, C. Gabbanini, M.D. Galati, L. Gibbons, J.L. Holzbauer, M. Incagli, C. Jensen, J. Kaspar, D. Kawall, A. Keshavarzi, D.S. Kessler, B. Kiburg, G. Krafczyk, R. Madrak, A.A. Mikhailichenko, H. Nguyen, K. Overhage, S. Park, H. Pfeffer, C.C. Polly, M. Popovic, R. Rivera, B.L. Roberts, D. Rubin, Y.K. Semertzidis, J. Stapleton, C. Stoughton, E. Voirin, and D. Wolff. The fast non-ferric kicker system for the muon <mml:math xmlns:mml=”http://www.w3.org/1998/math/mathml” display=”inline” id=”d1e1042” altimg=”si55.svg”><mml:mrow><mml:mi>g</mml:mi><mml:mo linebreak=”goodbreak” linebreakstyle=”after”>−</mml:mo><mml:mn>2</mml:mn></mml:mrow></mml:math> experiment at fermilab. *Nuclear Instruments and Methods in Physics Research Section A: Accelerators, Spectrometers, Detectors and Associated Equipment*, 1011: 165597, September 2021. ISSN 0168-9002. doi:10.1016/j.nima.2021.165597. URL `http://dx.doi.org/10.1016/j.nima.2021.165597`.

[105] T. Albahri, A. Anastasi, K. Badgley, S. Baeßler, I. Bailey, V. A. Baranov, E. Barlas-Yucel, T. Barrett, F. Bedeschi, M. Berz, et al. Beam dynamics corrections to the Run-1 measurement of the muon anomalous magnetic moment at Fermilab. *Phys. Rev. Accel. Beams*, 24:044002, Apr 2021. doi:10.1103/PhysRevAccelBeams.24.044002.

[106] On Kim. Two weeks Run-5 RF production data analysis. E989 DocDB 26315, 2021. URL `https://gm2-docdb.fnal.gov/cgi-bin/sso/ShowDocument?docid=26315`.

[107] On Kim, Meghna Bhattacharya, SeungPyo Chang, Jihoon Choi, Jason D Crnkovic, Sudeshna Ganguly, Selcuk Hacı̆ömeroğlu, Manolis Kargiantoulakis, Young-Im Kim, Soohyung Lee, William M Morse, Hogan Nguyen, Yuri F Orlov, B Lee Roberts, Yannis K Semertzidis, Vladimir Tishchenko, Nam H Tran, and Esra Barlas Yucel. Reduction of coherent betatron oscillations in a muon g − 2 storage ring experiment using rf fields. *New Jour-*

nal of Physics, 22(6):063002, jun 2020. doi:10.1088/1367-2630/ab83d0. URL `https://dx.doi.org/10.1088/1367-2630/ab83d0`.

[108] K.S. Khaw, M. Bartolini, H. Binney, R. Bjorkquist, A. Chapelain, A. Driutti, C. Ferrari, A.T. Fienberg, A. Fioretti, C. Gabbanini, S. Ganguly, L.K. Gibbons, A. Gioiosa, K. Giovanetti, W.P. Gohn, T.P. Gorringe, J.B. Hempstead, D.W. Hertzog, M. Iacovacci, J. Kaspar, A. Kuchibhotla, S. Leo, A. Lusiani, S. Mastroianni, G. Pauletta, D.A. Peterson, D. Počanić, N. Rider, C.D. Schlesier, M.W. Smith, T. Stuttard, D.A. Sweigart, T.D. Van Wechel, and G. Venanzoni. Performance of the muon g−2 calorimeter and readout systems measured with test beam data. *Nuclear Instruments and Methods in Physics Research Section A: Accelerators, Spectrometers, Detectors and Associated Equipment*, 945: 162558, 2019. ISSN 0168-9002. doi:https://doi.org/10.1016/j.nima.2019.162558. URL `https://www.sciencedirect.com/science/article/pii/S0168900219310824`.

[109] A.T. Fienberg, L.P. Alonzi, A. Anastasi, R. Bjorkquist, D. Cauz, R. Fatemi, C. Ferrari, A. Fioretti, A. Frankenthal, C. Gabbanini, L.K. Gibbons, K. Giovanetti, S.D. Goadhouse, W.P. Gohn, T.P. Gorringe, D.W. Hertzog, M. Iacovacci, P. Kammel, J. Kaspar, B. Kiburg, L. Li, S. Mastroianni, G. Pauletta, D.A. Peterson, D. Počanić, M.W. Smith, D.A. Sweigart, V. Tishchenko, G. Venanzoni, T.D. Van Wechel, K.B. Wall, P. Winter, and K. Yai. Studies of an array of pbf2 cherenkov crystals with large-area sipm readout. *Nuclear Instruments and Methods in Physics Research Section A: Accelerators, Spectrometers, Detectors and Associated Equipment*, 783:12–21, May 2015. ISSN 0168-9002. doi:10.1016/j.nima.2015.02.028. URL `http://dx.doi.org/10.1016/j.nima.2015.02.028`.

[110] A. Driutti, A. Basti, F. Bedeschi, G. Cantatore, D. Cauz, G. Corradi, S. Dabagov, S. Di Falco, G. Di Sciascio, R. Di Stefano, S. Donati, O. Escalante, C. Ferrari, A. Fioretti, C. Gabbanini, A. Gioiosa, D. Hampai, M. Iacovacci, M. Incagli, M. Karuza, A. Lusiani, F. Marignetti, S. Mastroianni, D. Moricciani, A. Nath, G. Pauletta, G.M. Piacentino, N. Raha, L. Santi, M. Smith, M. Sorbara, and G. Venanzoni. The calibration system of the muon g–2 experiment. *Nuclear Instruments and Methods in Physics Research Section A: Accelera-*

tors, Spectrometers, Detectors and Associated Equipment, 936:98–101, 2019. ISSN 0168-9002. doi:https://doi.org/10.1016/j.nima.2018.10.045. URL `https://www.sciencedirect.com/science/article/pii/S0168900218313597`. Frontier Detectors for Frontier Physics: 14th Pisa Meeting on Advanced Detectors.

[111] A. Anastasi, A. Basti, F. Bedeschi, A. Boiano, E. Bottalico, G. Cantatore, D. Cauz, A.T. Chapelain, G. Corradi, S. Dabagov, S. Di Falco, P. Di Meo, G. Di Sciascio, R. Di Stefano, S. Donati, A. Driutti, C. Ferrari, A.T. Fienberg, A. Fioretti, C. Gabbanini, L.K. Gibbons, A. Gioiosa, P. Girotti, D. Hampai, J.B. Hempstead, D.W. Hertzog, M. Iacovacci, M. Incagli, M. Karuza, J. Kaspar, K.S. Khaw, A. Lusiani, F. Marignetti, S. Mastroianni, S. Miozzi, A. Nath, G. Pauletta, G.M. Piacentino, N. Raha, L. Santi, M. Smith, M. Sorbara, D.A. Sweigart, and G. Venanzoni. The laser-based gain monitoring system of the calorimeters in the muon g−2 experiment at fermilab. *Journal of Instrumentation*, 14(11):P11025–P11025, November 2019. ISSN 1748-0221. doi:10.1088/1748-0221/14/11/p11025. URL `http://dx.doi.org/10.1088/1748-0221/14/11/P11025`.

[112] Bingzhi Li. GNN for track finding. E989 DocDB 29438, 2023. URL `https://gm2-docdb.fnal.gov/cgi-bin/sso/ShowDocument?docid=29438`.

[113] B.T. King, T. Albahri, S. Al-Kilani, D. Allspach, D. Beckner, A. Behnke, T.J.V. Bowcock, D. Boyden, R.M. Carey, J. Carroll, B.C.K. Casey, S. Charity, R. Chislett, M. Eads, A. Epps, S.B. Foster, D. Gastler, S. Grant, T. Halewood-Leagas, K. Hardin, E. Hazen, G. Hesketh, D.J. Hollywood, T. Jones, C. Kenziora, A. Keshavarzi, M. Kiburg, N. Kinnaird, J. Kintner, M. Lancaster, A. Lucà, G. Lukicov, G. Luo, L. Mapar, S.J. Maxfield, J. Mott, E. Motuk, H. Mourato, N. Pohlman, J. Price, B.L. Roberts, D. Sathyan, M. Shenk, D. Sim, T. Stuttard, G. Sweetmore, G. Thayer, K. Thomson, W. Turner, D. Vasilkova, J. Velho, E. Voirin, T. Walton, M. Warren, L. Welty-Rieger, M. Whitley, and M. Wormald. The straw tracking detector for the fermilab muon g-2 experiment. *Journal of Instrumentation*, 17(02):P02035, feb 2022. doi:10.1088/1748-0221/17/02/P02035. URL `https://dx.doi.org/10.1088/1748-0221/17/02/P02035`.

[114] Christine Claessens et al. Horizontal MiniSciFi vs. calo fast rotation comparison. E989 DocDB 29788, 2023. URL `https://gm2-docdb.fnal.gov/cgi-bin/sso/ShowDocument?docid=29788`.

[115] David S Kessler et al. June 2023 Kicker Transient BAM Presentation. E989 DocDB 29023, 2023. URL `https://gm2-docdb.fnal.gov/cgi-bin/sso/ShowDocument?docid=29023`.

[116] Tyler Barrett. E989 Note 302: Fast Rotation Analysis of Run-2 and Run-3. E989 DocDB 28236, 2023. URL `https://gm2-docdb.fnal.gov/cgi-bin/sso/ShowDocument?docid=28236`.

[117] Elia Bottalico et al. CERN 3 Update and Systematic Errors Progress Report Version 2. E989 DocDB 29032, 2023. URL `https://gm2-docdb.fnal.gov/cgi-bin/sso/ShowDocument?docid=29032`.

[118] David Tarazona et al. E989 Note 316, E-Field Correction from Tracker Data, Runs 2&3. E989 DocDB 29035, 2023. URL `https://gm2-docdb.fnal.gov/cgi-bin/sso/ShowDocument?docid=29035`.

[119] Tyler Barrett et al. Combined pitch results from run2&3. E989 DocDB 28714, 2023. URL `https://gm2-docdb.fnal.gov/cgi-bin/sso/ShowDocument?docid=28714`.

[120] On Kim. E989 Note 267: The origin of the pitch correction. E989 DocDB 25124, 2021. URL `https://gm2-docdb.fnal.gov/cgi-bin/sso/ShowDocument?docid=25124`.

[121] F.J.N. Farley. Pitch correction in (g-2) experiments. *Physics Letters B*, 42(1):66–68, 1972. ISSN 0370-2693. doi:https://doi.org/10.1016/0370-2693(72)90718-6. URL `https://www.sciencedirect.com/science/article/pii/0370269372907186`.

[122] Josh LaBounty. E989 Note 303: Muon Losses and Estimation of C_ml in Run-2/3. E989 DocDB 28451, 2023. URL `https://gm2-docdb.fnal.gov/cgi-bin/sso/ShowDocument?docid=28451`.

[123] Jason D. Crnkovic et al. Differential Decay Documentation. E989 DocDB 27912, 2023. URL `https://gm2-docdb.fnal.gov/cgi-bin/sso/ShowDocument?docid=27912`.

[124] Christine Claessens et al. MiniSciFi studies in run 6. E989 DocDB 28758, 2023. URL `https://gm2-docdb.fnal.gov/cgi-bin/sso/ShowDocument?docid=28758`.

[125] Dave Rubin. E989 Note 299, Spin Angle-Transverse Coordinate Correlation. E989 DocDB 28270, 2023. URL `https://gm2-docdb.fnal.gov/cgi-bin/sso/ShowDocument?docid=28270`.

[126] David Tarazona. Runs 2&3 BD Analysis: Differential Decay. E989 DocDB 29156, 2023. URL `https://gm2-docdb.fnal.gov/cgi-bin/sso/ShowDocument?docid=29156`.

[127] S. Agostinelli, J. Allison, K. Amako, J. Apostolakis, H. Araujo, P. Arce, M. Asai, D. Axen, S. Banerjee, G. Barrand, F. Behner, L. Bellagamba, J. Boudreau, L. Broglia, A. Brunengo, H. Burkhardt, S. Chauvie, J. Chuma, R. Chytracek, G. Cooperman, G. Cosmo, P. Degtyarenko, A. Dell'Acqua, G. Depaola, D. Dietrich, R. Enami, A. Feliciello, C. Ferguson, H. Fesefeldt, G. Folger, F. Foppiano, A. Forti, S. Garelli, S. Giani, R. Giannitrapani, D. Gibin, J.J. Gómez Cadenas, I. González, G. Gracia Abril, G. Greeniaus, W. Greiner, V. Grichine, A. Grossheim, S. Guatelli, P. Gumplinger, R. Hamatsu, K. Hashimoto, H. Hasui, A. Heikkinen, A. Howard, V. Ivanchenko, A. Johnson, F.W. Jones, J. Kallenbach, N. Kanaya, M. Kawabata, Y. Kawabata, M. Kawaguti, S. Kelner, P. Kent, A. Kimura, T. Kodama, R. Kokoulin, M. Kossov, H. Kurashige, E. Lamanna, T. Lampén, V. Lara, V. Lefebure, F. Lei, M. Liendl, W. Lockman, F. Longo, S. Magni, M. Maire, E. Medernach, K. Minamimoto, P. Mora de Freitas, Y. Morita, K. Murakami, M. Nagamatu, R. Nartallo, P. Nieminen, T. Nishimura, K. Ohtsubo, M. Okamura, S. O'Neale, Y. Oohata, K. Paech, J. Perl, A. Pfeiffer, M.G. Pia, F. Ranjard, A. Rybin, S. Sadilov, E. Di Salvo, G. Santin, T. Sasaki, N. Savvas, Y. Sawada, S. Scherer, S. Sei, V. Sirotenko, D. Smith, N. Starkov, H. Stoecker, J. Sulkimo, M. Takahata, S. Tanaka, E. Tcherniaev, E. Safai Tehrani, M. Tropeano, P. Truscott, H. Uno, L. Urban, P. Urban, M. Verderi, A. Walkden, W. Wander, H. Weber, J.P. Wellisch, T. Wenaus, D.C. Williams, D. Wright, T. Yamada, H. Yoshida, and D. Zschi-

esche. Geant4—a simulation toolkit. *Nuclear Instruments and Methods in Physics Research Section A: Accelerators, Spectrometers, Detectors and Associated Equipment*, 506(3): 250–303, 2003. ISSN 0168-9002. doi:https://doi.org/10.1016/S0168-9002(03)01368-8. URL `https://www.sciencedirect.com/science/article/pii/S0168900203013688`.

[128] J. Allison, K. Amako, J. Apostolakis, H. Araujo, P. Arce Dubois, M. Asai, G. Barrand, R. Capra, S. Chauvie, R. Chytracek, G.A.P. Cirrone, G. Cooperman, G. Cosmo, G. Cuttone, G.G. Daquino, M. Donszelmann, M. Dressel, G. Folger, F. Foppiano, J. Generowicz, V. Grichine, S. Guatelli, P. Gumplinger, A. Heikkinen, I. Hrivnacova, A. Howard, S. Incerti, V. Ivanchenko, T. Johnson, F. Jones, T. Koi, R. Kokoulin, M. Kossov, H. Kurashige, V. Lara, S. Larsson, F. Lei, O. Link, F. Longo, M. Maire, A. Mantero, B. Mascialino, I. McLaren, P. Mendez Lorenzo, K. Minamimoto, K. Murakami, P. Nieminen, L. Pandola, S. Parlati, L. Peralta, J. Perl, A. Pfeiffer, M.G. Pia, A. Ribon, P. Rodrigues, G. Russo, S. Sadilov, G. Santin, T. Sasaki, D. Smith, N. Starkov, S. Tanaka, E. Tcherniaev, B. Tome, A. Trindade, P. Truscott, L. Urban, M. Verderi, A. Walkden, J.P. Wellisch, D.C. Williams, D. Wright, and H. Yoshida. Geant4 developments and applications. *IEEE Transactions on Nuclear Science*, 53(1):270–278, 2006. doi:10.1109/TNS.2006.869826.

[129] J. Allison, K. Amako, J. Apostolakis, P. Arce, M. Asai, T. Aso, E. Bagli, A. Bagulya, S. Banerjee, G. Barrand, B.R. Beck, A.G. Bogdanov, D. Brandt, J.M.C. Brown, H. Burkhardt, Ph. Canal, D. Cano-Ott, S. Chauvie, K. Cho, G.A.P. Cirrone, G. Cooperman, M.A. Cortés-Giraldo, G. Cosmo, G. Cuttone, G. Depaola, L. Desorgher, X. Dong, A. Dotti, V.D. Elvira, G. Folger, Z. Francis, A. Galoyan, L. Garnier, M. Gayer, K.L. Genser, V.M. Grichine, S. Guatelli, P. Guèye, P. Gumplinger, A.S. Howard, I. Hřivnáčová, S. Hwang, S. Incerti, A. Ivanchenko, V.N. Ivanchenko, F.W. Jones, S.Y. Jun, P. Kaitaniemi, N. Karakatsanis, M. Karamitros, M. Kelsey, A. Kimura, T. Koi, H. Kurashige, A. Lechner, S.B. Lee, F. Longo, M. Maire, D. Mancusi, A. Mantero, E. Mendoza, B. Morgan, K. Murakami, T. Nikitina, L. Pandola, P. Paprocki, J. Perl, I. Petrović, M.G. Pia, W. Pokorski, J.M. Quesada, M. Raine, M.A. Reis, A. Ribon, A. Ristić Fira, F. Romano, G. Russo, G. Santin, T. Sasaki, D. Sawkey, J.I. Shin, I.I. Strakovsky, A. Taborda, S. Tanaka,

B. Tomé, T. Toshito, H.N. Tran, P.R. Truscott, L. Urban, V. Uzhinsky, J.M. Verbeke, M. Verderi, B.L. Wendt, H. Wenzel, D.H. Wright, D.M. Wright, T. Yamashita, J. Yarba, and H. Yoshida. Recent developments in geant4. *Nuclear Instruments and Methods in Physics Research Section A: Accelerators, Spectrometers, Detectors and Associated Equipment*, 835:186–225, 2016. ISSN 0168-9002. doi:https://doi.org/10.1016/j.nima.2016.06.125. URL `https://www.sciencedirect.com/science/article/pii/S0168900216306957`.

[130] David Tarazona. Differential decay correction - update. E989 DocDB 29773, 2023. URL `https://gm2-docdb.fnal.gov/cgi-bin/sso/ShowDocument?docid=29773`.

[131] Eite Tiesinga, Peter J. Mohr, David B. Newell, and Barry N. Taylor. The 2018 CODATA Recommended Values of the Fundamental Physical Constants (Web Version 8.1). `http://physics.nist.gov/constants`.

[132] William D Phillips, William E Cooke, and Daniel Kleppner. Magnetic moment of the proton in H_2O in bohr magnetons. *Metrologia*, 13(4):179–195, 1977. doi:10.1088/0026-1394/13/4/005. URL `https://doi.org/10.1088%2F0026-1394%2F13%2F4%2F005`.

[133] Savely G. Karshenboim and Vladimir G. Ivanov. The g factor of the proton. *Physics Letters B*, 566(1):27–34, 2003. ISSN 0370-2693. doi:https://doi.org/10.1016/S0370-2693(03)00807-4. URL `https://www.sciencedirect.com/science/article/pii/S0370269303008074`.

[134] Josh LaBounty. DAQ Crystal Chopping Overview. E989 DocDB 13723, 2018. URL `https://gm2-docdb.fnal.gov/cgi-bin/sso/ShowDocument?docid=13723`.

[135] Wes Gohn. DAQ Shutdown Plans. E989 DocDB 13098, 2018. URL `https://gm2-docdb.fnal.gov/cgi-bin/sso/ShowDocument?docid=13098`.

[136] Becky Chislett. Lessons learnt - DAQ. E989 DocDB 18172, 2019. URL `https://gm2-docdb.fnal.gov/cgi-bin/sso/ShowDocument?docid=18172`.

[137] S. Ritt and P.A. Amaudruz. New components of the midas data acquisition system. In *1999 IEEE Conference on Real-Time Computer Applications in Nuclear Particle and Plasma*

Physics. 11th IEEE NPSS Real Time Conference. Conference Record (Cat. No.99EX295), pages 116–118, 1999. doi:10.1109/RTCON.1999.842578. URL `https://bitbucket.org/tmidas/midas/src/develop/`.

[138] C. Green, J. Kowalkowski, M. Paterno, M. Fischler, L. Garren, and Q. Lu. The Art Framework. *J. Phys. Conf. Ser.*, 396:022020, 2012. doi:10.1088/1742-6596/396/2/022020.

[139] Rene Brun and Fons Rademakers. Root — an object oriented data analysis framework. *Nuclear Instruments and Methods in Physics Research Section A: Accelerators, Spectrometers, Detectors and Associated Equipment*, 389(1):81–86, 1997. ISSN 0168-9002. doi:https://doi.org/10.1016/S0168-9002(97)00048-X. URL `https://www.sciencedirect.com/science/article/pii/S016890029700048X`. New Computing Techniques in Physics Research V.

[140] Josh LaBounty. Recon East vs. Recon West Comparison. E989 DocDB 16604, 2019. URL `https://gm2-docdb.fnal.gov/cgi-bin/sso/ShowDocument?docid=16604`.

[141] Sean Foster. *Measurement of the muon anomalous precession frequency in runs 2 & 3 of the Muon g-2 Experiment at Fermilab*. PhD thesis, Boston University, 2023. URL `https://inspirehep.net/literature/2725166`.

[142] Cheng Chen. RW fitting threshold study. E989 DocDB 26964, 2022. URL `https://gm2-docdb.fnal.gov/cgi-bin/sso/ShowDocument?docid=26964`.

[143] Gaël Guennebaud, Benoît Jacob, et al. Eigen v3. http://eigen.tuxfamily.org, 2010.

[144] Pauli Virtanen, Ralf Gommers, Travis E. Oliphant, Matt Haberland, Tyler Reddy, David Cournapeau, Evgeni Burovski, Pearu Peterson, Warren Weckesser, Jonathan Bright, Stéfan J. van der Walt, Matthew Brett, Joshua Wilson, K. Jarrod Millman, Nikolay Mayorov, Andrew R. J. Nelson, Eric Jones, Robert Kern, Eric Larson, C J Carey, İlhan Polat, Yu Feng, Eric W. Moore, Jake VanderPlas, Denis Laxalde, Josef Perktold, Robert Cimrman, Ian Henriksen, E. A. Quintero, Charles R. Harris, Anne M. Archibald, Antônio H. Ribeiro, Fabian Pedregosa, Paul van Mulbregt, and SciPy 1.0 Contributors. SciPy 1.0: Fundamental Algorithms for

Scientific Computing in Python. *Nature Methods*, 17:261–272, 2020. doi:10.1038/s41592-019-0686-2.

[145] Paolo Girotti. Run-4/5 Temperature Changes and STDP correction. E989 DocDB 27961, 2022. URL `https://gm2-docdb.fnal.gov/cgi-bin/sso/ShowDocument?docid=27961`.

[146] Paolo Girotti. *Measurement of the muon anomalous precession frequency at the Muon $g-2$ Experiment at Fermilab*. PhD thesis, Pisa University, 2023. URL `https://inspirehep.net/literature/2738056`.

[147] Kim Siang Khaw. Nearline and offline updates. E989 DocDB 5652, 2017. URL `https://gm2-docdb.fnal.gov/cgi-bin/sso/ShowDocument?docid=5652`.

[148] Brendan Casey et al. Detector status. E989 DocDB 15193, 2018. URL `https://gm2-docdb.fnal.gov/cgi-bin/sso/ShowDocument?docid=15193`.

[149] Thomas Kluyver, Benjamin Ragan-Kelley, Fernando Pérez, Brian Granger, Matthias Bussonnier, Jonathan Frederic, Kyle Kelley, Jessica Hamrick, Jason Grout, Sylvain Corlay, Paul Ivanov, Damián Avila, Safia Abdalla, and Carol Willing. Jupyter notebooks – a publishing format for reproducible computational workflows. In F. Loizides and B. Schmidt, editors, *Positioning and Power in Academic Publishing: Players, Agents and Agendas*, pages 87 – 90. IOS Press, 2016.

[150] Hans Dembinski and Piti Ongmongkolkul et al. scikit-hep/iminuit. Dec 2020. doi:10.5281/zenodo.3949207. URL `https://doi.org/10.5281/zenodo.3949207`.

[151] F. James and M. Roos. Minuit: A System for Function Minimization and Analysis of the Parameter Errors and Correlations. *Comput. Phys. Commun.*, 10:343–367, 1975. doi:10.1016/0010-4655(75)90039-9.

[152] David Sweigart. *A Measurement of the Anomalous Precession Frequency of the Positive Muon.* PhD thesis, Cornell University, 2019. URL `https://inspirehep.net/literature/1773448`.

[153] J. Miller. Expressions for a(e) and n(e) in the lab frame. E821 Note 69, 1991.

[154] L Michel. Interaction between four half-spin particles and the decay of the *mu* meson. *Proc. Phys. Soc. (London)*, Vol: 63 A, 5 1950. doi:10.1088/0370-1298/63/5/311. URL `https://www.osti.gov/biblio/4424912`.

[155] Sean B Foster. Vertical frequencies in the BU analysis. E989 DocDB 29103, 2023. URL `https://gm2-docdb.fnal.gov/cgi-bin/sso/ShowDocument?docid=29103`.

[156] On Kim. Randomization kernel optimization. E989 DocDB 28169, 2022. URL `https://gm2-docdb.fnal.gov/cgi-bin/sso/ShowDocument?docid=28169`.

[157] Andy Edmonds. Generic CBO Envelope Notes. E989 DocDB 28208, 2023. URL `https://gm2-docdb.fnal.gov/cgi-bin/sso/ShowDocument?docid=28208`.

[158] James Mott et al. Systematics 101: CBO. E989 DocDB 27513, 2022. URL `https://gm2-docdb.fnal.gov/cgi-bin/sso/ShowDocument?docid=27513`.

[159] Tyler Barrett. Deriving Beam Dynamics Effects on the Wiggle Model from Scratch. E989 DocDB 29805, 2023. URL `https://gm2-docdb.fnal.gov/cgi-bin/sso/ShowDocument?docid=29805`.

[160] Esra Barlas Yucel. Comparison of Nominal and Moments Based Fit Type with IRMA fitter. E989 DocDB 24212, 2020. URL `https://gm2-docdb.fnal.gov/cgi-bin/sso/ShowDocument?docid=24212`.

[161] James Mott. Fitting sum of data from all calorimeters. E989 DocDB 25788, 2021. URL `https://gm2-docdb.fnal.gov/cgi-bin/sso/ShowDocument?docid=25788`.

[162] Hannah Binney. Time-changing CBO effect on 1.9 MHz frequency. E989 DocDB 26312, 2021. URL `https://gm2-docdb.fnal.gov/cgi-bin/sso/ShowDocument?docid=26312`.

[163] Kim Siang Khaw et al. Fit function, acceptance correlation and 1.9 MHz peak. E989 DocDB 26207, 2021. URL `https://gm2-docdb.fnal.gov/cgi-bin/sso/ShowDocument?docid=26207`.

[164] Josh LaBounty. Phase-Acceptance Maps: Calo Position Cuts. E989 DocDB 24730, 2021. URL `https://gm2-docdb.fnal.gov/cgi-bin/sso/ShowDocument?docid=24730`.

[165] Tyler Barrett et al. E989 Note 308: Cornell Run 2 and 3 Analysis Report. E989 DocDB 28103, 2023. URL `https://gm2-docdb.fnal.gov/cgi-bin/sso/ShowDocument?docid=28103`.

[166] Josh LaBounty. Lost Muon Detection Efficiency vs. Collimator Hit Position in gm2ringsim. E989 DocDB 22732, 2020. URL `https://gm2-docdb.fnal.gov/cgi-bin/sso/ShowDocument?docid=22732`.

[167] Zepyoor Khechadoorian. ReconEast start time scans Runs4-5 + short update on sliding fits using Tyler's new omega_a fitting technique. E989 DocDB 29931, 2024. URL `https://gm2-docdb.fnal.gov/cgi-bin/sso/ShowDocument?docid=29931`.

[168] Sean B Foster. Slow effect model testing. E989 DocDB 28221, 2022. URL `https://gm2-docdb.fnal.gov/cgi-bin/sso/ShowDocument?docid=28221`.

[169] David Sweigart. Investigations Related to Beam Displacement. E989 DocDB 18871, 2019. URL `https://gm2-docdb.fnal.gov/cgi-bin/sso/ShowDocument?docid=18871`.

[170] Josh LaBounty. Omega_a workshop systematic discussion: Residual Gain Correction. E989 DocDB 29231, 2023. URL `https://gm2-docdb.fnal.gov/cgi-bin/sso/ShowDocument?docid=29231`.

[171] Josh LaBounty. Quick Toy MC of A/T Differences. E989 DocDB 28825, 2023. URL `https://gm2-docdb.fnal.gov/cgi-bin/sso/ShowDocument?docid=28825`.

[172] Tyler Barrett. E989 Note 278: The Fast Rotation Fourier Method. E989 DocDB 26033, 2022. URL `https://gm2-docdb.fnal.gov/cgi-bin/sso/ShowDocument?docid=26033`.

[173] Josh LaBounty. Run-6 Momentum-Phase Measurements. E989 DocDB 28723, 2023. URL `https://gm2-docdb.fnal.gov/cgi-bin/sso/ShowDocument?docid=28723`.

[174] L. Bartoszek, E. Barnes, J. P. Miller, J. Mott, A. Palladino, J. Quirk, B. L. Roberts, J. Crnkovic, V. Polychronakos, V. Tishchenko, P. Yamin, C. h. Cheng, B. Echenard, K. Flood,

D. G. Hitlin, J. H. Kim, T. S. Miyashita, F. C. Porter, M. Röhrken, J. Trevor, R. Y. Zhu, E. Heckmaier, T. I. Kang, G. Lim, W. Molzon, Z. You, A. M. Artikov, J. A. Budagov, Yu. I. Davydov, V. V. Glagolev, A. V. Simonenko, Z. U. Usubov, S. H. Oh, C. Wang, G. Ambrosio, N. Andreev, D. Arnold, M. Ball, R. H. Bernstein, A. Bianchi, K. Biery, R. Bossert, M. Bowden, J. Brandt, G. Brown, H. Brown, M. Buehler, M. Campbell, S. Cheban, M. Chen, J. Coghill, R. Coleman, C. Crowley, A. Deshpande, G. Deuerling, J. Dey, N. Dhanaraj, M. Dinnon, S. Dixon, B. Drendel, N. Eddy, R. Evans, D. Evbota, J. Fagan, S. Feher, B. Fellenz, H. Friedsam, G. Gallo, A. Gaponenko, M. Gardner, S. Gaugel, K. Genser, G. Ginther, H. Glass, D. Glenzinski, D. Hahn, S. Hansen, B. Hartsell, S. Hays, J. A. Hocker, E. Huedem, D. Huffman, A. Ibrahim, C. Johnstone, V. Kashikhin, V. V. Kashikhin, P. Kasper, T. Kiper, D. Knapp, K. Knoepfel, L. Kokoska, M. Kozlovsky, G. Krafczyk, M. Kramp, S. Krave, K. Krempetz, R. K. Kutschke, R. Kwarciany, T. Lackowski, M. J. Lamm, M. Larwill, F. Leavell, D. Leeb, A. Leveling, D. Lincoln, V. Logashenko, V. Lombardo, M. L. Lopes, A. Makulski, A. Martinez, D. McArthur, F. McConologue, L. Michelotti, N. Mokhov, J. Morgan, A. Mukherjee, P. Murat, V. Nagaslaev, D. V. Neuffer, T. Nicol, J. Niehoff, J. Nogiec, M. Olson, D. Orris, R. Ostojic, T. Page, C. Park, T. Peterson, R. Pilipenko, A. Pla-Dalmau, V. Poloubotko, M. Popovic, E. Prebys, P. Prieto, V. Pronskikh, D. Pushka, R. Rabehl, R. E. Ray, R. Rechenmacher, R. Rivera, W. Robotham, P. Rubinov, V. L. Rusu, V. Scarpine, W. Schappert, D. Schoo, A. Stefanik, D. Still, Z. Tang, N. Tanovic, M. Tartaglia, G. Tassotto, D. Tinsley, R. S. Tschirhart, G. Vogel, R. Wagner, R. Wands, M. Wang, S. Werkema, H. B. White Jr. au2, J. Whitmore, R. Wielgos, R. Woods, C. Worel, R. Zifko, P. Ciambrone, F. Colao, M. Cordelli, G. Corradi, E. Dane, S. Giovannella, F. Happacher, A. Luca, S. Miscetti, B. Ponzio, G. Pileggi, A. Saputi, I. Sarra, R. S. Soleti, V. Stomaci, M. Martini, P. Fabbricatore, S. Farinon, R. Musenich, D. Alexander, A. Daniel, A. Empl, E. V. Hungerford, K. Lau, G. D. Gollin, C. Huang, D. Roderick, B. Trundy, D. Na. Brown, D. Ding, Yu. G. Kolomensky, M. J. Lee, M. Cascella, F. Grancagnolo, F. Ignatov, A. Innocente, A. L'Erario, A. Miccoli, A. Maffezzoli, P. Mazzotta, G. Onorato, G. M. Piacentino, S. Rella, F. Rossetti, M. Spedicato, G. Tassielli, A. Taurino, G. Zavarise, R. Hooper, D. No. Brown, R. Djilkibaev, V. Matushko,

C. Ankenbrandt, S. Boi, A. Dychkant, D. Hedin, Z. Hodge, V. Khalatian, R. Majewski, L. Martin, U. Okafor, N. Pohlman, R. S. Riddel, A. Shellito, A. L. de Gouvea, F. Cervelli, R. Carosi, S. Di Falco, S. Donati, T. Lomtadze, G. Pezzullo, L. Ristori, F. Spinella, M. Jones, M. D. Corcoran, J. Orduna, D. Rivera, R. Bennett, O. Caretta, T. Davenne, C. Densham, P. Loveridge, J. Odell, R. Bomgardner, E. C. Dukes, R. Ehrlich, M. Frank, S. Goadhouse, R. Group, E. Ho, H. Ma, Y. Oksuzian, J. Purvis, Y. Wu, D. W. Hertzog, P. Kammel, K. R. Lynch, and J. L. Popp. Mu2e technical design report, 2015.

[175] Sean B Foster. Background High Energy Events. E989 DocDB 25937, 2021. URL `https://gm2-docdb.fnal.gov/cgi-bin/sso/ShowDocument?docid=25937`.

[176] Sam Grant. E989 Note 284: Radial magnetic field measurements for an EDM search. E989 DocDB 26692, 2022. URL `https://gm2-docdb.fnal.gov/cgi-bin/sso/ShowDocument?docid=26692`.

[177] Elia Bottalico. First look at Phase acceptance Run-4/5. E989 DocDB 29290, 2023. URL `https://gm2-docdb.fnal.gov/cgi-bin/sso/ShowDocument?docid=29290`.

[178] James Mott. CBO Freq Change in Run 1 Datasets. E989 DocDB 20586, 2019. URL `https://gm2-docdb.fnal.gov/cgi-bin/sso/ShowDocument?docid=20586`.

[179] Volodja Tishchenko. High Voltage Pulser for Electrostatic Focusing Quadrupoles: User Manual. E989 DocDB 4417, 2016. URL `https://gm2-docdb.fnal.gov/cgi-bin/sso/ShowDocument?docid=4417`.

[180] Bill Morse. Voltage Change on Quad Electrodes. E989 DocDB 11352, 2020. URL `https://gm2-docdb.fnal.gov/cgi-bin/sso/ShowDocument?docid=11352`.

[181] Elia Bottalico. Attempt to model the variable CBO in Run-5/6 - Update. E989 DocDB 29911, 2024. URL `https://gm2-docdb.fnal.gov/cgi-bin/sso/ShowDocument?docid=29911`.

[182] Jürgen Mayer, Khaled Khairy, and Jonathon Howard. Drawing an elephant with four complex parameters. *American Journal of Physics*, 78(6):648–649, 06 2010. ISSN 0002-9505. doi:10.1119/1.3254017. URL `https://doi.org/10.1119/1.3254017`.

[183] Elia Bottalico. Variable CBO in Run-5/6 - Update. E989 DocDB 29978, 2024. URL `https://gm2-docdb.fnal.gov/cgi-bin/sso/ShowDocument?docid=29978`.

[184] Peter Athron, Csaba Balázs, Douglas H. J. Jacob, Wojciech Kotlarski, Dominik Stöckinger, and Hyejung Stöckinger-Kim. New physics explanations of a in light of the final muon g − 2 measurement. *Journal of High Energy Physics*, 2021(9), September 2021. ISSN 1029-8479. doi:10.1007/jhep09(2021)080. URL `http://dx.doi.org/10.1007/JHEP09(2021)080`.

[185] Claudia Cornella, Paride Paradisi, and Olcyr Sumensari. Hunting for alps with lepton flavor violation. *Journal of High Energy Physics*, 2020(1):158, Jan 2020. ISSN 1029-8479. doi:10.1007/JHEP01(2020)158. URL `https://doi.org/10.1007/JHEP01(2020)158`.

[186] G.C. Branco, P.M. Ferreira, L. Lavoura, M.N. Rebelo, Marc Sher, and João P. Silva. Theory and phenomenology of two-higgs-doublet models. *Physics Reports*, 516(1):1–102, 2012. ISSN 0370-1573. doi:https://doi.org/10.1016/j.physrep.2012.02.002. URL `https://www.sciencedirect.com/science/article/pii/S0370157312000695`. Theory and phenomenology of two-Higgs-doublet models.

[187] Peter Athron, Csaba Balazs, Adriano Cherchiglia, Douglas Jacob, Dominik Stöckinger, Hyejung Stöckinger-Kim, and Alexander Voigt. Two-loop prediction of the anomalous magnetic moment of the muon in the two-higgs doublet model with gm2calc 2. *The European Physical Journal C*, 82(3):229, Mar 2022. ISSN 1434-6052. doi:10.1140/epjc/s10052-022-10148-9. URL `https://doi.org/10.1140/epjc/s10052-022-10148-9`.

[188] Michihisa Takeuchi, Syuhei Iguro, Teppei Kitahara, and Martin S. Lang. Current status of the muon $g-2$ interpretations within two-higgs-doublet models. *Phys. Rev. D*, 108:115012, Dec 2023. doi:10.1103/PhysRevD.108.115012. URL `https://link.aps.org/doi/10.1103/PhysRevD.108.115012`.

[189] Luca Di Luzio, Antonio Masiero, Paride Paradisi, and Massimo Passera. New physics behind the new muon g-2 puzzle? *Physics Letters B*, 829:137037, 2022. ISSN 0370-2693. doi:https://-

doi.org/10.1016/j.physletb.2022.137037. URL `https://www.sciencedirect.com/science/article/pii/S037026932200171X`.

[190] Alexander Keshavarzi, William J. Marciano, Massimo Passera, and Alberto Sirlin. Muon $g-2$ and α connection. *Phys. Rev. D*, 102:033002, Aug 2020. doi:10.1103/PhysRevD.102.033002. URL `https://link.aps.org/doi/10.1103/PhysRevD.102.033002`.

[191] Luc Darmé, Giovanni Grilli di Cortona, and Enrico Nardi. The muon $\mathrm{g}-2$ anomaly confronts new physics in e± and μ± final states scattering. *Journal of High Energy Physics*, 2022(6): 122, Jun 2022. ISSN 1029-8479. doi:10.1007/JHEP06(2022)122. URL `https://doi.org/10.1007/JHEP06(2022)122`.

[192] David W. Hertzog. Low-energy precision tests of the standard model: a snapshot. *Annalen der Physik*, 528(1-2):115–122, 2016. doi:https://doi.org/10.1002/andp.201500167. URL `https://onlinelibrary.wiley.com/doi/abs/10.1002/andp.201500167`.

[193] Weiwen Liu et al. High precision measurements of the ground state hyperfine structure interval of muonium and of the muon magnetic moment. *Phys. Rev. Lett.*, 82:711–714, 1999. doi:10.1103/PhysRevLett.82.711.

[194] Josh LaBounty. DAQ High Rate Test Overview. E989 DocDB 13294, 2018. URL `https://gm2-docdb.fnal.gov/cgi-bin/sso/ShowDocument?docid=13294`.

[195] Josh LaBounty. Average Crystal Occupancy for Islands in Calorimeter. E989 DocDB 13297, 2018. URL `https://gm2-docdb.fnal.gov/cgi-bin/sso/ShowDocument?docid=13297`.

[196] Josh LaBounty. DAQ New Frontend Tests. E989 DocDB 13519, 2018. URL `https://gm2-docdb.fnal.gov/cgi-bin/sso/ShowDocument?docid=13519`.

[197] Josh LaBounty. DAQ CT vs. TT Banks. E989 DocDB 14689, 2018. URL `https://gm2-docdb.fnal.gov/cgi-bin/sso/ShowDocument?docid=14689`.

[198] Josh LaBounty. CT vs. TT Banks in Run 2 Data. E989 DocDB 19030, 2019. URL `https://gm2-docdb.fnal.gov/cgi-bin/sso/ShowDocument?docid=19030`.

[199] Josh LaBounty. Nearline Summary. E989 DocDB 16913, 2019. URL `https://gm2-docdb.fnal.gov/cgi-bin/sso/ShowDocument?docid=16913`.

[200] Josh LaBounty. First Look at the Nearline Run 2 Pre-Physics Data. E989 DocDB 16988, 2019. URL `https://gm2-docdb.fnal.gov/cgi-bin/sso/ShowDocument?docid=16988`.

[201] Josh LaBounty. Nearline Documentation. E989 DocDB 16180, 2019. URL `https://gm2-docdb.fnal.gov/cgi-bin/sso/ShowDocument?docid=16180`.

[202] Josh LaBounty. Online & Nearline Toolbox. E989 DocDB 26059, 2021. URL `https://gm2-docdb.fnal.gov/cgi-bin/sso/ShowDocument?docid=26059`.

[203] Josh LaBounty. Calorimeter/T-method v9_05_00 Production Report. E989 DocDB 13891, 2018. URL `https://gm2-docdb.fnal.gov/cgi-bin/sso/ShowDocument?docid=13891`.

[204] Josh LaBounty. Calorimeter/T-method v9_07_00 Production Report + Odd Laser Events. E989 DocDB 14130, 2018. URL `https://gm2-docdb.fnal.gov/cgi-bin/sso/ShowDocument?docid=14130`.

[205] Josh LaBounty. Calorimeter/T-method v9_08_00 Production Report. E989 DocDB 14307, 2018. URL `https://gm2-docdb.fnal.gov/cgi-bin/sso/ShowDocument?docid=14307`.

[206] Josh LaBounty. Calorimeter/T-method v9_10_00 Production Report. E989 DocDB 14779, 2018. URL `https://gm2-docdb.fnal.gov/cgi-bin/sso/ShowDocument?docid=14779`.

[207] Josh LaBounty. EndGame 5042A Calorimeter Production Verification. E989 DocDB 20733, 2019. URL `https://gm2-docdb.fnal.gov/cgi-bin/sso/ShowDocument?docid=20733`.

[208] Josh LaBounty. Fill-By-Fill DQC Monitor for Production. E989 DocDB 23149, 2020. URL `https://gm2-docdb.fnal.gov/cgi-bin/sso/ShowDocument?docid=23149`.

[209] Josh LaBounty. Subrun DQC: Run 2E, 2G, and 2H. E989 DocDB 23760, 2020. URL `https://gm2-docdb.fnal.gov/cgi-bin/sso/ShowDocument?docid=23760`.

[210] Josh LaBounty. DQC Skim Mysteries: Nearline vs. Offline CTAGs in Run 2C. E989 DocDB 25340, 2021. URL `https://gm2-docdb.fnal.gov/cgi-bin/sso/ShowDocument?docid=25340`.

[211] Josh LaBounty. Nearline CTAG Plot Problems and Resolution. E989 DocDB 25418, 2021. URL `https://gm2-docdb.fnal.gov/cgi-bin/sso/ShowDocument?docid=25418`.

[212] Josh LaBounty. Run 3C: Subruns with 2 Calos Missing. E989 DocDB 25548, 2021. URL `https://gm2-docdb.fnal.gov/cgi-bin/sso/ShowDocument?docid=25548`.

[213] Josh LaBounty. Template Paths in the Database. E989 DocDB 25365, 2021. URL `https://gm2-docdb.fnal.gov/cgi-bin/sso/ShowDocument?docid=25365`.

[214] Josh LaBounty. Channel Statuses at the Subrun Level. E989 DocDB 25396, 2021. URL `https://gm2-docdb.fnal.gov/cgi-bin/sso/ShowDocument?docid=25396`.

[215] Josh LaBounty. Run 2C Timing Alignment Constants. E989 DocDB 25437, 2021. URL `https://gm2-docdb.fnal.gov/cgi-bin/sso/ShowDocument?docid=25437`.

[216] Josh LaBounty. Run-6 Calorimeter Constants Status. E989 DocDB 27978, 2022. URL `https://gm2-docdb.fnal.gov/cgi-bin/sso/ShowDocument?docid=27978`.

[217] Josh LaBounty. Calo 7 in Run-6: Cutting out Xtal 26/35. E989 DocDB 28926, 2023. URL `https://gm2-docdb.fnal.gov/cgi-bin/sso/ShowDocument?docid=28926`.

[218] Hannah Binney et al. Run 2 snapshot. E989 DocDB 20625, 2019. URL `https://gm2-docdb.fnal.gov/cgi-bin/sso/ShowDocument?docid=20625`.

[219] Josh LaBounty. Run 3 Trend Plots and Preliminary Datasets. E989 DocDB 22276, 2020. URL `https://gm2-docdb.fnal.gov/cgi-bin/sso/ShowDocument?docid=22276`.

[220] Josh LaBounty. Proposal for Initial Run-4 Datasets. E989 DocDB 25393, 2021. URL `https://gm2-docdb.fnal.gov/cgi-bin/sso/ShowDocument?docid=25393`.

[221] Andy Edmonds et al. Skim File Data Products Spreadsheet. E989 DocDB 28499, 2023. URL `https://gm2-docdb.fnal.gov/cgi-bin/sso/ShowDocument?docid=28499`.

[222] Josh LaBounty. What's Wrong with Calorimeter 2? E989 DocDB 12539, 2018. URL `https://gm2-docdb.fnal.gov/cgi-bin/sso/ShowDocument?docid=12539`.

[223] Josh LaBounty. Calo Current Drift. E989 DocDB 26739, 2022. URL `https://gm2-docdb.fnal.gov/cgi-bin/sso/ShowDocument?docid=26739`.

[224] Josh LaBounty. Chi-Square Energy Spectrum Fits. E989 DocDB 23269, 2020. URL `https://gm2-docdb.fnal.gov/cgi-bin/sso/ShowDocument?docid=23269`.

[225] Josh LaBounty. Recon East vs. Recon West Comparison. E989 DocDB 15367, 2018. URL `https://gm2-docdb.fnal.gov/cgi-bin/sso/ShowDocument?docid=15367`.

[226] Josh LaBounty. Comparison of 'Raw' 60h Histograms from Omega_a Analyzers. E989 DocDB 21189, 2020. URL `https://gm2-docdb.fnal.gov/cgi-bin/sso/ShowDocument?docid=21189`.

[227] Josh LaBounty. Recon East vs. Recon West for Final Run 1 Datasets. E989 DocDB 21341, 2020. URL `https://gm2-docdb.fnal.gov/cgi-bin/sso/ShowDocument?docid=21341`.

[228] Josh LaBounty. Allowed Statistical Variation Between Recon East and Recon West. E989 DocDB 21567, 2020. URL `https://gm2-docdb.fnal.gov/cgi-bin/sso/ShowDocument?docid=21567`.

[229] Josh LaBounty. The Trouble with Triples: Muon Losses in Runs 2 and 3. E989 DocDB 24303, 2020. URL `https://gm2-docdb.fnal.gov/cgi-bin/sso/ShowDocument?docid=24303`.

[230] Josh LaBounty. Initial Results from DR Scraper Study. E989 DocDB 25447, 2021. URL `https://gm2-docdb.fnal.gov/cgi-bin/sso/ShowDocument?docid=25447`.

[231] Hannah Binney et al. Lost Muon Systematic in Run 2+. E989 DocDB 25638, 2021. URL `https://gm2-docdb.fnal.gov/cgi-bin/sso/ShowDocument?docid=25638`.

[232] Josh LaBounty. Run-2 Lost Muon Bump: Run-6 Study Proposal. E989 DocDB 27826, 2022. URL `https://gm2-docdb.fnal.gov/cgi-bin/sso/ShowDocument?docid=27826`.

[233] Josh LaBounty. Update: Muon Loss Systematic in Runs-2/3. E989 DocDB 28376, 2023. URL `https://gm2-docdb.fnal.gov/cgi-bin/sso/ShowDocument?docid=28376`.

[234] Josh LaBounty. Muon Losses and Cml in Run-2/3. E989 DocDB 28696, 2023. URL `https://gm2-docdb.fnal.gov/cgi-bin/sso/ShowDocument?docid=28696`.

[235] Kim Siang Khaw et al. Launched particles in Run 2 data. E989 DocDB 17089, 2019. URL `https://gm2-docdb.fnal.gov/cgi-bin/sso/ShowDocument?docid=17089`.

[236] Josh LaBounty. Protons in Run 4A (And Beyond). E989 DocDB 27645, 2022. URL `https://gm2-docdb.fnal.gov/cgi-bin/sso/ShowDocument?docid=27645`.

[237] Josh LaBounty. Muons, Protons, and Deuterons in Run-4/5. E989 DocDB 29283, 2023. URL `https://gm2-docdb.fnal.gov/cgi-bin/sso/ShowDocument?docid=29283`.

[238] Josh LaBounty. Run-6 Phase-Momentum Study Update and A Simplified Wedge Model. E989 DocDB 28588, 2023. URL `https://gm2-docdb.fnal.gov/cgi-bin/sso/ShowDocument?docid=28588`.

[239] Lars E Borchert et al. Calorimeter y Mean vs Time. E989 DocDB 22627, 2020. URL `https://gm2-docdb.fnal.gov/cgi-bin/sso/ShowDocument?docid=22627`.

[240] Josh LaBounty. y-RMS ADT Scan in EndGame and Run 2C. E989 DocDB 23034, 2020. URL `https://gm2-docdb.fnal.gov/cgi-bin/sso/ShowDocument?docid=23034`.

[241] Josh LaBounty. Comparing Clusters to Tracks: EndGame vs. Run-2C. E989 DocDB 22873, 2020. URL `https://gm2-docdb.fnal.gov/cgi-bin/sso/ShowDocument?docid=22873`.

[242] Elia Bottalico et al. E989 Note 262: Phase Acceptance Correction Analysis Report. E989 DocDB 24796, 2021. URL `https://gm2-docdb.fnal.gov/cgi-bin/sso/ShowDocument?docid=24796`.

[243] Anna Driutti et al. Calo y-Mean Comparisons with COSY/gm2ringsim. E989 DocDB 24886, 2021. URL `https://gm2-docdb.fnal.gov/cgi-bin/sso/ShowDocument?docid=24886`.

[244] Elia Bottalico et al. E989 Note 292: Phase Acceptance Note - Run-2/3. E989 DocDB 28030, 2023. URL `https://gm2-docdb.fnal.gov/cgi-bin/sso/ShowDocument?docid=28030`.

[245] Josh LaBounty. Using Laser Fills in omega_a Analysis via Masking. E989 DocDB 25771, 2021. URL `https://gm2-docdb.fnal.gov/cgi-bin/sso/ShowDocument?docid=25771`.

[246] Josh LaBounty. Masking/Re-Weighting Laser Fills. E989 DocDB 25871, 2021. URL `https://gm2-docdb.fnal.gov/cgi-bin/sso/ShowDocument?docid=25871`.

[247] Josh LaBounty. Run-6 Systematic Study Updates. E989 DocDB 28565, 2023. URL `https://gm2-docdb.fnal.gov/cgi-bin/sso/ShowDocument?docid=28565`.

[248] Josh LaBounty. Acceptance Maps - Potential for Data Driven Verification. E989 DocDB 29238, 2023. URL `https://gm2-docdb.fnal.gov/cgi-bin/sso/ShowDocument?docid=29238`.

[249] Esra Barlas Yucel et al. Run 2/3 Muon Precession Analysis Internal Review. E989 DocDB 28618, 2023. URL `https://gm2-docdb.fnal.gov/cgi-bin/sso/ShowDocument?docid=28618`.

[250] Josh LaBounty. Omega_a workshop - Run-4/5/6 random thoughts. E989 DocDB 28731, 2023. URL `https://gm2-docdb.fnal.gov/cgi-bin/sso/ShowDocument?docid=28731`.

[251] Josh LaBounty et al. Run-4/5/6: Omega-a Analysis. E989 DocDB 28761, 2023. URL `https://gm2-docdb.fnal.gov/cgi-bin/sso/ShowDocument?docid=28761`.

[252] Josh LaBounty. A Quick Look at Some Run-4/5/6 Puzzles: Run-4 Residual Gain and Run-5 CBO Amplitude/Frequency. E989 DocDB 29044, 2023. URL `https://gm2-docdb.fnal.gov/cgi-bin/sso/ShowDocument?docid=29044`.

[253] Josh LaBounty. Sensitivity of the UW Analysis to the Vertical Terms. E989 DocDB 29106, 2023. URL `https://gm2-docdb.fnal.gov/cgi-bin/sso/ShowDocument?docid=29106`.

[254] Josh LaBounty. Summary of the omega_a analyzer group survey. E989 DocDB 29235, 2023. URL `https://gm2-docdb.fnal.gov/cgi-bin/sso/ShowDocument?docid=29235`.

[255] Josh LaBounty. Changing CBO Frequency in Run-4/5. E989 DocDB 29280, 2023. URL `https://gm2-docdb.fnal.gov/cgi-bin/sso/ShowDocument?docid=29280`.

[256] Josh LaBounty. Introduction to ROOT and g-2 computing for Undergraduates. E989 DocDB 23073, 2020. URL `https://gm2-docdb.fnal.gov/cgi-bin/sso/ShowDocument?docid=23073`.

[257] Josh LaBounty. Introduction to g-2 Calorimeter Reconstruction Chain for Undergraduates. E989 DocDB 23239, 2020. URL `https://gm2-docdb.fnal.gov/cgi-bin/sso/ShowDocument?docid=23239`.

[258] Josh LaBounty. g-2 Undergraduate Questions. E989 DocDB 23381, 2020. URL `https://gm2-docdb.fnal.gov/cgi-bin/sso/ShowDocument?docid=23381`.

[259] Josh LaBounty. Standing on The Shoulders of Giants: Past, Present, and Future of Muon g-2. E989 DocDB 23420, 2020. URL `https://gm2-docdb.fnal.gov/cgi-bin/sso/ShowDocument?docid=23420`.

[260] Josh LaBounty. Thinking Like a Physicist: How Subatomic Tops Teach Us To Embrace Being Wrong. E989 DocDB 25343, 2021. URL `https://gm2-docdb.fnal.gov/cgi-bin/sso/ShowDocument?docid=25343`.

[261] Josh LaBounty. Future Opportunities: PIONEER. E989 DocDB 27498, 2022. URL `https://gm2-docdb.fnal.gov/cgi-bin/sso/ShowDocument?docid=27498`.

Appendix A

A Brief Tour of $g - 2$ Internal Documents and Presentations Prepared by the Author

Over the last several years, the author has contributed to a number of studies and improvements throughout the experiment. Presented here is a short list of contributions, compiled upon a request from a reader, along with references to the relevant internal documentation. Copies of these internal documents are available to the reader upon request.

A.1 Software

A.1.1 DAQ Improvements

In the shutdown between Run-1 and Run-2, the author worked with others to implement and test a novel island chopping technique that reduced the overall (chopped island) data rate from the calorimeters by 25% (75%). The author also served as a DAQ on-call expert for Run-2/3.

[194] Josh LaBounty. DAQ High Rate Test Overview. E989 DocDB 13294, 2018. URL `https://gm2-docdb.fnal.gov/cgi-bin/sso/ShowDocument?docid=13294`

[195] Josh LaBounty. Average Crystal Occupancy for Islands in Calorimeter. E989 DocDB 13297,

2018. URL `https://gm2-docdb.fnal.gov/cgi-bin/sso/ShowDocument?docid=13297`

[196] Josh LaBounty. DAQ New Frontend Tests. E989 DocDB 13519, 2018. URL `https://gm2-docdb.fnal.gov/cgi-bin/sso/ShowDocument?docid=13519`

[134] Josh LaBounty. DAQ Crystal Chopping Overview. E989 DocDB 13723, 2018. URL `https://gm2-docdb.fnal.gov/cgi-bin/sso/ShowDocument?docid=13723`

[197] Josh LaBounty. DAQ CT vs. TT Banks. E989 DocDB 14689, 2018. URL `https://gm2-docdb.fnal.gov/cgi-bin/sso/ShowDocument?docid=14689`

[198] Josh LaBounty. CT vs. TT Banks in Run 2 Data. E989 DocDB 19030, 2019. URL `https://gm2-docdb.fnal.gov/cgi-bin/sso/ShowDocument?docid=19030`

A.1.2 Nearline

The author managed the nearline analysis chain from Run-2 through the end of the experiment. This analysis chain was used by countless systematic studies which required $\mathcal{O}$(hour) turnaround time for their results. These included beam tuning studies, real-time data integrity verification, and others.

[199] Josh LaBounty. Nearline Summary. E989 DocDB 16913, 2019. URL `https://gm2-docdb.fnal.gov/cgi-bin/sso/ShowDocument?docid=16913`

[200] Josh LaBounty. First Look at the Nearline Run 2 Pre-Physics Data. E989 DocDB 16988, 2019. URL `https://gm2-docdb.fnal.gov/cgi-bin/sso/ShowDocument?docid=16988`

[201] Josh LaBounty. Nearline Documentation. E989 DocDB 16180, 2019. URL `https://gm2-docdb.fnal.gov/cgi-bin/sso/ShowDocument?docid=16180`

[202] Josh LaBounty. Online & Nearline Toolbox. E989 DocDB 26059, 2021. URL `https://gm2-docdb.fnal.gov/cgi-bin/sso/ShowDocument?docid=26059`

A.1.3 Production Verification

For the Run-1 production, before the automated DQC checks were put into place and while the reconstruction chain was still in a ‘beta’ phase, the author was responsible for manually checking a production dataset after each software update. The same set of files would be processed through the updated software, and any unexpected changes would be noted and (if necessary) addressed in a patch.

[203] Josh LaBounty. Calorimeter/T-method v9_05_00 Production Report. E989 DocDB 13891, 2018. URL `https://gm2-docdb.fnal.gov/cgi-bin/sso/ShowDocument?docid=13891`

[204] Josh LaBounty. Calorimeter/T-method v9_07_00 Production Report + Odd Laser Events. E989 DocDB 14130, 2018. URL `https://gm2-docdb.fnal.gov/cgi-bin/sso/ShowDocument?docid=14130`

[205] Josh LaBounty. Calorimeter/T-method v9_08_00 Production Report. E989 DocDB 14307, 2018. URL `https://gm2-docdb.fnal.gov/cgi-bin/sso/ShowDocument?docid=14307`

[206] Josh LaBounty. Calorimeter/T-method v9_10_00 Production Report. E989 DocDB 14779, 2018. URL `https://gm2-docdb.fnal.gov/cgi-bin/sso/ShowDocument?docid=14779`

[207] Josh LaBounty. EndGame 5042A Calorimeter Production Verification. E989 DocDB 20733, 2019. URL `https://gm2-docdb.fnal.gov/cgi-bin/sso/ShowDocument?docid=20733`

A.1.4 DQC

As detailed in Section 4.2.3.3, the author made contributions to setting up the DQC workflow for Run-2+. This involved the development of new DQC monitors (*art* filters and an analyzer for their outputs) for the production chain. The author also served as a calorimeter expert and would be called in for a 'consultation' whenever problems were noted in an individual calorimeter during the DQC process.

[208] Josh LaBounty. Fill-By-Fill DQC Monitor for Production. E989 DocDB 23149, 2020. URL `https://gm2-docdb.fnal.gov/cgi-bin/sso/ShowDocument?docid=23149`

[209] Josh LaBounty. Subrun DQC: Run 2E, 2G, and 2H. E989 DocDB 23760, 2020. URL `https://gm2-docdb.fnal.gov/cgi-bin/sso/ShowDocument?docid=23760`

[210] Josh LaBounty. DQC Skim Mysteries: Nearline vs. Offline CTAGs in Run 2C. E989 DocDB 25340, 2021. URL `https://gm2-docdb.fnal.gov/cgi-bin/sso/ShowDocument?docid=25340`

[211] Josh LaBounty. Nearline CTAG Plot Problems and Resolution. E989 DocDB 25418, 2021. URL `https://gm2-docdb.fnal.gov/cgi-bin/sso/ShowDocument?docid=25418`

[212] Josh LaBounty. Run 3C: Subruns with 2 Calos Missing. E989 DocDB 25548, 2021. URL `https://gm2-docdb.fnal.gov/cgi-bin/sso/ShowDocument?docid=25548`

A.1.5 Constants analysis and production conditions database

The author was responsible for computing (where applicable) the following constants and uploading them to the conditions database:

- Recon West Calorimeter Timing and Energy calibration constants, by run [Run-3+]
- Calorimeter channel statuses, by subrun [Run-3+]
- Paths to template files to be used by the fitter, by run [Run-2+]

This built on work by J. Hempstead [91] and others.

[213] Josh LaBounty. Template Paths in the Database. E989 DocDB 25365, 2021. URL `https://gm2-docdb.fnal.gov/cgi-bin/sso/ShowDocument?docid=25365`

[214] Josh LaBounty. Channel Statuses at the Subrun Level. E989 DocDB 25396, 2021. URL `https://gm2-docdb.fnal.gov/cgi-bin/sso/ShowDocument?docid=25396`

[215] Josh LaBounty. Run 2C Timing Alignment Constants. E989 DocDB 25437, 2021. URL `https://gm2-docdb.fnal.gov/cgi-bin/sso/ShowDocument?docid=25437`

[216] Josh LaBounty. Run-6 Calorimeter Constants Status. E989 DocDB 27978, 2022. URL `https://gm2-docdb.fnal.gov/cgi-bin/sso/ShowDocument?docid=27978`

[217] Josh LaBounty. Calo 7 in Run-6: Cutting out Xtal 26/35. E989 DocDB 28926, 2023. URL `https://gm2-docdb.fnal.gov/cgi-bin/sso/ShowDocument?docid=28926`

A.1.6 Production Dataset Definition

The author, with significant input from H. Binney for the Run-2 process, was responsible for preparing the dataset definitions used by the reconstruction for Run-2 through the end of the experiment.

[218] Hannah Binney et al. Run 2 snapshot. E989 DocDB 20625, 2019. URL `https://gm2-docdb.fnal.gov/cgi-bin/sso/ShowDocument?docid=20625`

[219] Josh LaBounty. Run 3 Trend Plots and Preliminary Datasets. E989 DocDB 22276, 2020. URL `https://gm2-docdb.fnal.gov/cgi-bin/sso/ShowDocument?docid=22276`

[220] Josh LaBounty. Proposal for Initial Run-4 Datasets. E989 DocDB 25393, 2021. URL `https://gm2-docdb.fnal.gov/cgi-bin/sso/ShowDocument?docid=25393`

A.1.7 Development of *art* Skim Files

The author aided in the preparation of the *art* skim files used by the Recon West groups, identifying which dataproducts were crucial to the nominal ω_a analysis and which were able to be dropped.

[221] Andy Edmonds et al. Skim File Data Products Spreadsheet. E989 DocDB 28499, 2023. URL `https://gm2-docdb.fnal.gov/cgi-bin/sso/ShowDocument?docid=28499`

A.2 Hardware

The author was a detector operations manager from Run-2 to the end of the experiment. This involved a significant amount of on-call support whenever the detector systems (with a special focus on the calorimeters) were behaving abnormally. Most of the Run-4+ time was spent doing this remotely, but from the summer before Run-1 to the end of Run-3 the author spent significant time at Fermilab.

[222] Josh LaBounty. What's Wrong with Calorimeter 2? E989 DocDB 12539, 2018. URL `https://gm2-docdb.fnal.gov/cgi-bin/sso/ShowDocument?docid=12539`

[223] Josh LaBounty. Calo Current Drift. E989 DocDB 26739, 2022. URL `https://gm2-docdb.fnal.gov/cgi-bin/sso/ShowDocument?docid=26739`

A.3 Analysis

A.3.1 Novel Analysis Attempts

A number of attempts have been made to try and construct analyses which are more robust against our various systematics. These involved novel fitting methods, additional fiducial cuts on the data, matching hits between the calorimeters and tracking detectors, and others. None of the investigations here yielded 'concrete' gains, but they were interesting nonetheless.

[224] Josh LaBounty. Chi-Square Energy Spectrum Fits. E989 DocDB 23269, 2020. URL `https://gm2-docdb.fnal.gov/cgi-bin/sso/ShowDocument?docid=23269`
Josh LaBounty. Restricting the Calorimeter Fiducial Volume. UW Group Meeting, 2023.

A.3.2 Run-1 Reconstruction Comparison

The author was responsible for doing reconstruction method comparisons for the Run-1 analysis. See Section 4.1.6.1 for more details.

[225] Josh LaBounty. Recon East vs. Recon West Comparison. E989 DocDB 15367, 2018. URL `https://gm2-docdb.fnal.gov/cgi-bin/sso/ShowDocument?docid=15367`
[140] Josh LaBounty. Recon East vs. Recon West Comparison. E989 DocDB 16604, 2019. URL `https://gm2-docdb.fnal.gov/cgi-bin/sso/ShowDocument?docid=16604`
[226] Josh LaBounty. Comparison of 'Raw' 60h Histograms from Omega_a Analyzers. E989 DocDB 21189, 2020. URL `https://gm2-docdb.fnal.gov/cgi-bin/sso/ShowDocument?docid=21189`
[227] Josh LaBounty. Recon East vs. Recon West for Final Run 1 Datasets. E989 DocDB 21341, 2020. URL `https://gm2-docdb.fnal.gov/cgi-bin/sso/ShowDocument?docid=21341`
[228] Josh LaBounty. Allowed Statistical Variation Between Recon East and Recon West. E989 DocDB 21567, 2020. URL `https://gm2-docdb.fnal.gov/cgi-bin/sso/ShowDocument?docid=21567`

A.3.3 Systematic Studies

Before the Run-4+ data was available, the author spent most of their time with evaluations of systematic effects. Many of these are detailed in the text, but additional citations are reproduced here for convenience.

A.3.3.1 Muon Losses

The author, and the UW group in general, spent a significant amount of time looking into the behavior of the lost muons. These studies included both data driven looks into the behavior of the lost muons — leading to the calculation of C_{ml} for Run-1 — and simulation. Simulations were crucial to determining that the loss spectrum measured by the calorimeters was not biased from the true loss rate by acceptance effects. Details on the implications of these studies can be found in Section 5.3.8.

[166] Josh LaBounty. Lost Muon Detection Efficiency vs. Collimator Hit Position in gm2ringsim. E989 DocDB 22732, 2020. URL `https://gm2-docdb.fnal.gov/cgi-bin/sso/ShowDocument?docid=22732`

[229] Josh LaBounty. The Trouble with Triples: Muon Losses in Runs 2 and 3. E989 DocDB 24303, 2020. URL `https://gm2-docdb.fnal.gov/cgi-bin/sso/ShowDocument?docid=24303`

[230] Josh LaBounty. Initial Results from DR Scraper Study. E989 DocDB 25447, 2021. URL `https://gm2-docdb.fnal.gov/cgi-bin/sso/ShowDocument?docid=25447`

[231] Hannah Binney et al. Lost Muon Systematic in Run 2+. E989 DocDB 25638, 2021. URL `https://gm2-docdb.fnal.gov/cgi-bin/sso/ShowDocument?docid=25638`

[232] Josh LaBounty. Run-2 Lost Muon Bump: Run-6 Study Proposal. E989 DocDB 27826, 2022. URL `https://gm2-docdb.fnal.gov/cgi-bin/sso/ShowDocument?docid=27826`

[233] Josh LaBounty. Update: Muon Loss Systematic in Runs-2/3. E989 DocDB 28376, 2023. URL `https://gm2-docdb.fnal.gov/cgi-bin/sso/ShowDocument?docid=28376`

[122] Josh LaBounty. E989 Note 303: Muon Losses and Estimation of C_ml in Run-2/3. E989 DocDB 28451, 2023. URL `https://gm2-docdb.fnal.gov/cgi-bin/sso/ShowDocument?docid=28451`

[234] Josh LaBounty. Muon Losses and Cml in Run-2/3. E989 DocDB 28696, 2023. URL `https://gm2-docdb.fnal.gov/cgi-bin/sso/ShowDocument?docid=28696`

A.3.3.2 Protons and Deuterons

Particles which are not muons or positrons have the potential to introduce backgrounds into the analysis if not properly accounted for. Great care was taken by the author to identify these particles in the data — to the best of our knowledge, just protons and deuterons — and ensure they do not couple to our extraction of ω_a. More details can be found in the text (Section 6.2).

[235] Kim Siang Khaw et al. Launched particles in Run 2 data. E989 DocDB 17089, 2019. URL `https://gm2-docdb.fnal.gov/cgi-bin/sso/ShowDocument?docid=17089`

[236] Josh LaBounty. Protons in Run 4A (And Beyond). E989 DocDB 27645, 2022. URL `https://gm2-docdb.fnal.gov/cgi-bin/sso/ShowDocument?docid=27645`

[237] Josh LaBounty. Muons, Protons, and Deuterons in Run-4/5. E989 DocDB 29283, 2023. URL `https://gm2-docdb.fnal.gov/cgi-bin/sso/ShowDocument?docid=29283`

A.3.3.3 Phase-Momentum

The author spent a great deal of Run-6 attempting to understand the initial $g-2$ phase vs. momentum relationship for Run-2+ conditions. Data driven analyses found a significant difference from the evaluation in Run-1, and toy Monte Carlo studies as well as additional systematic measurements were undertaken to explain these effects. Details and implications of this analysis can be found in Section 6.1

[173] Josh LaBounty. Run-6 Momentum-Phase Measurements. E989 DocDB 28723, 2023. URL `https://gm2-docdb.fnal.gov/cgi-bin/sso/ShowDocument?docid=28723`

[238] Josh LaBounty. Run-6 Phase-Momentum Study Update and A Simplified Wedge Model. E989 DocDB 28588, 2023. URL `https://gm2-docdb.fnal.gov/cgi-bin/sso/ShowDocument?docid=28588`

A.3.3.4 Phase-Acceptance and Calo Slopes

For the Run-1 evaluation of the phase-acceptance correction (C_{pa}), the author independently generated a set of acceptance maps from Monte Carlo data in order to provide a cross check of the main analysis. The author also extracted the $\bar{y}$ value for positions as seen by the calorimeters over the course of the fill, which was used as a cross check for the extrapolation of the correction around the ring from the two tracker stations.

[239] Lars E Borchert et al. Calorimeter y Mean vs Time. E989 DocDB 22627, 2020. URL `https://gm2-docdb.fnal.gov/cgi-bin/sso/ShowDocument?docid=22627`

[240] Josh LaBounty. y-RMS ADT Scan in EndGame and Run 2C. E989 DocDB 23034, 2020. URL `https://gm2-docdb.fnal.gov/cgi-bin/sso/ShowDocument?docid=23034`

[241] Josh LaBounty. Comparing Clusters to Tracks: EndGame vs. Run-2C. E989 DocDB 22873, 2020. URL `https://gm2-docdb.fnal.gov/cgi-bin/sso/ShowDocument?docid=22873`

[164] Josh LaBounty. Phase-Acceptance Maps: Calo Position Cuts. E989 DocDB 24730, 2021. URL `https://gm2-docdb.fnal.gov/cgi-bin/sso/ShowDocument?docid=24730`

[242] Elia Bottalico et al. E989 Note 262: Phase Acceptance Correction Analysis Report. E989 DocDB 24796, 2021. URL `https://gm2-docdb.fnal.gov/cgi-bin/sso/ShowDocument?docid=24796`

[243] Anna Driutti et al. Calo y-Mean Comparisons with COSY/gm2ringsim. E989 DocDB 24886, 2021. URL `https://gm2-docdb.fnal.gov/cgi-bin/sso/ShowDocument?docid=24886`

[244] Elia Bottalico et al. E989 Note 292: Phase Acceptance Note - Run-2/3. E989 DocDB 28030, 2023. URL `https://gm2-docdb.fnal.gov/cgi-bin/sso/ShowDocument?docid=28030`

A.3.3.5 Laser Fills

As stated in Section 4.1.5.1, up to 9% of the data in a dataset is contaminated with laser pulses from the in-fill gain calibration procedure. The author investigated whether those fills were able to be used in the analysis, and developed a method of masking the data in the areas where the laser had fired. More details can be found in Section 6.3.

[245] Josh LaBounty. Using Laser Fills in omega_a Analysis via Masking. E989 DocDB 25771, 2021. URL `https://gm2-docdb.fnal.gov/cgi-bin/sso/ShowDocument?docid=25771`

[246] Josh LaBounty. Masking/Re-Weighting Laser Fills. E989 DocDB 25871, 2021. URL `https://gm2-docdb.fnal.gov/cgi-bin/sso/ShowDocument?docid=25871`

A.3.3.6 Misc. Studies

Many other smaller studies were also undertaken by the author. Additional references to these are here.

[247] Josh LaBounty. Run-6 Systematic Study Updates. E989 DocDB 28565, 2023. URL `https://gm2-docdb.fnal.gov/cgi-bin/sso/ShowDocument?docid=28565`

[171] Josh LaBounty. Quick Toy MC of A/T Differences. E989 DocDB 28825, 2023. URL `https://gm2-docdb.fnal.gov/cgi-bin/sso/ShowDocument?docid=28825`

[248] Josh LaBounty. Acceptance Maps - Potential for Data Driven Verification. E989 DocDB 29238, 2023. URL `https://gm2-docdb.fnal.gov/cgi-bin/sso/ShowDocument?docid=29238`

A.3.4 Precession Frequency Analysis

The author played a supporting role in the Run-1/2/3 UW ω_a analysis and a leading role in the Run-4/5/6 analysis. The author was a convener for the Run-4/5/6 ‘kick-off’ workshop at the Summer 2023 Liverpool Collaboration Meeting. Details of these contributions can be found in Chapter 5.

[249] Esra Barlas Yucel et al. Run 2/3 Muon Precession Analysis Internal Review. E989 DocDB 28618, 2023. URL `https://gm2-docdb.fnal.gov/cgi-bin/sso/ShowDocument?docid=28618`

[250] Josh LaBounty. Omega_a workshop - Run-4/5/6 random thoughts. E989 DocDB 28731, 2023. URL `https://gm2-docdb.fnal.gov/cgi-bin/sso/ShowDocument?docid=28731`

[251] Josh LaBounty et al. Run-4/5/6: Omega-a Analysis. E989 DocDB 28761, 2023. URL `https://gm2-docdb.fnal.gov/cgi-bin/sso/ShowDocument?docid=28761`

[252] Josh LaBounty. A Quick Look at Some Run-4/5/6 Puzzles: Run-4 Residual Gain and Run-5 CBO Amplitude/Frequency. E989 DocDB 29044, 2023. URL `https://gm2-docdb.fnal.gov/cgi-bin/sso/ShowDocument?docid=29044`

[253] Josh LaBounty. Sensitivity of the UW Analysis to the Vertical Terms. E989 DocDB 29106, 2023. URL `https://gm2-docdb.fnal.gov/cgi-bin/sso/ShowDocument?docid=29106`

[254] Josh LaBounty. Summary of the omega_a analyzer group survey. E989 DocDB 29235, 2023. URL `https://gm2-docdb.fnal.gov/cgi-bin/sso/ShowDocument?docid=29235`

[170] Josh LaBounty. Omega_a workshop systematic discussion: Residual Gain Correction. E989 DocDB 29231, 2023. URL `https://gm2-docdb.fnal.gov/cgi-bin/sso/ShowDocument?docid=29231`

[255] Josh LaBounty. Changing CBO Frequency in Run-4/5. E989 DocDB 29280, 2023. URL `https://gm2-docdb.fnal.gov/cgi-bin/sso/ShowDocument?docid=29280`

A.4 Misc.

A.4.1 Undergraduate Talks

The author has spent a good deal of time mentoring undergraduate researchers who were doing research in the UW $g-2$ group. The author developed a standard set of 'onboarding' resources to help get started, which were then used by others in the collaboration.

[256] Josh LaBounty. Introduction to ROOT and g-2 computing for Undergraduates. E989 DocDB 23073, 2020. URL `https://gm2-docdb.fnal.gov/cgi-bin/sso/ShowDocument?docid=23073`

[257] Josh LaBounty. Introduction to g-2 Calorimeter Reconstruction Chain for Undergraduates. E989 DocDB 23239, 2020. URL `https://gm2-docdb.fnal.gov/cgi-bin/sso/ShowDocument?docid=23239`

[258] Josh LaBounty. g-2 Undergraduate Questions. E989 DocDB 23381, 2020. URL `https://gm2-docdb.fnal.gov/cgi-bin/sso/ShowDocument?docid=23381`

A.4.2 Public Research Talks

[259] Josh LaBounty. Standing on The Shoulders of Giants: Past, Present, and Future of Muon g-2. E989 DocDB 23420, 2020. URL `https://gm2-docdb.fnal.gov/cgi-bin/sso/ShowDocument?docid=23420`

Josh LaBounty. Muon $g-2$ In 10 Minutes. In: oSTEM 2019.

Josh LaBounty. An Updated Measurement of Muon $g-2$ to 0.2 ppm. 2023. URL `https://indico.bnl.gov/event/20145/`

A.4.3 Outreach

[260] Josh LaBounty. Thinking Like a Physicist: How Subatomic Tops Teach Us To Embrace Being Wrong. E989 DocDB 25343, 2021. URL `https://gm2-docdb.fnal.gov/cgi-bin/sso/ShowDocument?docid=25343`

[261] Josh LaBounty. Future Opportunities: PIONEER. E989 DocDB 27498, 2022. URL `https://gm2-docdb.fnal.gov/cgi-bin/sso/ShowDocument?docid=27498`